

ABSTRACT

Title of dissertation: NEAR-INFRARED INSTRUMENTATION
FOR RAPID-RESPONSE ASTRONOMY

John Isaac Capone
Doctor of Philosophy, 2016

Dissertation directed by: Professor Sylvain Veilleux
Department of Astronomy

γ -ray bursts (GRBs) are the Universe’s most luminous transient events. Since the discovery of GRBs was announced in 1973, efforts have been ongoing to obtain data over a broader range of the electromagnetic spectrum at the earliest possible times following the initial detection. The discovery of the theorized “afterglow” emission in radio through X-ray bands in the late 1990s confirmed the cosmological nature of these events.

At present, GRB afterglows are among the best probes of the early Universe ($z \gtrsim 9$). In addition to informing theories about GRBs themselves, observations of afterglows probe the circum-burst medium (CBM), properties of the host galaxies and the progress of cosmic reionization.

To explore the early-time variability of afterglows, I have developed a generalized analysis framework which models near-infrared (NIR), optical, ultra-violet (UV) and X-ray light curves without assuming an underlying model. These fits are then used to construct the spectral energy distribution (SED) of afterglows at

arbitrary times within the observed window. Physical models are then used to explore the evolution of the SED parameter space with time. I demonstrate that this framework produces evidence of the photodestruction of dust in the CBM of GRB 120119A, similar to the findings from a previous study of this afterglow. The framework is additionally applied to the afterglows of GRB 140419A and GRB 080607. In these cases the evolution of the SEDs appears consistent with the standard fireball model.

Having introduced the scientific motivations for early-time observations, I introduce the Rapid Infrared Imager-Spectrometer (RIMAS). Once commissioned on the 4.3 meter Discovery Channel Telescope (DCT), RIMAS will be used to study the afterglows of GRBs through photometric and spectroscopic observations beginning within minutes of the initial burst. The instrument will operate in the NIR, from $0.97 \mu\text{m}$ to $2.37 \mu\text{m}$, permitting the detection of very high redshift ($z \gtrsim 7$) afterglows which are attenuated at shorter wavelengths by Lyman- α absorption in the intergalactic medium (IGM).

A majority of my graduate work has been spent designing and aligning RIMAS's cryogenic (~ 80 K) optical systems. Design efforts have included an original camera used to image the field surrounding spectroscopic slits, tolerancing and optimizing all of the instrument's optics, thermal modeling of optomechanical systems, and modeling the diffraction efficiencies for some of the dispersive elements. To align the cryogenic optics, I developed a procedure that was successfully used for a majority of the instrument's sub-assemblies.

My work on this cryogenic instrument has necessitated experimental and com-

putational projects to design and validate designs of several subsystems. Two of these projects describe simple and effective measurements of optomechanical components in vacuum and at cryogenic temperatures using an 8-bit CCD camera. Models of heat transfer via electrical harnesses used to provide current to motors located within the cryostat are also presented.

NEAR-INFRARED INSTRUMENTATION FOR
RAPID-RESPONSE ASTRONOMY

by

John Isaac Capone

Dissertation submitted to the Faculty of the Graduate School of the
University of Maryland, College Park in partial fulfillment
of the requirements for the degree of
Doctor of Philosophy
2016

Advisory Committee:
Professor Sylvain Veilleux, Chair/Advisor
Dr. Alexander Kutyrev, Co-Advisor
Dr. S. Bradley Cenko
Professor Andrew Harris
Professor Suvi Gezari
Professor Gregory Sullivan

© Copyright by
John Isaac Capone
2016

Preface

Portions of Chapters 3, 4 and 5 were previously published in non-refereed SPIE conference proceeding manuscripts (Capone et al., 2013, 2014b). The progress of RIMAS's optomechanical systems has routinely been presented at meetings of the American Astronomical Society (Capone et al., 2012, 2014a; Capone and RIMAS Collaboration, 2016).

This work made use of data supplied by the UK Swift Science Data Centre at the University of Leicester.

Table 1: I have worked on many components of the RIMAS instrument since joining the project in 2011. This table summarizes where my efforts described in this thesis have involved collaborating with other team members.

Dr. Alexander Kuttyrev	Supervised my work in the laboratory at NASA-GSFC. Assisted in taking laboratory measurements on many occasions. Led alignment efforts of the HK-band camera in Q1 and Q2 of 2016.
Prof. Sylvain Veilleux	Advised my long-term contributions to RIMAS.
Dr. David Content	Created the preliminary designs for the scientific optics.
Ms. Vicki Toy	Developed hardware and software to operate NIR detectors. Assisted in taking laboratory measurements on many occasions. Worked on designs for electrical harnesses. Wrote exposure time calculator script for RIMAS.
Mr. Gennadiy Lotkin	Designed all of RIMAS's mechanical components. Produced fabrication drawings for components.
Mr. Frederick D. Robinson	Developed cryogenic systems. Advised optomechanical alignment.
Dr. Thomas Hams	Developed software to operate NIR detectors.
Dr. Neil Gehrels	Primary investigator for RIMAS. Participated in the December 2011 critical design review.
Prof. Stuart Vogel	Participated in the December 2011 critical design review.
Dr. Samuel H. Moseley	Participated in the December 2011 critical design review.

Dedication

For my Dad, who never stopped wondering

Acknowledgments

I owe much to the community that is the Department of Astronomy at the University of Maryland, College Park. I have never before met so many wonderful and intelligent people in one place. My thanks especially to Prof. Sylvain Veilleux for advising and supporting my research and for helping me prepare presentations and manuscripts. I would also like to thank the many individuals at NASA-GSFC who have shared with me their time and expertise. In particular, I thank Dr. Alexander Kuttyrev for introducing me to many laboratory techniques and for his consistently positive attitude. I also thank Dr. Brad Cenko for all of his assistance and patience. At home, I am forever indebted to my wife and partner, Meghan, for supporting me emotionally and financially. I thank my Mom for helping proofread the entirety of this document. Finally, I would never have pursued this degree if it were not for the love and encouragement of my very large family.

Acknowledgments (continued)

I'm a scientist and I know what constitutes proof. But the reason I call myself by my childhood name is to remind myself that a scientist must also be absolutely like a child. If he sees a thing, he must say that he sees it, whether it was what he thought he was going to see or not. See first, think later, then test. But always see first. Otherwise you will only see what you were expecting. Most scientists forget that.

Douglas Adams, So Long, and Thanks for All the Fish

Table of Contents

List of Tables	x
List of Figures	xi
List of Abbreviations	xiv
1 Introduction	1
1.1 γ -ray Bursts	1
1.1.1 A Brief History	1
1.1.2 Standard Afterglow Model	16
1.2 Thesis Overview	18
2 GRB Afterglow Temporal Analysis Framework	25
2.1 SED Color Evolution	25
2.1.1 External Reverse Shock	27
2.1.2 Dust	31
2.1.2.1 Reddening by Host Galaxies	31
2.1.2.2 Dust Destruction	34
2.1.3 Other Scenarios	35
2.2 Analysis Framework	35
2.2.1 SED Construction	35
2.2.1.1 Natural Smoothing Splines	36
2.2.2 SED Fitting	42
2.3 GRB 140419A	53
2.3.1 Observations	53
2.3.1.1 <i>Swift</i> Space Observatory	53
2.3.1.2 RATIR	55
2.3.1.3 GMOS-N	55
2.3.2 Analysis	62
2.3.2.1 Optical Spectrum	62
2.3.2.2 Optical and Near-Infrared Light Curves	62
2.3.2.3 X-ray Light Curve	64
2.3.2.4 Temporal Evolution	69

2.3.3	Discussion and Conclusions	69
2.4	GRB 080607	70
2.4.1	Observations	71
2.4.1.1	<i>Swift</i> Space Observatory	71
2.4.1.2	Optical and Near-Infrared Observations	74
2.4.2	Analysis	74
2.4.2.1	Optical and Near-Infrared Light Curves	74
2.4.2.2	X-ray Light Curve	76
2.4.2.3	Temporal Evolution	78
2.4.3	Discussion and Conclusions	78
2.5	Summary	81
3	RIMAS: Background	85
3.1	Requirements	85
3.1.1	Response Time	85
3.1.2	Spectral Coverage	85
3.1.3	Spatial Coverage	90
3.1.4	LGRB Afterglow Detection Rate Estimates	90
3.2	Discovery Channel Telescope	92
3.2.1	Ritchey-Chrétien Design	94
3.2.2	Instrument Cube	95
3.2.3	Site	96
3.3	RIMAS Design Overview	96
3.3.1	Optical Definitions	96
3.3.2	Cryostat	98
3.3.3	Slit-Imaging Camera	98
3.3.4	Imaging Systems	101
3.3.5	Spectroscopic Systems	105
4	RIMAS: Cryogenic Optics	107
4.1	Slit-Imaging Camera	107
4.1.1	Requirements	107
4.1.2	Basic Design and Materials Selection	108
4.1.2.1	Achromatic Doublet	108
4.1.2.2	Two doublet design	110
4.1.3	Tolerancing and Desensitizing	110
4.1.4	Optomechanics and Thermal Modeling	112
4.1.5	Room Temperature Alignment	113
4.1.6	Evaluation	114
4.2	Imaging Systems	114
4.2.1	Tolerancing and Desensitizing	115
4.2.2	Thermal Modeling for Fabrication	116
4.2.2.1	Optics	117
4.2.2.2	Optomechanical Assemblies	120
4.2.2.3	Thermal Compensating Design	121

4.2.3	Metrology and Re-optimization	124
4.2.4	Room Temperature Assembly and Alignment	126
4.2.4.1	Microscope Alignment	126
4.2.4.2	HK-band Camera Alignment	127
4.2.5	Room Temperature Testing	127
4.2.6	Cryogenic Verification of Imaging Performance	129
4.3	Spectroscopic Systems	129
4.3.1	Design Selection	129
4.3.2	Grism Efficiency Modeling	131
4.3.2.1	RCWA-1D Testing	132
4.3.2.2	RIMAS Grism Efficiency Modeling and Optimization	135
5	RIMAS: Cryogenic Methods	143
5.1	Thermal Contraction Measurements	143
5.1.1	Motivation	143
5.1.2	Experimental Design	144
5.1.2.1	Materials	146
5.1.2.2	Procedure	149
5.1.3	Analysis	151
5.1.3.1	Phase-only Correlation	152
5.1.4	Results	153
5.1.5	Further Applications	156
5.2	Electrical Harness Modeling	161
5.2.1	Modeling Heat Transfer	161
5.2.1.1	1-D Relaxation Method	162
5.2.1.2	Model Testing	164
5.2.2	Design Optimization	168
5.3	Cold-Plate Vibration Measurements	171
5.3.1	Motivation	171
5.3.2	Experimental Design	172
5.3.2.1	Procedure	172
5.3.3	Analysis	174
5.3.4	Results	174
6	Final Considerations	179
6.1	Summary	179
6.2	Lessons from RIMAS	180
6.3	Future Applications	183
6.3.1	HARMONI Spectrograph	183
6.3.2	Planned Research in Transient Astronomy	183
A	Lens Metrology Report	187
	Bibliography	216

List of Tables

1	RIMAS Collaboration Involvement	iii
2.1	GRB 120119A: Extinction Fits	45
2.2	GRB 140419A: r-Band Photometry	56
2.3	GRB 140419A: i-Band Photometry	57
2.4	GRB 140419A: Z-Band Photometry	58
2.5	GRB 140419A: Y-Band Photometry	59
2.6	GRB 140419A: J-Band Photometry	60
2.7	GRB 140419A: H-Band Photometry	61
2.8	GRB 140419A: Fit Summary	70
3.1	Slit-imaging Requirements	101
3.2	RIMAS Optical Requirements	102
4.1	Typical Tolerance Levels	111
4.2	Slit-imaging Sensitivities	112
4.3	Temperature Dependent Refractive Indices	113
4.4	Thermal Contraction: Metal Alloys	114
4.5	Thermal Contraction: Optical Substrates	115
4.6	Thermal Contraction: Plastics	116
4.7	RIMAS Sensitivities	119
5.1	Electrical Resistivity Values	164
5.2	Thermal Conductivity Values	165

List of Figures

1.1	First Detected GRB	2
1.2	BATSE GRB Sky Map	4
1.3	BATSE GRB Spectrum	5
1.4	BATSE GRB Light Curves	6
1.5	GRB Populations	7
1.6	GCN Activity	11
1.7	Photometric Dust Profile	13
1.8	GRB Afterglow Spectroscopy	14
1.9	Rapid Decay of GRB 140215A	15
1.10	Fireball Model	17
1.11	Synchrotron Spectrum	19
2.1	GRB Shock Cartoon	28
2.2	GRB Shock Simulations	29
2.3	First Reverse Shock Detection	30
2.4	Multi-band Reverse Shock Detection	32
2.5	Dust Extinction Curves	33
2.6	GRB 120119A: Optical Light Curves Fits	38
2.7	GRB 120119A: XRT Flux Light Curve Fit	39
2.8	GRB 120119A: XRT Spectra Fits	40
2.9	GRB 120119A: Times of Constant X-ray Hardness Ratio	41
2.10	GRB Dust-to-Gas Ratios	43
2.11	GRB 120119A: Optical Fit Corner Plot	46
2.12	GRB 120119A: Optical Fit	47
2.13	GRB 120119A: Optical + X-ray Fit Corner Plot	48
2.14	GRB 120119A: Optical + X-ray Fit	49
2.15	GRB 120119A: Optical + X-ray Evolution	51
2.16	GRB 120119A: Optical + X-ray Comparison	52
2.17	GRB 120119A: Optical Comparison	54
2.18	GRB 140419A: GMOS-N Spectrum	63
2.19	GRB 140419A: Optical/NIR Light Curve Fits	65
2.20	GRB 140419A: XRT Flux Light Curve Fit	66
2.21	GRB 140419A: Times of Constant X-ray Hardness Ratio	67

2.22	GRB 140419A: XRT Spectra Fits	68
2.23	GRB 140419A: Evolution, $A_V = 0$	71
2.24	GRB 140419A: Evolution	72
2.25	GRB 080607: Dust Extinction	73
2.26	GRB 080607: Optical/NIR Light Curve Fits	75
2.27	GRB 080607: XRT Flux Light Curve Fit	76
2.28	GRB 080607: Times of Constant X-ray Hardness Ratio	77
2.29	GRB 080607: Optical Evolution	79
2.30	GRB 080607: Optical + X-ray Evolution	80
3.1	The Lyman- α Forest	87
3.2	Spectroscopic Drop-out of GRB	88
3.3	Optical and NIR filters	89
3.4	ZnII Absorption Line at Different Spectral Resolutions	91
3.5	RIMAS Sensitivity Estimates	93
3.6	DCT First Light Image	94
3.7	DCT Ray-tracing	95
3.8	Lens Definitions	97
3.9	RIMAS Cryostat CAD Model	99
3.10	Slit-imaging Camera CAD Model	100
3.11	Optomechanical Overview CAD Model	103
3.12	Lens Assembly CAD Model	104
4.1	P-V Diagram	109
4.2	Slit-imaging Camera Design	110
4.3	Microscope Lens Alignment	117
4.4	Slit-viewing Camera Performance	118
4.5	Thermal Compensator Design	122
4.6	YJ-band First Image	128
4.7	YJ-band Imaging Performance	130
4.8	Grism Definition	132
4.9	Comparison with OSMOS Calculations	134
4.10	Comparison with LMIRcam Calculations	135
4.11	Variation of Blaze Angle	136
4.12	Variation of Apex Angle	137
4.13	Apex Shadow Model	138
4.14	Apex Shadow Explanation	139
4.15	YJ Grism Performance	140
4.16	HK Grism Performance	141
5.1	Push-rod Dilatometer	145
5.2	Drawing of Dilatometer Test Setup	146
5.3	Thermal Expansion Sample Mount	147
5.4	Improved Contrast Setup	148
5.5	Thermal Expansion Temperature Curves	150
5.6	Thermal Expansion Comparison	151

5.7	Phase-only Correlation Function	154
5.8	Test Setup Validation	155
5.9	Measurement of POM and PMMA	157
5.10	POM and PMMA in Linear Regime	158
5.11	Systematic Error Estimates	159
5.12	POC Error Estimates	160
5.13	Heat Transfer Model	163
5.14	Analytical Comparison	166
5.15	Assumed Emissivity	167
5.16	Required Number of Nodes	168
5.17	Cold-Shield Wire Temperature Profile	169
5.18	Impact of Cold-Shield	169
5.19	Electrical Harness Optimization	170
5.20	Motor Current	171
5.21	Vibration Test Setup	173
5.22	Position Determination	175
5.23	Starting Cold-Plate Vibrations	176
5.24	Final Cold-Plate Vibrations	177

List of Abbreviations

AWG	American wire gauge
BBAR	broadband anti-reflection
CAD	computer-aided design
CBM	circum-burst medium
CCD	charge-coupled device
CHARMS	Cryogenic High Accuracy Refraction Measuring System
CMM	coordinate measuring machine
COG	curve of growth
DCT	Discovery Channel Telescope
DFT	discrete Fourier transforms
EE	encircled energy
FWHM	full width at half maximum
GCN	Gamma-ray Coordinates Network
GCV	generalized cross-validation
GRB	γ -ray burst
HARMONI	High Angular Resolution Monolithic Optical and Near-infrared Integral field spectrograph
IDFT	inverse discrete Fourier transform
IGM	intergalactic medium
ISM	interstellar medium
LGRB	long duration γ -ray burst
MCMC	Markov chain Monte Carlo
NASA-GSFC	National Aeronautics and Space Administration, Goddard Space Flight Center
NIR	near-infrared
OFHC	oxygen-free high thermal conductivity
PAH	polycyclic aromatic hydrocarbon
PMMA	poly(methyl methacrylate) - e.g. Plexiglas
POC	phase-only correlation
POM	polyoxymethylene - e.g. Delrin
PSF	point spread function
RATIR	Reionization and Transients Infrared/Optical Project multi-channel imager
RCWA	rigorous coupled wave analysis
RIMAS	Rapid Infrared Imager-Spectrograph
RMS	root mean square
SED	spectral energy distribution
SGRB	short duration γ -ray burst
SN	supernova
SNR	signal-to-noise ratio
ToO	target of opportunity
UMCP	University of Maryland, College Park
UV	ultraviolet

Chapter 1: Introduction

1.1 γ -ray Bursts

1.1.1 A Brief History

The Vela satellites, equipped with CsI(Tl) scintillation detectors sensitive to photon energies of $\approx 0.2 - 1.5$ MeV, were designed to verify compliance with the Nuclear Test Ban Treaty (Singer, 1965). The first detected γ -ray burst (GRB) was recorded in 1967 by the Vela 3, 4a and 4b satellites as a sudden increase in coincident γ -ray events. The multi-peaked structure of the episode was inconsistent with the single peak expected for a nuclear warhead (Figure 1.1). Additional GRB detections by later Vela satellites with better timing precision eliminated the Earth and Sun as possible sources (Klebesadel et al., 1973; Bonnell and Klebesadel, 1996).

The first spectra obtained in the early 1970s confirmed that GRBs were truly γ -ray events (i.e., most emission at $E_\gamma \gtrsim 0.1$ MeV) rather than the high-energy tail of X-ray events (Cline et al., 1973). Over the next decade, it was determined that GRBs with $E_\gamma > 1$ MeV were common (Matz et al., 1985). The discovery of high-energy emission demonstrated that at least part of the spectrum was non-thermal in nature (e.g., Brainerd and Lamb, 1987, see Figure 1.3).

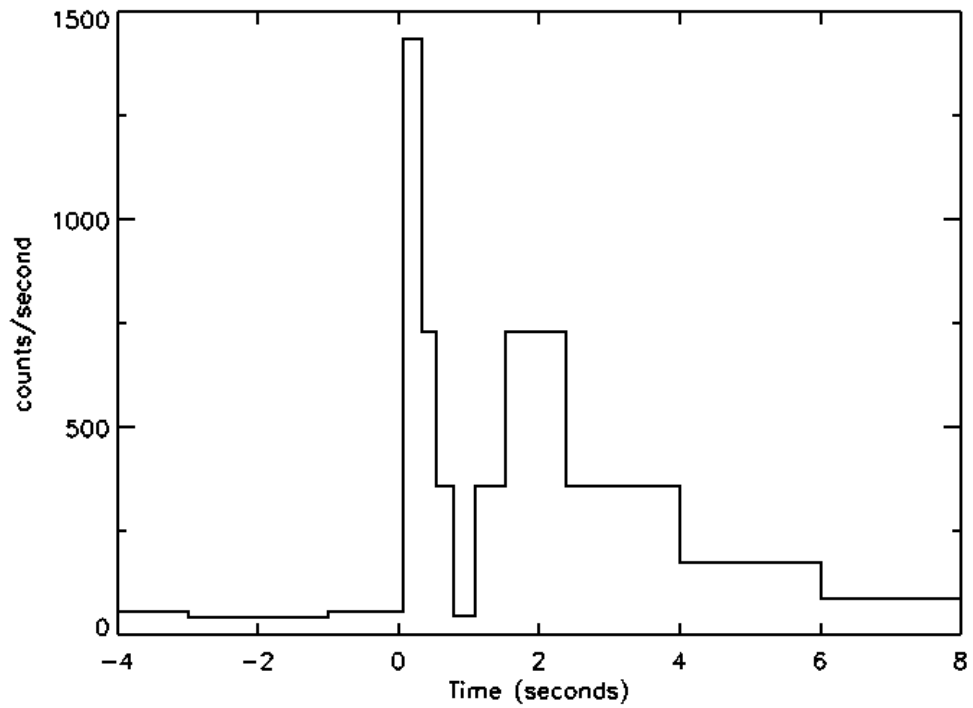


Figure 1.1: The light curve of the first detected GRB taken from [Bonnell and Klebesadel \(1996\)](#). The GRB was recorded between $\sim 0.2-1.5$ MeV by the Vela 3, 4a and 4b satellites on July 2, 1967.

The launch of the Compton Gamma Ray Observatory (CGRO) in 1991 greatly increased the amount of data on these transient sources. The Burst and Transient Source Experiment (BATSE) on-board CGRO increased the rate of GRB detections to $\sim 1/\text{day}$. In addition to confirming the angular distribution’s high degree of isotropy (Figure 1.2), high SNR spectra of these events led to the adoption of the empirical “Band” function (Figure 1.3).

The time during which 90% of the background-subtracted counts are detected (T_{90}) is used as a simple measure of the durations of these complex and diverse events (see Figure 1.4). BATSE measurements of T_{90} range from $\lesssim 100$ ms up to $\gtrsim 10^3$ s. With thousands of bursts detected by BATSE, it was determined from the distribution of T_{90} values and spectral hardness ratios ($S_{100-300\text{ keV}}/S_{50-100\text{ keV}}$, where $S_x \triangleq$ fluence in band x) that there are at least two sub-populations of GRBs. “Short” GRBs (SGRBs) are typically spectrally harder and have shorter durations ($T_{90} \lesssim 2$ sec), while “long” GRBs (LGRBs) are typically softer with longer durations ($T_{90} \gtrsim 2$ sec, see Figure 1.5, Kouveliotou et al., 1993; Fox and Roming, 2007).

Since the first detected GRBs, the diversity of light curve structure and the variability on short time-scales ($\delta t \lesssim 10$ ms) has been noted, as seen in Figure 1.4. This implies that the sources must be smaller than $\sim c\delta t = 3 \times 10^8$ cm if they are not expanding relativistically or highly beamed (Ruderman, 1975; Piran, 2004).

The observed average fluence of 1283 bursts detected by channel 2 of BATSE (50 – 300 keV) was $\sim 10^{-6}$ erg cm $^{-2}$ (Paciesas et al., 1999, see BATSE 4B Peak Flux and Fluence Table, http://gammaray.msfc.nasa.gov/batse/grb/catalog/4b/4br_flux.html). The small source size combined with high observed fluences

2704 BATSE Gamma-Ray Bursts

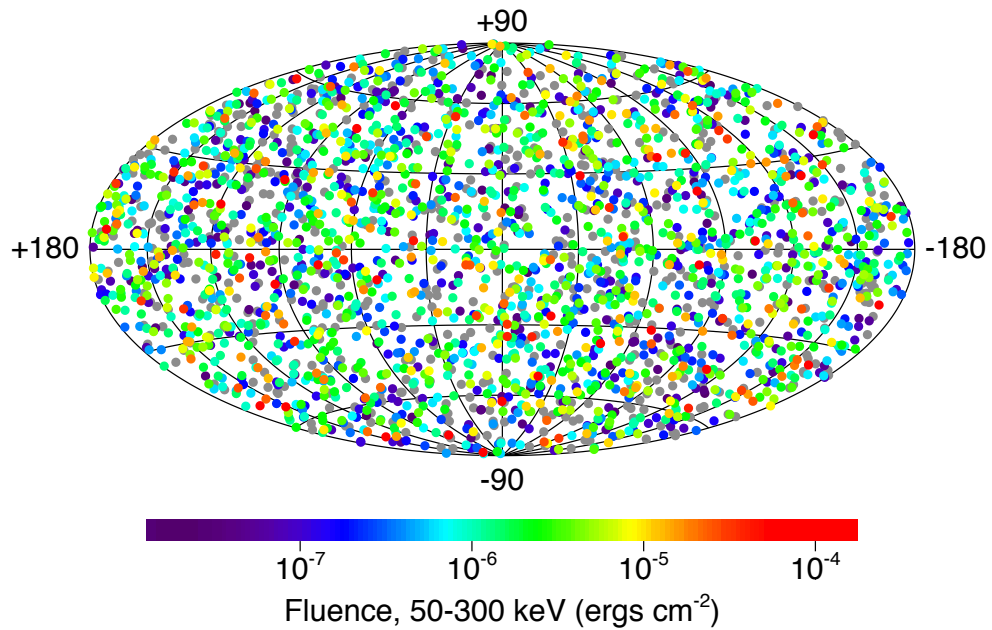


Figure 1.2: The angular distribution of GRBs detected by BATSE on the sky. The high level of isotropy in the distribution was an early clue to the extragalactic nature of these sources. Also note the intense fluence ranging from $\lesssim 10^{-7}$ erg cm^{-2} to $\gtrsim 10^{-4}$ erg cm^{-2} . This figure was downloaded from <http://gammaray.nsstc.nasa.gov/batse/grb/skymap/>.

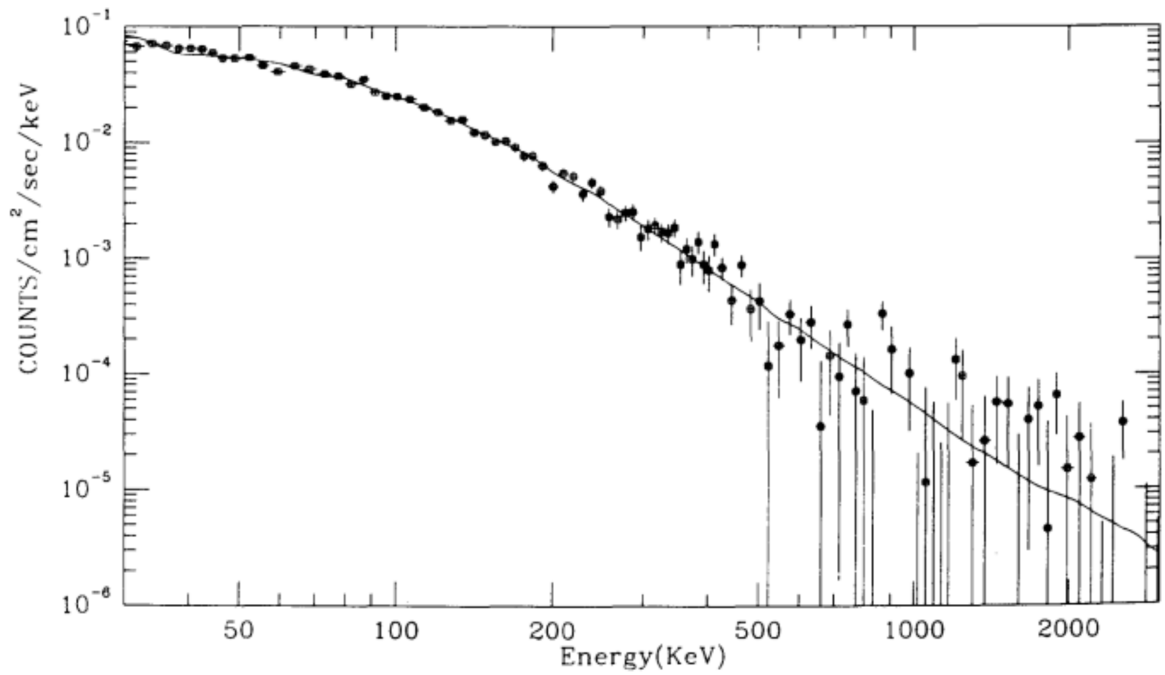


Figure 1.3: This BATSE spectrum of GRB 911127 was taken from [Band et al. \(1993\)](#). The spectrum is fit with an empirical model consisting of two smoothly joined power-laws (i.e., the “Band function”) which cannot be produced by a thermal distribution.

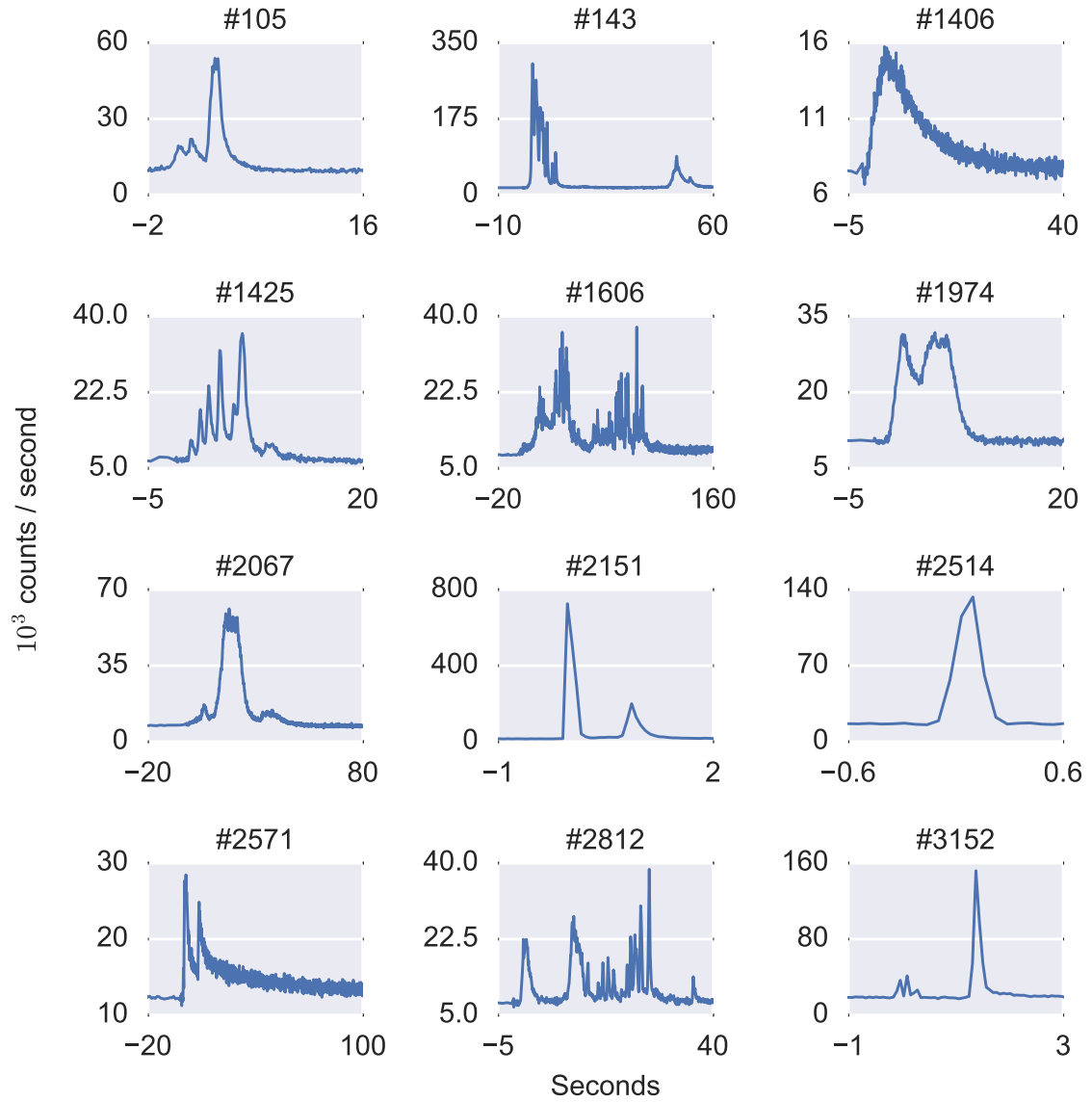


Figure 1.4: BATSE GRB light curves from 30 keV to 2 MeV. The selected sample of bursts was taken from Figure 1 of [Mészáros \(2006\)](#) and the data are from [Paciesas et al. \(1999\)](#). Event numbers are provided above each plot. The number and duration of peaks differs greatly between events. Additionally, the short time-scale variability suggests emission originating from a compact object. This leads to the “compactness problem.”

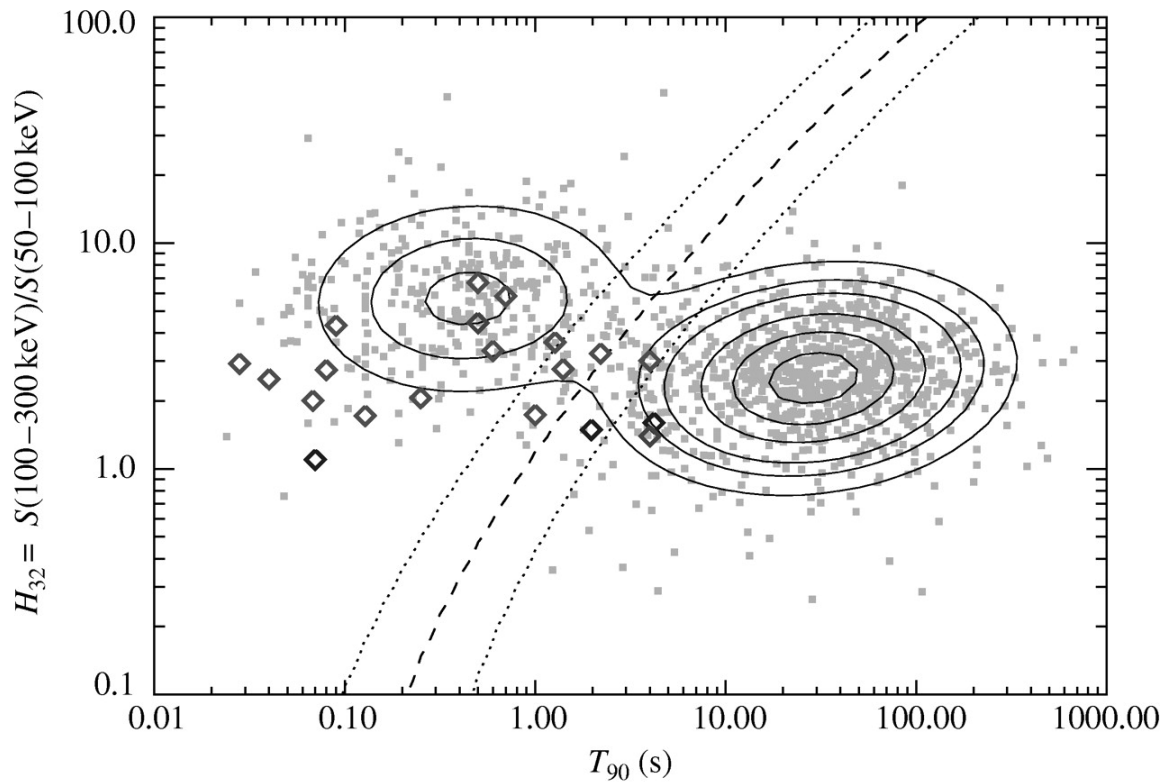


Figure 1.5: T_{90} plotted against the spectral hardness ratio, taken from [Fox and Roming \(2007\)](#). BATSE detections from the 4B Catalog ([Paciesas et al., 1999](#)) are shown as grey squares while selected SGRBs detected by *Swift* are plotted as diamonds. The contours are two bivariate lognormal distributions fit to these data while the dashed line shows where a GRB has equal chances of being from either distribution. The dotted lines show where a burst has 10-1 odds of being from the nearer population.

and a non-thermal spectrum were recognized as a problem soon after the discovery of GRBs (e.g., [Ruderman, 1975](#); [Schmidt, 1978](#)). The “compactness problem” was the observation that, were GRBs extragalactic, they would have such a large density of high-energy photons (> 511 keV) as to be optically thick to such photons via $\gamma-\gamma$ pair production. Additionally, the rapid formation of $e^- e^+$ pairs would lead to a large optical depth for all photons via Compton scattering ([Piran, 2004](#)).

Alternatively, were the ejecta to expand ultra-relativistically towards the observer, the measured variability will be dilated by a factor of Γ^2 (the Lorentz factor $= \Gamma \triangleq 1/\sqrt{1 - v^2/c^2}$), leading to an emitting region of radius $\approx \Gamma^2 c \delta t$. The detected photons would also be emitted at energies lower by a factor of Γ , decreasing the number with energy sufficient for pair-production ([Goodman, 1986](#); [Paczynski, 1986](#); [Krolik and Pier, 1991](#)). The average optical depth is given as a function of Γ in Equation 1.1 (Equation 10 from [Piran, 1999](#)). In this equation, α is the high-energy spectral index (≈ 1.25) and f_p is the fraction of photo pairs with sufficient energy to produce an electron, positron pair. From this, $\Gamma \gtrsim 100$ results in $\tau_{\gamma\gamma} \lesssim 1$. In this case photons are able to escape without reaching thermal equilibrium, producing a non-thermal spectrum.

$$\tau_{\gamma\gamma} \approx \frac{10^{13}}{\Gamma^{(4+2\alpha)}} f_p \left(\frac{F}{10^{-7} \text{ erg / cm}^2} \right) \left(\frac{D}{3000 \text{ Mpc}} \right)^2 \left(\frac{\delta T}{10 \text{ ms}} \right)^{-2} \quad (1.1)$$

[Paczynski and Rhoads \(1993\)](#) predicted that there would be a radio counterpart to GRBs. In this letter, the authors argued that there must be ultra-relativistic ejecta based on the observed rapid variability and large peak luminosities of GRBs. When this ejecta interacts with the circum-burst medium (CBM), it would produce

synchrotron emission. Today this is known as the “afterglow” emission.

The compactness problem was originally used to argue for a Galactic origin, however BATSE detected GRBs isotropically on the sky (Figure 1.2). Additionally, a deficit was observed in the number of bursts with low peak intensities versus what would be expected for a population homogeneously distributed within a given spherical volume (Meegan et al., 1992). Both of these facts revealed by BATSE argued for an extragalactic origin, but the several square degree localizations provided by BATSE prevented counterparts at lower energies from being identified.

In 1997, shortly after the launch of *BeppoSAX*, the theorized GRB afterglows were detected in X-rays for the first time for GRB 970111 and GRB 970228, providing arc-minute positions (Costa et al., 1997; Piro et al., 1999). Additional detections at optical and radio wavelengths followed these bursts (van Paradijs et al., 1997; Frail et al., 2000). Afterglows are now understood to originate from shocks formed as an ultra-relativistic ($\Gamma \gtrsim 100$) jet interacts with the CBM (see Section 1.1.2). One immediate impact of the discovery of GRB afterglows was to definitively demonstrate the cosmological origin of GRBs via the detection of absorption features in the optical spectrum at a redshift of 0.835 (Metzger et al., 1997).

Observations of GRB afterglows soon provided evidence associating at least some LGRBs with the deaths of massive stars. GRB 980425 was followed by SN 1998bw (Galama et al., 1998). Since then “supernova bumps” have been detected following a number of bursts (e.g., Hjorth et al., 2003; Malesani et al., 2004). The observed GRB-supernovae (SNe) are broad-lined type Ic, which are linked to the core-collapse of massive stars. Although still unconfirmed, the previously mentioned

SGRB population is thought to be the result of compact object mergers.

Since 1997, GRB afterglows have been routinely detected at X-ray, optical and radio wavelengths. LGRB afterglows are often detected for days or weeks and are sometimes detected for many months (e.g., [Perley et al., 2014](#)). When the *Swift* mission began distributing burst alerts via the Gamma-ray Coordinates Network (GCN, <http://gcn.gsfc.nasa.gov/>) in December of 2004, the frequency of follow up observations across the electromagnetic spectrum increased more than fourfold, as shown in [Figure 1.6](#). Earlier observations in more wavelength regimes have led to better tests of GRB and afterglow theories (see [Section 1.1.2](#)).

Today LGRBs are recognized as an excellent tool for probing many aspects of the history of the Universe. Due to the extreme luminosities ($L_{\text{iso}} \lesssim 10^{54} \text{ erg s}^{-1}$, [Frederiks et al., 2013](#)) achieved by these events, they have been observed out to cosmological redshifts of ~ 9 ([Tanvir et al., 2009](#); [Cucchiara et al., 2011](#)) and are thought to be observable to redshifts as high as 20 ([Lamb and Reichart, 2000](#)). The simple power-law shape of the afterglow emission’s spectral energy distribution (SED) makes these sources ideal for absorption studies.

In recent years galaxies have been observed out to $z \lesssim 9\text{--}10$ ([Bouwens et al., 2014](#)), however studies relying on these objects are by definition biased towards the most massive and luminous galaxies in the early Universe. This is problematic, for example, when studying the era of reionization where low luminosity galaxies were responsible for a significant fraction of ionizing photons. On the other hand, LGRBs provide potentially unbiased access to the properties of early galaxies since the death of a single massive star is sufficient for a given galaxy to be studied.

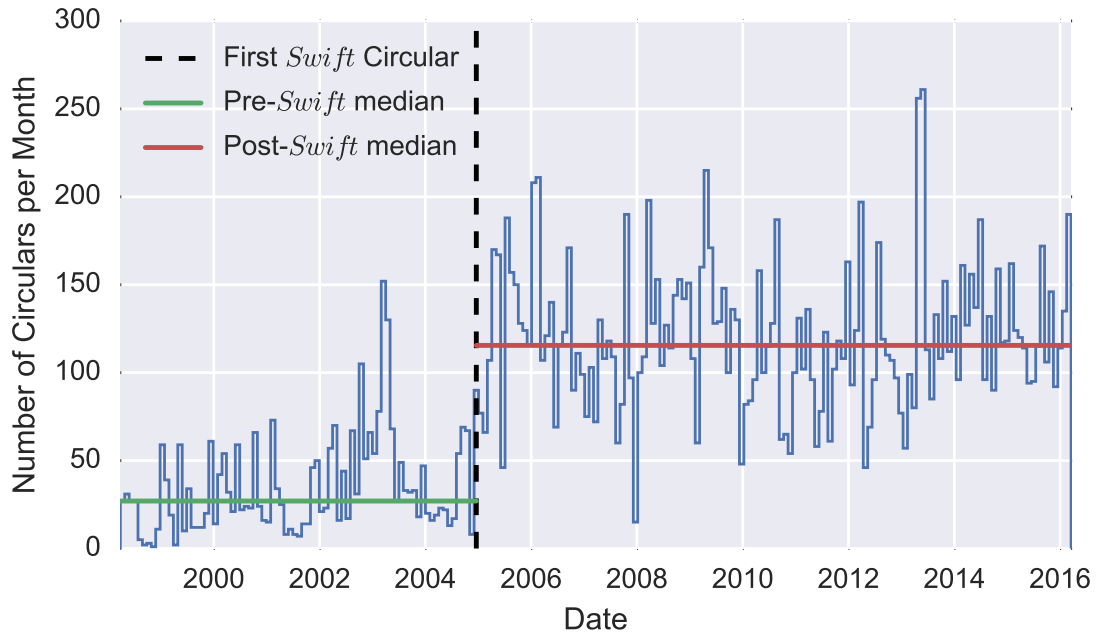


Figure 1.6: The start of the *Swift* mission marked a dramatic increase in the GRB community’s activity. The median number of Gamma-ray Coordinates Network (GNC, <http://gcn.gsfc.nasa.gov/>) circulars per month increased from 27 to 115. In addition to providing γ -ray, X-ray, ultra-violet and optical data, *Swift* is able to provide \sim few arc-second localizations in approximately 1 minute (Burrows et al., 2005). This enables observers and robotic telescopes around the world to begin observations within minutes of a burst.

Information about intervening matter along the line-of-sight to a GRB can be accessed by studying how the afterglow emission is attenuated. Photometric observations constrain dust extinction profiles from the host galaxy (Figure 1.7, see Section 2.1.2). For sufficiently bright afterglows, spectroscopy reveals absorption lines allowing studies of host galaxy metallicity (Figure 1.8).

At intervening redshifts, the afterglow is attenuated by the intergalactic medium (IGM). Neutral hydrogen in the IGM is believed to have been reionized at $z \gtrsim 6$ based on observations of quasars (e.g. Kim et al., 2015) and $z \lesssim 15$ from cosmic microwave background (CMB) measurements (Zaroubi, 2013). Additional spectroscopic observations of LGRB afterglows at $z > 7$ will constrain the progress of reionization.

In addition to being a tool for observational cosmology, LGRBs are highly relativistic, with initial Lorentz factors ~ 100 . These extreme conditions are studied through the emission of the resulting shocks.

Accessing the wealth of information imprinted on the afterglow is a race against time. Following the prompt emission, the afterglow begins to decay as a power-law in time, as shown in Figure 1.9. Additionally, any time variability due to the destruction of dust in the local environment will likely happen within minutes (Morgan et al., 2014). Fortunately, projects like the GCN allow observers and robotic telescopes to respond on the minute time scale.

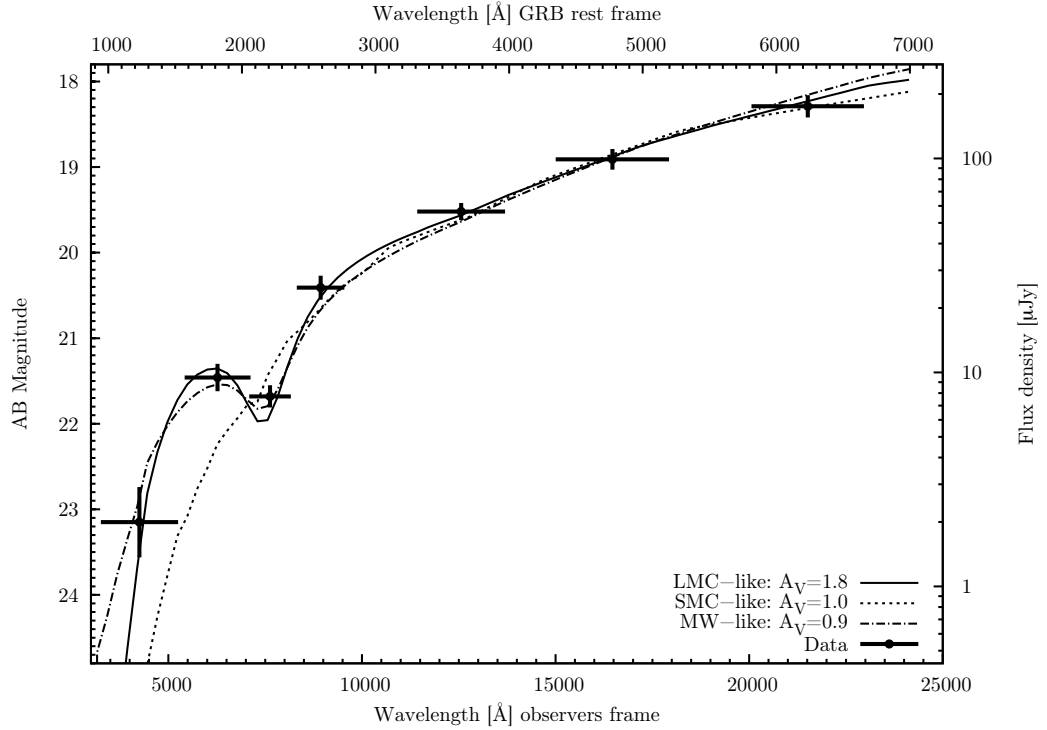


Figure 1.7: This plot of the photometric SED of GRB 070802’s optical afterglow was taken from [Krühler et al. \(2008\)](#). The afterglow was observed by the Gamma-Ray Burst Optical and Near Infrared Detector (GROND) and the resulting optical SED was fit along with X-ray data to constrain the dust extinction profile of the host galaxy. The three curves fit to the above data are models for the average dust extinction of the Large Magellanic Cloud (LMC), Small Magellanic Cloud (SMC) and Milky Way (MW). The dust feature at 2175 \AA is clearly identified above. Most GRB afterglows lack such a strong extinction feature at their rest-frame wavelength, in which cases the SMC profile is a better match. See Section 2.1.2 for more details.

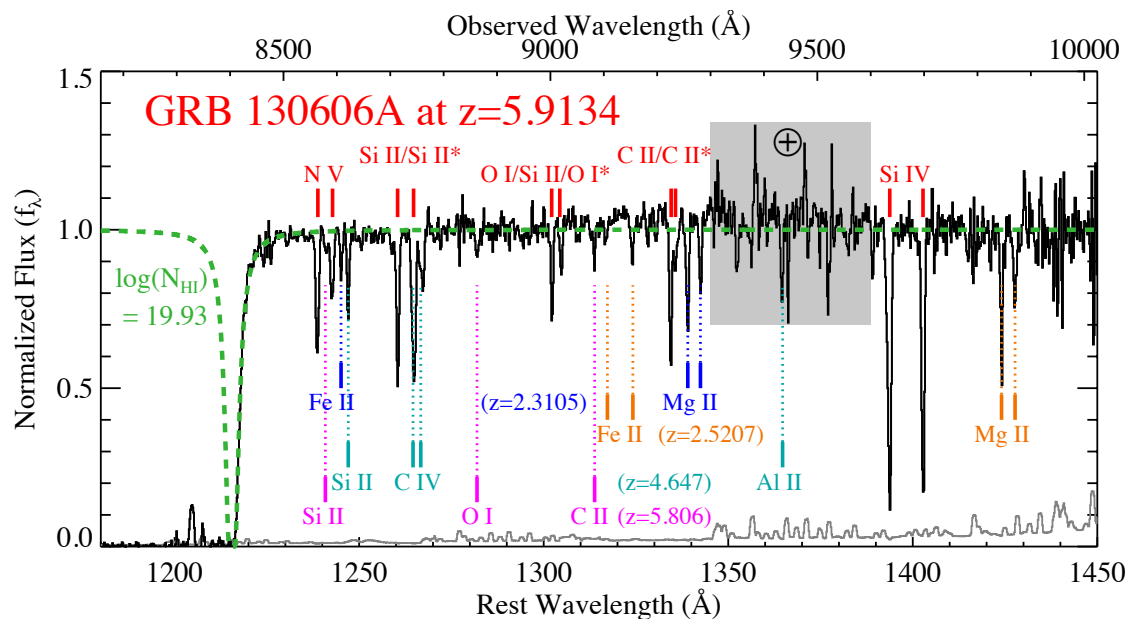


Figure 1.8: A spectrum of GRB 130606A taken from [Chornock et al. \(2013\)](#). The column density of HI (N_{HI}) is determined by fitting the damped wing of the rest-frame Lyman- α line. The metallicity of the host galaxy's interstellar medium (ISM) is determined using N_{HI} and fitting unsaturated absorption features. Intervening systems at lower redshifts are also labeled.

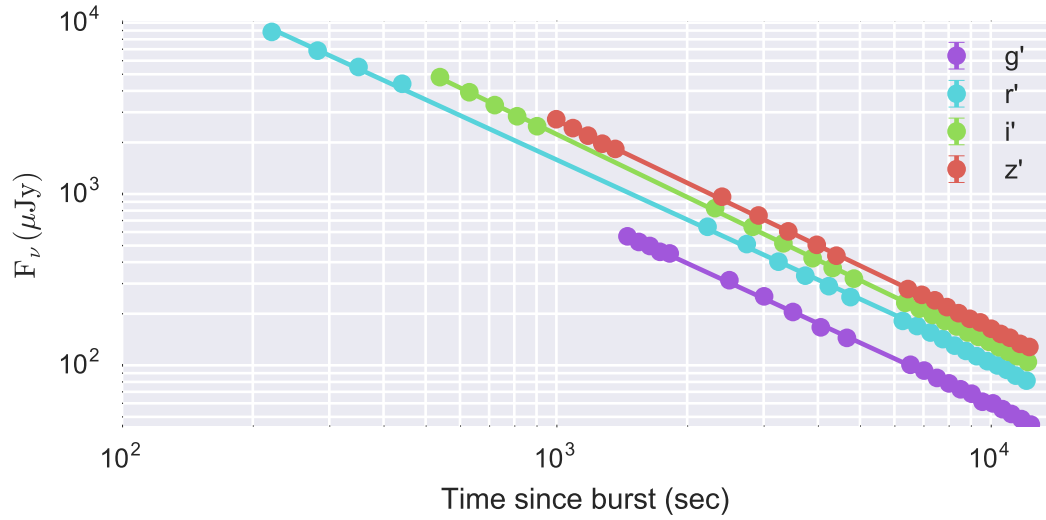


Figure 1.9: The optical afterglow of GRB 140215A was observed by the Discovery Channel Telescope (DCT) using the Large Monolithic Imager (LMI) beginning ~ 2.7 minutes after the start of the burst (Cenko et al., 2014; Toy et al., 2014). The optical light curves have been fit with constant index power-law decay curves ($f_\nu \propto t^{-\alpha}$) where $\alpha = 1.19 \pm 0.03$.

1.1.2 Standard Afterglow Model

For the past couple of decades, the dominant model of GRBs has been the “fireball” model (Sari et al., 1998). This model begins with the release of a high density of γ -ray photons into a compact region which becomes opaque due to $e^- - e^+$ pair production (i.e., the “fireball”, Piran, 1999). This fireball expands and cools, and in this way it accelerates. Baryons in this region are accelerated along with the fireball. Eventually all of the energy is in this matter’s kinetic energy.

In this scenario, an unidentified central engine produces a highly relativistic, collimated outflow ($\Gamma \gtrsim 100$). “Internal shocks” result from the interaction of ejected matter with different Lorentz factors, while “external shocks” occur as the ejecta sweeps up and accelerates e^- in the CBM. The former results in the prompt γ -ray emission, while the latter produces the lower frequency, long-lived afterglow emission. A cartoon of this model is shown in Figure 1.10.

The synchrotron process produces the afterglow emission in the fireball model. The model assumes a constant fraction of the total internal energy of the shock (ϵ_e) accelerates electrons to a power-law distribution of Γ with a cutoff energy at Γ_m . Similarly, it is assumed that the magnetic energy density following the shock receives a constant fraction (ϵ_B) of the shock’s energy. Using ϵ_e and ϵ_B to estimate the electron energy distribution and magnetic field strength simplifies the model and avoids the difficulties of the shock’s microphysics. The resulting afterglow spectrum is a series of broken power-law functions, as shown in Figure 1.11.

The three critical break frequencies defined in Sari et al. (1998) are due to self-

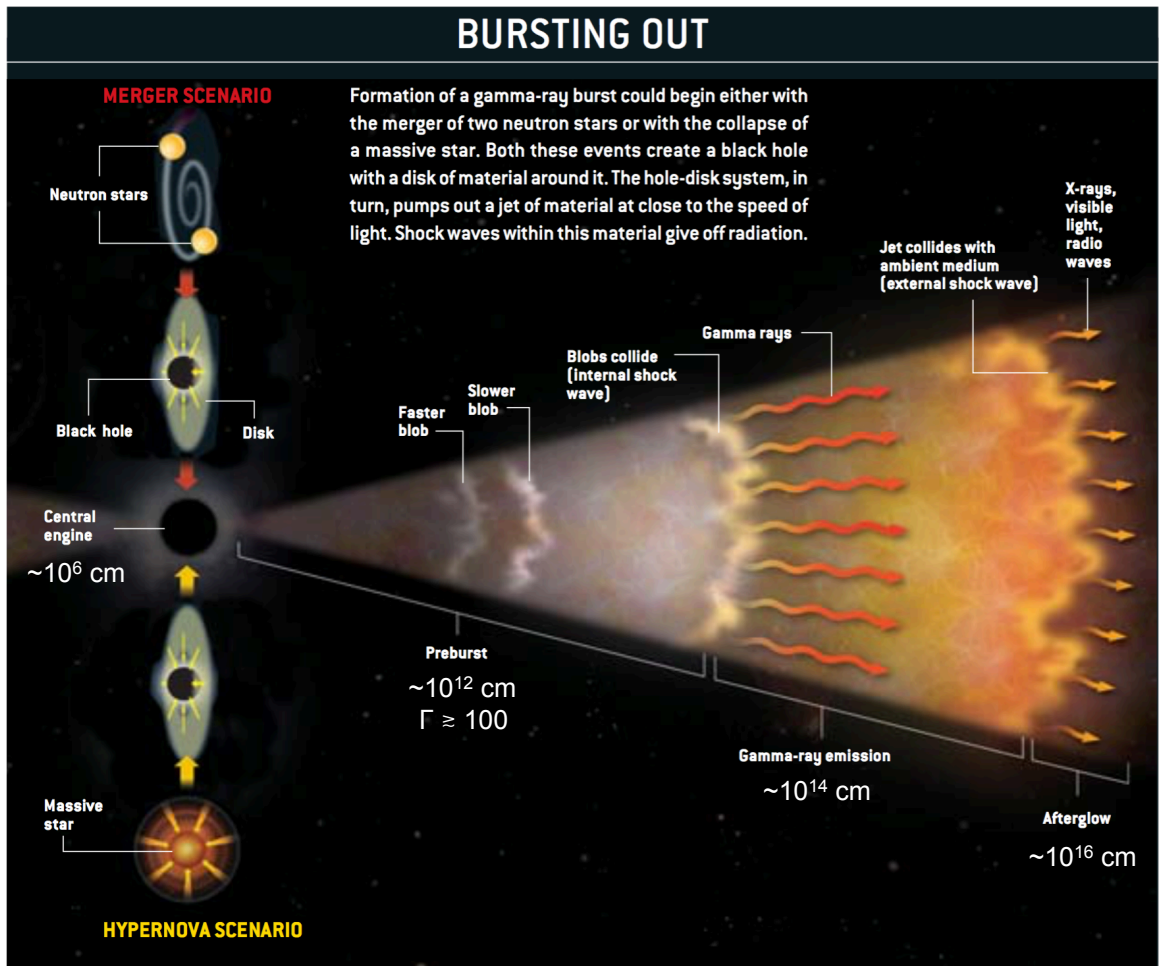


Figure 1.10: This schematic description of the “fireball” model taken from [Gehrels et al. \(2002\)](#) shows internal shocks caused by the interaction of ejecta with different Lorentz factors and external shocks caused by the ejecta interacting with the surrounding medium. The latter is the source of the relatively long-lived afterglow emission.

absorption (ν_a , sometimes ν_{sa}), e^- cooling (ν_c), and Γ_m (ν_m). Below ν_a , the power-law index of 2 is the thermal tail from synchrotron self-absorption. Frequencies between ν_a and the adjacent break frequency are dominated by the summed low-frequency tails of the individual electron spectra. At early times when the minimum Lorentz factor of the electron distribution (Γ_m) is greater than the Lorentz factor of an electron which will cool on a hydrodynamic timescale (Γ_c), the electrons are in the “fast cooling” phase. During the later, “slow cooling” phase, only the high end of the electron energy distribution is cooling, while the majority of electrons are not cooling. The highest frequency emission is always from rapidly cooling electrons.

How the spectral breaks shown in Figure 1.11 vary with time depends on the density profile of the CBM, however the spectral power-law indices are independent of this environment. For this reason, an analysis of the broadband SED permits studies of the afterglow without requiring an assumed density profile.

1.2 Thesis Overview

My graduate research has been heavily focused on developing the Rapid Infrared Imager-Spectrograph (RIMAS) which will enable existing studies of GRB afterglows. To better understand the limitations of ongoing and historical projects and to prepare for the eventual availability of RIMAS, I have also developed an analysis framework and applied it to data sets from existing instruments.

Chapter 2 – GRB Afterglow Temporal Analysis Framework Given the variability of LGRB afterglows, it is useful to have a flexible framework with which

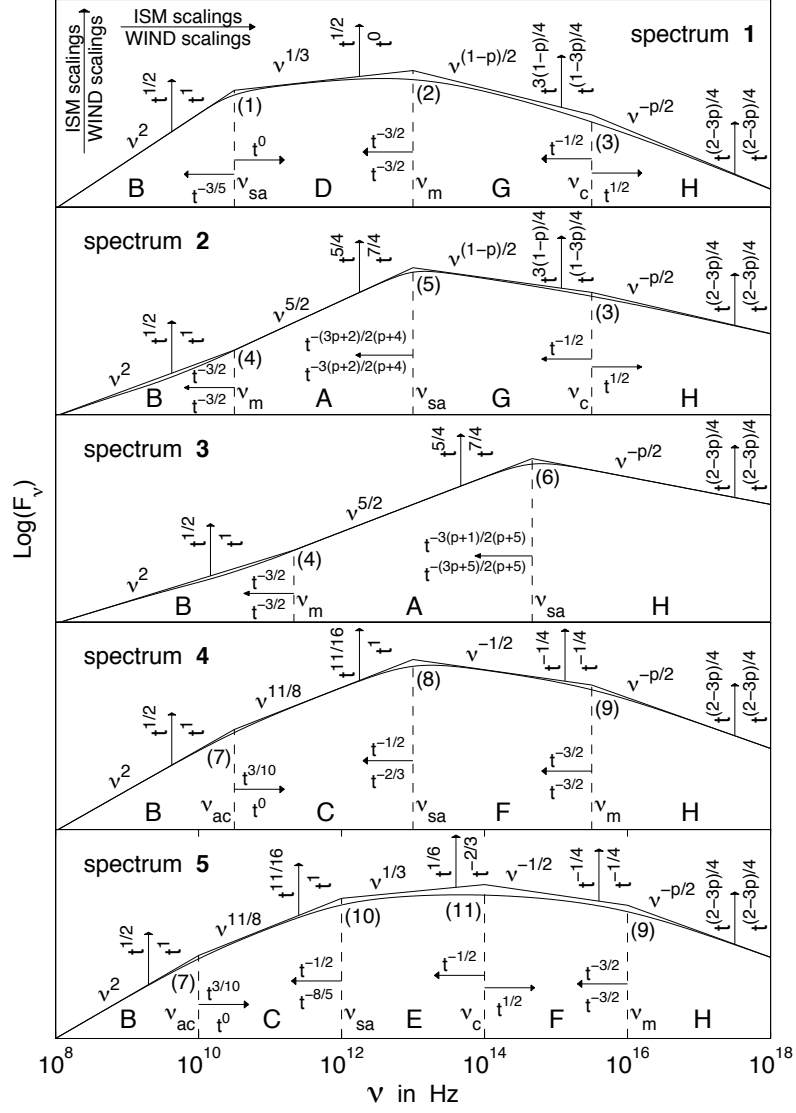


Figure 1.11: Synchrotron spectral energy distributions (SEDs) predicted by the fireball model. This figure, taken from [Granot and Sari \(2002\)](#), shows how flux densities and critical frequencies ($\nu_{sa} \equiv \nu_a$, ν_m and ν_c) are predicted to vary with time for expansion into a constant density ($\rho(r) = \text{constant}$) environment (“ISM”) and one where $\rho(r) \propto r^{-2}$ (“WIND” \rightarrow wind medium surrounding a massive star). Each panel shows a different possible ordering of the spectral break frequencies.

to study their evolution. To this end, I have developed an analysis pipeline for studying photometric and/or spectroscopic data from infrared to X-ray wavelengths. The work of [Morgan et al. \(2014\)](#) is taken as a starting point. Third order, natural smoothing splines are used to interpolate light curve data between measurements at near-infrared (NIR) and optical wavelengths. This same interpolation method is used to smooth X-ray flux light curves, which are used to scale X-ray spectra flux densities. These spline fits allow SEDs to be constructed at arbitrary times within the observed window.

SEDs are created at times where enough bands are available to produce useful fits. These SEDs are then fit with various extinction profiles and intrinsic afterglow power-law functions to determine whether a given fit parameter evolves versus time. Fits are done using Markov chain Monte Carlo (MCMC) methods, providing a better understanding of each fit's parameter space. MCMC methods also allow parameters to be automatically marginalized, which is an essential feature when understanding fits with nuisance and degenerate parameters.

These analysis techniques are applied to afterglow data of GRB 120119A from [Morgan et al. \(2014\)](#) to validate the methods. The output is compared with the published results.

Photometric data are available for a number of GRB afterglows from the Reionization and Transients InfraRed camera (RATIR, [Butler et al., 2012](#)). GRB 140419A, which was detected by RATIR in six photometric bands at early times ($t_{\text{rest}} \gtrsim 2$ min) has been studied using the same analysis as for GRB 120119A. The analysis is additionally applied to a second high extinction source from the literature,

GRB 080607 (Perley et al., 2011).

Chapter 3 – RIMAS: Background Typically, the earliest time data for GRB afterglows are photometric. When sources are determined to be sufficiently interesting and bright by researchers with target of opportunity (ToO) time on large $\gtrsim 8$ meter class telescopes, spectroscopic observations are often made. Optical and NIR spectra allow researchers to determine the cosmological redshift of the event either by absorption features in the afterglow, or by emission lines from the host galaxy. Spectra of sufficiently high spectral resolution ($R \gtrsim 4000$, e.g., Prochaska et al., 2007; Jorgenson et al., 2013; Cucchiara et al., 2015) can additionally be used to study the metallicity of the region where the GRB occurred and the progress of hydrogen reionization of the IGM.

The optical afterglow light curve reaches its maximum flux quickly, typically within minutes of the GRB. The optical flux then decays as a power-law in time. If the time to spectroscopic observations is reduced, the same observations can be attempted using a smaller telescope. Additionally, events which have been highly extinguished by host galaxy dust or which have occurred at high cosmological redshifts are better observed at NIR wavelengths. These are the basic design motivations for RIMAS and are discussed in more detail in Chapter 3.

RIMAS is a collaborative effort between the University of Maryland, College Park (UMCP) and the National Aeronautics and Space Administration’s Goddard Space Flight Center (NASA-GSFC). As such, I have worked as part of a team. In Table 1 on page iii I have listed where others have contributed to the work detailed

in Chapters 4 and 5.

Chapter 4 – RIMAS: Cryogenic Optics A majority of my efforts as a graduate student have been on the cryogenic optical systems for this instrument. I have used methods available in commercial optical software to design, optimize and tolerance these systems. Cryogenic operating temperatures required me to model these systems at room temperature. Additionally, the behavior of some dispersive elements were modeled using rigorous coupled-wave analysis (RCWA) semi-analytical methods.

After concluding the design efforts, I worked with optical manufacturers to obtain optical elements. Once the optics were procured, I successfully aligned the spectroscopic slit-viewing camera, the collimator and the YJ-band camera so that they will be limited by atmospheric seeing once commissioned on the Discovery Channel Telescope (DCT). Due in part to the increased complexity of the HK-band camera, and in part to manufacturing issues, the alignment of this optical subsystem is not yet confirmed. In my absence from the laboratory, Dr. Alexander Kuttyrev has taken the lead on the alignment.

Chapter 5 – RIMAS: Cryogenic Methods I have conducted a number of experimental and computational projects to design and validate designs of the cryogenic subsystems used in RIMAS. In this chapter, I present three cases of general interest. For two of these projects I used an 8-bit CCD detector and a zoom-lens mounted outside of the cryostat chamber to measure the behavior of objects within. For the third project, I wrote a numerical code to model heat flow into the cryostat

via electrical harnesses. This code was used to help design these harnesses.

Chapter 6 – Final Considerations In the final section I will summarize the results of my thesis work and briefly discuss my planned post-doctoral research. The majority of this upcoming three year position at the University of Oxford will be spent developing an engineering model of the optomechanical assembly for the spectrograph units of the High Angular Resolution Monolithic Optical and Near-infrared Integral field spectrograph (HARMONI). I will also describe some early ideas for improving the efficiency of transient searches via machine learning.

Chapter 2: GRB Afterglow Temporal Analysis Framework

The focus of this thesis is on the development of new instrumentation to obtain prompt NIR photometry and spectra of GRB afterglows. This chapter will set the stage for how the Rapid Infrared Imager-Spectrograph (RIMAS) will enable exciting new studies by demonstrating some of what is currently possible with existing instruments. RIMAS is designed to acquire early-time GRB afterglow spectra in the NIR, but at present most observations starting within minutes of a GRB are photometric.

This chapter introduces a generalized analysis framework used to study the time variability of the spectral energy distributions (SEDs) of GRB afterglows. The routines have been applied to two published data sets for comparison (GRB 120119A and GRB 080607), as well as to new optical and NIR afterglow data (GRB 140419A). In addition to validating the methods, this will serve to highlight some challenges for which RIMAS will be uniquely suited.

2.1 SED Color Evolution

As discussed previously (Figure 1.6), the launch of the *Swift* satellite has greatly increased the availability of early-time, broadband data for GRB afterglows.

Thanks to the X-ray Telescope (XRT, [Burrows et al., 2005](#)), X-ray afterglow spectra and light curves are usually obtained (for LGRBs $\sim 80\%$). In the cases where they are not, it is because of the satellite’s observing constraints (i.e., too close to Sun, Moon, or Earth). Equally important are the ~ 3 arcminute and ~ 5 arcsecond localizations provided by BAT in ~ 20 seconds and XRT in $\lesssim 5$ minutes respectively. The nearly instantaneous communication of these positions via the GCN has resulted in the detection of optical afterglows by ground-based telescopes and *Swift*’s Ultraviolet/Optical Telescope (UVOT, [Roming et al., 2005](#)) for $\sim 60\%$ of LGRBs. In these cases, non-detections are typically due to the afterglow being too faint.

The most basic fireball model predicts the broadband afterglow SED to be a series of broken power-laws with breaks at ν_a , ν_c and ν_m (Section 1.1.2). In this model, the time evolution of the spectral indices depends on properties of the ejecta and the CBM (i.e., shocked e^- power-law index, CBM density profile, etc.). In a given observed band, the flux density of the afterglow is usually parameterized as $F_\nu(t) \propto \nu^{-\beta} t^{-\alpha}$, where expected values are $\alpha \sim 1.1 - 1.5$ (before the “jet break” in the light curve due to the edge of the jet becoming visible and the jet spreading laterally) and $\beta \sim 0.7 - 1.0$ ([Mészáros, 2006](#)). Color changes (i.e., changes in β) are either the result of evolving break frequencies or a transition from fast to slow cooling electrons (see Figure 1.11).

In practice, observations often fail to be explained fully by the fireball model (e.g., [Mészáros, 2006](#)). These discrepancies provide means to test GRB theories and to probe the impact of the GRB on the CBM. Sections 2.1.1 – 2.1.3 will describe several potential additions to the standard model which would result in

color evolution, particularly at NIR to X-ray wavelengths.

2.1.1 External Reverse Shock

As the ejecta expand into the CBM, both a forward and reverse external shock will form as shown in Figure 2.1. Simulations of physical conditions in regions surrounding a relativistic shock are shown in Figure 2.2. The reverse shock is relativistic if the dimensionless parameter $\xi < 1$ (defined in Equation 2.1, Sari and Piran, 1995).

$$\xi \triangleq 2(l_{18}/\Delta_{12})^{1/2}\Gamma_{100}^{-4/3} \quad (2.1)$$

$$l \approx 10^{18} \text{ cm } E_{52}^{1/3} n_1^{1/3} \quad (2.2)$$

In Equation 2.1, Δ is the width of the relativistic shell in the observer's frame. The subscripts indicate the power of 10 each value is divided by in the equation. The Sedov length (l) given in Equation 2.2 is the radius of the shock front when the rest mass energy of the swept up matter equals the energy of the fireball, in this case for a constant density CBM. For the GRB ejecta, l depends on the energy of the explosion and the CBM density (Piran, 2004).

For a relativistic reverse shock, electron Lorentz factors will be less than the bulk Lorentz factor by $\xi^{3/2}$. The afterglow emitted by such a reverse shock has the same broken power-law shape as that of the forward shock (Figure 1.11), but with the spectral breaks at different frequencies. The synchrotron frequencies depend strongly on Γ and ϵ_e and the peak frequency for slow-cooling, ν_m , will typically coincide with NIR or optical wavelengths at early times ($\lesssim 1$ hr). At later times,

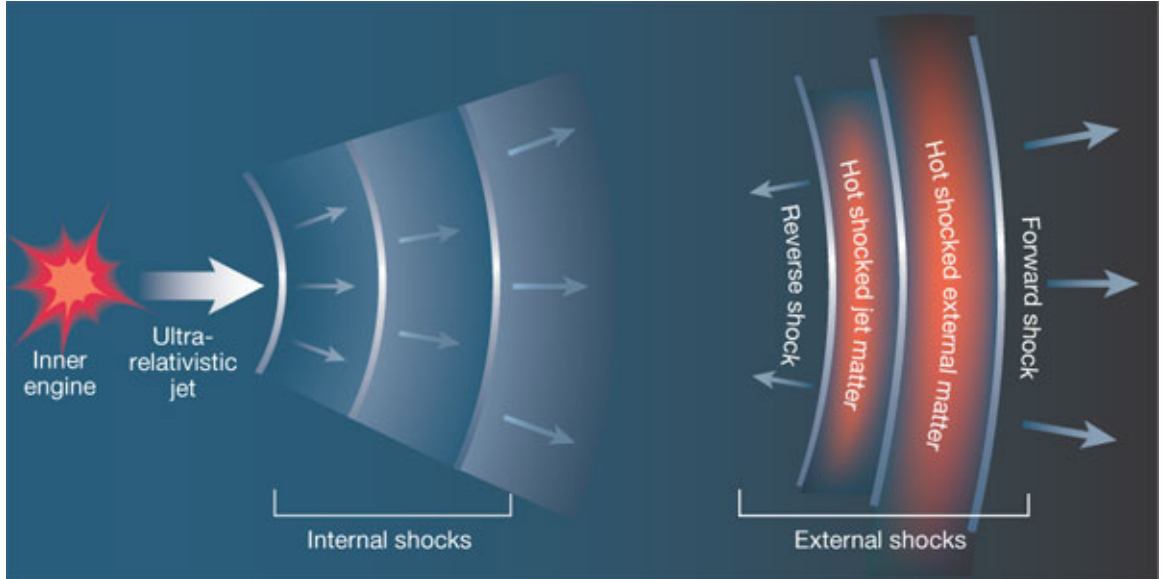


Figure 2.1: A schematic showing the regions of the GRB ejecta where relativistic shocks form, taken from Piran (2003). The GRB is emitted by internal shocks while the afterglow comes from the external shocks. Emission from the reverse shock is predicted to appear as an optical flash at early times (\lesssim hours, Sari and Piran, 1999) while the forward shock is responsible for the afterglow commonly observed at later times. Although the reverse shock is short lived at optical wavelengths, it dominates the radio afterglow on the order of days. The reverse shock never dominates the X-ray afterglow.

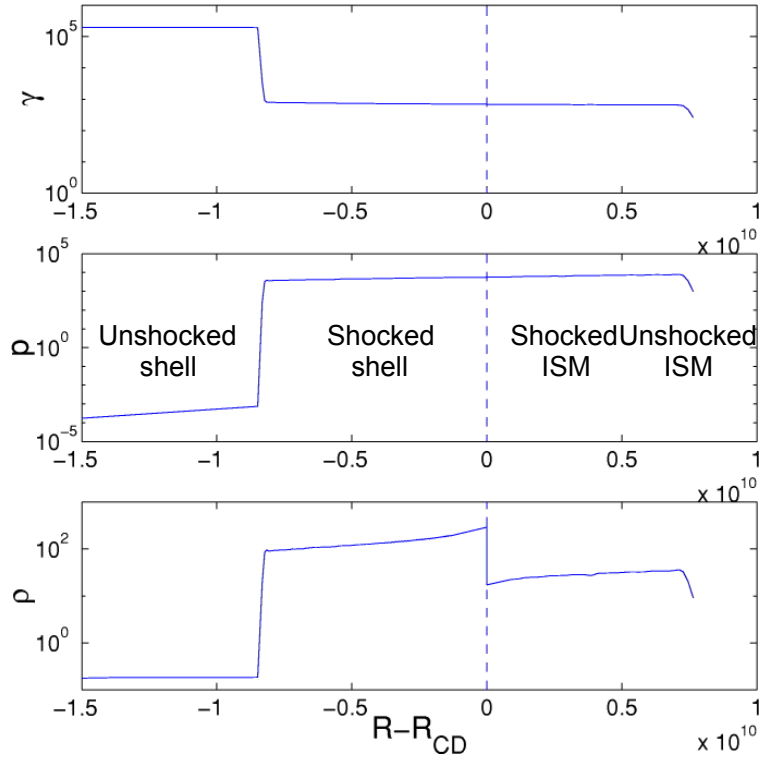


Figure 2.2: Simulation of Lorentz factor (γ), pressure (p) and density (ρ) as a function of the distance from the contact discontinuity (dashed line) taken from Kobayashi and Sari (2000). These conditions are calculated at the time when the energy of the shocked shell is equal to that of the unshocked shell.

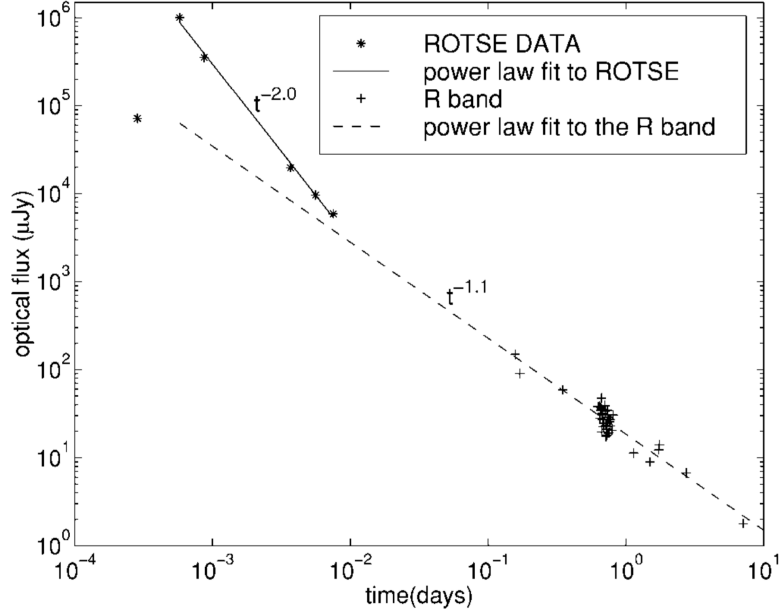


Figure 2.3: The optical flash of GRB 990123 detected by ROTSE-I as presented in [Sari and Piran \(1999\)](#). The change in the temporal-decay index from -2 to -1.1 is believed to originate from the reverse shock afterglow dominating at early times after which the forward shock afterglow dominates.

this frequency will pass to longer wavelengths.

The reverse shock is thought to appear as a short lived optical flash towards the end of the prompt GRB emission ([Piran, 2004](#)). ROTSE-I detected an optical flash for GRB 990123 as late as a few minutes after the burst in the host frame ([Sari and Piran, 1999](#)). In this case the optical power-law decay index went from -2 to -1.1 as shown in Figure 2.3. Unfortunately the lack of multi-band observations prevented the construction of the early-time SED.

The reverse shock of GRB 130427A was detected in multiple NIR, optical and UV bands (ugriz, BVRIJHK, and *Swift*–UVOT’s UVW2, UVM2, UVW1, U, B and V) where it dominated the afterglow emission for ~ 30 min. Figure 2.4 shows how

the SED evolved over ~ 16 orders of magnitude in frequency. The model includes emission from both forward and reverse shocks, demonstrating the close agreement with the observations of this well-studied GRB afterglow.

2.1.2 Dust

The dimming of astronomical sources, now known to be caused by interstellar dust, was first noted over a century ago (Barnard, 1907). Today it is understood that the emission from these sources is reddened by this dust via absorption and scattering. The resulting “extinction profile” is dependent on the size and composition of the dust grains, and is typically modeled using parametric fits to observed stars with known intrinsic spectra.

2.1.2.1 Reddening by Host Galaxies

The same challenge arises when observing GRB afterglows, but with cosmologically redshifted extinction from the host galaxy in addition to the Galactic reddening. The expected foreground Galactic component is calculated and removed using Schlafly and Finkbeiner (2011) and Schlegel et al. (1998). The redshifted host component is then fit by various common extinction curves (Figure 2.5).

In this chapter the model for averaged Small Magellanic Cloud (SMC) extinction is taken from Gordon et al. (2003). Two models used for the Large Magellanic Cloud (LMC2 and LMCAVG) as well as one for the Milky Way (MW) were taken from Misselt et al. (1999). These models use the parameterization described in Fitzpatrick (1999, hereafter FM99). This model includes up to eight free parameters:

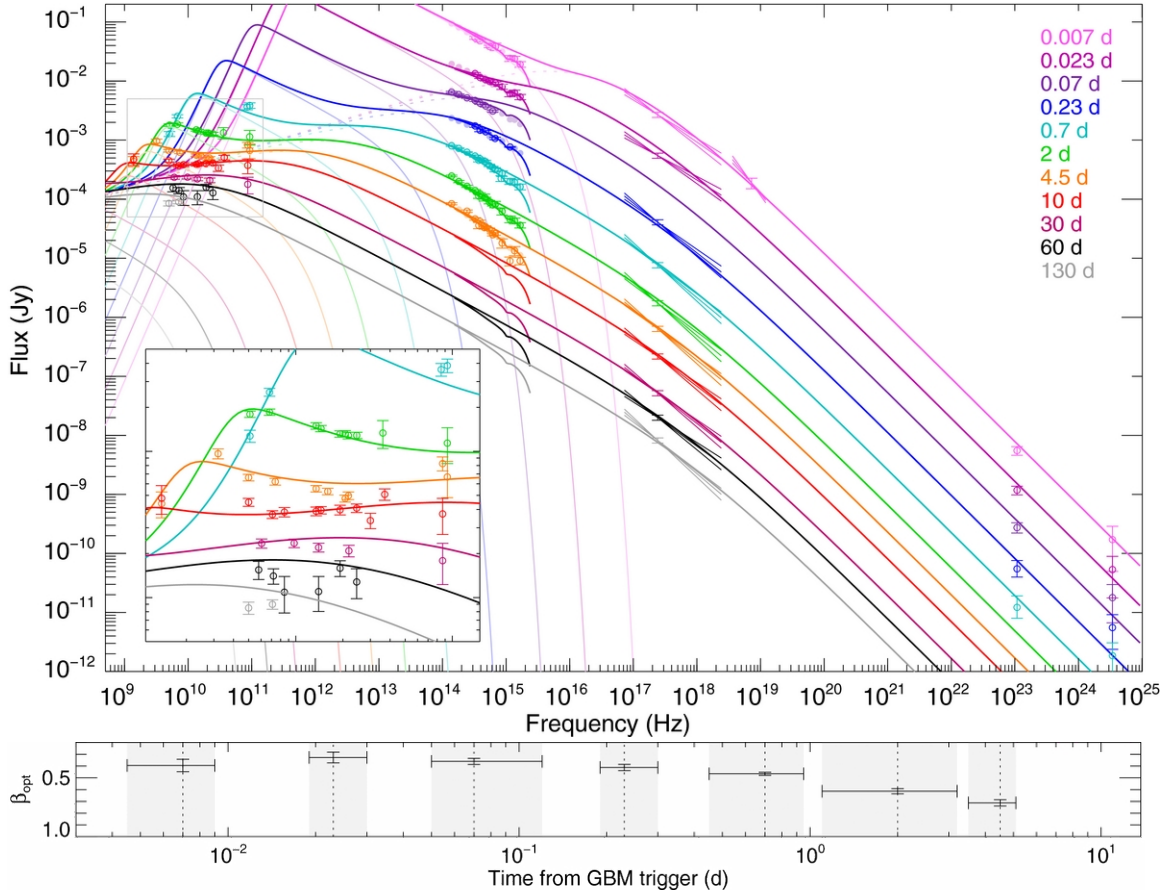


Figure 2.4: The evolution of the broadband SED of GRB 130427A presented in [Perley et al. \(2014\)](#). The dark, solid curves show the combined forward and reverse shock model. The pale, solid lines represent the reverse shock while the pale, dashed lines represent the forward shock. Note that the reverse shock dominates the optical and NIR emission for $t_{\text{obs}} \lesssim 30$ min for this burst at $z = 0.340$. The bottom panel shows how the optical power-law index (β_{opt}) evolves. For this afterglow, the changes in β_{opt} are due to the transition from the reverse to forward shock afterglow dominating the emission as well as the evolution of forward shock's peak flux density frequency to lower frequencies.

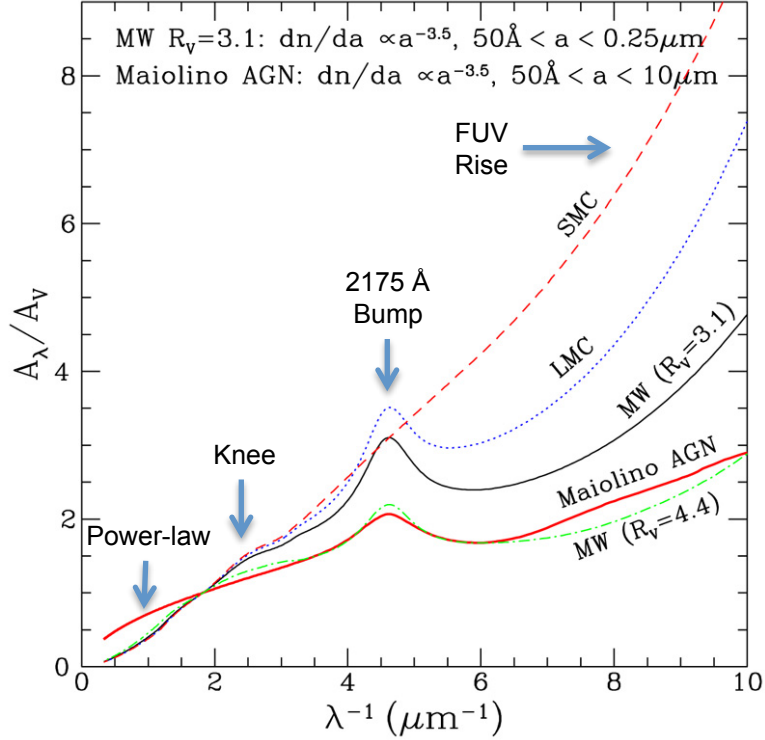


Figure 2.5: Absolute extinction (A_λ/A_V) curves shown in (Li, 2007). For a given wavelength, $A_\lambda \triangleq 2.5 \log_{10}(F_\lambda^0/F_\lambda)$ in magnitudes, where F_λ^0 is the intrinsic flux density. A_V is the total extinction in the V photometric band ($\lambda_{\text{eff}} \sim 0.55 \mu\text{m}$). Another important parameter is the slope of the curve at visible wavelengths, $R_V \triangleq A_V/E_{B-V}$, where the selective extinction, $E_{B-V} \triangleq A_B - A_V$. Because this extinction due to dust is greater at shorter wavelength, it is also referred to as “reddening.” The important features of the extinction curve are the power-law decrease at longer wavelengths, the “knee” at optical wavelengths, the 2175 Å feature in the near-UV and rise in the far-UV. The 2175 Å bump is thought to be due to electronic excitations of polycyclic aromatic hydrocarbon (PAH) molecules (Draine, 2011). The Maiolino curve found in AGNs is compared with the MW model with $R_V = 4.4$ (Maiolino et al., 2001).

c_1 , c_2 , c_3 , c_4 , γ , x_0 , R_V and A_V . This somewhat complicated empirical model is summarized in the following paragraphs. A software implementation is available in the IDL Astronomy User's Library (http://idlastro.gsfc.nasa.gov/ftp/pro/astro/fm_unred.pro).

c_1 and c_2 are the intercept and slope of the linear background in the UV. The 2175Å feature is described by a Lorentzian function where γ is the width, x_0 the position, and c_3 the amplitude. c_4 is the curvature of the FUV increase. R_V normalizes the extinction curve. FM99 models the optical curve using cubic, natural splines between fixed knots in the UV, optical and IR. Values at these knot wavelengths are a function of R_V .

A majority of GRB afterglows are best fit by the averaged SMC extinction curve where there is a negligible 2175Å feature. This is consistent with the fact that GRBs are typically observed in low-mass galaxies with high rates of star formation. These hosts contain many young, blue stars which emit lots of UV radiation. This abundant UV emission will photodissociate the polycyclic aromatic hydrocarbons (PAHs) which produce the 2175Å feature. This bump, however, has been detected in at least a couple of afterglows (Zafar et al., 2012).

2.1.2.2 Dust Destruction

Dust in the CBM is expected to be destroyed soon after the GRB by ultraviolet emission. This could happen on timescales as short as tens of seconds after the GRB (Waxman and Draine, 2000). As reddening along the line-of-sight decreases, the observed afterglow will become bluer, as shorter wavelengths are most

extinguished. Observing the destruction of dust may provide clues about the composition of the CBM.

2.1.3 Other Scenarios

As mentioned previously, the basic fireball model takes ϵ_e and ϵ_B to be constant. If ejecta microphysics vary, however, this would impact the evolution of the afterglow ([Barniol Duran et al., 2013](#); [Barniol Duran and Piran, 2013](#)).

The basic model also takes the system's energy to be constant. If, however, additional material is ejected at later times, this could interact with the earlier ejecta as it is slowed by interaction with the CBM. This would result in a shallower temporal decay of the afterglow emission ([Piran, 2004](#)).

2.2 Analysis Framework

2.2.1 SED Construction

An analysis of the evolution of a GRB afterglow's SED with time requires contemporaneous measurements, however a broadband SED requires observations from a number of instruments covering the electromagnetic spectrum. For this reason, it is necessary to model the evolution of each bandpass in some way to simulate the SED at each time within the observed window. Traditionally, the interpolation is accomplished by fitting power-law slopes to the measured light curves, but this solution lacks the flexibility required for more complex spectral changes.

The framework described below, developed as part of this thesis, uses [Morgan](#)

et al. (2014, hereafter MP14) as a starting point. MP14 detected significant color change in the afterglow of GRB 120119A which is attributed to the destruction of dust in the CBM at early times. The remainder of Section 2.2 will use GRB 120119A to describe this analysis framework and to compare its results with those presented in MP14.

GRB 120119A triggered the Burst Alert Telescope (BAT, Barthelmy et al., 2005) on-board the *Swift* satellite (Gehrels et al., 2004) at 04:04:30.21 UT on 19 January, 2012 (Beardmore et al., 2012). The burst was observed to have a T_{90} of 253.8 ± 24.5 s and a 15 – 150 keV fluence of 1.7×10^{-5} erg cm⁻² (Stamatikos et al., 2012). *Swift* slewed to the source and began observing with XRT at $T_0 + 53.3$ s and UVOT at $T_0 + 61$ s. An uncatalogued source was detected by both instruments (Beardmore et al., 2012). The GRB was determined to have occurred at a redshift of 1.728 by several identified absorption lines (Cucchiara and Prochaska, 2012). Optical and NIR photometry from ground-based observatories presented in MP14 are also used in the following analysis.

2.2.1.1 Natural Smoothing Splines

One flexible method for comparing non-contemporaneous measurements is presented in MP14 and Richards et al. (2012). Rather than using a physical model, cubic, natural, smoothing splines are used to model light curves. Cubic refers to the order of the polynomial spline segments while natural splines have the conditions that the second derivatives be zero at the two end knots. The positions of internal knots are fixed at equal percentiles in log space between the end knots, while the

number of internal knots is chosen by minimizing the generalized cross-validation (GCV) value of the fit (for details, see [Craven and Wahba, 1978](#)). Fits to the NIR and optical data of the GRB 120119A afterglow presented in MP14 are shown in [Figure 2.6](#). Times beyond the observed windows are not extrapolated. In general, I only constructed SEDs at times when fitted values are available in at least four bands in the UV, optical and NIR.

In MP14 optical bands were modeled using splines while the X-ray light curve from *Swift*'s XRT was fit with a series of power-laws. My analysis diverges significantly at this point. For the same reason the optical light curves are fit with splines (i.e., to not impose an assumed behavior), the X-ray light curve is similarly fit as shown in [Figure 2.7](#).

Fit X-ray flux values are then used to scale the unfolded X-ray spectra shown in [Figure 2.8](#) to the time of the SED being constructed. This approach is necessary to attain spectra with reasonable signal-to-noise ratios (SNR). The time over which XRT observations are integrated to generate a spectrum as well as the times during which the resulting spectrum is valid are determined by examining the ratio of the count rates of hard ($E = 1.5 - 10$ keV) to soft ($E = 0.3 - 1.5$ keV) photons. Variations in this hardness ratio are an indication of spectral evolution. [Figure 2.9](#) shows constant fits over ranges of observed times where the reduced χ^2 values are used to determine whether the selected range is acceptable.

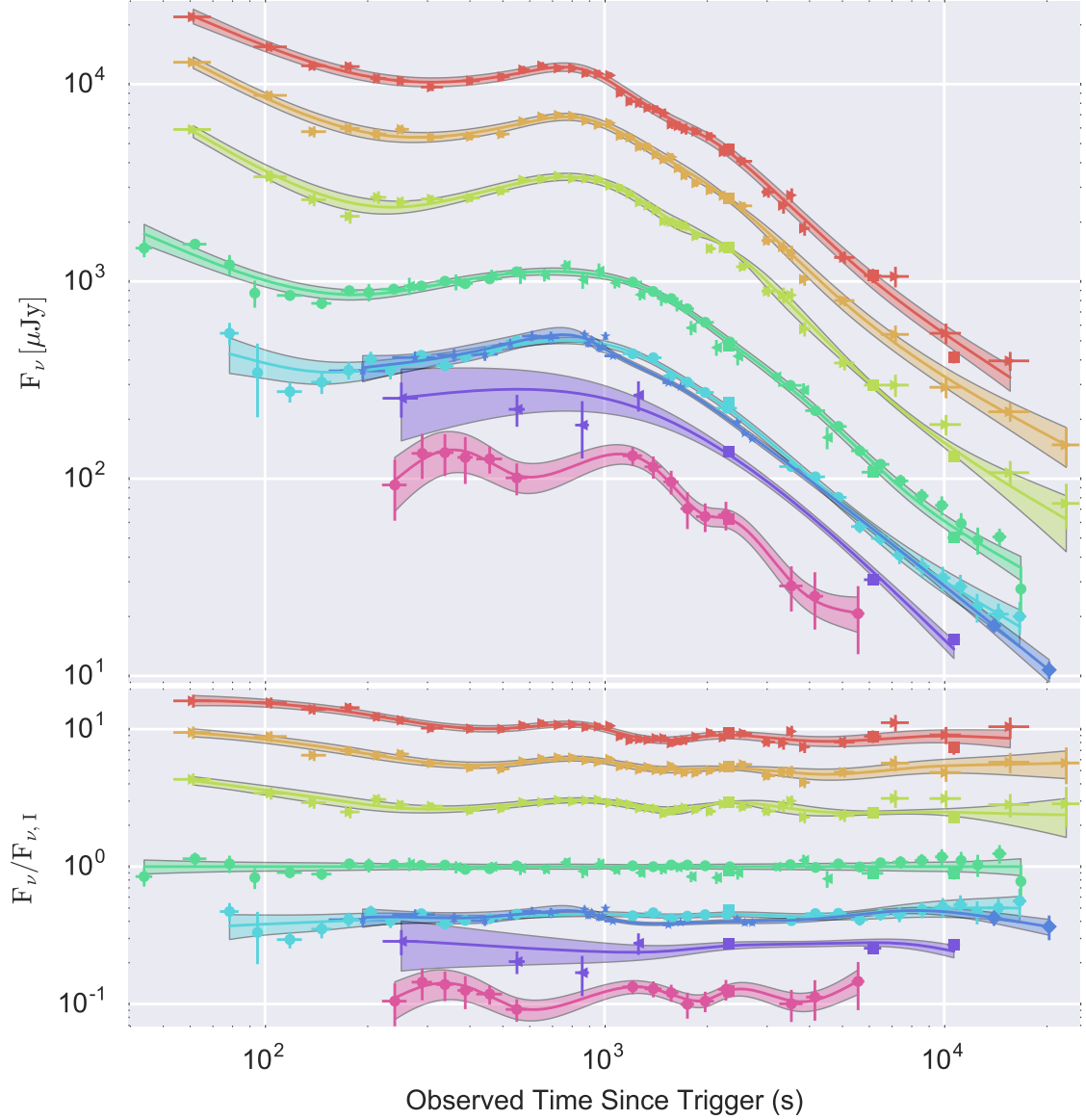


Figure 2.6: GRB 120119A – The optical and NIR photometric light curves presented by [Morgan et al. \(2014\)](#) are fit by the method described in their work. Using smoothing splines in this way allows SED variability to be studied when measurements are not contemporaneous. The bottom panel shows these light curves normalized to I band to highlight color evolution. For a discussion of how uncertainties are estimated, see [Figure 2.7](#).

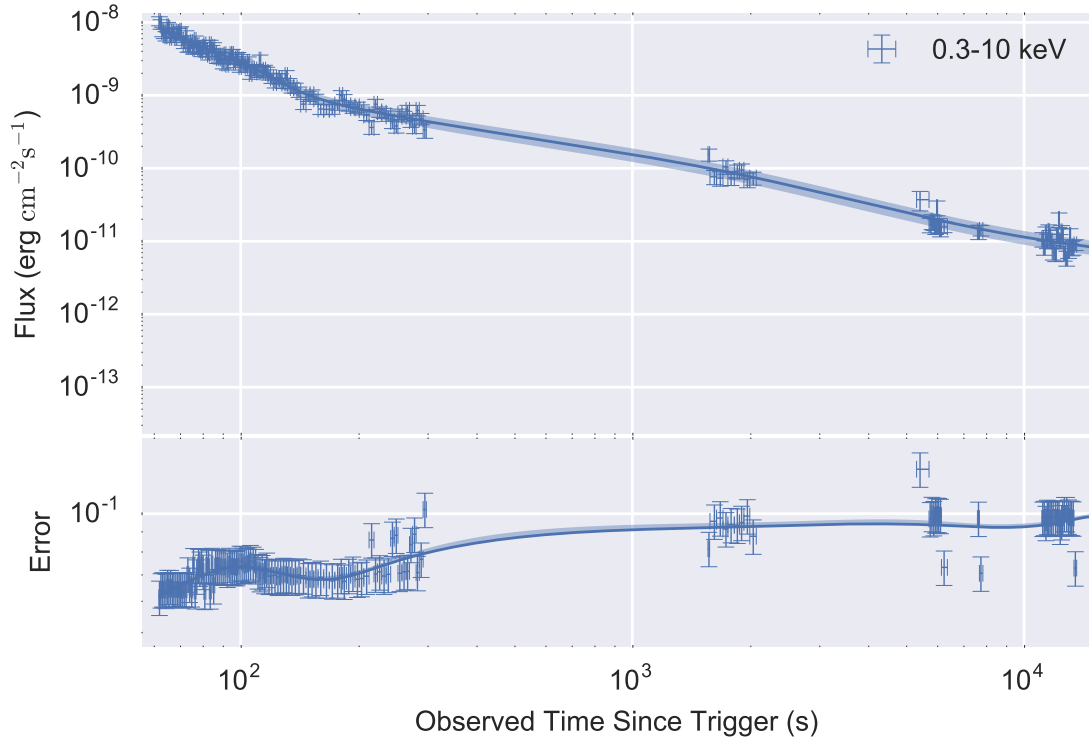


Figure 2.7: GRB 120119A – These 0.3 – 10 keV flux data were taken from the online analysis page (Evans et al., 2007, 2009). The spline fit to the flux light curve was performed using the same method as for the optical and NIR flux density light curves (Figure 2.6). The bottom panel shows how the uncertainties of interpolated times were estimated. For all light curve fits, uncertainties were estimated by fitting the flux or flux density measurement uncertainties, including systematic contributions, using the same spline methods as for the light curves. In this case each sample is assumed to have a 10% systematic uncertainty. This follows the MP14 procedure for optical and NIR light curves, but additionally applied to X-ray data.

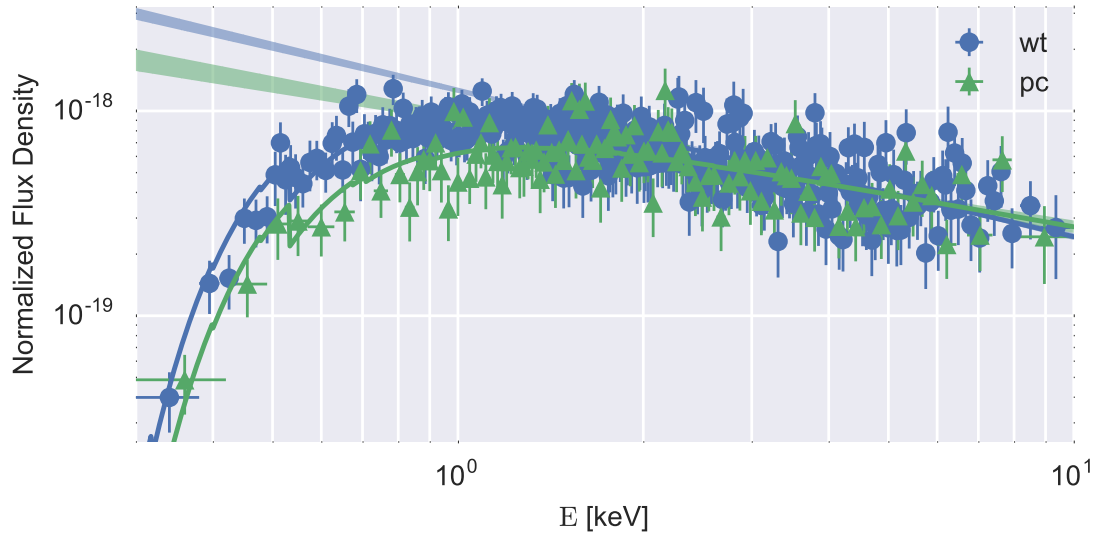
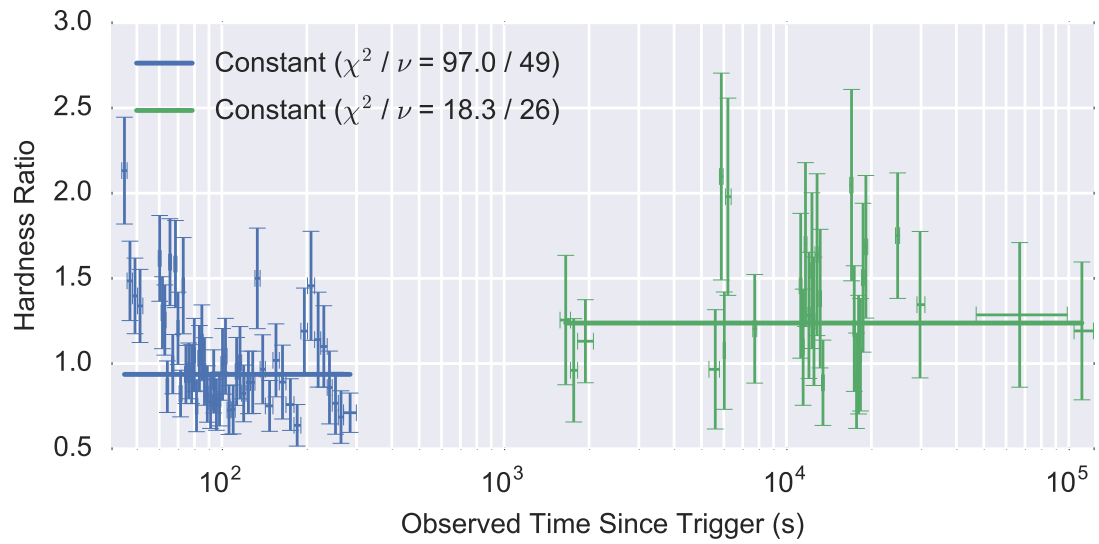


Figure 2.8: GRB 120119A – These 0.3 – 10 keV spectra were taken from the online page ([Evans et al., 2009](#)). Plotted points are binned so as to have 3σ significance. The solid curves show the fits including Galactic and host galaxy absorption. The intrinsic, power-law spectra are shown by the shaded regions where the size is set to 1σ level fit error of the slope as estimated from the covariance matrix. $\beta_{\text{WT}} = 0.70^{+0.06}_{-0.05}$ and $\beta_{\text{PC}} = 0.5^{+0.1}_{-0.1}$. Note that the X-ray spectral index (β_{X}) = the photon index (Γ_{X}) - 1.



2.2.2 SED Fitting

With the ability to generate optical to X-ray SEDs at arbitrary times between observations, the next step is to define physically meaningful SED models. The most basic function is a single power-law, $F_\nu \propto \nu^{-\beta}$. When an X-ray spectrum is included in this fit, absorption from the Galactic ISM and that of the host galaxy must be added to the model as a multiplicative term dependent on the column density of hydrogen (N_{H}) and redshift. Galactic N_{H} is fixed to the value calculated from [Willingale et al. \(2013\)](#) in the direction of the burst while the host N_{H} is left as a free parameter. If a spectral break appears between the optical and X-ray bands, the single power-law must be replaced with a broken power-law.

The SED model is further improved by the inclusion of extinction from dust in the host galaxy. This analysis adopts the commonly used parameterization from FM99 discussed in Section 2.1.2. In the minimal form an averaged extinction curve, such as those shown in Figure 2.5, is used to fit the absolute extinction at each wavelength with A_{V} as a free parameter. If additional freedom is merited, R_{V} and any of the remaining six parameters can be fit.

The association between dust (A_{V}) and gas (N_{H}) in GRB host galaxies has been investigated in the literature (e.g., [Zafar et al., 2012](#)). Although the gas-to-dust ratio has been measured for many bursts, the destruction of dust may diminish this ratio (Figure 2.10).

Because the parameter space can potentially include many free terms, some of which may have a high degree of covariance, I perform fits using a Markov chain

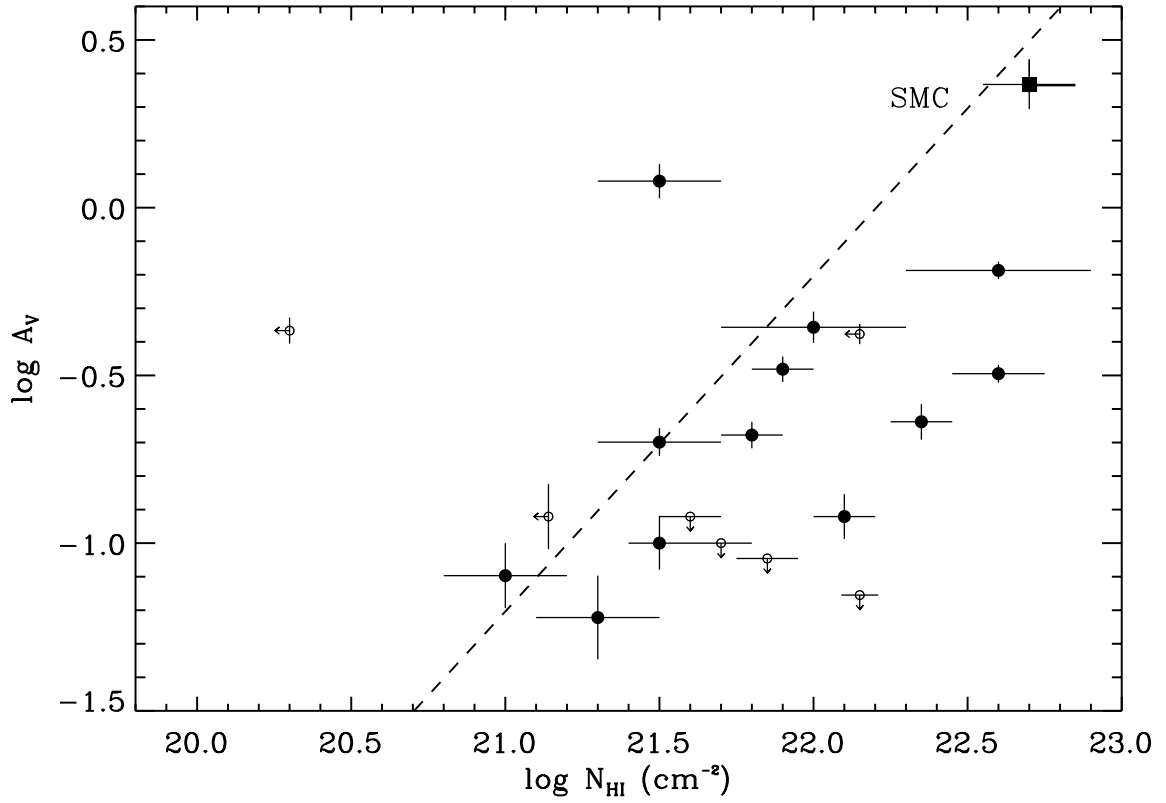


Figure 2.10: This plot of observed GRB dust-to-gas ratios was taken from [Zafar et al. \(2012\)](#). Most of these values fall below the SMC level, possibly because of dust destruction at early times.

Monte Carlo (MCMC) method implemented in the emcee Python package (Foreman-Mackey et al., 2013). This approach allows parameters to be marginalized without further calculation; a useful feature for understanding results without nuisance parameters (e.g., power-law normalization).

The SED at $T_0 + 5,000$ seconds was fit with various extinction models to determine which best represents the afterglow emission (Table 2.1). This time was selected as the latest time where B-band observations were available. These rest-frame UV detections allowed the dust model to be constrained, and demonstrated that the SMC model best fits the data (see fits in Figures 2.12 and 2.14).

Corner plots in Figures 2.11 and 2.13 show the parameter space for fits of the GRB 120119A afterglow at $T_0 + 5,000$ seconds with and without XRT data. The corresponding fits are shown in Figures 2.12 and 2.14. This demonstrates how X-ray data can break the degeneracy between the spectral power-law index (β) and A_V .

SEDs were created for 40 times evenly spaced in $\log_{10}(t)$ during which observations were ongoing in four or more optical bands ($T_0 + 62$ seconds – $T_0 + 4.7$ hours). The final results are presented in Figure 2.15. There is very strong evidence for evolution in both the optical to X-ray spectral index (β) and A_V . β started at 0.53 ± 0.01 ($\pm 1\sigma$) and increased at a constant rate in $\log_{10}(t)$ until $\sim T_0 + 800$ s when it flattened out at 0.869 ± 0.009 . Around $T_0 + 3,000$ s β began to decrease, reaching a value of 0.81 ± 0.03 by $T_0 + 16,800$ s. This evolution is qualitatively similar to that observed for GRB 130427A (bottom panel of Figure 2.4), but with the evolution occurring on a much shorter timescale.

A_V began at $\sim 1.63 \pm 0.07$ ($\pm 1\sigma$) and decreased at a constant rate in $\log_{10}(t)$

Table 2.1: GRB 120119A – The afterglow SED at $T_0 + 5,000$ s was fit to determine which extinction profile best represents these data. This time was selected for being the latest time where all bands were available, particularly the bluest observed band, B. This was vital for constraining the UV behavior and the 2175\AA feature. The following abbreviations are used to refer to the models in the table: (PL) a single power-law for the intrinsic afterglow spectrum at all fitted wavelengths, (XRT) the X-ray spectrum from XRT was included in the fit, (SMC) A_V was fit using the averaged extinction model for the SMC from [Gordon et al. \(2003\)](#), (LMC2) A_V was fit using the averaged model for the LMC 2 sample from [Misselt et al. \(1999\)](#), (LMCAVG) A_V was fit using the averaged model for the LMC from [Misselt et al. \(1999\)](#), (MW) A_V was fit using the averaged model for the Milky Way from [Misselt et al. \(1999\)](#). Note that when “+ XRT” is not listed, X-ray data were left out of the fit.

Model	χ^2/dof @ 5,000 sec
PL	$40_{-2}^{+4}/5$
PL+XRT	$2025_{-105}^{+112}/120$
PL+SMC	$10.1_{-1.6}^{+2.9}/4$
PL+SMC+XRT	$178_{-13}^{+15}/119$
PL+LMC2	$26.6_{-2.1}^{+3.8}/4$
PL+LMC2+XRT	$204_{-13}^{+16}/119$
PL+LMCAVG	$37.3_{-2.8}^{+5.0}/4$
PL+LMCAVG+XRT	$263_{-14}^{+17}/119$
PL+MW	$41.6_{-3.4}^{+5.9}/4$
PL+MW+XRT	$346_{-17}^{+19}/119$

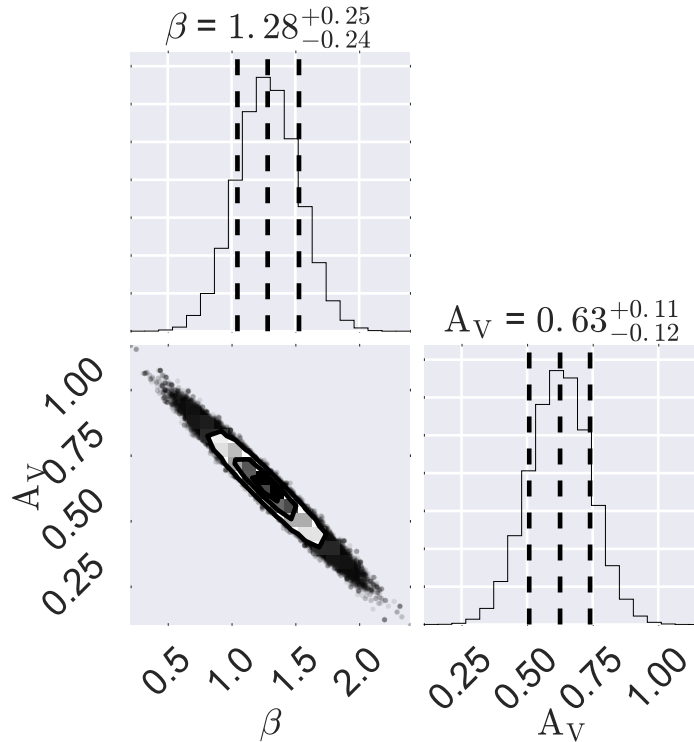


Figure 2.11: GRB 120119A – Corner plot for an optical only fit of the afterglow at $T_0 + 5,000$ seconds (for plotting details see [Foreman-Mackey et al., 2014](#)). Contours enclose 39%, 63% and 78% of samples in two dimensions which correspond to the 1, 2 and 3 σ values for each plotted parameter. Quoted uncertainties are for 68% containment (i.e., $\pm 1\sigma$). The dashed lines on the marginalized probability distributions show the same. Note the strong anti-correlation between A_V and β . See [Figure 2.12](#) for a plot of this fit.

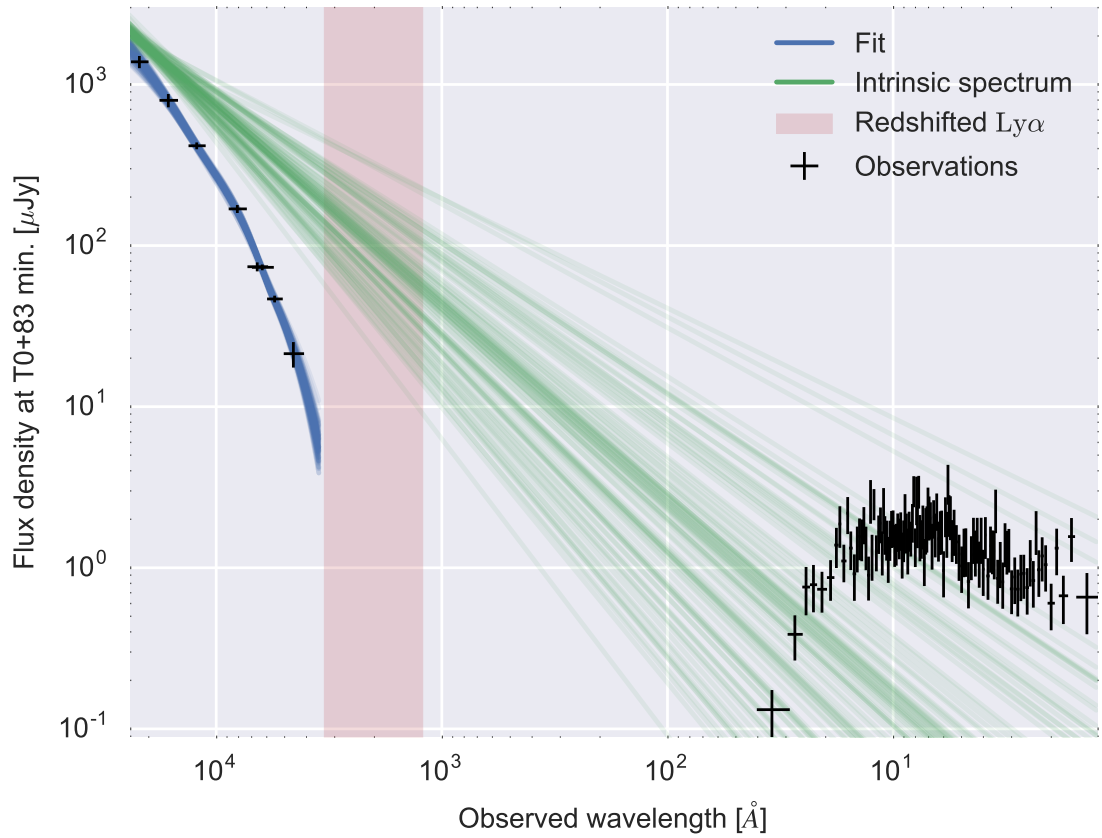


Figure 2.12: GRB 120119A – An optical only fit of the afterglow at $T_0 + 5,000$ seconds. This SED was fit with the SMC extinction curve given in [Gordon et al. \(2003\)](#). The scaled XRT spectrum is provided to show how the $\beta - A_V$ degeneracy is removed by the inclusion of the spectrum.

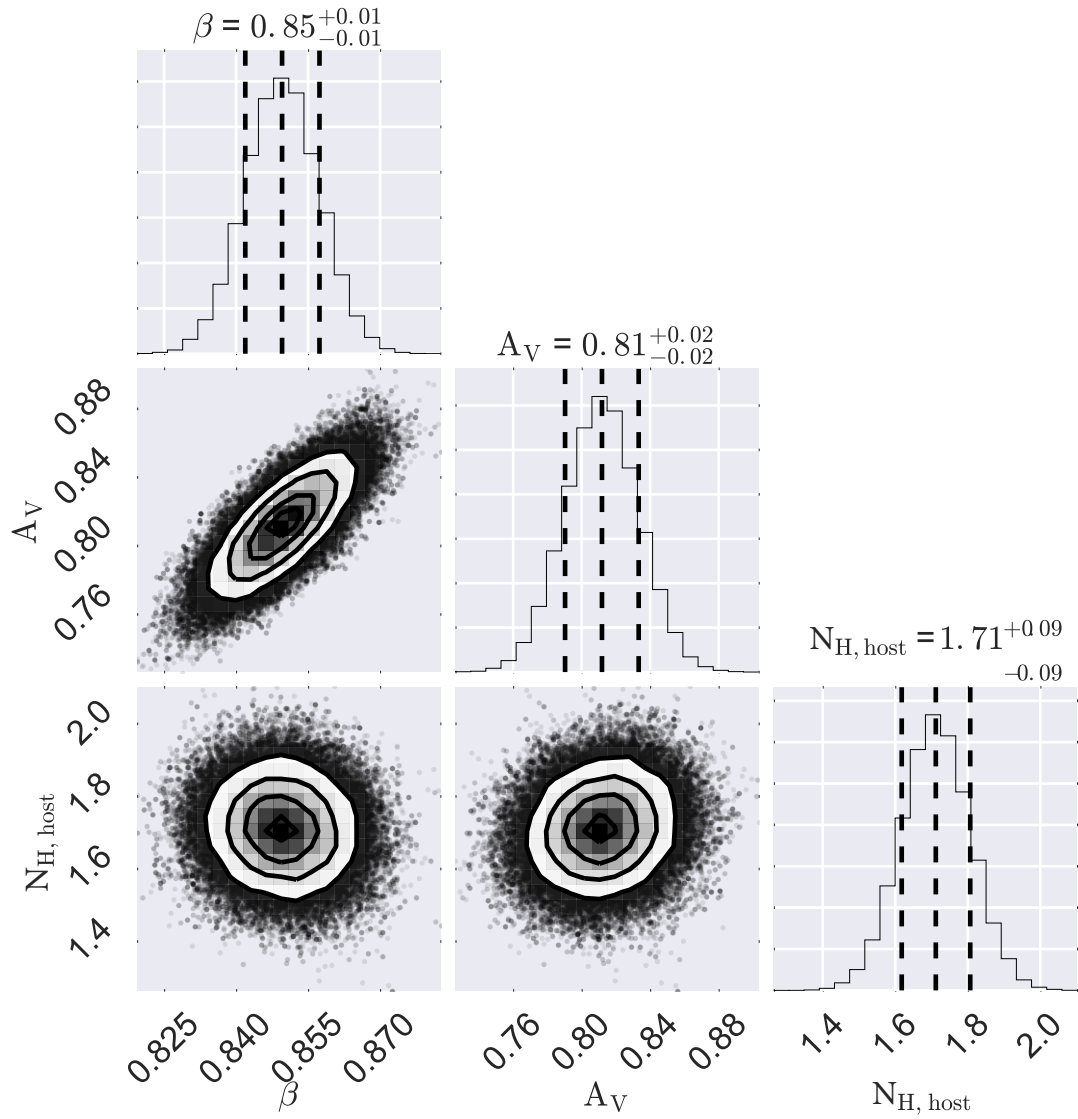


Figure 2.13: GRB 120119A – Corner plot for an optical to X-ray fit of the afterglow at $T_0 + 5,000$ seconds (for plotting details see [Foreman-Mackey et al., 2014](#)). $N_{H,host}$ has units of 10^{22} cm^{-2} . For details about the plot, please see the caption of Figure 2.11. Including the X-ray data has constrained the fit values of A_V and β , breaking the strong degeneracy. See Figure 2.14 for a plot of this fit.

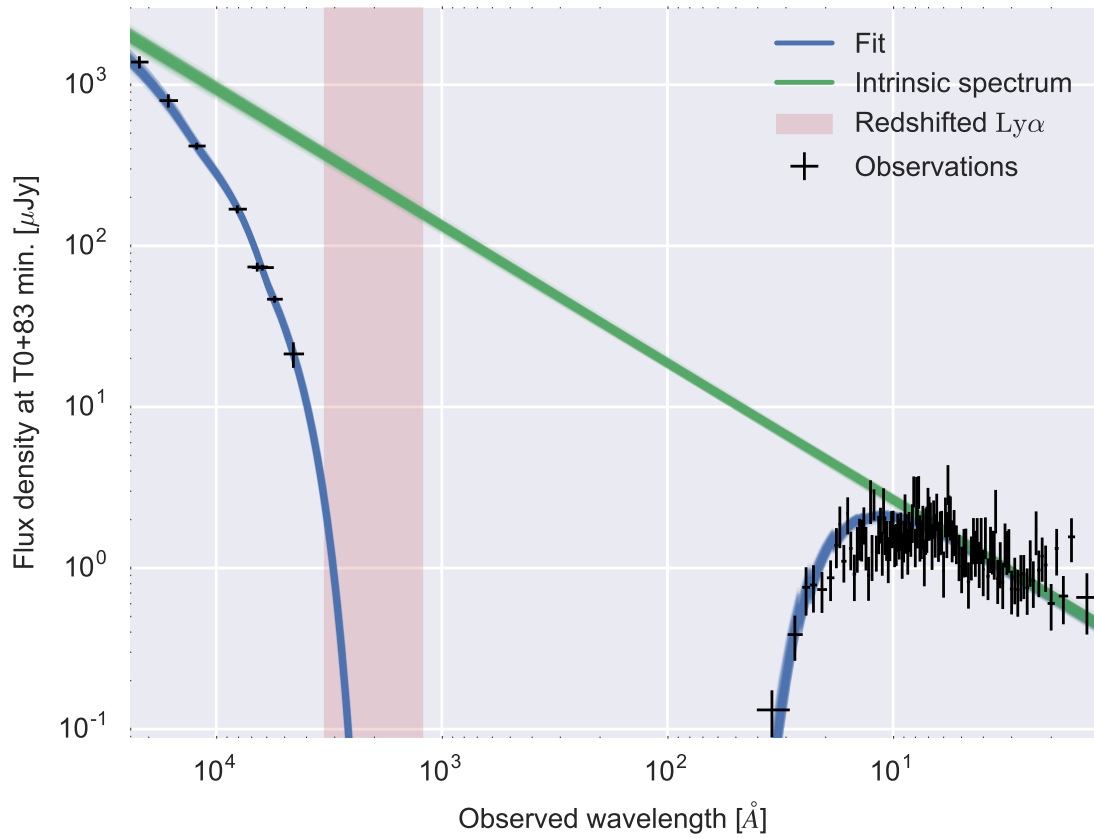


Figure 2.14: GRB 120119A – An optical + X-ray fit of the afterglow at $T_0 + 5,000$ seconds. This SED was fit with the SMC extinction curve given in [Gordon et al. \(2003\)](#). Including the scaled XRT spectrum has constrained β , which in turn constrains A_V .

until $\sim T_0 + 350$ s when it flattened out somewhat at a value of 1.08 ± 0.03 . The extinction value continued to decrease at a lower rate, reaching a value of 0.96 ± 0.09 by $T_0 + 16,800$ s. This extreme change, especially in the first 350 seconds of observed time (130 seconds in the rest-frame) presents evidence for the photodestruction of dust by the afterglow emission.

These results are plotted alongside the most comparable results from MP14 in Figure 2.16. There are clear discrepancies, most notable in the size of the fit uncertainties and the amount of scatter in the points from MP14. First, it should be noted that the authors in the published case elected to use a dust model with four additional free parameters (R_V , c_1 , c_2 , and c_3) rather than the SMC model used here where only A_V was allowed to vary. While the fits in Figure 2.14 deviate somewhat from the longest wavelength data point, added free parameters are unnecessary as the curve passes within the 1σ error bars for all other NIR and optical points.

Second, in MP14 only a single X-ray data point is used rather than the scaled spectra used here. Including the full spectrum serves to further constrain the optical to X-ray power-law index, β . While the values of MP14 have not been successfully reproduced, the most likely causes of the increased fit volatility and estimated fit errors are the additional free parameters in the extinction model and the looser constraints on β .

As a sanity check, the analysis was repeated without including any X-ray data. This serves to eliminate the newly introduced method for including X-ray spectra as the cause of the divergence. The results, shown in Figure 2.17, are broadly consistent with both the values from MP14 and the previous analysis where X-ray

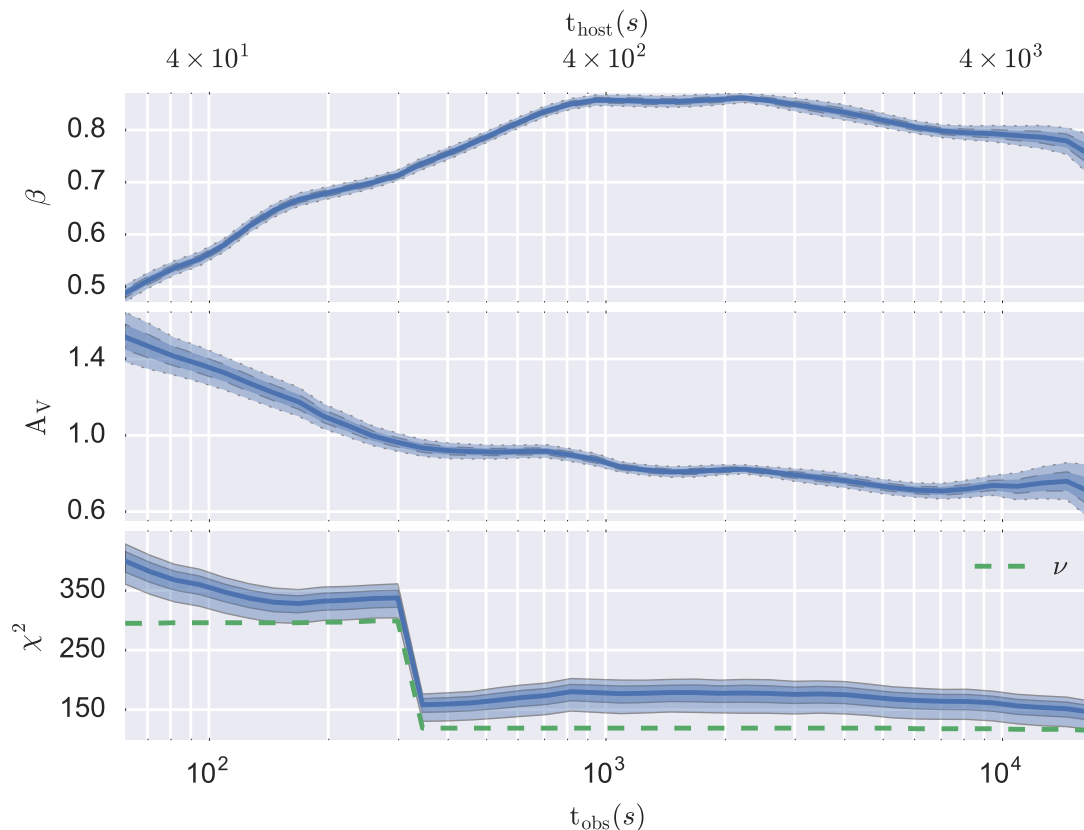


Figure 2.15: GRB 120119A – Fitted parameters are plotted versus time since the *Swift* trigger. Solid lines show the 50th percentile of each calculated distribution, while the dark and light shaded regions show the 1 and 2 σ levels (68% and 95% probabilities) respectively. χ^2 values were calculated for each MCMC sample and the resulting distributions are plotted in the bottom panel as an indicator of the quality of the fits. Since the number of degrees of freedom (ν) changes depending on the number of bands available for a given SED, this value is also plotted. Note that the jump at $T_0 + 300$ seconds is due to a switch from the early-time to late-time X-ray spectrum. Also note that there are no corresponding discontinuities in the fitted values.

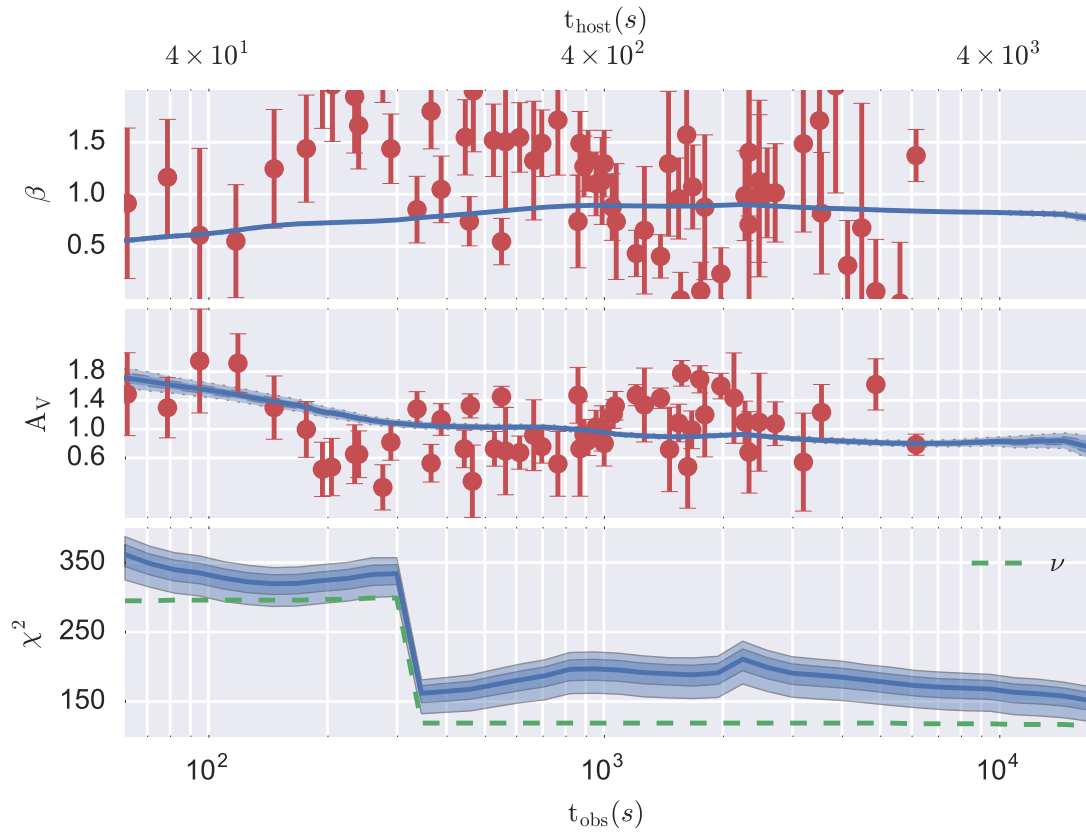


Figure 2.16: GRB 120119A – The same results as plotted in Figure 2.15 with the addition of values extracted from the right panel of Figure 6 in MP14, shown as red circles. These represent the most analogous analysis presented in that work since it includes optical and X-ray data.

spectra were included. The smaller parameter uncertainties are likely due to the fewer free parameters included in the extinction model.

2.3 GRB 140419A

Having validated the ability of the analysis framework to detect the previously reported color evolution of GRB 120119A’s afterglow, the method was applied to new data. Of the afterglows detected in multiple bands by RATIR, that of GRB 140419A was selected due to its high cosmological redshift ($z = 3.956$, [Tanvir et al., 2014](#)). Selecting an event at a high redshift, where observed optical photons will have been emitted in the UV, is advantageous since differences in extinction laws are most significant and dust destruction would be most apparent in the UV.

2.3.1 Observations

2.3.1.1 *Swift* Space Observatory

GRB 140419A triggered *Swift*-BAT at 04:06:51 UT on 19 April, 2014 ([Marshall et al., 2014](#)). The spectrum of the prompt emission detected by BAT was fit well by a simple power-law and had $T_{90} = 94.7 \pm 11.0$ s ([Baumgartner et al., 2014](#)). *Swift* slewed to the source and began observing with XRT at $T_0 + 86.5$ s and UVOT at $T_0 + 97$ s. A bright, uncatalogued source was detected by both instruments ([Marshall et al., 2014](#)). UVOT detected the source in white, V and B filters ([Kuin and Marshall, 2014](#)).

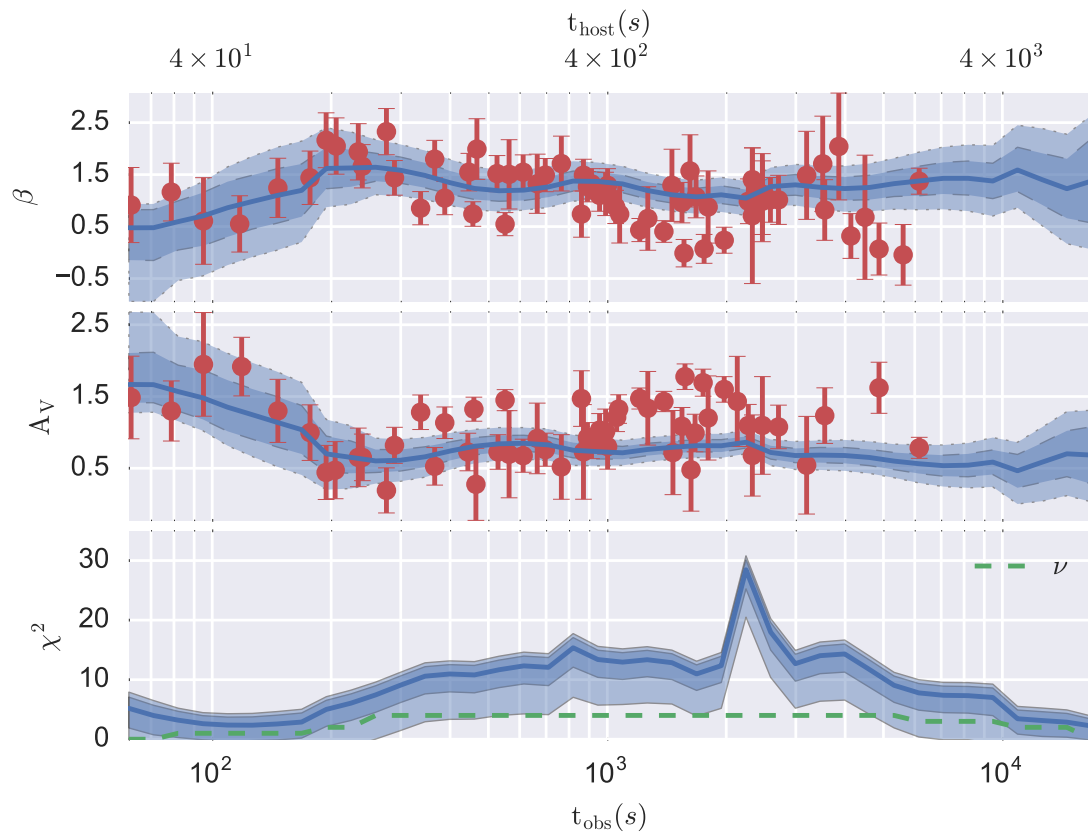


Figure 2.17: GRB 120119A – The same analysis as in Figures 2.15 and 2.16 but without the inclusion of X-ray spectra. The results now match those from MP14, but with reduced scatter. These results are broadly consistent with those shown in Figure 2.15, but with much larger errors due to the anti-correlation between β_O and A_V . Additionally, the above fits to the optical only SEDs are broadly consistent with the MP14 but more constrained, most likely due to the inclusion of fewer free parameters.

2.3.1.2 RATIR

The Reionization and Transients Infrared/Optical Project multi-channel imager (RATIR, [Butler et al., 2012](#)) on the robotic 1.5 meter telescope at the Observatorio Astronómico Nacional de la Sierra de San Pedro Mártir began observations at 04:15:41 UT ($T_0 + 9$ minutes, [Butler et al., 2014](#)). RATIR provides simultaneous coverage in two optical bands and two NIR bands. Fixed, split filters near the NIR focal planes allow near-simultaneous observations in six photometric bands by dithering the telescope.

The afterglow emission of GRB 140419A was detected in the r, i, Z, Y, J, and H bands in a series of 60 and 80 second exposures. I bias and dark current subtracted and flat fielded these data. Cosmic rays were removed from frames using the L.A.Cosmic algorithm ([van Dokkum, 2001](#)). Astrometric corrections were calculated using custom code as well as SExtractor and SCAMP ([Bertin and Arnouts, 1996](#); [Bertin, 2006](#)). Aperture photometry with radii proportional to measured atmospheric seeing was determined using PhotoZPE (<http://classy.astro.berkeley.edu/upload>) calibrated to stars from SDSS Data Release 7 ([Abazajian et al., 2009](#)). The final photometric values are presented in Tables 2.2 – 2.7.

2.3.1.3 GMOS-N

The optical afterglow of GRB 140419A was observed by the Gemini Multi-Object Spectrograph (GMOS, [Hook et al., 2004](#)) on the 8.1 meter Gemini North telescope beginning at 06:24 UT ($T_0 + 2.3$ hours, [Tanvir et al., 2014](#)). Observations

Table 2.2: RATIR r-band photometry of the GRB 140419A afterglow. These data have not been corrected for Galactic extinction.

t_{mid} (s)	t_{exp} (s)	m_{AB}	σ_{AB}	t_{mid} (s)	t_{exp} (s)	m_{AB}	σ_{AB}
571	80	15.36	0.02	5529	80	18.17	0.09
690	80	15.70	0.12	5638	80	18.20	0.07
784	80	15.77	0.04	5732	80	18.23	0.04
880	80	15.93	0.03	6323	80	18.32	0.03
974	80	16.06	0.03	6425	80	18.41	0.05
1095	80	16.39	0.21	6593	80	18.48	0.14
1213	80	16.34	0.03	6690	80	18.38	0.03
1310	80	16.47	0.01	6878	80	18.42	0.04
1575	80	16.66	0.04	6980	80	18.48	0.06
1681	80	16.73	0.06	7098	80	18.51	0.12
1806	80	16.82	0.03	7202	80	18.43	0.03
1900	80	16.89	0.03	7295	80	18.52	0.04
1997	80	17.05	0.12	7398	80	18.49	0.03
2088	80	17.08	0.13	7495	80	18.66	0.14
2380	80	17.18	0.03	7605	80	18.55	0.04
2484	80	17.38	0.13	7699	80	18.55	0.03
2669	80	17.33	0.03	7796	80	18.70	0.15
2761	80	17.37	0.03	7888	80	18.71	0.16
2861	80	17.43	0.11	8015	80	18.60	0.03
3062	80	17.52	0.02	8141	80	18.62	0.04
3173	80	17.55	0.03	8236	80	18.70	0.12
3269	80	17.57	0.06	8326	80	18.75	0.15
3446	80	17.64	0.10	8428	80	18.64	0.05
3547	80	17.67	0.04	8521	80	18.64	0.04
3636	80	17.74	0.03	8615	80	18.88	0.23
3736	80	17.85	0.15	8731	80	18.78	0.16
3850	80	17.84	0.11	8834	80	18.67	0.04
3945	80	17.81	0.02	8925	80	18.69	0.05
4070	80	17.86	0.03	9097	80	18.81	0.14
4165	80	18.03	0.14	9277	80	18.77	0.06
4275	80	17.97	0.14	9388	80	18.73	0.04
4376	80	17.94	0.03	9480	80	18.85	0.06
4466	80	17.97	0.04	9577	80	18.80	0.08
4563	80	18.14	0.15	9669	80	18.83	0.13
4662	80	18.06	0.16	9839	80	18.82	0.05
4777	80	18.06	0.03	90064	8400	21.06	0.05
4941	80	18.09	0.03	176778	8880	22.04	0.07
5042	80	18.07	0.13	263318	8640	22.61	0.10
5260	80	18.14	0.04	435831	8574	23.46	0.17
5427	80	18.21	0.03				

Table 2.3: RATIR i-band photometry of the GRB 140419A afterglow. These data have not been corrected for Galactic extinction.

t_{mid} (s)	t_{exp} (s)	m_{AB}	σ_{AB}	t_{mid} (s)	t_{exp} (s)	m_{AB}	σ_{AB}
571	80	14.91	0.02	5529	80	17.85	0.10
690	80	15.21	0.09	5638	80	17.87	0.13
784	80	15.40	0.12	5732	80	17.85	0.02
880	80	15.50	0.02	6323	80	17.93	0.02
974	80	15.63	0.02	6425	80	18.00	0.11
1213	80	15.94	0.07	6593	80	18.06	0.07
1310	80	16.02	0.02	6690	80	18.04	0.02
1575	80	16.26	0.09	6878	80	18.04	0.03
1681	80	16.36	0.13	6980	80	18.09	0.09
1806	80	16.42	0.03	7098	80	18.20	0.09
1900	80	16.48	0.02	7202	80	18.09	0.03
1997	80	16.59	0.12	7295	80	18.12	0.03
2088	80	16.62	0.11	7398	80	18.16	0.10
2380	80	16.77	0.02	7495	80	18.26	0.13
2484	80	16.87	0.11	7605	80	18.12	0.03
2669	80	16.95	0.02	7699	80	18.18	0.02
2761	80	16.98	0.02	7796	80	18.19	0.12
2861	80	17.04	0.13	7888	80	18.19	0.15
3062	80	17.10	0.02	8015	80	18.20	0.03
3173	80	17.14	0.02	8141	80	18.22	0.03
3269	80	17.18	0.11	8236	80	18.29	0.15
3446	80	17.33	0.10	8326	80	18.30	0.13
3547	80	17.29	0.03	8428	80	18.26	0.03
3636	80	17.33	0.04	8521	80	18.26	0.03
3736	80	17.36	0.13	8615	80	18.34	0.09
3850	80	17.38	0.10	8731	80	18.34	0.10
4070	80	17.49	0.03	8834	80	18.34	0.03
4165	80	17.55	0.11	8925	80	18.29	0.03
4275	80	17.52	0.10	9097	80	18.42	0.10
4376	80	17.55	0.03	9277	80	18.43	0.13
4466	80	17.56	0.03	9388	80	18.31	0.04
4563	80	17.62	0.11	9577	80	18.45	0.11
4662	80	17.65	0.09	9669	80	18.39	0.14
4777	80	17.64	0.02	9839	80	18.38	0.04
4941	80	17.67	0.02	90064	8480	20.75	0.04
5042	80	17.70	0.10	176778	8880	21.60	0.06
5144	80	17.80	0.09	263318	8640	22.28	0.10
5260	80	17.76	0.02	435831	9518	22.74	0.10
5427	80	17.80	0.03				

Table 2.4: RATIR Z-band photometry of the GRB 140419A afterglow. Upper limits are signified by a dash. These data have not been corrected for Galactic extinction.

t_{mid} (s)	t_{exp} (s)	m_{AB}	σ_{AB}	t_{mid} (s)	t_{exp} (s)	m_{AB}	σ_{AB}
561	60	14.73	0.08	5417	60	17.64	0.08
871	60	15.33	0.09	5722	60	17.72	0.10
964	60	15.46	0.12	6313	60	17.85	0.08
1300	60	15.89	0.08	6680	60	17.85	0.09
1797	60	16.25	0.10	7192	60	17.97	0.11
1890	60	16.33	0.10	7285	60	18.04	0.11
2370	60	16.59	0.11	7595	60	17.99	0.09
2659	60	16.75	0.08	7689	60	17.95	0.08
2751	60	16.78	0.11	8131	60	18.04	0.09
3052	60	16.94	0.09	8419	60	18.02	0.10
3163	60	16.99	0.10	8511	60	18.08	0.08
3537	60	17.07	0.10	8915	60	18.19	0.12
3626	60	17.16	0.09	9378	60	18.22	0.11
3935	60	17.23	0.10	9471	60	18.21	0.09
4060	60	17.27	0.11	9829	60	18.31	0.10
4367	60	17.41	0.11	90064	5940	20.40	0.08
4456	60	17.41	0.12	176778	6480	21.52	0.14
4767	60	17.52	0.09	263322	3296	22.07	0.13
4931	60	17.48	0.09	435843	3293	23.16	—
5250	60	17.57	0.10				

Table 2.5: RATIR Y-band photometry of the GRB 140419A afterglow. These data have not been corrected for Galactic extinction.

t_{mid} (s)	t_{exp} (s)	m_{AB}	σ_{AB}	t_{mid} (s)	t_{exp} (s)	m_{AB}	σ_{AB}
681	60	14.76	0.08	5628	60	17.54	0.08
774	60	14.93	0.09	6415	60	17.59	0.09
1086	60	15.36	0.07	6584	60	17.59	0.10
1203	60	15.50	0.09	6970	60	17.70	0.10
1565	60	15.86	0.08	7388	60	17.73	0.09
1672	60	15.92	0.08	7485	60	17.78	0.08
1987	60	16.11	0.06	7786	60	17.75	0.09
2078	60	16.21	0.08	7878	60	17.93	0.09
2474	60	16.42	0.08	8226	60	17.96	0.10
2851	60	16.62	0.09	8316	60	18.05	0.10
3259	60	16.80	0.09	8605	60	18.26	0.10
3436	60	16.86	0.08	8721	60	18.03	0.10
3726	60	16.97	0.08	9087	60	18.01	0.08
3840	60	16.98	0.09	9267	60	17.99	0.09
4155	60	17.10	0.07	9567	60	18.03	0.10
4265	60	17.17	0.08	9659	60	18.14	0.10
4553	60	17.22	0.08	90064	6300	20.35	0.12
4652	60	17.27	0.08	176778	6720	21.65	0.22
5032	60	17.33	0.08	263322	6224	21.77	0.16
5134	60	17.33	0.07	435843	4752	21.69	0.17
5519	60	17.42	0.08				

Table 2.6: RATIR J-band photometry of the GRB 140419A afterglow. Upper limits are signified by a dash. These data have not been corrected for Galactic extinction.

t_{mid} (s)	t_{exp} (s)	m_{AB}	σ_{AB}	t_{mid} (s)	t_{exp} (s)	m_{AB}	σ_{AB}
561	60	14.43	0.06	7192	60	17.66	0.07
964	60	15.14	0.07	7285	60	17.76	0.06
1300	60	15.56	0.06	7595	60	17.68	0.07
1797	60	15.97	0.06	7689	60	17.88	0.07
1890	60	16.06	0.07	8005	60	17.85	0.08
2370	60	16.40	0.06	8131	60	17.85	0.10
2659	60	16.51	0.07	8419	60	17.75	0.08
2751	60	16.53	0.14	8511	60	17.84	0.07
3163	60	16.76	0.07	8824	60	17.94	0.09
3626	60	16.97	0.06	8915	60	17.94	0.07
3935	60	17.06	0.05	9378	60	18.03	0.09
4367	60	17.18	0.07	9471	60	17.96	0.08
4456	60	17.15	0.08	9829	60	18.04	0.11
4767	60	17.23	0.06	90064	5760	20.32	0.11
4931	60	17.33	0.04	176829	5262	22.08	0.13
5250	60	17.42	0.07	263282	4970	22.00	0.13
5417	60	17.43	0.06	435839	3680	23.14	—
6680	60	17.68	0.07				

Table 2.7: RATIR J-band photometry of the GRB 140419A afterglow. Upper limits are signified by a dash. These data have not been corrected for Galactic extinction.

t_{mid} (s)	t_{exp} (s)	m_{AB}	σ_{AB}	t_{mid} (s)	t_{exp} (s)	m_{AB}	σ_{AB}
681	60	14.45	0.08	4652	60	17.08	0.10
774	60	14.59	0.09	5032	60	17.13	0.15
1086	60	15.08	0.10	5134	60	17.23	0.10
1566	60	15.60	0.07	5519	60	17.23	0.15
1672	60	15.68	0.13	5628	60	17.30	0.14
1987	60	15.90	0.14	6970	60	17.50	0.10
2078	60	15.96	0.09	7388	60	17.54	0.15
2474	60	16.21	0.14	7787	60	17.59	0.11
2851	60	16.42	0.13	8316	60	17.91	0.11
3259	60	16.62	0.13	9567	60	18.08	0.17
3436	60	16.68	0.14	9659	60	17.66	0.15
3726	60	16.81	0.13	90064	5520	20.03	0.16
3840	60	16.84	0.09	176829	4053	22.69	0.20
4155	60	16.92	0.13	263282	4041	22.66	0.24
4265	60	16.93	0.09	435839	4027	23.07	—
4553	60	17.04	0.14				

were made covering $\lambda \approx 4400 - 10100\text{\AA}$ at a spectral resolving power (R) of ~ 1200 . Data were processed using standard routines within the Gemini IRAF package. The spectrum was normalized by the continuum since no flux standard was available.

2.3.2 Analysis

2.3.2.1 Optical Spectrum

The reduced optical/NIR spectrum is presented in Figure 2.18 highlighting a series of absorption lines at a common redshift of 3.956. The blue region is attenuated by redshifted Ly α . This spectrum was part of the sample discussed by Cucchiara et al. (2015) where the spectral resolving power was found to be too low for metal abundance measurements using the Curve of Growth methodology (COG, Spitzer, 1978).

2.3.2.2 Optical and Near-Infrared Light Curves

All photometric values are presented in Tables 2.2 – 2.7. Suitable optical and NIR data were available from five of six RATIR bands. Due to the cosmological redshift of the GRB, r-band data were attenuated by neutral hydrogen along the line-of-sight and were not included in the analysis. The remaining bands were corrected for Galactic extinction of $E(B - V) = 0.026$ mag in the direction of the event using the work of Schlegel et al. (1998) and Schlafly and Finkbeiner (2011).

Photometric values in each band were interpolated as described in Section 2.2.1.1. The resulting fits are shown in Figure 2.19. In the middle panel of Figure

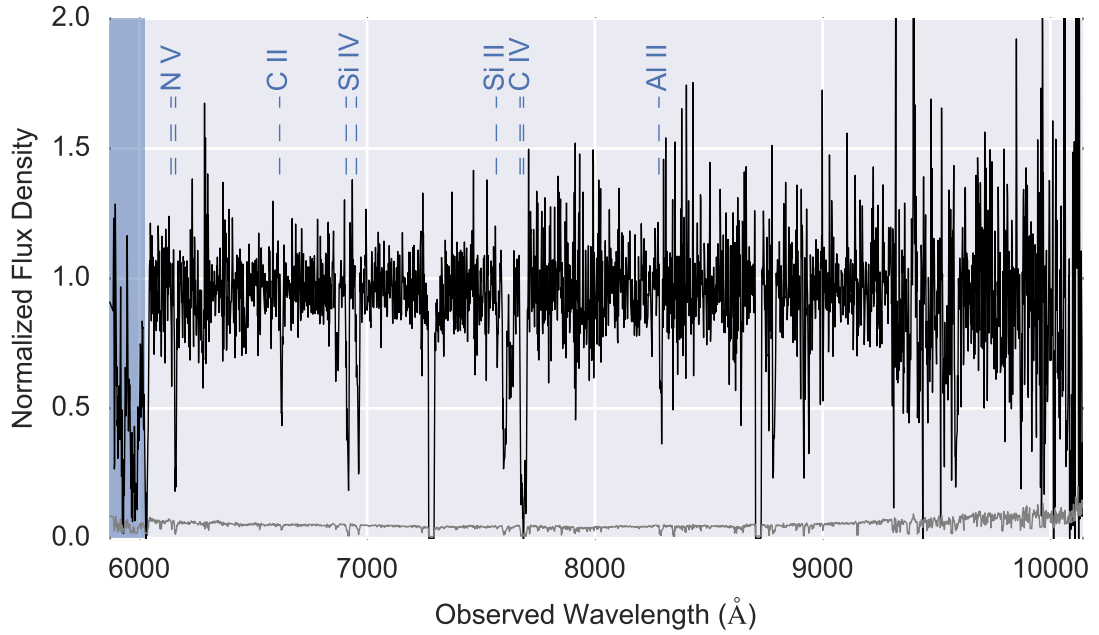


Figure 2.18: GRB 140419A – The black curve shows the normalized spectrum of the afterglow at $T_0 + 2.3$ hours (Tanvir et al., 2014). The gray curve is the noise spectrum. The two regions ($\sim 7300 \text{ \AA}$ and $\sim 8700 \text{ \AA}$) where the signal and noise spectra are zero are CCD chip gaps. The blue, shaded region highlights the onset of Lyman- α attenuation at different cosmological redshifts along the line-of-sight. This Ly- α “drop-out” provides a lower limit on the GRB’s redshift. The redshift of 3.956 is confirmed by the detection of numerous absorption lines from the host galaxy.

2.19, there is some evidence of the SED flattening out versus time in the $i - H$ curve.

2.3.2.3 X-ray Light Curve

The 0.3 – 10 keV flux light curve was downloaded from the University of Leicester website (Evans et al., 2007, 2009). I interpolated in log-space using the same spline methods used for the optical and NIR light curves. The resulting fit is shown in Figure 2.20.

X-ray Spectrum Selection I produced XRT spectra using the online tool (Evans et al., 2009). Due to a lack of significant evolution in the 1.51–10 keV to 0.3–1.5 keV hardness ratio during times where RATIR data were available, only two spectra were created, one for window timing data at early times ($< T_0 + 300$ s) and one for photon counting data at later times ($> T_0 + 300$ s, Figure 2.21). Figure 2.22 shows that these spectra are the same except at low energies ($E \lesssim 0.6$ keV). Given that the spectral indices of the two spectra were consistent ($\beta_{\text{WT}} = 0.82 \pm 0.03$, $\beta_{\text{PC}} = 0.85 \pm 0.04$), both spectra constrain fits of the X-ray to optical/NIR SED in the same way. Because of known increased systematic errors at lower energies in the window timing (WT) mode, only the photon counting (PC) spectrum was used for SED construction (http://www.swift.ac.uk/analysis/xrt/digest_cal.php#abs).

X-ray Spectrum Scaling As described for GRB 120119A in the previous section, the XRT spectra were scaled using the 0.3 – 10 keV light curve (Figure 2.20). The xspec cflux function is used in the X-ray model to fit the observed flux of the

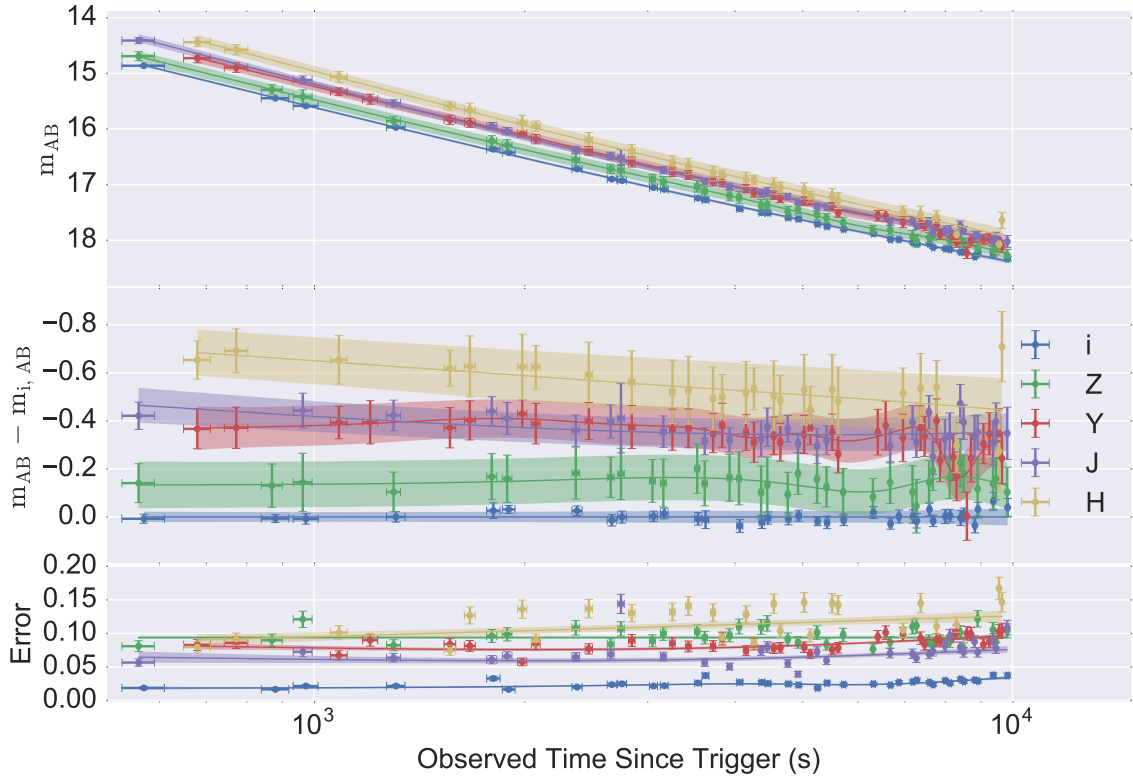


Figure 2.19: GRB 140419A – NIR light curves measured by RATIR were fit in R using 3rd order natural regression splines. In the middle plot, each band is plotted relative to the interpolated i-band magnitude at a given time to emphasize changes in the SED versus time. Errors were estimated by a second fit, shown in the bottom panel, where calibration uncertainties were taken to be 10%. In both cases, the number of knots were selected by minimizing the generalized cross validation estimate (Craven and Wahba, 1978).

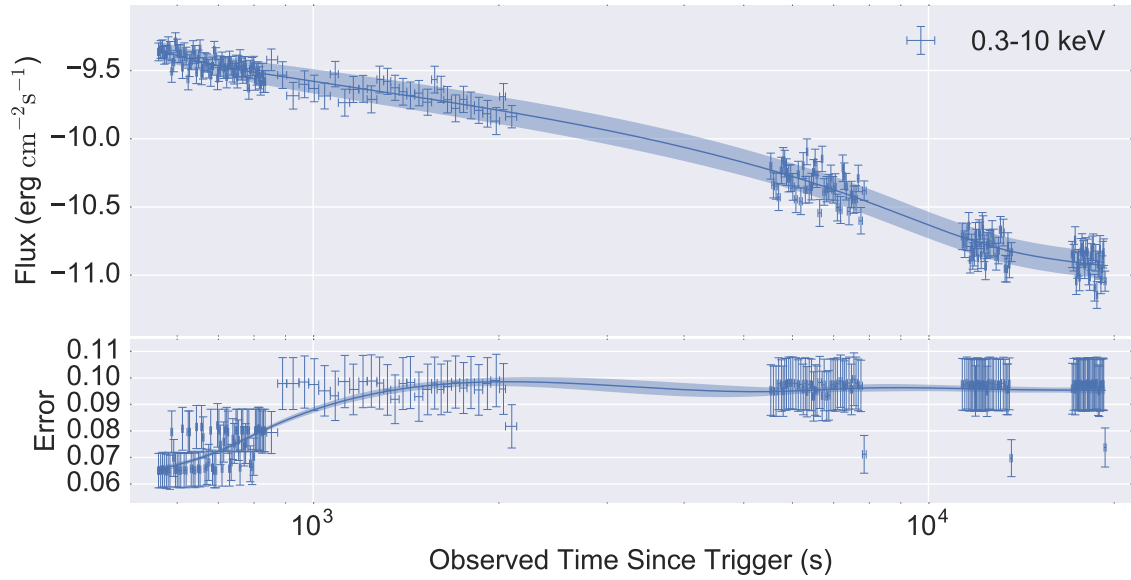


Figure 2.20: GRB 140419A – The 0.3 – 10 keV light curve measured by XRT was fit using 3rd order natural regression splines. The bottom panel shows how the uncertainties of interpolated times were estimated by fitting measured uncertainties with a smoothing spline, assuming 10% errors for the systematic calibration. In both cases, the number of knots were selected by minimizing the generalized cross validation estimate (Craven and Wahba, 1978).

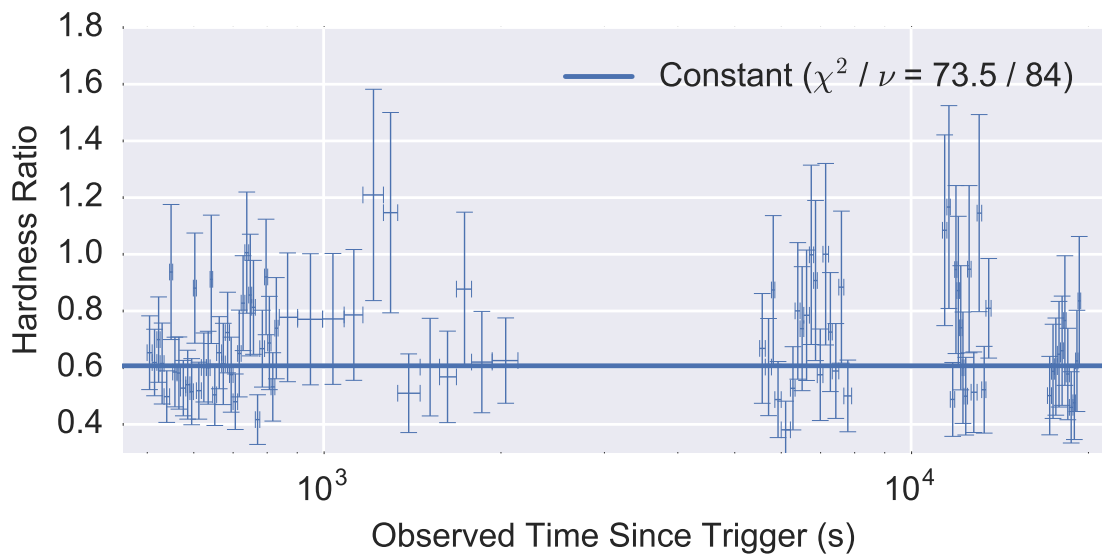


Figure 2.21: GRB 140419A – The ratio of hard (1.51 – 10 keV) to soft (0.3 – 1.5 keV) photons detected by XRT during RATIR observations is consistent with a constant value. For this reason, a single, time-averaged spectrum is sufficient.

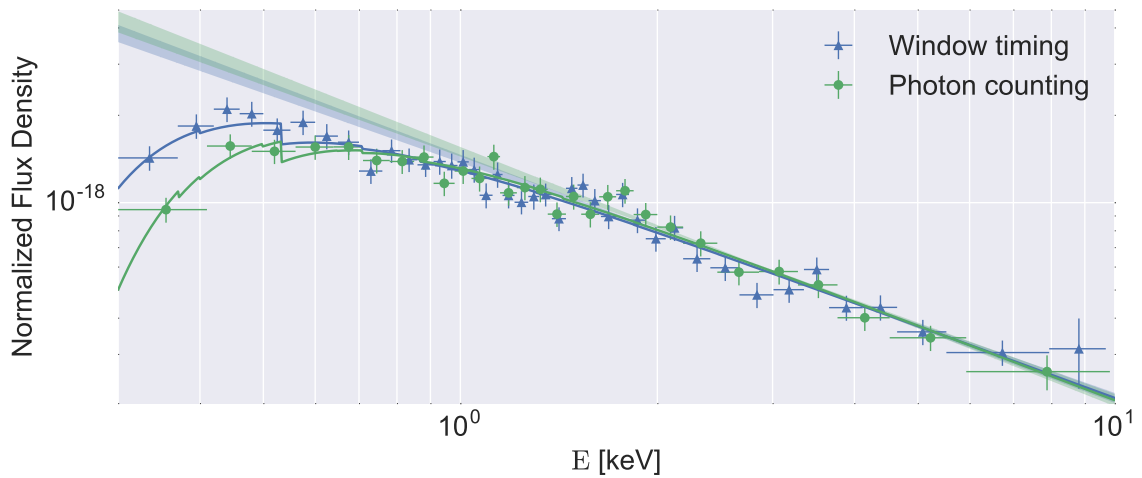


Figure 2.22: GRB 140419A – Time averaged XRT spectra. The window timing (WT) mode spectrum is integrated from $T_0 + 400 - 838$ seconds and the photon counting (PC) mode spectrum from $T_0 + 845 - 19440$ seconds. The spectra have been normalized to highlight discrepancies. Solid lines show fits including photoelectric absorption. Shaded regions are the underlying power-law with 1σ uncertainties. The greatest deviation is at low energies where the effects of rest frame photoelectric absorption dominate.

spectrum, which is then used to scale the spectrum to the fitted flux at the requested time (Arnaud, 1996).

2.3.2.4 Temporal Evolution

I constructed NIR to X-ray SEDs from the interpolated light curves as discussed previously for GRB 120119A. These SEDs were fit using the emcee Markov chain Monte Carlo (MCMC) Python package (Foreman-Mackey et al., 2013). When included, the X-ray spectrum was always fit with a power-law with redshifted photoelectric absorption from the host galaxy. Galactic N_{H} was fixed to the value calculated from Willingale et al. (2013) in the direction of the burst while the host N_{H} is left as a free parameter. The optical/NIR SEDs were fit with various dust extinction profiles. When both X-ray and optical/NIR data were fit simultaneously, fits were done both with and without a break in the spectral index. A summary of attempted fits is shown in Table 2.8. Results for the two best models ($A_{\text{V}} = 0$ and SMC extinction, selected based on reduced χ^2) are presented in Figures 2.23 and 2.24.

2.3.3 Discussion and Conclusions

The optical/NIR fits in Table 2.8 indicate that the rest frame A_{V} must be small. Additionally, there is no evidence of evolution in A_{V} from early to late times. When optical data and X-ray data are fit simultaneously, the SEDs are best explained by the introduction of a break in the spectral index (possibly the cooling break, ν_{c}). When A_{V} is assumed to be 0, there is evidence of a change in the spectral

index at optical wavelengths (β_{O} , Figure 2.23). When A_{V} is allowed to vary freely, the degeneracy with β_{O} produces results consistent with no evolution (Figure 2.24).

Table 2.8: GRB 140419A – Various fits of interpolated SEDs. Quoted uncertainties are based on the 16th, 50th and 84th percentiles of the marginalized parameter posterior distributions. For model definitions please see the caption of Table 2.1. In addition to the models listed there, “BPL” listed for some fits below stands for a broken power-law, where the break frequency was fit as a free parameter between optical and X-ray data. This is the only case where β_{optical} and $\beta_{\text{X-ray}}$ were not fixed to the same value.

Model	Time [s]	β_{optical}	A_{V}	$\beta_{\text{X-ray}}$	χ^2/ν
PL	764	$0.84^{+0.09}_{-0.09}$	0	–	$2.3^{+2.3}_{-1.1}/2$
PL	7593	$0.65^{+0.11}_{-0.11}$	0	–	$4.0^{+2.4}_{-1.1}/2$
PL+SMC	764	$0.4^{+0.3}_{-0.3}$	$0.11^{+0.08}_{-0.08}$	–	$2.6^{+2.3}_{-1.0}/1$
PL+SMC	7593	$0.3^{+0.2}_{-0.2}$	$0.10^{+0.06}_{-0.06}$	–	$3.5^{+2.4}_{-1.1}/1$
PL+MW	764	$0.81^{+0.09}_{-0.09}$	$0.05^{+0.07}_{-0.03}$	–	$4.2^{+2.9}_{-1.6}/1$
PL+MW	7593	$0.6^{+0.1+}_{-0.1}$	$0.05^{+0.07}_{-0.03}$	–	$5.5^{+3.0}_{-1.7}/1$
PL+XRT	764	$0.688^{+0.004}_{-0.004}$	0	$0.688^{+0.004}_{-0.004}$	$50^{+4}_{-2}/30$
PL+XRT	7593	$0.619^{+0.004}_{-0.004}$	0	$0.619^{+0.004}_{-0.004}$	$73^{+6}_{-4}/30$
PL+SMC+XRT	764	$0.72^{+0.01}_{-0.01}$	$0.06^{+0.02}_{-0.02}$	$0.72^{+0.01}_{-0.01}$	$42^{+4}_{-3}/29$
PL+SMC+XRT	7593	$0.65^{+0.01}_{-0.01}$	$0.06^{+0.02}_{-0.02}$	$0.65^{+0.01}_{-0.01}$	$67^{+5}_{-3}/29$
BPL+XRT	764	$0.674^{+0.007}_{-0.031}$	0	$0.89^{+0.10}_{-0.06}$	$30^{+4}_{-2}/28$
BPL+XRT	7593	$0.56^{+0.04}_{-0.06}$	0	$0.86^{+0.06}_{-0.04}$	$29^{+4}_{-2}/28$
BPL+SMC+XRT	764	$0.5^{+0.2}_{-0.3}$	$0.09^{+0.07}_{-0.05}$	$0.85^{+0.04}_{-0.04}$	$27^{+4}_{-3}/27$
BPL+SMC+XRT	7593	$0.4^{+0.2}_{-0.2}$	$0.08^{+0.06}_{-0.05}$	$0.85^{+0.04}_{-0.04}$	$28^{+4}_{-3}/27$

2.4 GRB 080607

One possible explanation for the lack of evidence of dust destruction in the afterglow of GRB 1404019A is the very low observed host galaxy extinction ($A_{\text{V}} \lesssim 0.2$) relative to that seen in GRB 120119A ($A_{\text{V}}(T_0 + 62 \text{ sec}) \sim 1.5$). For this reason, I applied the same analysis to another previously studied afterglow, that of GRB 080607. [Perley et al. \(2011, hereafter PM11\)](#) determined the best-fit dust extinction

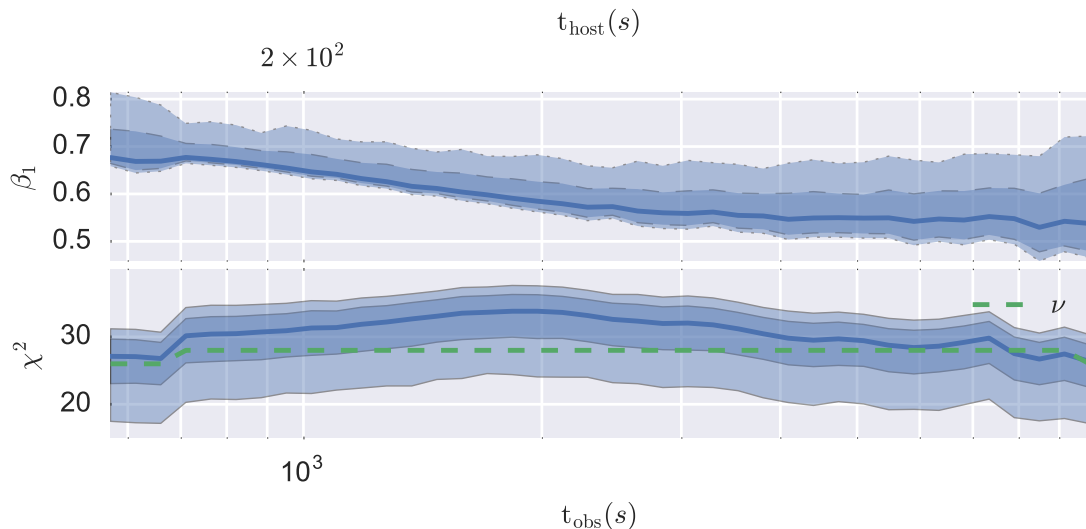


Figure 2.23: GRB 140419A – The evolution of $\beta_1 \equiv \beta_{\text{O}}$ with $A_{\text{V}} = 0$ and a power-law break between optical and X-ray bands.

profile using both photometric and spectroscopic observations and found the afterglow to be relatively highly extinguished by the host galaxy ($A_{\text{V}} \sim 3.5$, see Figure 2.25).

2.4.1 Observations

2.4.1.1 *Swift* Space Observatory

GRB 080607 triggered *Swift*-BAT at 06:07:27 UT on 7 June, 2008 (Mangano et al., 2008). The multi-peaked emission detected by BAT had $T_{90} = 79 \pm 5$ s (Stamatikos et al., 2008). *Swift* slewed to the source and began observing with XRT at $T_0 + 82.1$ s and UVOT at $T_0 + 92$ s. An uncatalogued source was detected by both instruments (Mangano et al., 2008). UVOT detected the source in white

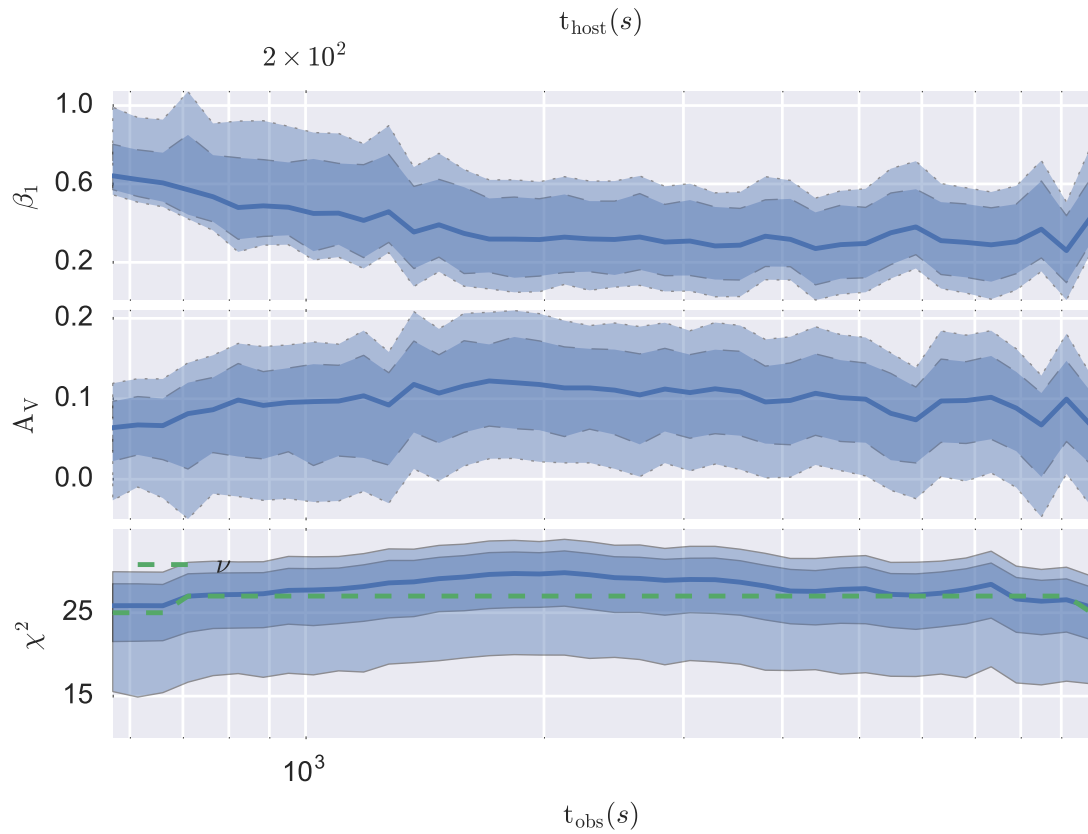


Figure 2.24: GRB 140419A – The evolution of $\beta_1 \equiv \beta_{\text{O}}$ and A_V with power-law break between optical and X-ray bands.

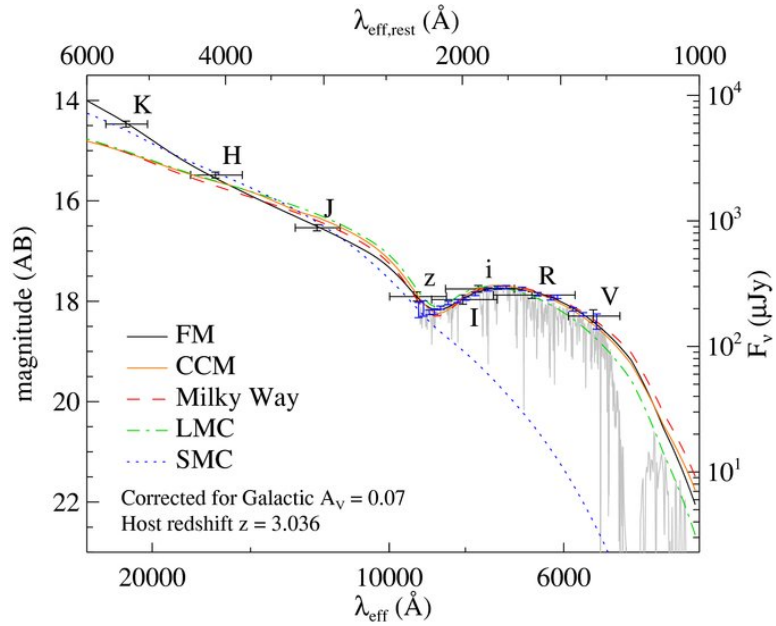


Figure 2.25: GRB 080607 – This figure from [Perley et al. \(2011\)](#) shows the authors’ fits to the photometric and spectroscopic SED of the afterglow used to determine best fit values for the dust extinction parameterization from [Fitzpatrick \(1999\)](#). In this section I use the fit from PM11 where $R_V = 4.69$, $c_1 = 1.29$, $c_2 = 0.30$, $c_3 = 1.66$, $c_4 = 0.31$, and $\gamma = 1.07$ ($\chi^2/\text{dof} = 22.9/20$). See Section 2.1.2 for a description of these parameters.

and V filters (Schady and Mangano, 2008).

2.4.1.2 Optical and Near-Infrared Observations

In addition to the detections by UVOT on-board *Swift*, the afterglow of GRB 080607 was detected by a number of ground-based observatories. Optical and NIR photometric flux density light curves, corrected for Galactic extinction, were taken from PM11 for use in this section. The earliest filtered observations began at $T_0 + 40$ sec. Spectroscopic measurements determined that the burst occurred at a redshift of $z = 3.036$ (Prochaska et al., 2008). As previously mentioned, these spectra were also used by PM11 to determine the best-fit host galaxy extinction profile.

2.4.2 Analysis

2.4.2.1 Optical and Near-Infrared Light Curves

The photometric light curves taken from PM11 were fit using the same spline methods as in Sections 2.2.1.1 and 2.3.2.2. Published flux density values measured by different instruments were combined where observations were taken in the same photometric bands. The resulting light curve fits are shown in Figure 2.26. Looking at the bottom panel of this figure, the evolution of these light curves appears achromatic.

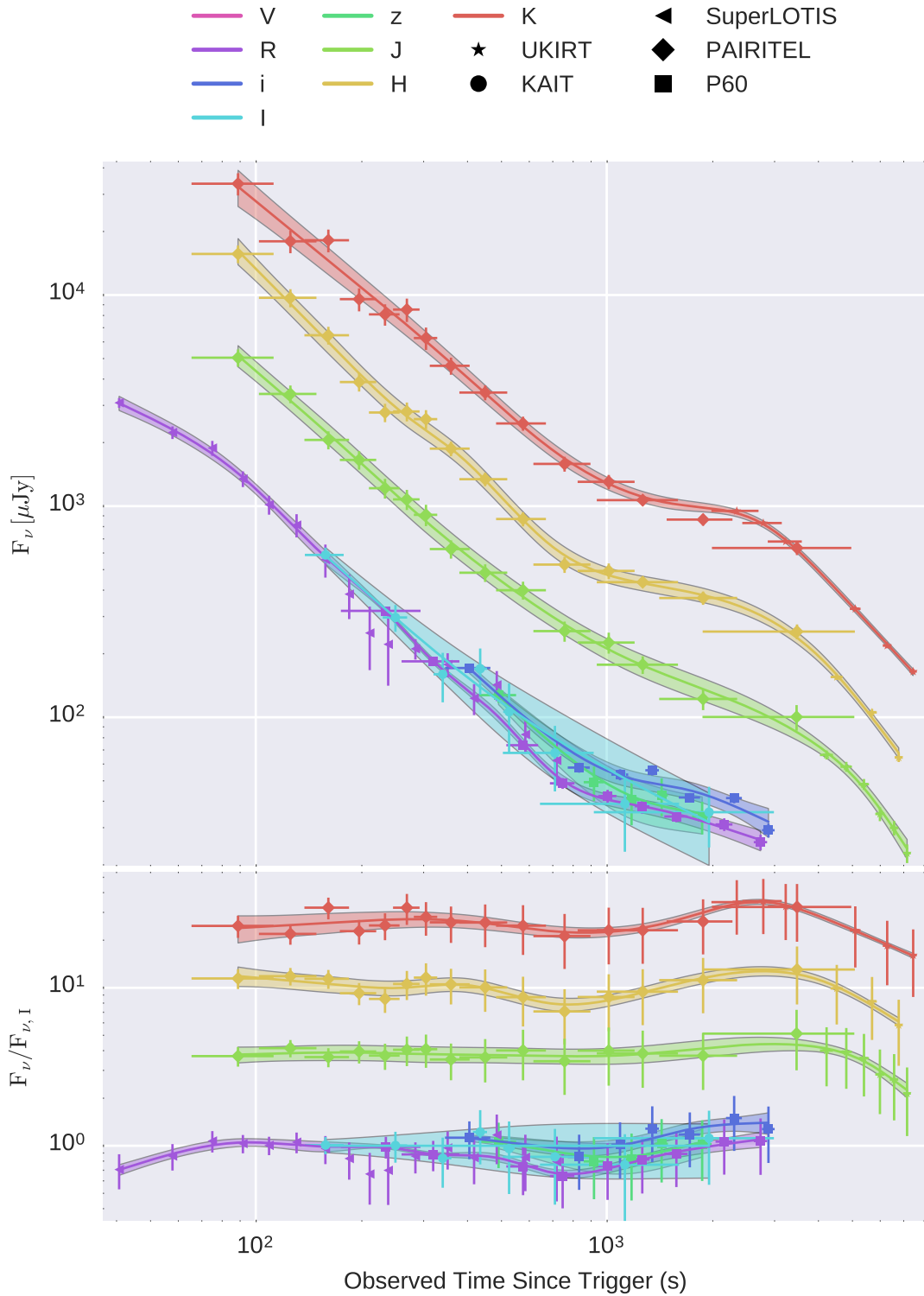


Figure 2.26: GRB 080607 – The optical and NIR photometric light curves presented by Perley et al. (2011) are fit by the same method described in previous sections.

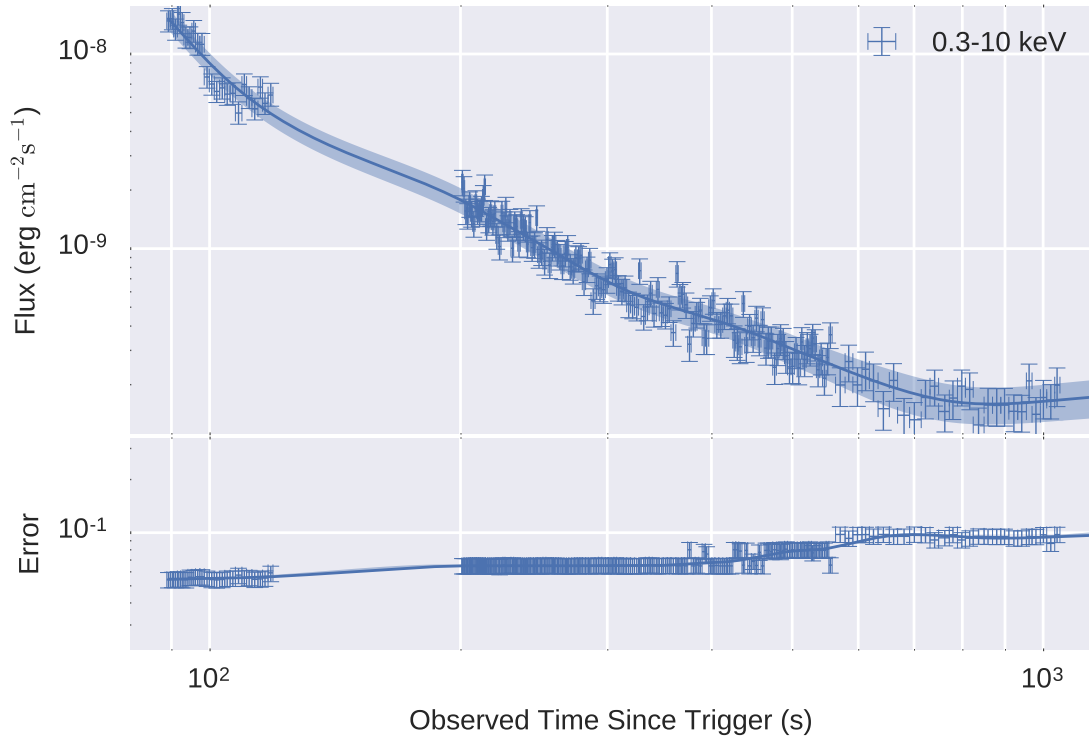


Figure 2.27: GRB 080607 – The 0.3 – 10 keV light curve measured by XRT was fit using 3rd order natural regression splines. The bottom panel shows how the uncertainties of interpolated times were estimated by fitting measured uncertainties with a smoothing spline, assuming 10% errors for the systematic calibration. In both cases, the number of knots were selected by minimizing the generalized cross validation estimate (Craven and Wahba, 1978).

2.4.2.2 X-ray Light Curve

The 0.3 – 10 keV flux light curve was downloaded from the University of Leicester website (Evans et al., 2007, 2009). I interpolated in log-space using the same spline methods used for the optical and NIR light curves. The resulting fit is shown in Figure 2.27.

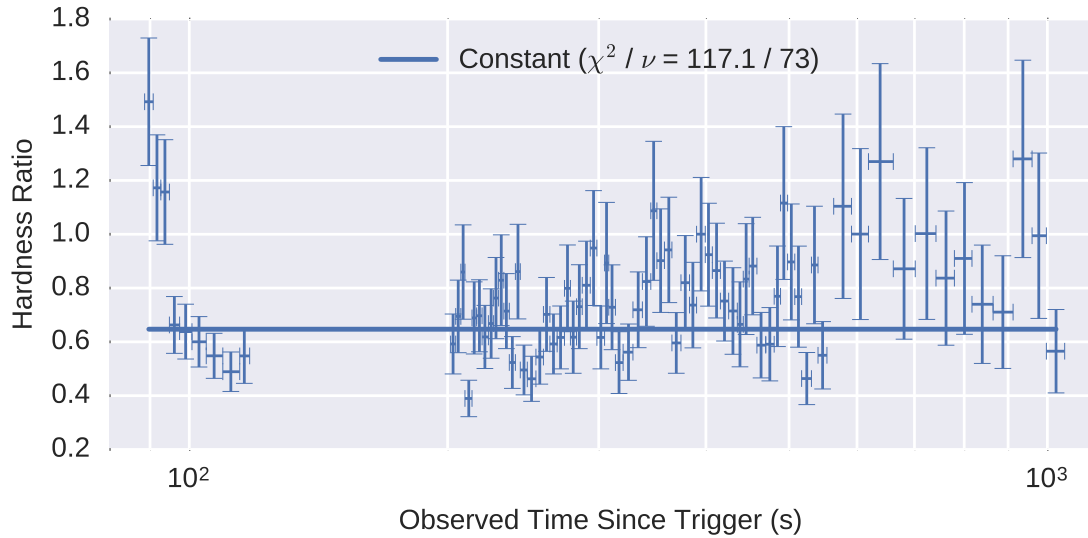


Figure 2.28: GRB 080607 – The ratio of hard (1.51 – 10 keV) to soft (0.3 – 1.5 keV) photons detected by XRT during optical and NIR observations is consistent with a constant value except at very early times. Since a high SNR spectrum cannot be produced for these early-time observations, a single, time-averaged spectrum is used.

X-ray Spectrum Selection I produced XRT spectra using the online tool ([Evans et al., 2009](#)). Due to a lack of significant evolution in the 1.51 – 10 keV to 0.3 – 1.5 keV hardness ratio during times where optical and NIR data were available, a single spectrum was generated from photon counting data (Figure 2.28). As in the case of GRB 120119A, the hardness ratio is greater at very early times, however there are insufficient data to produce a useful spectrum with a high SNR.

X-ray Spectrum Scaling As described for GRB 120119A, the XRT spectra were scaled using the 0.3 – 10 keV light curve (Figure 2.27). The xspec cflux function is used in the X-ray model to fit the observed flux of the spectrum, which is then used

to scale the spectrum to the fitted flux at the requested time (Arnaud, 1996).

2.4.2.3 Temporal Evolution

I constructed NIR to X-ray SEDs from the interpolated light curves as discussed previously for GRB 120119A. These SEDs were fit using the emcee Markov chain Monte Carlo (MCMC) Python package (Foreman-Mackey et al., 2013). When included, the X-ray spectrum was always fit with a power-law with redshifted photoelectric absorption from the host galaxy. Galactic N_{H} is fixed to the value calculated from Willingale et al. (2013) in the direction of the burst while the host N_{H} is left as a free parameter. The optical/NIR SEDs were fit with the best-fit dust extinction profile presented in PM11. Results of the analysis without and with including the X-ray spectrum are presented in Figures 2.29 and 2.30.

2.4.3 Discussion and Conclusions

PM11 determined that the afterglow of GRB 080607 was highly extinguished by the host galaxy. Using photometric and spectroscopic data, the authors determined the dust profile which best reproduced the observed afterglow. The authors additionally noted the apparent lack of evidence for color evolution in the optical/NIR afterglow.

The analysis presented here differs from that of PM11 by using splines rather than broken power-laws to model light curves. This analysis also considers the full X-ray spectrum when fitting the afterglow SED at each interpolated time. When considering only the optical/NIR SED, the results of this analysis framework are

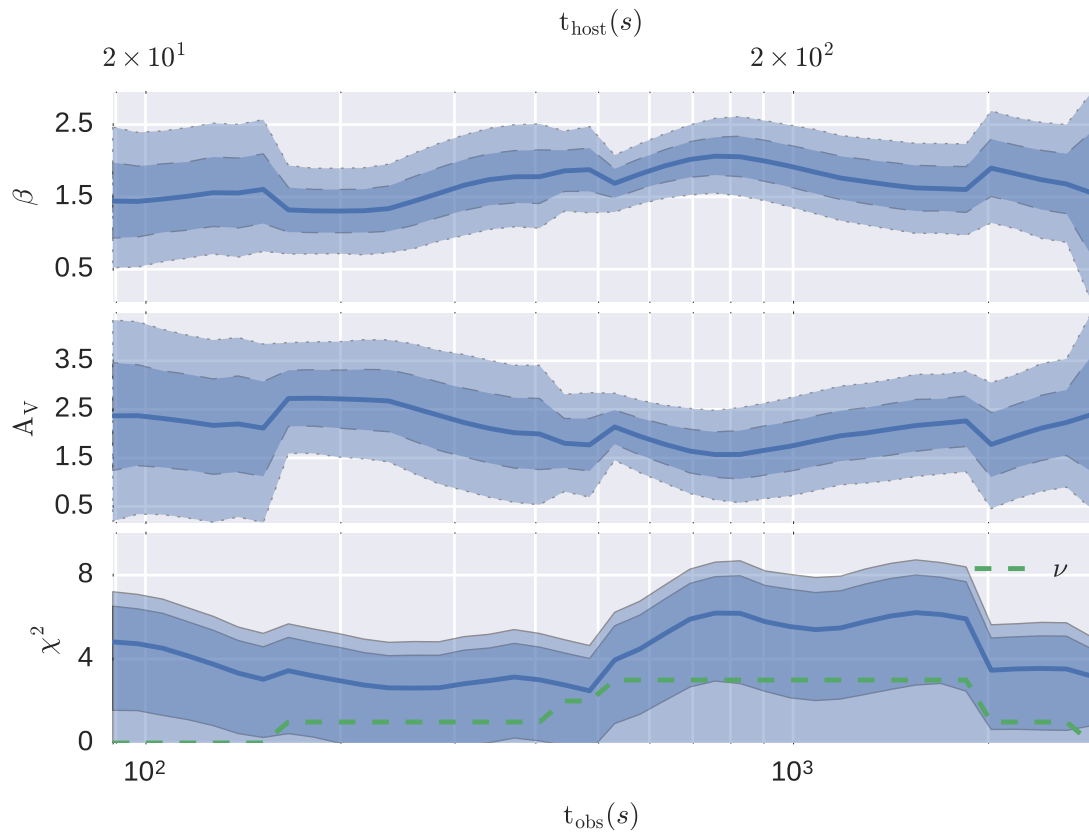


Figure 2.29: GRB 080607 – The evolution of the spectral power-law index (β) and A_V when only the optical and NIR afterglow SEDs are considered.

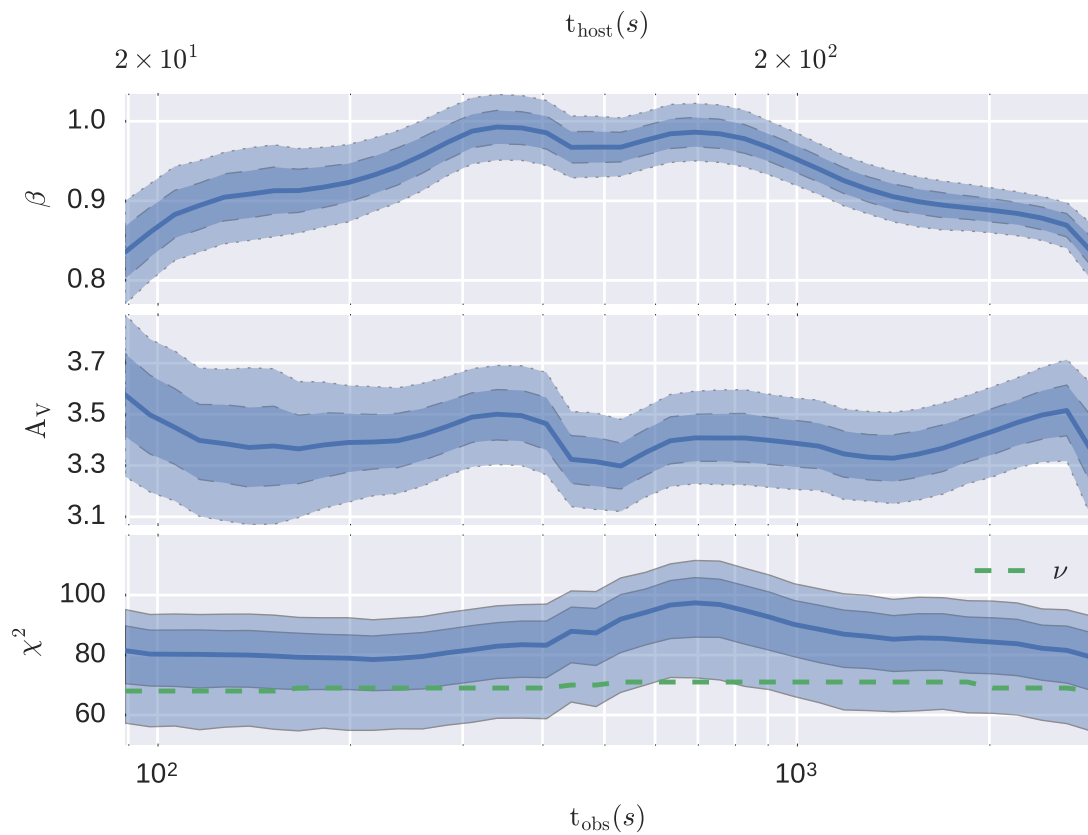


Figure 2.30: GRB 080607 – The evolution of the spectral power-law index (β) and A_V when the optical/NIR to X-ray afterglow SEDs are considered.

consistent with no evolution in either β or A_V (Figure 2.29). Adding X-ray data to the SEDs significantly constrains both β or A_V and demonstrates a lack of evidence for changes in A_V (Figure 2.30).

Given the very early time at which this analysis begins in the GRB’s rest-frame (~ 20 sec.) and the relatively high extinction from the host galaxy ($A_V \sim 3.5$), it is interesting that there is no evidence for the photodestruction of dust at early times.

2.5 Summary

This chapter has set out to describe a new analysis framework designed to detect color evolution of GRB afterglows without imposing a physical model for SED evolution. The procedure successfully identified a decrease in A_V from early to late times in GRB 120119A consistent with the destruction of dust, as suggested by MP14. The results of the analysis without the inclusion of X-ray spectra are broadly consistent with those of MP14, but without the high degree of variability.

Given this successful detection of color evolution, the framework was applied to the early-time optical and NIR data for the high redshift afterglow of GRB 140419A. In this case no evidence was found for a change in A_V . Several possible reasons for this result are:

- A spectral break in the intrinsic power-law spectrum between the optical and X-ray bands left a high degree of covariance between A_V and β_O despite the inclusion of X-ray spectra.
- Even given the high redshift ($z = 3.956$) of the burst, this first SED was 115

seconds after the GRB in the rest-frame, compared with 23 seconds in the case of GRB 120119A. Still, the detected evolution of A_V in GRB 120119A's afterglow continues for $\gtrsim 10^3$ s.

- $A_V \lesssim 0.1$ and in most cases consistent with 0 versus the initial $A_V \sim 1.8$ in the case of GRB 120119A. This means that there was little dust in the CBM to be destroyed.

To test these explanations, the afterglow of GRB 080607 was selected as a final test case. This previously published afterglow was known to have a high redshift ($z = 3.036$) and early-time optical/NIR photometry starting at $T_0 \lesssim 20$ seconds in the host-frame. Additionally, the host galaxy extinction profile was well determined by photometric and spectroscopic observations and extinction from the host galaxy was known to be greater than that of either GRB 120119A or GRB 140419A (Perley et al., 2011, $A_V \sim 3.5$). Given these facts, this afterglow was an ideal candidate for detecting further evidence for the destruction of dust in the CBM, however no such evolution of A_V was found. This deviation from the behavior of GRB 120119A could be due to the dust extinction occurring outside of the immediate CBM. A system further away along the line-of-sight would be exposed to a reduced flux of photodissociating radiation.

This framework was written to be easily applied to any GRB afterglow data set. Having tested the method with the afterglows of GRB 120119A, GRB 140419A, and GRB 080607, I plan to apply it to a larger sample of events to investigate SED evolution of LGRB afterglows more generally. It will be particularly interesting to

look at additional cases of afterglows known to be highly extinguished where any evidence of photodestruction would be most easily observed.

Chapter 3: RIMAS: Background information

The Rapid Infrared Imager / Spectrometer (RIMAS) has been designed to study long duration γ -ray bursts (LGRBs) at high cosmological redshifts ($z \gtrsim 7$). Motivations for doing so are reviewed in Section 1.1.1. This chapter will describe the challenges as they relate to the design requirements for RIMAS. An overview of the instrument’s final optomechanical design is presented.

3.1 Requirements

3.1.1 Response Time

Due to the power-law decay of the afterglow emission of LGRBs with time (Figure 1.9), it is essential to observe these sources as soon as possible to maximize the detected signal. Additionally, afterglows have exhibited spectral variations at early times (Section 2.1). For both of these reasons, RIMAS must be capable of beginning observations within minutes of the initial event.

3.1.2 Spectral Coverage

Optically “dark” GRBs are bursts with either no detected optical afterglow or with observed optical emissions significantly less than what would be expected from

the synchrotron model based on the observed X-ray spectrum (i.e. the optical to X-ray spectral index, $\beta_{\text{OX}} < 0.5$, Jakobsson et al., 2004). Some of these afterglows are now known to be the result of significant dust extinction by host galaxies (e.g. GRBs 120119A and 080607 in Sections 2.2 and 2.4). In these cases, NIR observations are preferred since longer wavelengths interact weakly with interstellar dust compared with optical and UV emissions.

Additionally, sources at very high cosmological redshifts are attenuated by systems of neutral hydrogen (HI) existing within the intergalactic medium (IGM). Sources, such as the afterglows of LGRBs, are absorbed at the rest frame Lyman- α wavelength ($\text{Ly}\alpha$, $\lambda_{\text{rest}} = 1215.7 \text{ \AA}$). In spectroscopic observations where $R = \lambda/\Delta\lambda \gtrsim 4000$, the collection of these features at different redshifts along the line of sight leads to the “Lyman- α forest” (Figure 3.1, e.g., Rauch, 1998). In lower resolution spectroscopic or broadband photometric observations, these features manifest as the “Lyman- α dropout” due to the coarse spectral resolution (Figure 3.2). Additionally, when the optical depth of HI is sufficiently large ($\tau \geq 1$) the afterglow will drop out at wavelengths shorter than the Lyman limit ($\lambda_{\text{rest}} \lesssim 912 \text{ \AA}$).

The presence of these HI systems in the IGM means that Ly α features will attenuate optical wavelengths at high redshifts. Figure 3.3 shows in which observed optical/NIR bands the dropout will appear for a given redshift. For RIMAS to observe afterglows from GRBs at $z \gtrsim 7$, the instrument must observe at $\lambda \gtrsim 1\mu\text{m}$. For a brief discussion of potential research interests at such high redshifts, see the end of Section 1.1.1.

To produce useful SEDs, RIMAS must be able to detect an afterglow in as

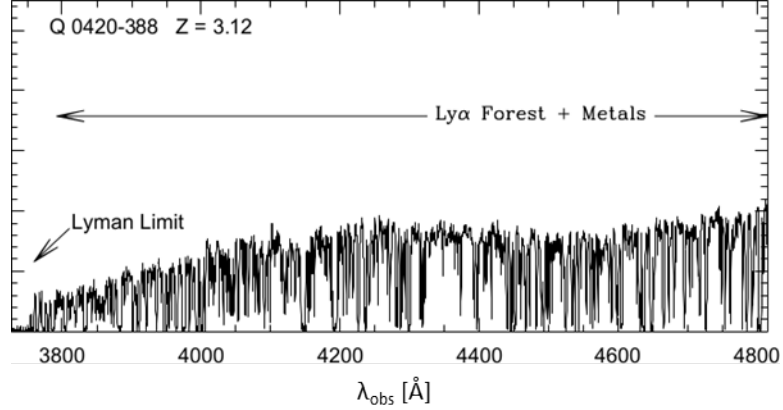


Figure 3.1: Intervening HI systems at different cosmological redshifts along the line of sight attenuate the emission of high redshift sources leading to the “Lyman- α (Ly α) forest”. The figure above shows the Ly α forest in the spectrum of a quasar at $z = 3.12$. These features appear the same way in spectra of GRB afterglows.

many bands as possible. Multi-band detections can be used to estimate a burst’s redshift. Photometry in conjunction with X-ray detections can additionally constrain dust extinction from the host galaxy and inform spectroscopic observations (see Chapter 2). To maximize detections of high redshift events, RIMAS will cover from $\sim 1.0 - 2.4 \mu\text{m}$. For photometric observation, RIMAS will use the four UKIRT-WFCAM filters falling in this bandpass: Y ($0.97 - 1.07 \mu\text{m}$), J ($1.17 - 1.33 \mu\text{m}$), H ($1.49 - 1.78 \mu\text{m}$) and K ($2.03 - 2.37 \mu\text{m}$). Details on these filters are found in [Hewett et al. \(2006\)](#).

Given the limitations of constraining GRB redshifts and host galaxy properties with detections in four or fewer bands (see Section 2.5), RIMAS will also include low spectral resolving power ($R \sim 30$) dispersive modes. This mode will allow SEDs to be constructed with more sampled wavelengths, versus photometry, when an after-

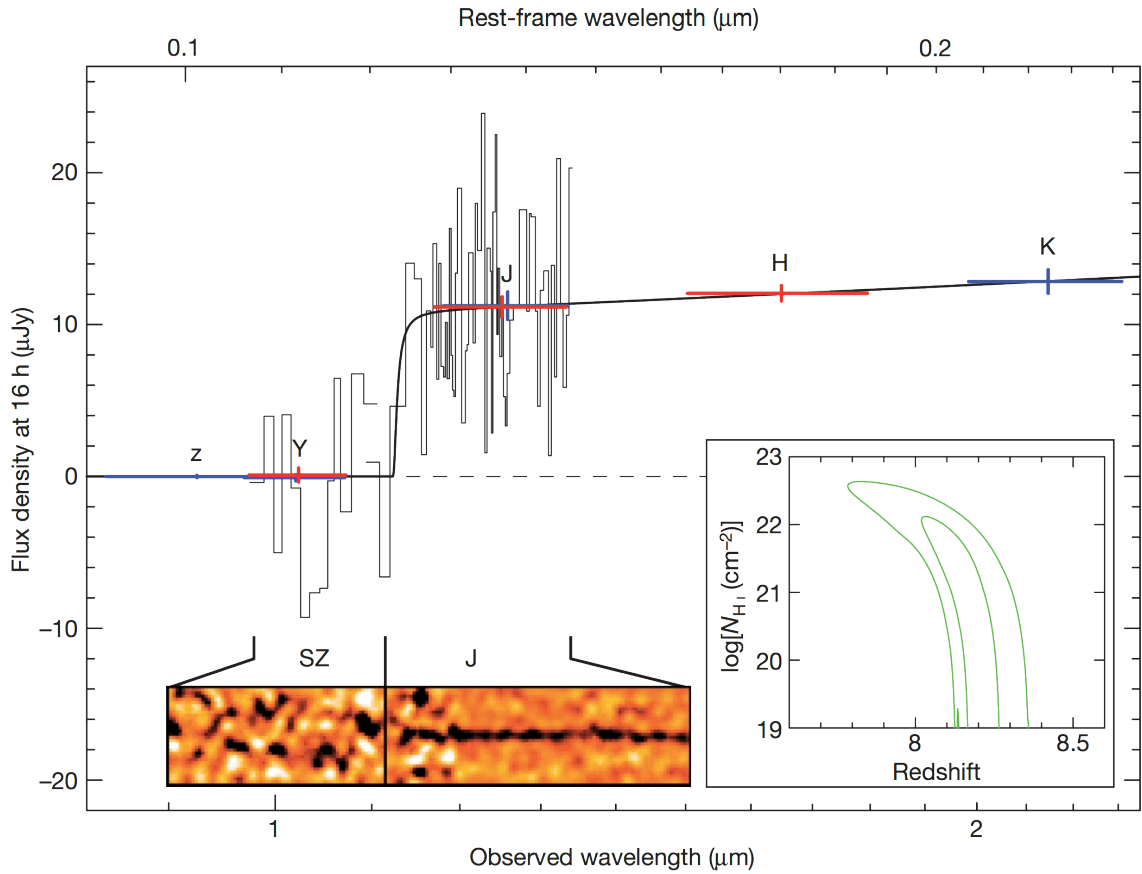


Figure 3.2: The composite NIR spectrum of GRB 090423 is taken from [Tanvir et al. \(2009\)](#). The sharp drop in the measured flux density of the afterglow for $\lambda \lesssim 1.1\mu\text{m}$ is due to attenuation by neutral hydrogen ($\text{Ly}\alpha$ transition, $\lambda_{\text{rest}} = 1216\text{\AA}$) at a cosmological redshift of ~ 8.2 (see [Figure 3.3](#)). Scaled photometry is also plotted, demonstrating how even low resolution spectroscopy can dramatically improve a redshift estimate.

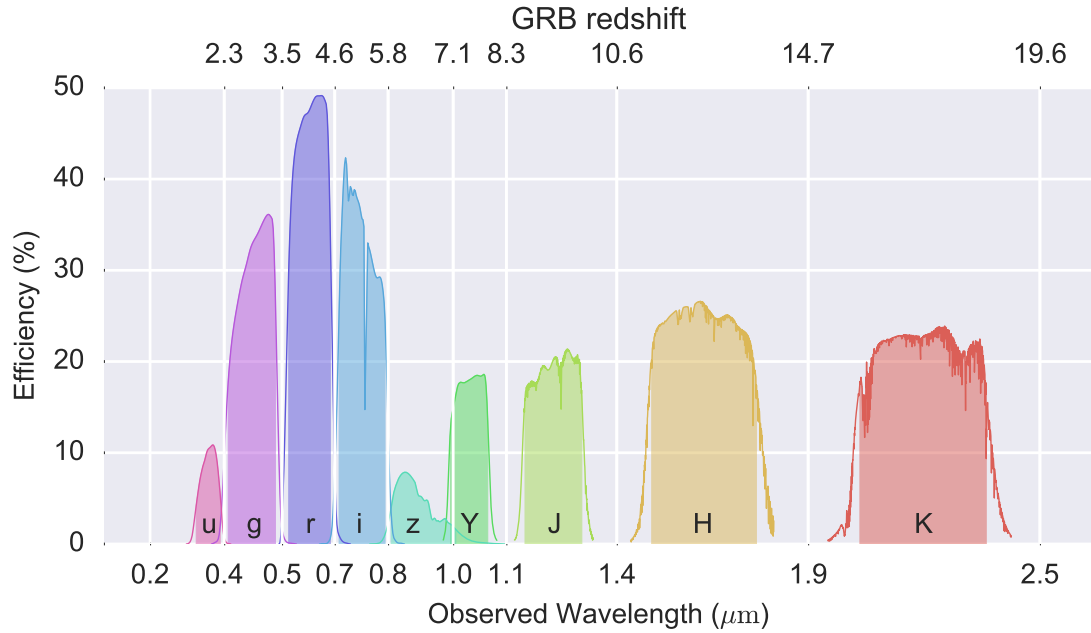


Figure 3.3: Common optical and near-infrared filters are plotted versus the observed wavelengths of Ly α absorption at different cosmological redshifts. RIMAS will operate in the Y, J H and K photometric bands. The plotted transmission curves include atmospheric and other instrument losses for SDSS and UKIDSS filters (Fukugita et al., 1996; Hewett et al., 2006). The shaded regions highlight wavelengths where 90% of a band’s light is transmitted. For a given redshift on the top axis, the Ly α -dropout will appear at approximately the corresponding wavelengths on the bottom axis. This demonstrates the need to observe at NIR wavelengths for very high redshift events.

glow is too faint for higher resolution spectroscopy. Potential applications include redshift estimations via Ly α drop-out and better constraining dust extinction profile features (e.g., 2175 Å bump, see Section 2.1.2).

For sufficiently bright afterglows ($m_{AB} \lesssim 19$, see Figure 3.5), moderate resolution spectroscopy ($R \sim 4500$) will be possible. This resolution allows for redshift determinations via absorption lines in afterglow spectra or emission lines from host galaxies. Additionally, studies of host galaxy metallicities and the progress of the reionization of the IGM become possible. Figure 3.4 shows an example of how abundance measurements are possible using $R \sim 6,000$ spectra of GRB afterglows. Previous studies have drawn the same conclusion for GRB afterglow and quasar spectra ($R \gtrsim 4000$, e.g., Fan et al., 2006; Prochaska et al., 2007; Jorgenson et al., 2013; Cucchiara et al., 2015).

3.1.3 Spatial Coverage

RIMAS will be capable of imaging the full 3 arcmin \times 3 arcmin FOV provided by the telescope. Maximizing the FOV is important for identifying transients with arc-minute scale localization provided by *Swift*-BAT and for the photometric calibration of images using field stars. A larger FOV increases the average number of cataloged stars in a given image.

3.1.4 LGRB Afterglow Detection Rate Estimates

Currently ~ 100 GRBs are detected every year, primarily by the *Swift* satellite. Of these, $\sim 86\%$ are LGRBs which sometimes occur at very high redshifts ($z \gtrsim 7$).

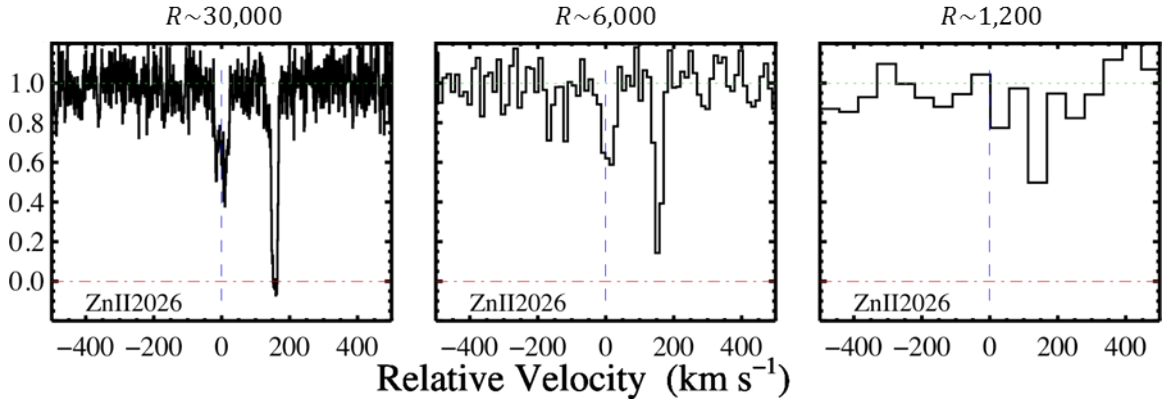


Figure 3.4: The bottom panel of Figure 1 from [Cucchiara et al. \(2015\)](#). The plot on the left shows a weak metal line from a Keck-HIRES spectrum of GRB 050820. The center and rightmost plots are simulated spectra at $R \sim 6,000$ and $1,200$ respectively. In the center case, abundances can still be measured, but only upper limits are possible for the coarsest spectrum. RIMAS will include moderate resolution diffractive modes of $R \sim 4500$.

In general, LGRB afterglows are detected by at least one ground based observatory $\sim 60\%$ of the time (~ 52 times/year).

The average night where RIMAS will operate, measured from astronomical twilight, is 8 hours and 46 minutes (36.5% of the day). Limiting observations to airmasses less than 2 (i.e. $\gtrsim 30$ degrees above the horizon), $\sim 25\%$, $\sim 30\%$, and $\sim 50\%$ of the sky is observable at a given moment, in a two hour window, and on a given night respectively. Based on 47 nights of observed conditions at the telescope site, observations are possible $\sim 65\%$ of the time. Additionally, 65 nights per year are reserved for engineering work. Combining these factors, RIMAS will be able to observe approximately 11 afterglows within minutes of a LGRB, 14 afterglows within an hour of a LGRB, and 23 afterglows in less than one day of a LGRB every

year. These estimates are roughly consistent with observation rates for ongoing rapid-response projects (Cenko et al., 2009; Littlejohns et al., 2015).

The actual fraction of LGRBs occurring at the very high redshifts targeted by RIMAS is unknown, but Greiner et al. (2011) found $\sim 5.5\%$ of LGRBs in their sample at $z > 5$, with the number increasing to 12.8% if all bursts without measured redshifts were at $z > 5$. Other studies have found consistent results (e.g. Fynbo et al., 2009; Littlejohns et al., 2015). Taking the fraction of LGRBs at $z > 5$ to be 5.5% , RIMAS will observe a very high redshift burst within minutes to hours roughly once per 1.5 years and within a day once per 0.8 years. Figure 3.5 compares LGRB light curves to RIMAS's estimated sensitivities to predict the frequency of 10σ detections of GRB afterglows at $z = 8.5$. Assuming similar sensitivity in other NIR bands, this plot shows that RIMAS should obtain a high SNR SED in multiple photometric bands $\sim 90\%$ of the time when observing an afterglow within an hour of the LGRB. The probability for $R \sim 30$ spectroscopy is $\sim 2/3$ and $\sim 1/3$ for $R \sim 4000$ spectroscopy. From this, RIMAS is expected to obtain a high SNR, moderate resolution spectrum of a LGRB afterglow at $z > 5$ once every ~ 4 years. The fraction of LGRBs at $z > 7$ is likely a couple percent, leading to detections at approximately half the rate as at $z > 5$.

3.2 Discovery Channel Telescope

The Discovery Channel Telescope (DCT) is Lowell Observatory's new 4.3 meter telescope located near Happy Jack, Arizona. After seven years of construction,

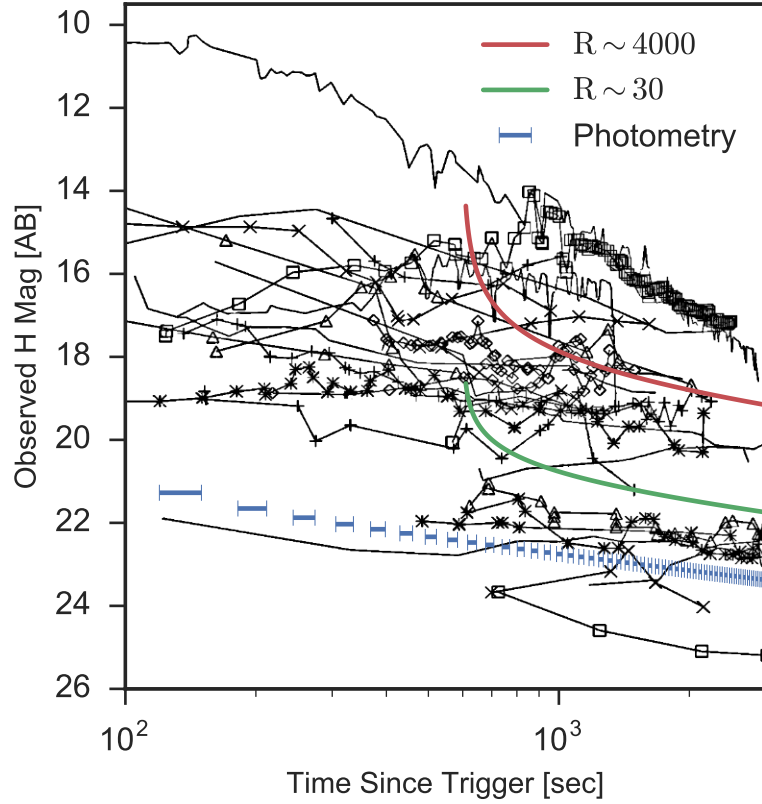


Figure 3.5: The black curves are 41 GRB afterglow light curves transformed to $z = 8.5$ taken from [Butler et al. \(2012\)](#). The blue lines show the 10σ limiting magnitudes for H band photometric observations. These limits are for coadded 30 second exposures at a 50% duty cycle, where observations are alternating between H and K bands. This demonstrates that RIMAS is expected to be capable of producing photometric SEDs for nearly all ($\gtrsim 90\%$) LGRB afterglows observed within $\lesssim 1$ hour. The green and red curves show limiting magnitudes for $R \sim 30$ and $R \sim 4000$ spectroscopy respectively as a function of exposure time for observations beginning 10 minutes after the GRB. In the case of $R \sim 30$, $\sim 2/3$ of these afterglows would be detected at 10σ . For $R \sim 4000$, detections are expected to be possible for $\lesssim 1/3$ of LGRB afterglows with observations beginning at $\lesssim 10$ minutes. These limiting magnitudes were calculated using a preliminary exposure time calculator written by Vicki Toy.



Figure 3.6: The first-light image of from the 4.3 meter Discovery Channel Telescope (DCT), taken in May of 2012. The image is of a barred spiral galaxy, M109. The image was retrieved from <https://lowell.edu/>.

the telescope acquired its first-light image in May of 2012 (Figure 3.6). The first scientific observations were made during the commissioning phase in early 2013. In the first quarter of 2015, DCT was declared fully-operational.

3.2.1 Ritchey-Chrétien Design

DCT uses a two mirror Ritchey-Chrétien (RC) design, shown in Figure 3.7. In this setup, the telescope provides instruments with a 15 arc-minute square field of view (FOV). The RC setup has the advantages of being free of spherical aberration and coma, but does suffer from astigmatism. The central obscuration is 13% of the entrance pupil (MacFarlane and Dunham, 2004). The telescope's plate scale is 8 arc-seconds / mm.

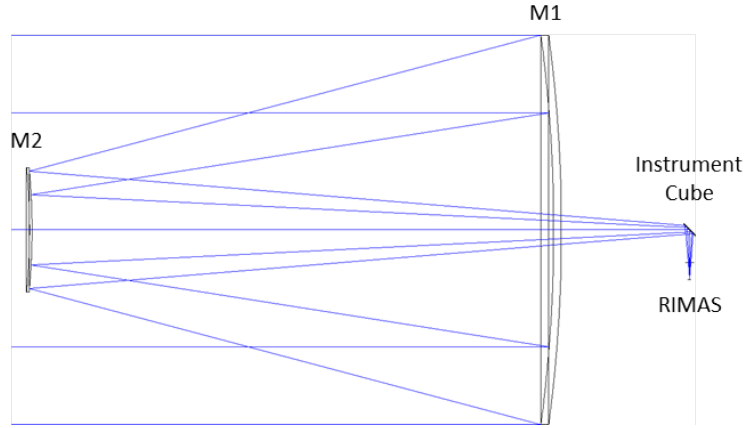


Figure 3.7: This schematic view of the Discovery Channel Telescope shows rays from an object at infinity entering the telescope from the left. After being focused by the primary (M1) and secondary (M2) mirrors, the light is passed into the “instrument cube” where a fold-mirror is shown prior to the Ritchey-Chrétien (RC) focus.

3.2.2 Instrument Cube

DCT instruments using the RC focus are mounted on an “instrument cube” located behind the primary mirror. The entire cube is able to rotate, allowing the field to be de-rotated before the beam reaches the instruments. Observers are able to quickly switch between instruments mounted on the cube by the insertion of a fold mirror or dichroic beam splitter. At the straight-through position on the cube is the Large Monolithic Imager (LMI) which obtains 12.5×12.5 arc-minute², single-band images at optical wavelengths. By inserting a dichroic, observers will be able to simultaneously obtain optical images with LMI and NIR images or spectra with RIMAS.

3.2.3 Site

DCT is located near Happy Jack, Arizona, approximately 45 miles southeast of Flagstaff. The telescope is at an elevation of 2361 meters. During site testing, the median full width at half max (FWHM) atmospheric seeing in R-band ($\lambda_{\text{eff}} \sim 0.66 \mu\text{m}$) was 0.84 arc-seconds (Bida et al., 2004). In the first two years of operations, however, the median has been closer to 1 arc-second FWHM. Seeing improves as $\lambda^{1/5}$, so that at 1 μm and 2 μm the expected seeing for RIMAS will be approximately 0.9 and 0.8 arc-seconds respectively (Boyd, 1978). During the best conditions (i.e., dark and seeing ~ 0.5 arc-seconds), LMI is able to achieve an SDSS-R band limiting magnitude of $m_{\text{AB}} \gtrsim 25$ in under 100 seconds.

3.3 RIMAS Design Overview

3.3.1 Optical Definitions

All lenses used in RIMAS’s slit-imaging and scientific assemblies are characterized by the following design parameters.

- Radius of curvature [mm] – every lens has a radius specified for each side.
- Conic constant [dimensionless] – aspherical lenses used in RIMAS have a non-zero conic term on one or both optical surfaces.
- Polynomial terms [variable] – additional design freedom for a lens surface can be achieved by describing deviations from a spherical sag profile in terms of a

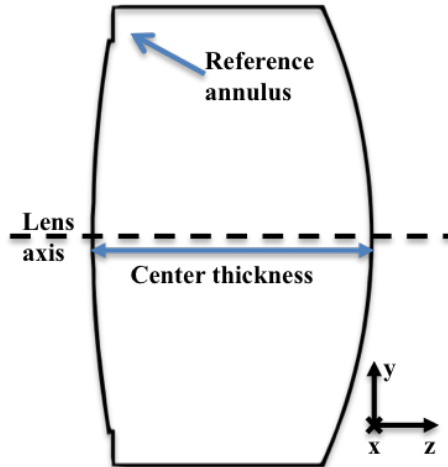


Figure 3.8: This diagram shows the profile of a biconvex lens used in RIMAS. Most lenses were fabricated with a “reference annulus” around the circumference of one side. This surface provides a flat reference which sits on the optomechanical assembly. When discussing an individual lens, the origin is defined as the center of the lens cylinder in the plane of the reference annulus. The z-axis points into the lens from the origin.

polynomial function of radial distance from the lens axis. For the definition of the lens axis, see Figure 3.8.

- Center thickness [mm] – the separation of the two lens surfaces along the lens axis.
- Substrate – the lens substrate defines the wavelength and temperature dependent refractive index.

Most of RIMAS’s lenses have a “reference annulus” fabricated around the circumference of one optical surface, as shown in Figure 3.8. This annulus is used to precisely define a lens’s position along the optical axis within the optomechanical design.

3.3.2 Cryostat

Because RIMAS must operate out to $\sim 2.4\ \mu\text{m}$, the thermal emission of the instrument must be considered. To mitigate the thermal background, the entire instrument, including imaging optics and dispersive elements, is cooled to $\sim 80\ \text{K}$ in a cryostat. The cryostat is divided into two sections: the main chamber containing the scientific instrument, and a front compartment containing spectroscopic slits, specialty filters and optics for a “slit-imaging” camera. The chamber is pumped to $\lesssim 10^{-8}$ Torr using a turbopump at which time a two stage helium gas cryocooler is activated. The first stage cools the optics bench ($\sim 80\ \text{K}$) and two Teledyne HAWAII-2RG (H2RG) HgCdTe detectors ($\sim 65\ \text{K}$) at the focal planes of the main optical arms. The second stage is used to cool a legacy InSb Spitzer IRCAM detector ($\sim 20\ \text{K}$). A computer-aided design (CAD) model of the cryostat mounted on the instrument cube is shown in Figure 3.9.

3.3.3 Slit-Imaging Camera

RIMAS will include elongated rectangular field stops located on a wheel, allowing them to be positioned at the telescope focus. These slits provide a variety of dimensions, allowing observers to select the optimal slit for a target given atmospheric conditions. The area surrounding the slit will be mirrored and tilted to reflect the blocked portions of the field into a “slit-imaging” camera. A CAD model of this setup is provided in Figure 3.10.

This camera is essential as it will allow observers to align their spectroscopic

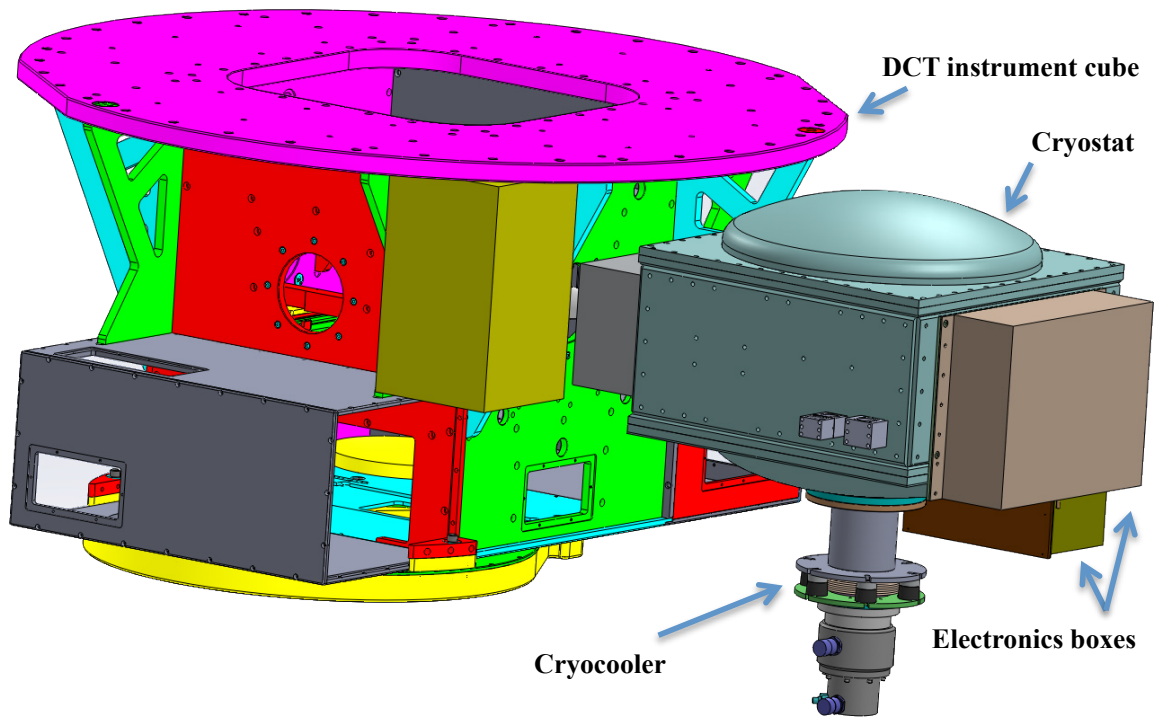


Figure 3.9: A CAD model of RIMAS mounted on the instrument cube. The primary mirror (M1) of DCT is above the instrument cube in this image but not shown.

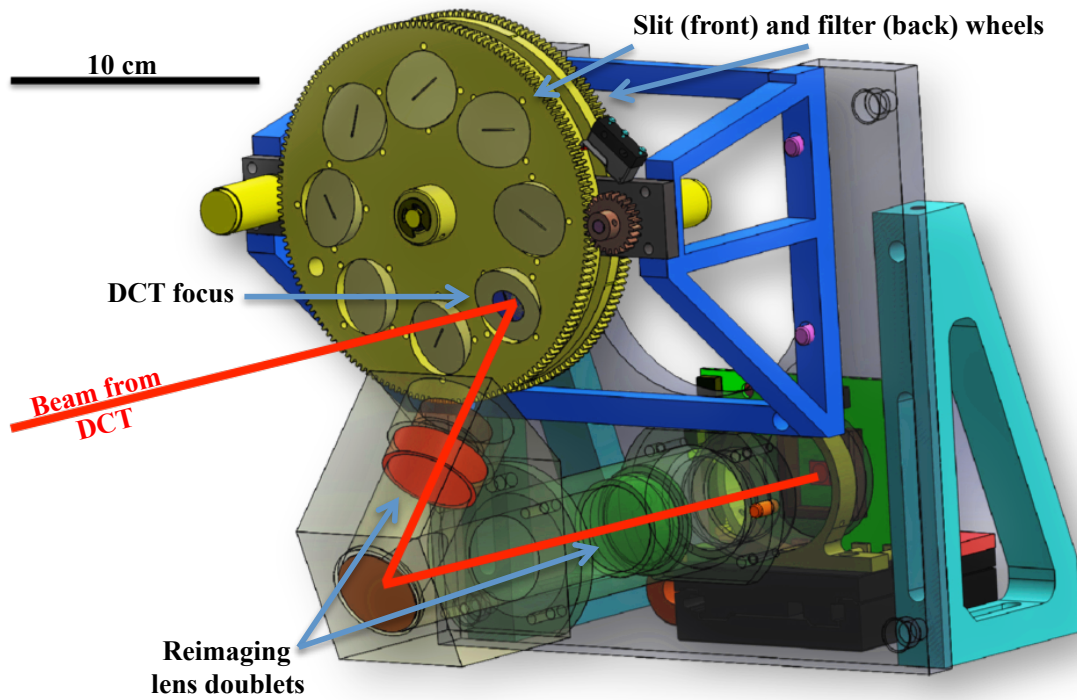


Figure 3.10: The optomechanical design for the “slit-imaging” camera. This assembly is located in the front compartment of the cryostat.

targets with the slit. The design requirements are given in Table 3.1. The image of the 80 arc-second diameter region surrounding the slit will allow observers to see that bright sources are passed through, or to perform blind offsets for fainter sources. This camera can also be used as a guide camera during long exposures.

Table 3.1: Design requirements for the slit-imaging camera.

Wavelength range	$\lambda \approx 1.17 - 2.37 \mu\text{m}$
Operating temperature	$\sim 80K$
Detector	InSb, $\lambda = 0.6 - 5.5 \mu\text{m}$
Pixel pitch	$30 \times 30 \mu\text{m}^2$
Image scale	0.35 arc-seconds / pixel
f-ratio	4.23
FOV	$80 \times 80 \text{ arc-seconds}^2$
Imaging quality	50% ensquared energy in one pixel

3.3.4 Imaging Systems

When RIMAS is configured to acquire images, the slit-wheel will be moved to an open position. Following the telescope’s focus, the full $3 \times 3 \text{ arc} - \text{minute}^2$ diameter beam will be passed into a collimator assembly consisting of five lenses. The collimated beam will then be divided by a dichroic beam splitter ($\lambda_{\text{split}} = 1.4 \mu\text{m}$, $\lambda > \lambda_{\text{split}}$ transmitted, $\lambda < \lambda_{\text{split}}$ reflected). A cold stop is located at the pupil position of each arm following the dichroic. This stop blocks light coming from outside

the primary aperture. Wheels housing photometric filters and dispersive elements are located immediately after the pupils. The beams are then focused by cameras, each consisting of five lenses. The design requirements are given in Table 3.2. A CAD model of the full optomechanical design is shown in Figure 3.11. A second CAD model of the optomechanical assembly of the collimator is shown in Figure 3.12. The camera designs are very similar.

Table 3.2: Design requirements for RIMAS.

Collimator λ_{range}	0.97 - 2.37 μm
YJ-band Camera λ_{range}	0.97 - 1.33 μm
YJ-Detector	HgCdTe, $\lambda = 0.85 - 1.7 \mu\text{m}$
HK-band Camera λ_{range}	1.49 - 2.37 μm
HK-Detector	HgCdTe, $\lambda = 0.85 - 2.5 \mu\text{m}$
Operating temperature	$\sim 80\text{K}$
Pixel pitch	$18 \times 18 \mu\text{m}^2$
Image scale	0.35 arc-seconds / pixel
f-ratio	2.53
FOV	$3 \times 3 \text{ arc-minutes}^2$
Imaging quality	50% ensquared energy in one pixel
Low-R spectroscopy	$R \sim 30$
Moderate-R spectroscopy	$R \sim 4500$

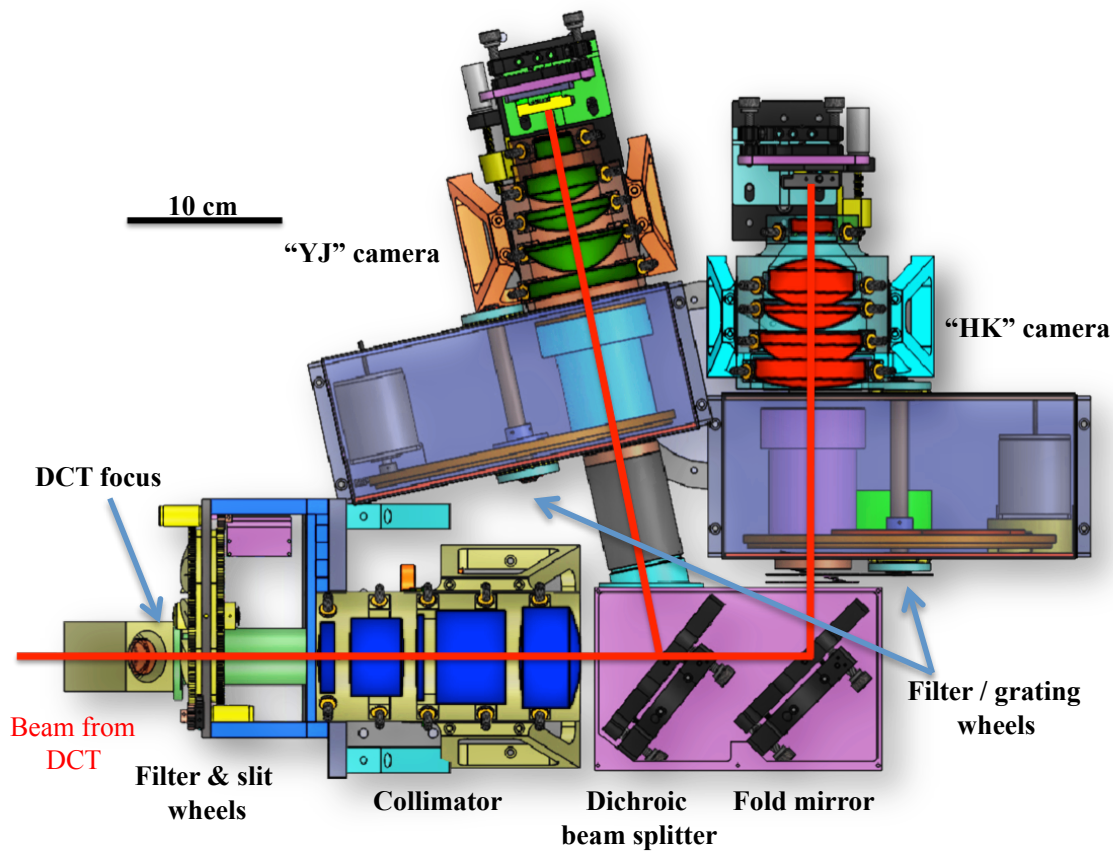


Figure 3.11: An overview of the RIMAS optomechanical design. All of these assemblies are located within the cryostat.

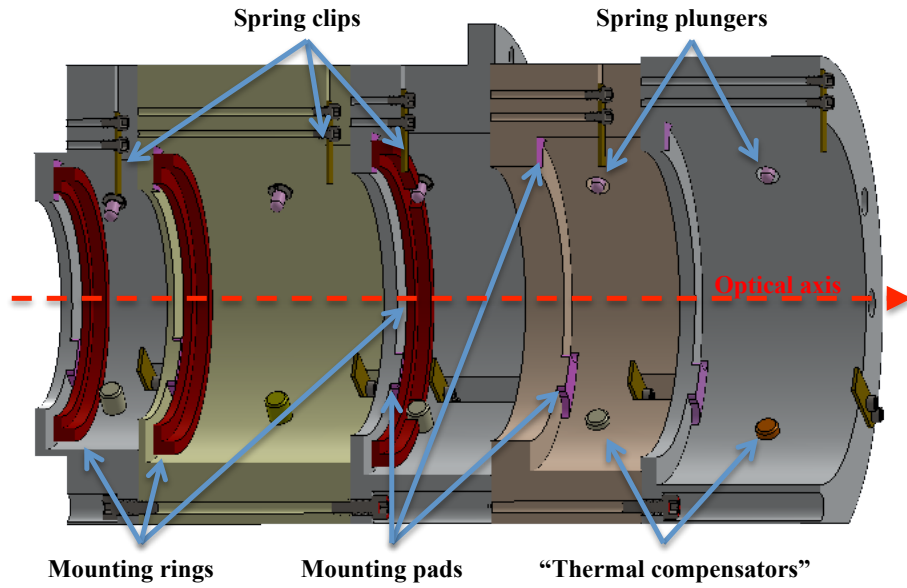


Figure 3.12: A cross section view of the collimator optomechanical design without lenses. The designs for YJ-band and HK-band cameras are very similar. Spring plungers provide $\gtrsim 3$ lbs of force in x and y axes to keep the lenses flush with the “thermal compensators” (see Section 4.2.2.3) which define the aligned position in these axes. Lenses are numbered by order in the optical train (i.e., position along optical axis). Lenses 1, 2, and 3 in the collimator (also several lenses in the cameras) rest on torlon “mounting rings” which provide protection for lenses with convex surfaces where the reference annuli are $\lesssim 3$ mm wide. Spring clips provide the force required to keep each lens’s reference annulus in contact with either the mounting ring or the mounting pads (see Figure 3.8 for description).

3.3.5 Spectroscopic Systems

To use RIMAS as a spectrometer, transmission gratings are placed in the beams by rotating the filter/grating wheels. The small deflection angle of the low-R modes means that a single grating can be used for each. The image spectra will be translated on the focal planes by ~ 2 mm. The higher dispersion modes require a combination of grating prisms (“grisms”) followed by cross-dispersing volume phase holographic (VPH) gratings and prisms to correct for the VPH deflection angles.

Chapter 4: RIMAS: Cryogenic Optics

A majority of my graduate work has been on designing, aligning and characterizing RIMAS’s cryogenic optical systems. As previously discussed in Sections 3.3.3, 3.3.4 and 3.3.5, these systems are divided into a slit-imaging camera and the primary imaging and spectroscopic optics. The former is a simple camera used to image the field surrounding spectroscopic slits, while the latter is composed of a collimator assembly and two cameras, each composed of five lenses. The slit-viewing camera is an original design created as part of this thesis while early designs for the remainder of the optics were contributed by a collaborator (see Table 1 on page iii).

4.1 Slit-Imaging Camera

4.1.1 Requirements

Given that RIMAS is designed to observe high- z GRB afterglows, the slit-imaging camera must also image NIR wavelengths for targets to be detected. If possible, it was desirable that the camera be capable of working out to the InSb detector’s cutoff wavelength of $5.5\mu m$, with focal adjustments. Given the modest purpose of this system, it should have a simple design (i.e., loose design tolerances). For this reason, it should use as few elements as possible with simple optical designs

(i.e., spherical surfaces). Table 3.1 summarizes the basic design requirements for this camera.

4.1.2 Basic Design and Materials Selection

4.1.2.1 Achromatic Doublet

Given that this system needs to re-image the telescope’s focal plane across one or more NIR photometric bands, the simplest design possible would be an achromatic doublet. In this design, the refractive indices of two lenses are selected to minimize chromatic aberration. Chromatic aberration is the wavelength dependence of the focal position resulting from the change in the lens material’s refractive index with wavelength. Materials were selected using the method described by [Ren and Allington-Smith \(1999, hereafter R&A\)](#). R&A shows that the residual chromatic aberration of a doublet is a function of the partial dispersion (P, Equation 4.1) and Abbe number (V, Equation 4.2) of the two materials.

For $\lambda_1 < \lambda_2 < \lambda_3$ with corresponding refractive indices n_1 , n_2 and n_3 ,

$$P \triangleq \frac{n_2 - n_3}{n_1 - n_3} \quad (4.1)$$

$$V \triangleq \frac{n_2 - 1}{n_1 - n_3} \quad (4.2)$$

For a doublet with a given optical power (Φ) R&A find the residual chromatic aberration (∇l),

$$\nabla l = \frac{P_1 - P_2}{V_1 - V_2} \frac{1}{\Phi} \quad (4.3)$$

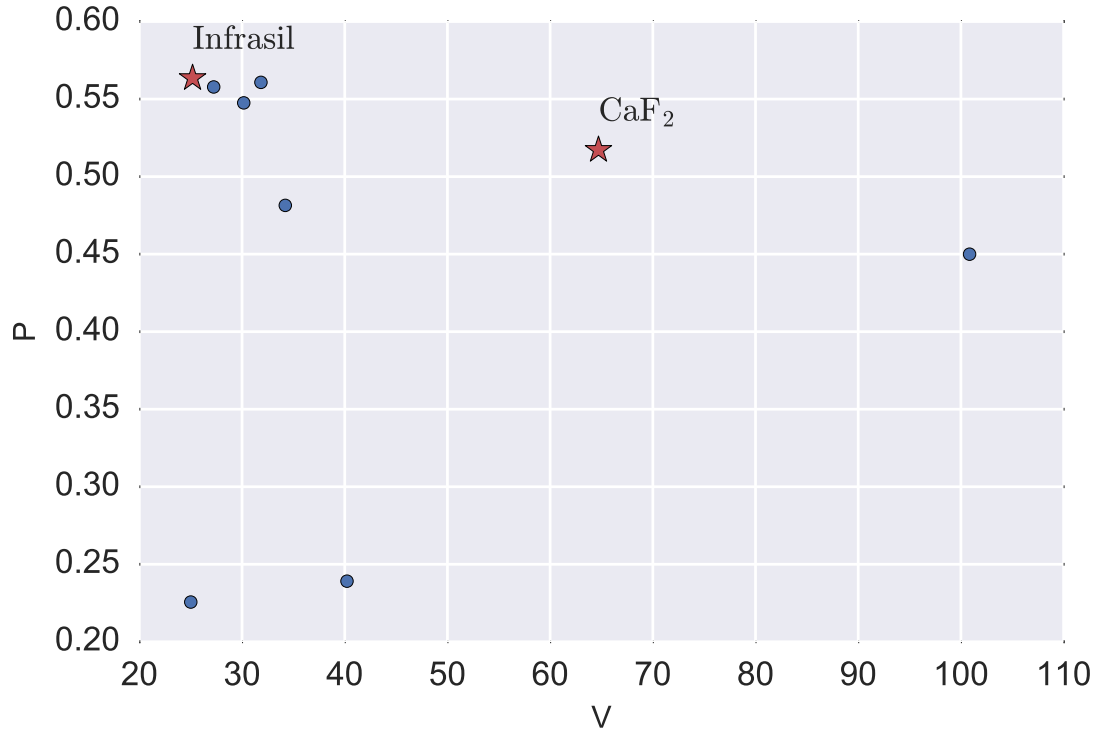


Figure 4.1: This P-V diagram shows potential NIR materials where $\lambda_1 = 1.1 \mu\text{m}$, $\lambda_2 = 1.75 \mu\text{m}$ and $\lambda_3 = 2.4 \mu\text{m}$. Values above are for the design temperature of 80 K calculated using data from the CHARMS papers (Leviton et al., 2005, 2006, 2007a,b). A number of possible combinations were considered as starting points when designing the lens doublets forming the slit-imaging camera. The final design uses Infrasil 301 and CaF_2 , which are highlighted above.

From Equation 4.3, the chromatic aberration can be minimized by selecting lens materials where the difference in partial dispersion is small and difference in Abbe number is large. Only materials transparent at the design wavelengths with measured refractive indices at the design temperature were considered. These materials are plotted in Figure 4.1.

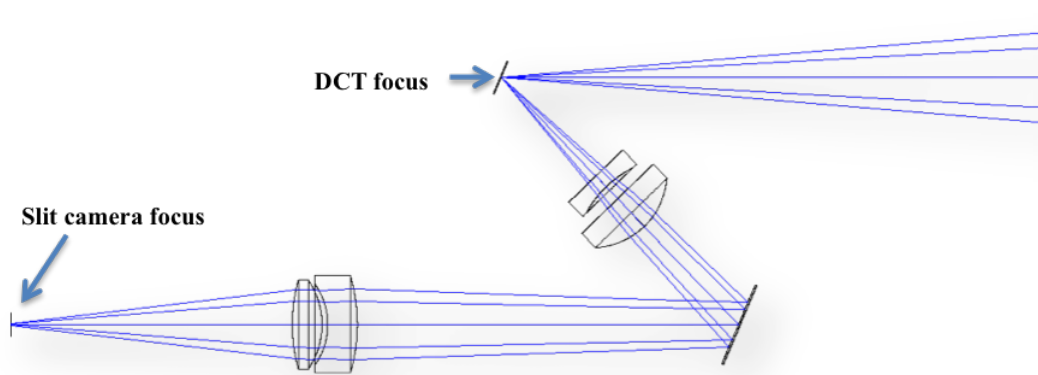


Figure 4.2: The two doublet design used to image the field surrounding spectroscopic slits. All design work was done using the Zemax ray tracing software (<http://www.zemax.com/>).

4.1.2.2 Two doublet design

If this camera were designed without considering the rest of the instrument, it would have been possible to use a single doublet. However, due to mechanical constraints on the position of the focal plane, it was necessary to extend the length traveled by the beam. Given the design value for the plate scale, this necessitated adding a second doublet to the design, as shown in Figure 4.2. The first doublet slows the beam, while the second focuses the beam on the detector. The design was simplified by selecting Infrasil 301 and CaF₂ for both doublets (Figure 4.1).

4.1.3 Tolerancing and Desensitizing

With the preliminary design completed, its sensitivity to imperfect lens fabrication and alignment were determined using a Monte Carlo analysis within Zemax.

Critical design parameters were varied by random values drawn from normal distributions about the nominal values. The standard deviations of these distributions are the “tolerances” of these parameters. Approximate difficulty levels are shown in Table 4.1.

Table 4.1: Typical tolerancing values from [Nelson et al. \(2009\)](#) and [Optimax Systems, Inc. \(2012\)](#). These values were used to estimate the design viability during the desensitizing process.

Parameter	Tolerance Levels		
	Commercial	Precision	High Precision
Refractive index	$\pm 10^{-3}$	$\pm 5 \times 10^{-4}$	material specific
Center thickness	± 0.15 mm	± 0.05 mm	± 0.0025 mm
Radius of curvature	± 2 part per thou.	± 1 part per thou.	± 0.5 part per thou.
Surface irregularity	2 fringes @HeNe	0.5 fringes @HeNe	0.2 fringes @HeNe
Edge thickness difference (wedge)	± 0.05 mm	± 0.01 mm	± 0.005 mm
Axial position / centration align.	± 0.13 mm	± 0.05 mm	± 0.01 mm
Tip/tilt alignment	± 0.91 degrees	± 0.18 degrees	± 0.036 degrees

An iterative re-optimization was performed where the design’s sensitivities to key manufacturing and alignment parameters were reduced. Through this process,

it was possible to reduce tolerances to those shown in Table 4.2.

Table 4.2: The lens manufacturing and alignment tolerances of the desensitized slit-imaging camera design (Capone et al., 2013).

Tolerancing Parameter	Typical Final Design Sensitivity
Refractive indices	$> 10^{-3}$
Radii of curvature	± 23 parts per thousand
Center thickness	$\pm 225 \mu m$
Edge thickness difference (i.e., wedge)	$\pm 88 \mu m$
RMS Surface irregularity	2.5 fringes @632.8 nm
Axial position and centration alignment	$\pm 190 \mu m$
Tip/tilt alignment	± 0.1 degrees

4.1.4 Optomechanics and Thermal Modeling

With a complete cryogenic optical design, the next step was to model the system at room temperature to fabricate the components. Data were available for all lens materials on rates of thermal contraction and changes in refractive indices (Tables 4.3 – 4.6). Using this information, I wrote a custom Python script to calculate changes to all affected design parameters and create a model of the system at room temperature.

With the slit imaging camera design modeled at room temperature, fabrication drawings were prepared.

Table 4.3: The relative change between room temperature and the operating temperature of the refractive indices of materials used for optics in RIMAS. Values are averaged over $0.97 - 2.37 \mu\text{m}$. The stated uncertainties are the standard deviation of values over this range.

Material	$\frac{n_{293\text{K}} - n_{80\text{K}}}{n_{293\text{K}}} \times 10^5$	Source
Infrasil 301	86.8 ± 0.3	Leviton et al. (2007a)
CaF ₂	-126.8 ± 0.4	Leviton et al. (2007a)
BaF ₂	-186.5 ± 0.3	Leviton et al. (2005)
ZnSe	520 ± 19	Leviton et al. (2005)
SF15	-7 ± 1	Leviton et al. (2007b)
E-SF03	-46 ± 1	Leviton et al. (2007b)

4.1.5 Room Temperature Alignment

Given the loose alignment tolerances (Table 4.2), it was possible to align the lenses of each doublet relative to the optomechanical assembly using a microscope. The distances from the lens edge to the mount were measured at multiple positions to determine the centration. An example of how a single measurement was taken is provided in Figure 4.3. Given a microscope scale of $\sim 1\mu\text{m} / \text{pixel}$, the alignment errors were dominated by how well the edges of the lens and mount could be identified. The repeatability of the measurements was found to be within a few pixels so that the overall uncertainty of the final position was $< 20\mu\text{m}$.

Table 4.4: Thermal contraction measurements of metal alloys used in RIMAS’s optomechanical assemblies.

Material	$\frac{L_{293\text{ K}} - L_{80\text{ K}}}{L_{293\text{ K}}} \times 10^5$	Source
Aluminium 6061	393	Arp et al. (1962)
Stainless Steel – AISI 302	296	Arp et al. (1962)
Brass 7030	337	Arp et al. (1962)

4.1.6 Evaluation

It was determined based on the room temperature and cryogenic ray tracing models of this simple camera that the performance does not change significantly with temperature. For this reason, the point spread function (PSF) was measured at room temperature. Figure 4.4 compares the slit-imaging camera performance with on-sky data taken using DCT-LMI. The camera meets the design requirement, and more importantly it is limited by atmospheric seeing even in the best observed conditions of ~ 0.5 arc-seconds FWHM.

4.2 Imaging Systems

The imaging systems in RIMAS re-image the telescope focal plane with the F-ratio set for the required plate-scale. The beam is divided into two optical arms by a dichroic beamsplitter, with short wavelengths ($\lambda \lesssim 1.4\ \mu\text{m}$) reflected and long wavelengths ($\lambda \gtrsim 1.4\ \mu\text{m}$) transmitted.

Table 4.5: Thermal contraction measurements of optical materials used as substrates for RIMAS’s lenses and gratings. The value for fused silica is not for Infrasil 301 (they variety used in RIMAS), but is meant only to show that thermal contraction is minimal for this type of material. Thermal contraction data were not available for S-TIH53, so data for a similar material, SF6, was scaled to match the room temperature curve.

Material	$\frac{L_{293\text{ K}} - L_{80\text{ K}}}{L_{293\text{ K}}} \times 10^5$	Source
Fused Silica (Infrasil 301)	-1	Corruccini and Gniewek (1961)
CaF ₂	309	Feldman et al. (1978)
BaF ₂	328	Feldman et al. (1978)
ZnSe	123	Browder and Ballard (1969)
SF6 (S-TIH53)	148	NOAO

4.2.1 Tolerancing and Desensitizing

Before attempting to implement a design, the sensitivities of the system to imperfections needed to be determined. This tolerancing analysis can be subdivided into analyses for contributions from manufacturing the optics, from the optomechanical alignment, and from other considerations such as vibrations from the cryocooler. Each analysis began by considering what parameters were expected to dominate. Then a tolerancing function was built in Zemax. Within this software, a sensitivity analysis was first done where all parameters are changed to their minimum and

Table 4.6: Thermal contraction measurements of plastics used in optomechanical designs in RIMAS.

Material	$\frac{L_{293\text{ K}} - L_{80\text{ K}}}{L_{293\text{ K}}} \times 10^5$	Source
Delrin (POM)	1383	Schwarz (1988)
Teflon (TFE)	1930	Kirby (1956)
Plexiglas (PMMA)	1050	Laquer and Head (1952)
Torlon 4203	387	Ventura et al. (1999)
Vespel SP-22	558	Swift and Packard (1979)

maximum perturbed values to determine the most sensitive parameters. Typical tolerances for the three assemblies are provided in Table 4.7. Monte Carlo simulations were run to estimate the compliance of the final system’s performance. All toleranced parameters were selected from normal distributions centered on the nominal value with the tolerance as the width. Additionally, a tolerancing analysis done by Optical Support, Inc. during an independent review found similar tolerances ([Trissel and Piccirillo, 2012](#)).

4.2.2 Thermal Modeling for Fabrication

The same script was used to “warm” the Zemax designs to room temperature as was used for the slit-imaging camera in Section 4.1.4. The calculations were done in the same way, using cryogenic thermal contraction data to predict the change in radii of curvature, aspherical terms with units of length, center thicknesses and

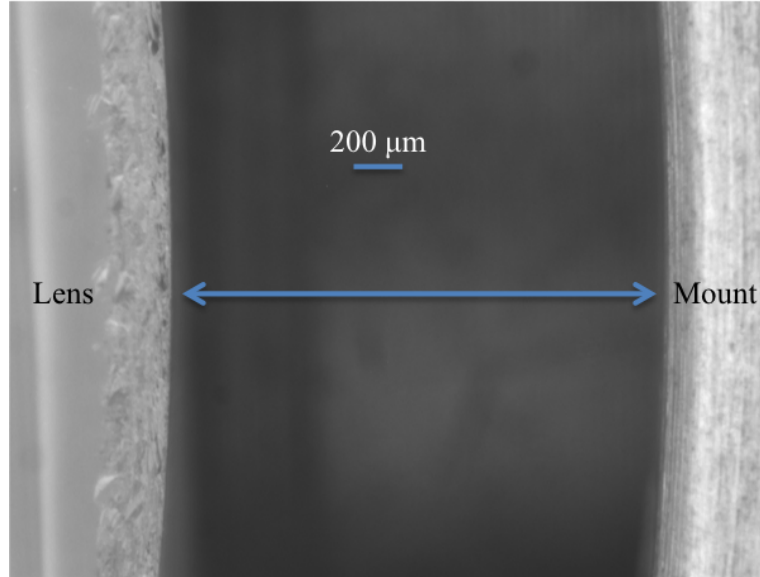


Figure 4.3: The centration of each lens was determined by measuring the distance from the edge of the lens to the edge of the mount. Each lens was translated in the axes perpendicular to the optical axis.

optomechanical positioning. Refractive indices were calculated using data from the literature (Leviton et al., 2005, 2006, 2007a,b). The resulting models were useful not only for fabrication, but also helped in verifying the alignment of these systems before cooling to cryogenic temperatures.

4.2.2.1 Optics

As described in Section 3.3.4, the primary optical systems include a collimator and two cameras. Each assembly uses five lenses to convert the beam between a given focal ratio ($f/6.1$ from telescope, $f/2.53$ for the cameras) and collimation over the required bandpass. The increased complexity of these systems required a wider range of potential materials than were identified for the slit-viewing camera. The

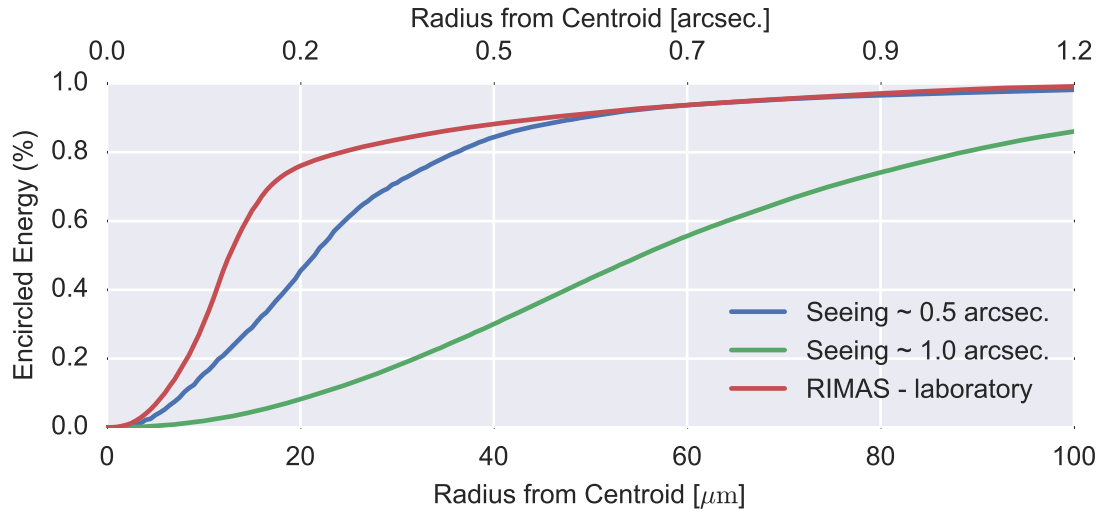


Figure 4.4: The performance of the guide camera measured in the laboratory is seeing-limited. In this instance a $10 \mu\text{m}$ diameter pinhole was illuminated with a red LED. The camera demagnifies the image at DCT’s focal plane by a factor of 0.69, so the final image of the pinhole is $\sim 7 \mu\text{m}$ in diameter. The numerical aperture of the pinhole light source was not set to that of the telescope, so the tail in the above plot is likely overrepresented. The ray tracing model predicts that the performance of the camera focused for $\sim 0.6\text{--}0.7 \mu\text{m}$ is representative of the NIR performance. These measurements were made at room temperature using a CCD, which is expected to be representative of the cryogenic performance based on the optical model.

Table 4.7: Typical lens manufacturing and alignment tolerances for the collimator and the YJ-band and HK-band cameras.

Tolerancing Parameter	Typical Final Design Sensitivity
Refractive indices	$\sim 10^{-3}$
Radii of curvature	± 3 parts per thousand
Center thickness	$\pm 70 \mu\text{m}$
Edge thickness difference (i.e., wedge)	$\pm 25 \mu\text{m}$
Surface irregularity	4 fringes @632.8 nm
Axial position and centration alignment	$\pm 25 \mu\text{m}$
Tip/tilt alignment	± 0.02 degrees

original design called for a Hikari glass, E-SF03, however this material was no longer in production. A similar material, S-TIH53, was identified to replace E-SF03 for the #4 collimator lens.

Given a lack of cryogenic measurements for S-TIH53, cryogenic properties were estimated from similar materials. The thermal expansion curve of Schott's SF6 glass was scaled to the room temperature value for S-TIH53 (Table 4.5). Data available on the cryogenic refractive indices of E-SF03 suggested that the lens is insensitive to the change in S-TIH53's refractive indices between 293 K and 80 K (see Tables 4.3 and 4.7).

4.2.2.2 Optomechanical Assemblies

The design for the slit-imaging camera was sufficiently simple as to be insensitive to alignment errors at the level of those introduced by thermal contraction, however the same is not true for the primary optical systems. This problem has been addressed by other projects in the past in a variety of ways.

Mimir, a NIR imager and spectrometer similar to RIMAS, used cryogenic thermal contraction data on the lens mount material to predict the translation offsets introduced between room temperature and the operating temperature ([Clemens et al., 2007](#)). The mounts were fabricated so that the lenses would shift into the optimal alignment as the system cooled. This method provides an attractive simplicity when aligning lenses, however if problems are discovered in the alignment, the process is complicated by the lack of adjustment screws. Additionally, the systems will have optical aberrations at room temperatures introduced by translation offsets between the lens axes and the system's optical axis, preventing the alignment from being verified without cooling the system. The cooling process takes $\gtrsim 1$ day since cooling lenses quickly will create a temperature gradient and cause them to shatter. This is particularly true for lenses made of CaF_2 and BaF_2 .

Other projects, including NIRCAM and HARMONI, use self-centering designs in which radially mounted flexures maintain the lens axis alignment relative to the system's optical axis ([Kvamme et al., 2005](#); [Allen et al., 2014](#)). This is an attractive option since it does not rely on offset predictions and it allows alignment testing at room temperature. Given the relatively modest requirements of RIMAS, however,

this approach was determined to be too complex ([Kutyrev et al., 2012](#)).

The final method often used in cryogenic systems is to match the thermal contraction of different materials. This is usually done for mechanical reasons, such as reducing strain, however the same idea method can be used for optomechanical designs. This is the design approach described in Section [4.2.2.3](#).

4.2.2.3 Thermal Compensating Design

To prevent lens axes from translating relative to the optical axis as the system cools, lengths of materials with a very high rate of thermal contraction (“thermal-compensators”) are positioned between the lens mount’s translation screws and the lens, as depicted in [Figure 4.5](#). In the case where no compensating material is used, the predicted translation of a lens in an aluminum mount is given by [Equation 4.4](#). This design has been successfully used by other NIR instruments (e.g., [Clemens et al., 2007](#)), but it does not permit room temperature testing of the optical alignment.

$$\Lambda(T) \triangleq \frac{L_{293K} - L(T)}{L_{293K}}$$

$$\Delta L_{Lens} = L_{Lens} \Lambda_{Lens}(T)$$

$$\Delta L_{Al} = (L_{Lens}) \Lambda_{Al}(T)$$

$$\rightarrow \Delta L_{offset} = L_{Lens} (\Lambda_{Lens}(T) - \Lambda_{Al}(T)) \quad (4.4)$$

Since the mounts are all made of Aluminum 6061 (hereafter Al), only materials

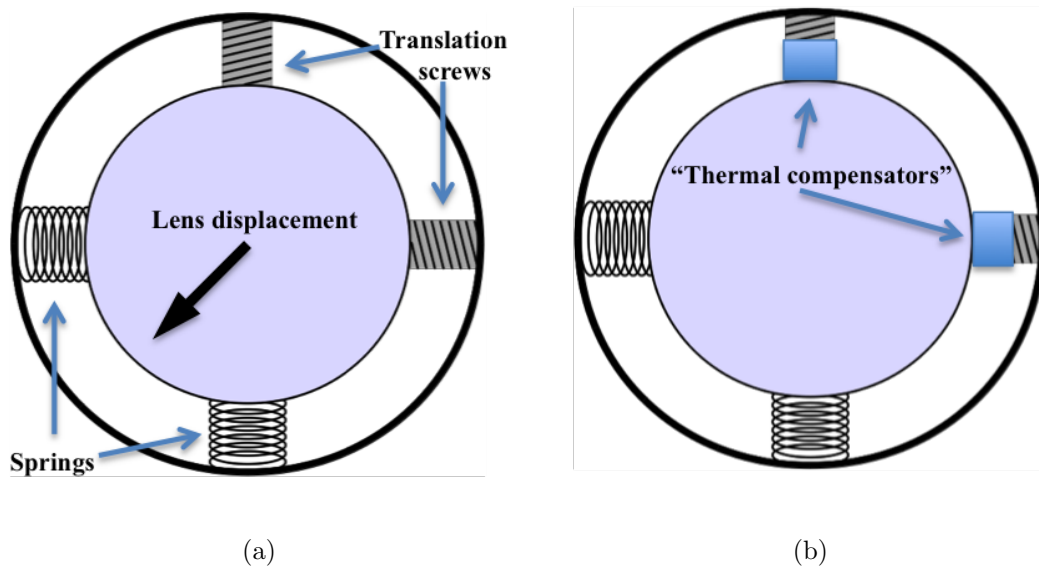


Figure 4.5: Two schematic drawings of optomechanical designs. (a) shows a design where screws are used to translate the lens in the axes perpendicular to the optical axis. When the system is cooled, the aluminum mount will contract by more than the lens causing a translation away from the aligned position as indicated by the black arrow. (b) shows the same design with the addition of “thermal-compensators”. These are lengths of materials which contract by more than the aluminum frames as the system cools. The length of this material is set so that the average radial contraction is equal to that of the aluminum mount (see Equation 4.5).

with a greater fractional decrease in length between room temperature ($T_{\text{hot}} \sim 293$ K) and the cryogenic temperature ($T_{\text{cold}} \sim 60\text{-}80$ K) are candidates. For a lens of length L at T_{hot} and a fractional change in length of Λ between T_{hot} and T_{cold} , the required length of a given compensating material is given by Equation 4.5.

$$\Delta L_{\text{Lens+Comp.}} = L_{\text{Lens}}\Lambda_{\text{Lens}}(T) + L_{\text{Comp.}}\Lambda_{\text{Comp.}}(T)$$

$$\Delta L_{\text{Al}} = (L_{\text{Lens}} + L_{\text{Comp.}})\Lambda_{\text{Al}}(T)$$

$$\Delta L_{\text{Lens+Comp.}} \triangleq \Delta L_{\text{Al}}$$

$$\rightarrow L_{\text{Comp.}} = L_{\text{Lens}} \frac{\Lambda_{\text{Lens}}(T) - \Lambda_{\text{Al}}(T)}{\Lambda_{\text{Al}}(T) - \Lambda_{\text{Comp.}}(T)} \quad (4.5)$$

The manufacturing tolerances of the thermal-compensators are determined by calculating the expected offsets for an incorrect length and comparing these with the optical alignment tolerances. The offset for a fabrication error of $L_{\text{Err.}}$ is found using Equation 4.6.

$$\Delta L_{\text{Lens+Comp.}} = L_{\text{Lens}}\Lambda_{\text{Lens}}(T) + (L_{\text{Comp.}} - L_{\text{Err.}})\Lambda_{\text{Comp.}}(T)$$

$$\Delta L_{\text{Al}} = (L_{\text{Lens}} + L_{\text{Comp.}} - L_{\text{Err.}})\Lambda_{\text{Al}}(T)$$

$$\rightarrow \Delta L_{\text{offset}} = L_{\text{Lens}}(\Lambda_{\text{Lens}}(T) - \Lambda_{\text{Al}}(T)) + (L_{\text{Comp.}} - L_{\text{Err.}})(\Lambda_{\text{Comp.}}(T) - \Lambda_{\text{Al}}(T)) \quad (4.6)$$

Similarly, if the expected fractional change in the length of the compensator is inaccurate, the introduced offset is given by Equation 4.7.

$$\begin{aligned}\Delta L_{Lens+Comp.} &= L_{Lens}\Lambda_{Lens}(T) + L_{Comp.}\Lambda_{Comp.}(T)\Lambda_{Err.}(T) \\ \Delta L_{Al} &= (L_{Lens} + L_{Comp.})\Lambda_{Al}(T)\end{aligned}$$

$$\begin{aligned}\rightarrow \Delta L_{offset} &= L_{Lens}(\Lambda_{Lens}(T) - \Lambda_{Al}(T)) + L_{Comp.}(\Lambda_{Comp.}(T)\Lambda_{Err.}(T) - \Lambda_{Al}(T))\end{aligned}\tag{4.7}$$

All but five of the 15 lenses in the collimator and camera would be translated by more than their maximum tolerated value between T_{hot} and T_{cold} without thermal-compensators. Delrin and Vespel SP-22, both manufactured by DuPont, were selected from the many candidate materials for their fractional contraction at T_{cold} , their common usage at cryogenic temperatures, and their mechanical resilience. Two materials were required to satisfy Equation 4.5 for the range of lens materials and sizes while keeping the compensator lengths between 6 mm and 25 mm for 6 mm diameter cylinders. This range of acceptable compensator lengths was intended to prevent jamming and warping.

4.2.3 Metrology and Re-optimization

Some metrology data were provided by the manufacturer of the lenses, however these data were lacking. In several cases, the reports stated that lens parameters were out of compliance with the quoted tolerances. To determine whether these man-

ufacturing errors were acceptable, measurements were taken by the Optics Branch (Code 552) at NASA GSFC. They were able to provide three-dimensional point data on lens surfaces measured with a coordinate measuring machine (CMM). The stated uncertainties in each axis (x, y and z) were $\sim 1 \mu\text{m}$.

These data were fit with the various design functions. In most cases, it was possible to constrain all key lens parameters to the level of the quoted tolerance or better. The sole exception was the # 1 HK-band camera lens. In this case, it was not possible to confidently constrain the polynomial aspheric terms. However it was possible to determine that this lens was out of compliance on these terms. The results of this analysis were summarized in an internal report included as Appendix [A](#).

The results of these fits were used to inform the alignment process by re-optimizing the design in Zemax with the lenses altered to reflect the fabricated optics. Fitted radii of curvature, conic terms, center thickness and lens wedge were included in the updated model. Lenses were permitted to translate by small distances ($< 1 \text{ mm}$) in x, y and z. Additionally, each lens was allowed to rotate about the optical axis (“clocking”). This allowed the wedge of one lens to compensate for the wedge of another. The end result of this process was to produce a design capable of achieving near-diffraction limited performance if perfectly aligned.

Since the time of this work, the alignment process has shown that at least one lens (HK-band camera lens #2) may have moved between the CMM measurement of one lens side and the other. This appears as a coordinate shift in x, y and possibly z.

4.2.4 Room Temperature Assembly and Alignment

4.2.4.1 Microscope Alignment

The same procedure was initially followed for all 15 lenses in the collimator, YJ-band camera, and HK-band camera. A lens was lowered into the corresponding mount using a suction tool. The lens was released when the reference annulus was resting on either the torlon mounting ring, or the teflon tape on the mounting pads (see Figures 3.8 and 3.12 for layout and definitions). The lens was then centered by eye using the translation adjustment screws.

Each lens was set to the optimal position as determined by the Zemax model using the same procedure described in Section 4.1.5. Images were taken at multiple positions around the circumference of the lens in which both the edge of the lens and the edge of the mount were visible. By measuring distances between the edge of the lens and the edge of the mount in these frames, it was possible to calculate the position of the lens axis to $\sim \pm 10 \mu\text{m}$.

Given the number of lenses to be aligned, I attempted to simplify the process. The microscope was mounted on a precision ($\sim 25 \mu\text{m}$ positioning repeatability) translation stage and a custom LabVIEW Virtual Instrument (VI) was written to quickly move the microscope between different focus positions.

Once a lens was measured to be in alignment, the spring clips were attached to keep the lens flush with the mounting ring or pads. With these clips tightened, the microscope was used to verify that the lens was still positioned correctly.

4.2.4.2 HK-band Camera Alignment

One of the HK-band camera lenses (lens # 1) was determined to have been fabricated unacceptably out of compliance. A second lens (lens # 3) had damage within the clear aperture. Replacements were procured for both of these lenses, but the precise CMM surface metrology obtained for the original lenses was not available for these. Additionally, there appeared to be an inconsistency in the measurements taken for a third lens (lens # 2). For this lens, the CMM data suggested a very large wedge between the two lens surfaces. Since both surfaces of this lens are spherical, this appears as a ~ 1.2 mm offset perpendicular to the lens axis between the two optical surfaces.

Due to the longer operating wavelengths of the HK-band camera, the alignment tolerances are tighter than any of the other assemblies. This, combined with a lack of complete metrology for 3 out of 5 lenses, meant that the microscope alignment would only work if the lens sag apex positions all coincided with the mechanical centers of these lenses. For this reason, a different alignment method is required. Efforts are ongoing at NASA-GSFC (Table 1).

4.2.5 Room Temperature Testing

Since the collimator and YJ-camera operate at wavelengths shorter than the silicon energy gap (1.14 eV $\rightarrow 1.09$ μm at 273 K), it was possible to quickly test their alignment by measuring the PSF at room temperature. A 10 μm diameter pinhole was illuminated by a 1050 nm LED. A circular aperture was inserted between the

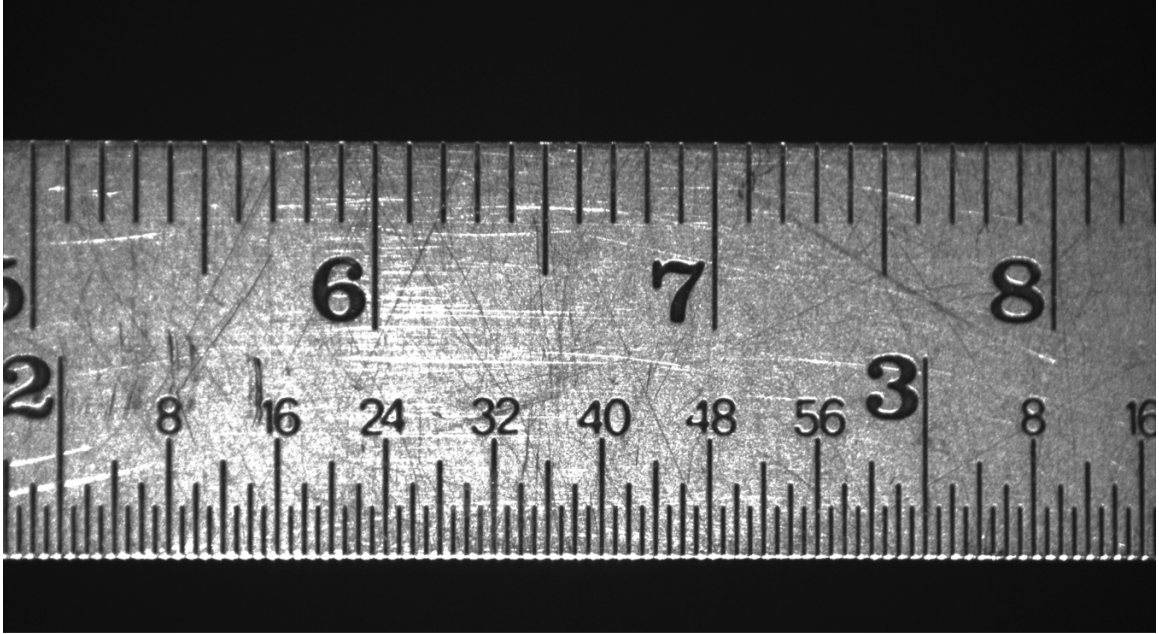


Figure 4.6: The first image taken with the collimator and YJ-band camera. The imaged ruler was illuminated by a 1050 nm LED. This image verified that the system’s demagnification is consistent with the design value of 2.43

LED and the pinhole to set the f /ratio of the light source. To ensure the aperture was uniformly illuminated, a diffuser was placed between the LED and the aperture. This setup was used for all room temperature and cryogenic PSF measurements. Although the room temperature performance was expected to suffer due to the thermal expansion of the lens holder and lenses as well as the changes in refractive indices, any significant asymmetries would have been apparent. The first image ever taken with the collimator and YJ-band camera is shown in Figure 4.6.

It was recently determined by [Toy and Kuttyrev \(2016\)](#) that similar tests are possible for the HK-band camera using a H2RG detector at room temperature. This unexpected behavior is far from perfect, as the resulting PSFs are noisy, but allows

for large scale misalignments to be detected.

4.2.6 Cryogenic Verification of Imaging Performance

Room temperature measurements are useful for detecting significant problems, however characterizing the system requires measurements at the operating temperature of ~ 80 K. The same illumination source used for the room temperature tests was mounted outside of the cryostat on a 3-axis translation stage.

Once the optical assemblies and detector reached their final temperatures, frames were acquired to determine the optimal focus. The measured PSF was used to calculate the radially encircled energy (EE) from the centroid. The EE calculations make the conservative assumption that energy is uniformly distributed within a pixel. Results assuming a Gaussian energy distribution produce similar results. The performance of the final collimator plus YJ-band camera is plotted in Figure 4.7. This plot compares the laboratory RIMAS measurements with measured DCT PSFs to demonstrate that the system is seeing limited.

4.3 Spectroscopic Systems

4.3.1 Design Selection

RIMAS must use the same cameras for both imaging and spectroscopic modes. For the low resolution modes ($R \sim 30$) the deflection angles as determined by the grating equation are small enough that the first diffraction order of any transmission grating will only be offset by ~ 1 mm.

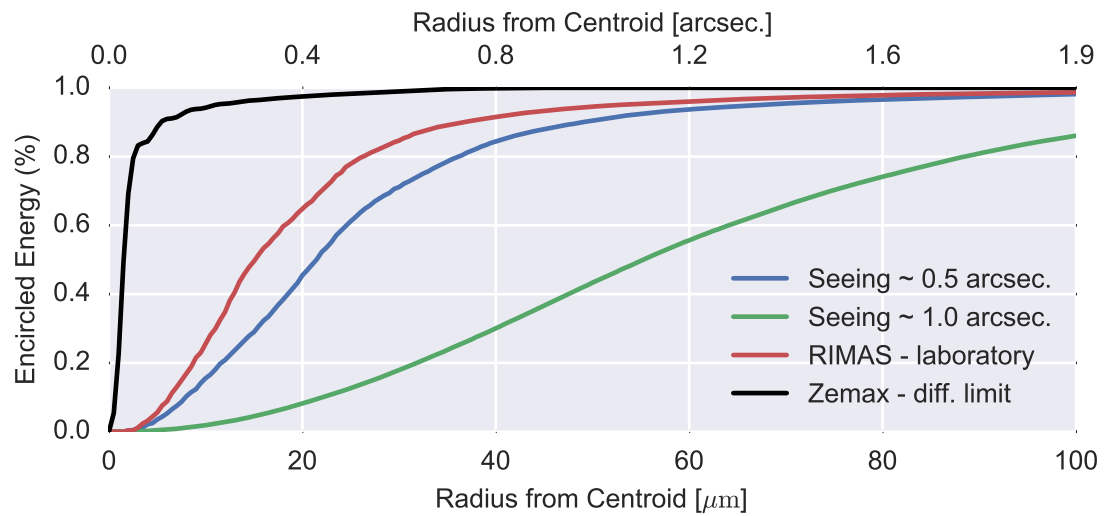


Figure 4.7: The EE of the collimator and YJ-band camera compared with the diffraction limit calculated by Zemax and measured DCT profiles for average seeing (~ 1 arc-second) and the best observed seeing (~ 0.5 arc-seconds). It should be noted that the system was designed to satisfy the Nyquist sampling condition for $18 \mu\text{m}$ pixels while being limited by atmospheric seeing.

However, the same is not true for the moderate resolution modes ($R \sim 4500$). These gratings must operate in multiple diffractive orders to achieve the required spectral resolving power as well as the required spectral coverage. This in turn means that a second, cross-dispersing grating must be used to prevent adjacent diffractive orders from overlapping. In summary, these modes require multi-order operation where the desired diffractive orders are transmitted nearly on-axis.

The best basic grating design given these requirements is a grating-prism (“grism”) operating in an Echelle mode. Grism angles are defined as shown in Figure 4.8. To achieve $R \sim 4500$, RIMAS’s grisms require a high index of refraction (n) and large prism apex angles (ϕ , $m\lambda = d(n - 1)\sin\phi$). The YJ-band grism will be made of ZnSe ($n \gtrsim 2.4$) with a prism angle of 43.075° and a grating period (Λ) of $40 \mu\text{m}$. The HK-band grism will also be made of ZnSe with a prism angle of 43.075° and a grating period of $50 \mu\text{m}$. The collimated beam is 40 mm in diameter near the pupil position for both optical arms.

4.3.2 Grism Efficiency Modeling

Early on scalar calculations were attempted, however they produced unreasonably low efficiency estimates. These calculations, described by [Loewen and Popov \(1997\)](#) and others, are usually valid when the grating period (Λ) $\gg \lambda$. The inaccuracy is likely due to the extremely deep groove profiles required for RIMAS’s grisms. Instead, the semi-analytical rigorous coupled-wave analysis (RCWA) was used to confirm that the designs were optimal and the predicted performance reasonable.

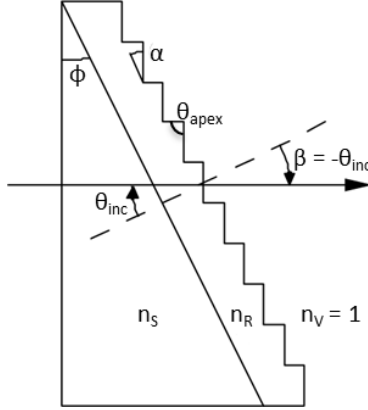


Figure 4.8: This drawing of a grism is taken from page 195 of [Palmer et al. \(2005\)](#). RIMAS’s grism will be ruled directly into ZnSe prisms so that $n_s = n_R$. α is the blaze angle, θ_{inc} is the incident angle with respect to the grating plane, ϕ is the prism’s apex angle and θ_{apex} is the apex angle of the blazes profile (nominally, $\alpha = \theta_{inc} = \phi$ and $\theta_{apex} = 90^\circ$).

4.3.2.1 RCWA-1D Testing

Computational methods solving Maxwell’s equations in the partial differential form have been used to successfully model Echelle grisms since the early 1990s when quadruple-precision representations became available ([Nevière, 1992](#)). Over twenty years later, there are numerous software packages capable of calculating diffraction order efficiencies for semi-infinite, periodic optics.

One such option, RCWA-1D, is built on the MATLAB environment (<https://sourceforge.net/projects/rcwa-1d/>). RCWA-1D can use either the numerically stable scattering matrices (S-matrix method) or transfer matrices (T-matrix method). The T-matrix approach combines field amplitudes at the top and bottom of a numerical layer. This approach is useful for designing anti-reflection coatings, but numerical instabilities arise in the layered “staircase” representation of a

grating's periodic structure. Alternatively, the S-matrix approach combines field amplitudes going into and out of a given layer. The latter type of calculation avoids the exponentially increasing/decreasing modes which lead to numerical instabilities. Since all of RIMAS's diffractive optics are periodic in a single dimension and RCWA-1D offers both transparency and flexibility as open-source software, the calculations were attempted using this package.

In recent years, numerous groups set out to model grisms operating in the first or second diffractive orders. To test the performance of RCWA-1D, calculations were repeated for scenarios as similar as available to those found in RIMAS.

OSMOS: Grism efficiency models generated using GSolver, a stand-alone RCWA software package, were found at <http://www.astronomy.ohio-state.edu/~stoll/OSMOS/Dispersers/grisms.htm>. These models were created for the Ohio-State Multi-Object Spectrograph (OSMOS) (Stoll et al., 2010). A comparison for the first diffractive order of the 54-810R grism is shown in Figure 4.9. Both the scalar and RCWA-1D calculations closely match the GSolver model found online.

LMIRcam: Grism models used to design LMIRcam optics were extracted from Figure 1 of Kuzmenko et al. (2012). These curves were calculated for order 1 of grism 1 and orders 1 and 2 of grism 2. The calculations were repeated using GSolver, RCWA-1D and the scalar code. The results are shown in Figure 4.10. The slight offsets in the curves could be due to slight differences in how the models were initialized. As suggested by Loewen and Popov (1997), the scalar calculations produce results unrealistically close to the Fresnel limit. For this particular exam-

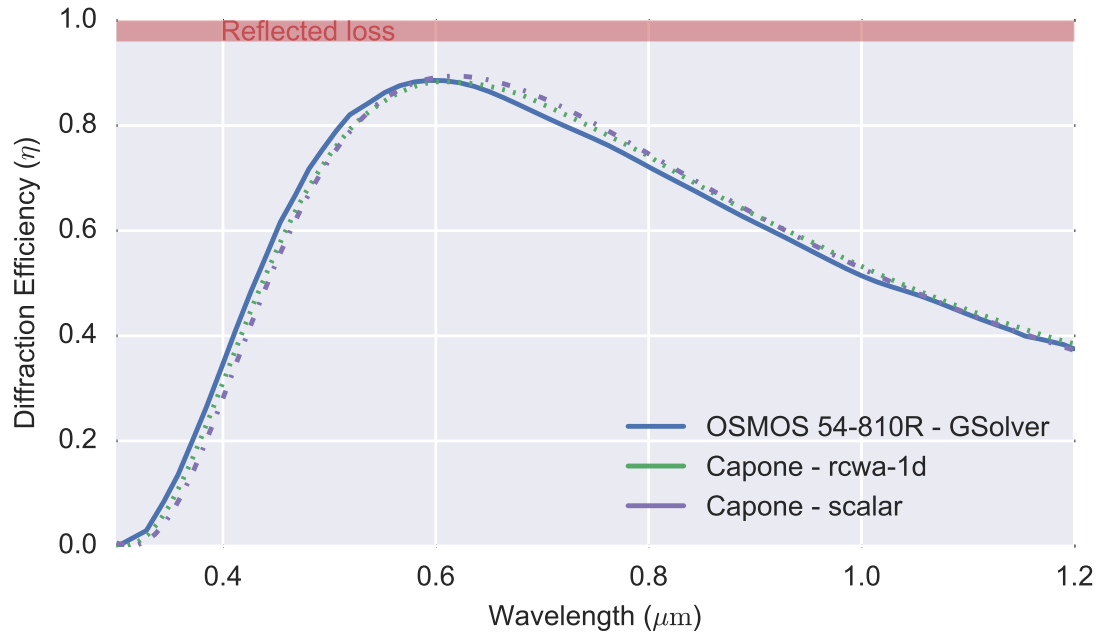


Figure 4.9: A comparison of scalar and RCWA-1D diffraction efficiency calculations with those of GSolver. The GSolver curve was extracted from a plot found at <http://www.astronomy.ohio-state.edu/~stoll/OSMOS/Dispersers/grisms.htm>. The grism has 150 lines/mm ($\Lambda = 6.7 \mu\text{m}$) and $\phi = \alpha = 10.8^\circ$. All models are calculated for a constant refractive index of 1.5.

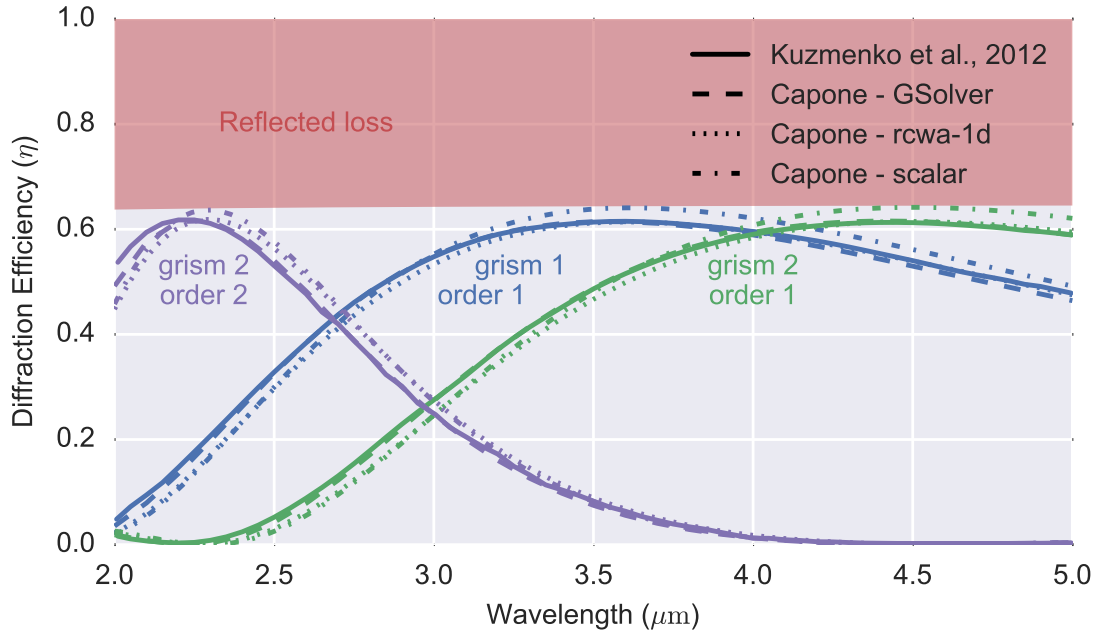


Figure 4.10: The solid curve shows GSolver calculations presented in [Kuzmenko et al. \(2012\)](#). Grism 1 has 40 lines/mm ($\Lambda = 25 \mu\text{m}$) while grism 2 has 32 lines/mm ($\Lambda = 31.25 \mu\text{m}$). Both gratings have $\phi = \alpha = 2.8^\circ$ and $n = n_{\text{Ge}}(\lambda, T = 80\text{K})$.

ple, however, these models produce results so similar that it would be challenging to determine which is most accurate experimentally due to fabrication errors.

4.3.2.2 RIMAS Grism Efficiency Modeling and Optimization

Having validated the agreement between RCWA-1D and GSolver, the former was selected to model RIMAS's grism for its improved flexibility and transparency. To confirm that the nominal grism design ($\theta = \phi$, $\theta_{\text{apex}} = 90^\circ$) was optimal, ϕ and θ_{apex} were each varied in turn. Figure 4.11 shows that for small changes in α , the blazed wavelength (λ_{B}) changes while the amplitude of the order's efficiency remains

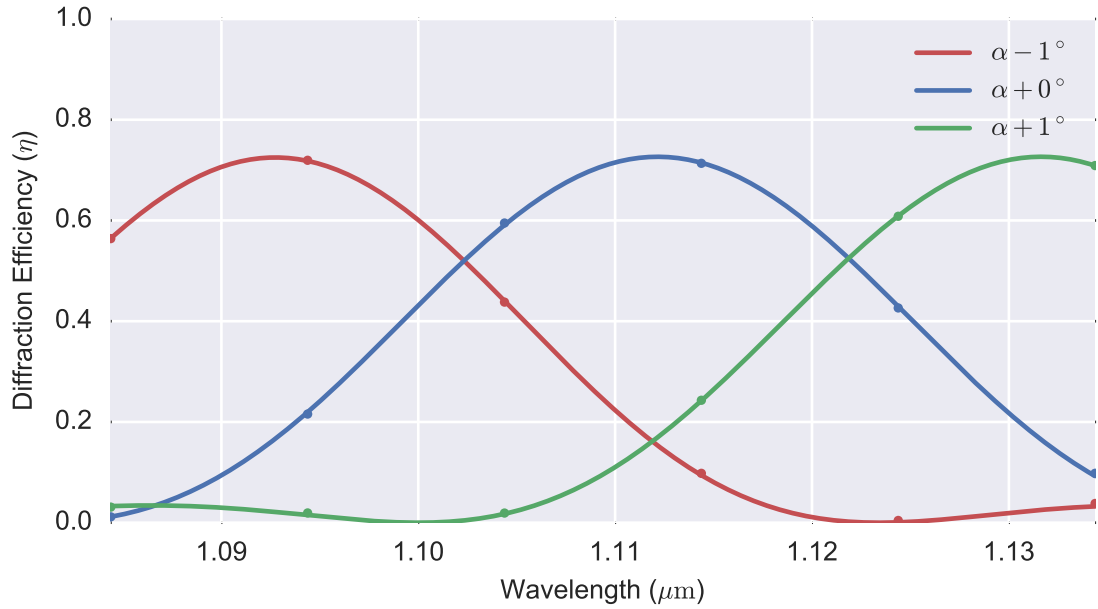


Figure 4.11: Variations of the blaze angle (α) for the 36th transmitted diffraction order of RIMAS’s YJ-band grism. Dots mark modeled wavelengths while the solid lines are sinc functions fit to these points. This demonstrates the design’s low level of sensitivity to errors in α .

the same.

The possibility of improving performance by deviating from $\theta_{\text{apex}} = 90^\circ$ was investigated. The ratios of calculated efficiencies shown in Figure 4.12 demonstrate that 90° is optimal. A simple geometrical argument is made for this being the case in Figure 4.13. The blue curve is the geometrical function describing the “shadow” created when $\theta_{\text{apex}} \neq 90^\circ$. The reasoning behind this explanation is provided in Figure 4.14.

Both of these tests conclude that the nominal grism design is optimal. Figures 4.15 and 4.16 show the final performance models for the YJ-band and HK-band

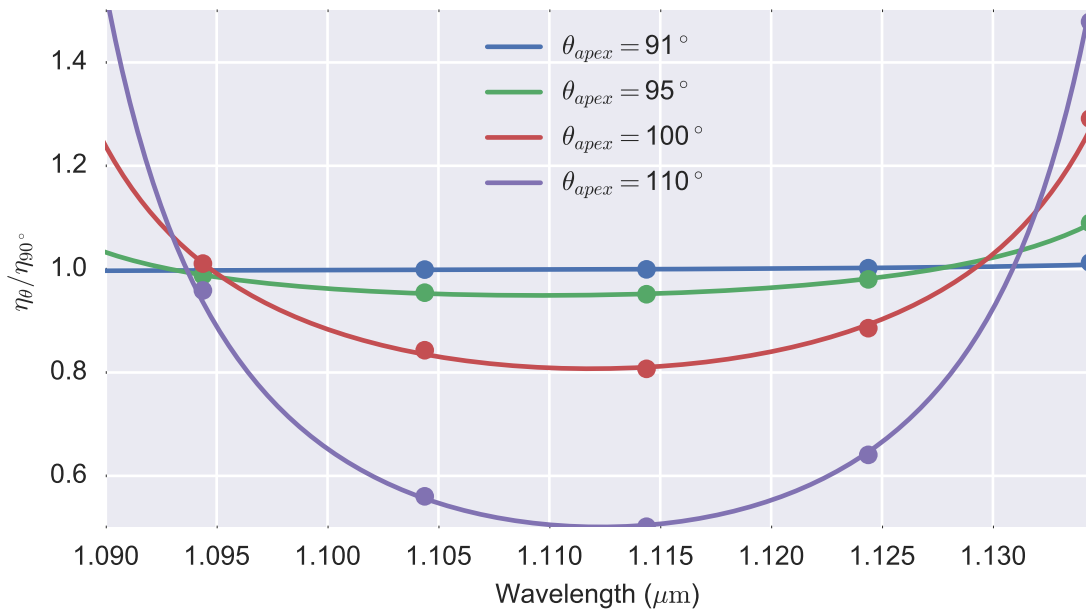


Figure 4.12: Efficiencies (η) are plotted as a fraction of $\eta(\theta_{apex} = 90^{\circ})$ for four angles. Dots show calculated wavelengths while the solid curves are calculated from sinc function fits. This shows that 90° is optimal for RIMAS's grism, and possibly for all grisms of this type. A simple physical model is presented in Figures 4.13 and 4.14.

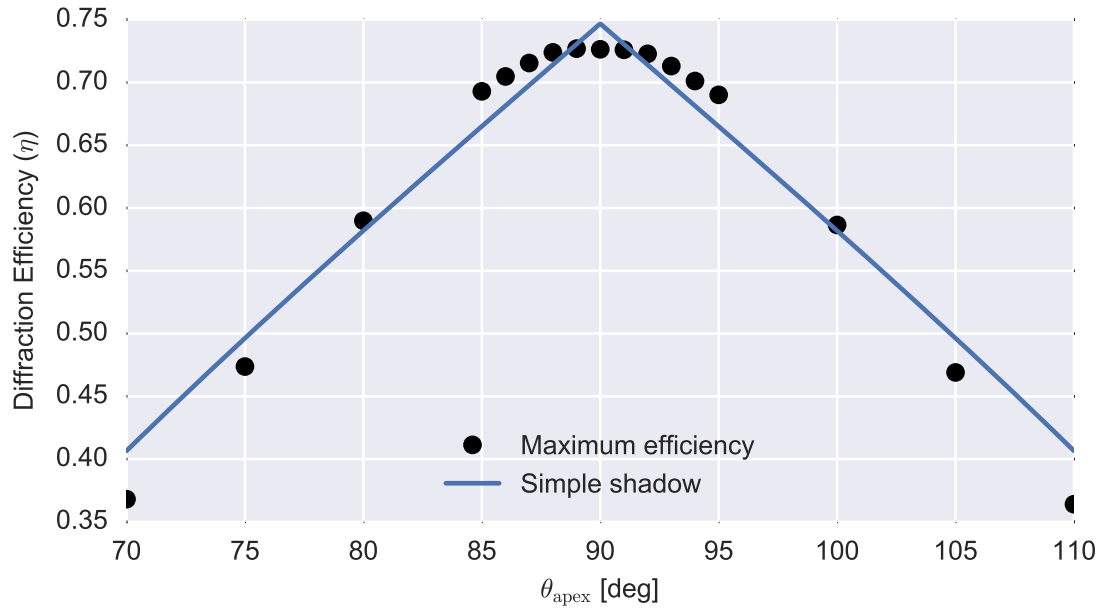


Figure 4.13: The peak efficiency for the 36th order of the YJ-band grism is plotted versus θ_{apex} . The black dots are calculated peak efficiencies for each angle while the blue curve is a geometrical “shadow” with the amplitude scaled down from 1 to fit the calculated points. The model which produced this curve is shown in Figure 4.14. Although not a perfect match to the RCWA calculated values, it is close enough qualitatively as to indicate a likely understanding.

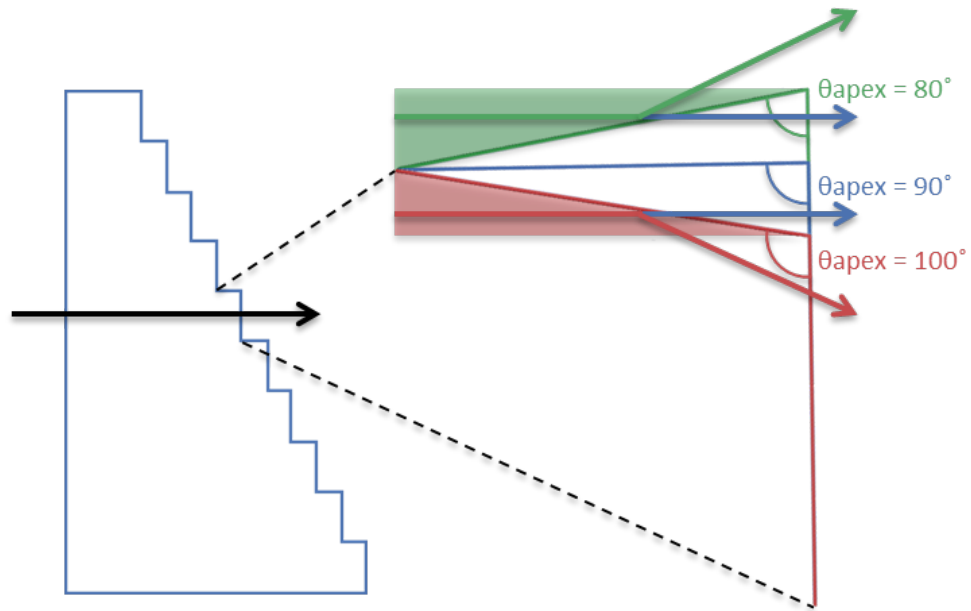


Figure 4.14: A drawing of the geometrical shadow argument for decreasing efficiencies as θ_{apex} deviates from 90° . The enlarged view is of a single period of the blaze profile for three different values of θ_{apex} . The arrows represent incident rays at different positions along the blazed profile. The shaded regions are the shadow created when $\theta_{\text{apex}} \neq 90^\circ$. Rays in those regions would reflect from the grating profile face given the very steep angles.

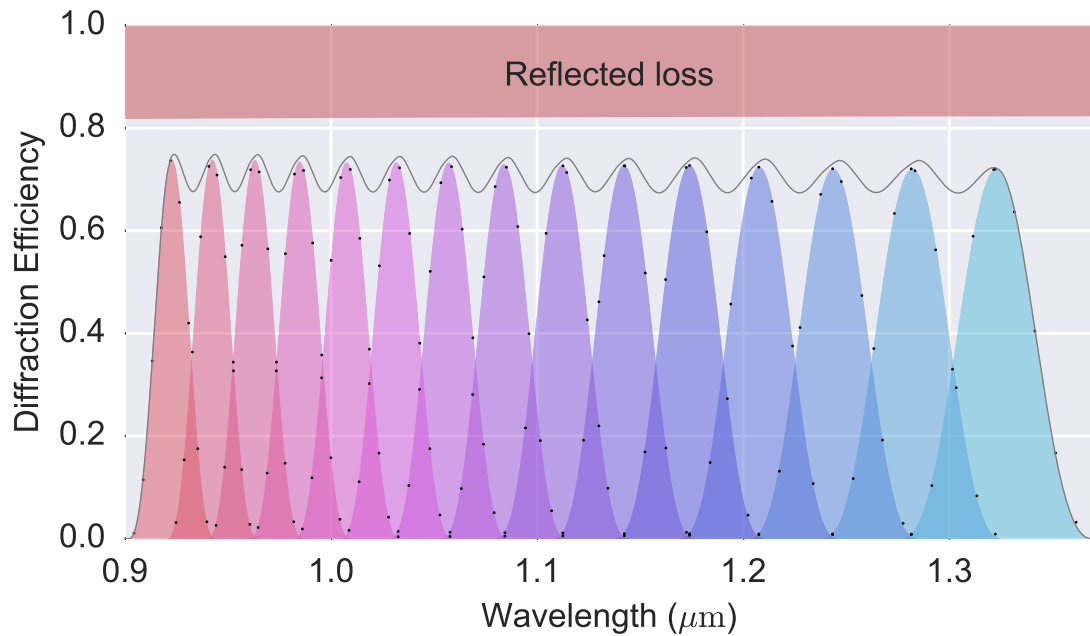


Figure 4.15: The predicted efficiency of the YJ-band grism. The black dots show modeled wavelengths while the shaded regions are sinc function fit to these points for each diffractive order. The plotted transmitted diffractive orders are 44 – 30 from left to right. The solid curve shows the summed efficiency out to the first side lobe of each order. Note that the dips in this curve are due to the non-inclusion of non-adjacent diffractive orders in the sums.

grisms.

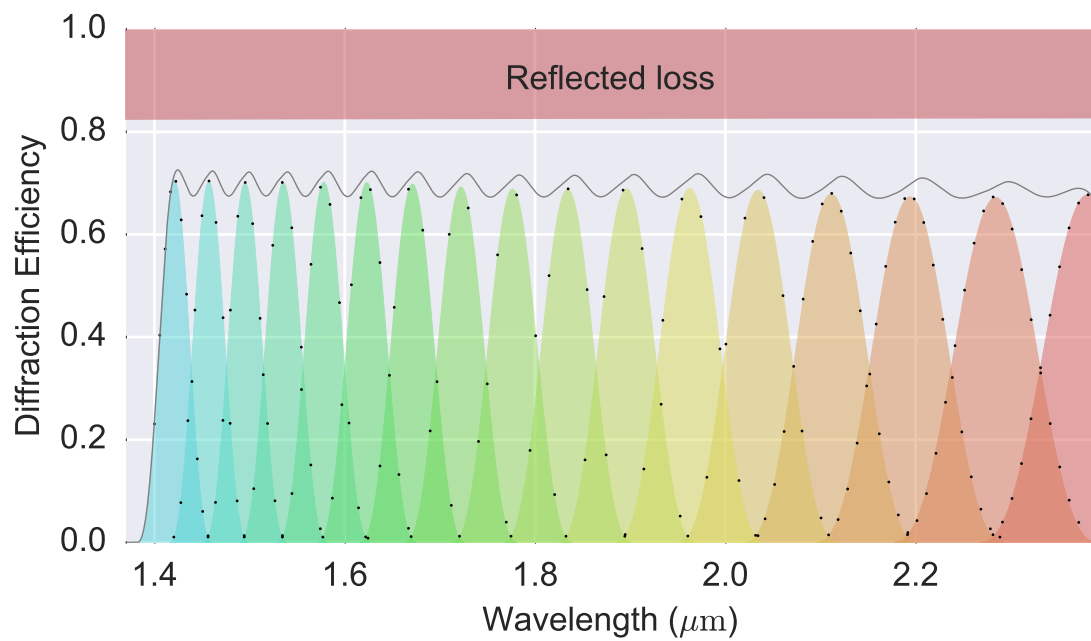


Figure 4.16: The same as Figure 4.15, but for the HK-band grism.

Chapter 5: RIMAS: Cryogenic Methods

This thesis has by necessity included the development of numerical and experimental methods. The following chapter presents three methods with broad applications. Since much of these methods are built on the work of others, I have made efforts to distinguish my original contributions.

5.1 Thermal Contraction Measurements

5.1.1 Motivation

As described previously in Section 4.2.2.3, the optomechanical design relies on a knowledge of the thermal contraction versus temperature (Equation 5.1) of various materials down to ~ 80 K. Since the dawn of cryogenics in the late-19th century, the thermal expansion of many materials has been measured and many data are available in the literature (e.g., [Jensen et al., 1980](#)). The RIMAS design relies on the accuracy of the thermal contraction models based on these data to achieve the required cryogenic optical performance. Given this importance, and the fact that non-standardized materials may differ from those previously measured, independent measurements were essential to verify the temperature-dependent length of some materials.

$$\Lambda(T) \triangleq (L_{293K} - L(T))/L_{293K} \quad (5.1)$$

To estimate the required accuracy, we take the worst case scenario: the first lens in the HK-band camera. For this 40.32 mm radius lens (L_{Lens}) made of fused silica ($\Lambda_{\text{FS}}(80\text{K}) \sim 1.41 \times 10^{-5}$, [Corruccini and Gniewek, 1961](#)) held in an Aluminum 6061 (hereafter Al) mount ($\Lambda_{\text{Al}}(80\text{K}) = 393 \times 10^{-5}$, [Arp et al., 1962](#)), the corresponding thermal-compensator is 16.06 mm long ($L_{\text{Comp.}}$) and made of Delrin (POM) ($\Lambda_{\text{POM}}(80\text{K}) \sim 1380 \times 10^{-5}$; [Schwarz, 1988](#), see Equation 4.5). If the actual fractional contraction value of the compensator is 90% of the design value ($\Lambda_{\text{Err.}} = 0.9$) the offset calculated using Equation 4.7 is 22 μm , which is close to the tolerance for translation of this lens. Therefore RIMAS's thermal-compensator design requires knowledge of fractional thermal contraction for optomechanical materials to $\lesssim 10\%$.

5.1.2 Experimental Design

A relatively simple method (i.e., no interferometer, etc.) of achieving high precision results is to use a push-rod dilatometer setup such as the one shown in Figure 5.1. Since the sample is immersed in a liquid at a fixed point, the sample's temperature is made stable and uniform by conduction. This fairly simple and fast setup obtains results accurate to $\sim 1\%$ or better ([Swift and Packard, 1979](#)).

Lacking an existing setup for these measurements, a similar approach was taken. The RIMAS cryostat chamber was used to bring samples to cryogenic measurement temperatures via radiation and conduction through the cold-plate. Mea-

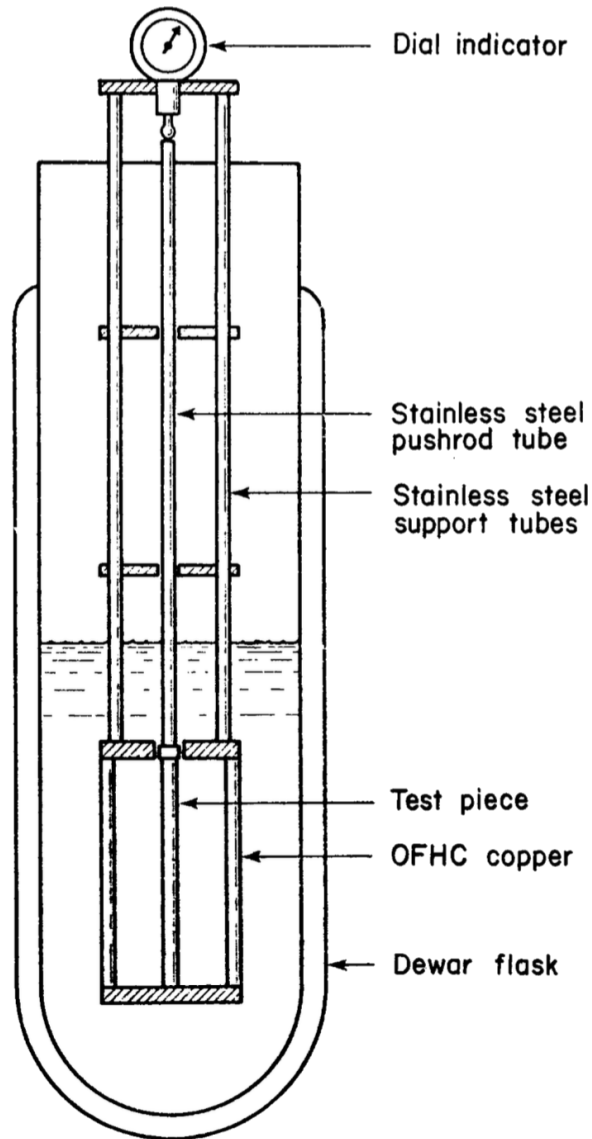


Figure 5.1: This figure is taken from [Swift and Packard \(1979\)](#). A push-rod dilatometer measures the difference in the change in length between the test piece and the reference material which supports the sample. In this case, oxygen-free high thermal conductivity (OFHC) copper is used as the reference because of previous, high-precision measurements. The bucket dewar is filled with liquids at various cryogenic temperatures (e.g., liquid nitrogen = 77 K, liquid helium = 4 K) to obtain a measurement at that temperature.

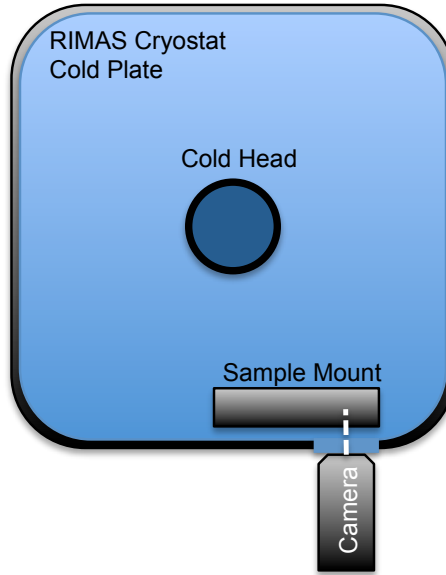


Figure 5.2: An overview of the thermal contraction measurement setup. The camera images the ends of samples mounted in the test assembly (see Figure 5.5) through a cold-window mounted on the assembly and a warm window mounted on the cryostat chamber.

surement and reference samples were then imaged through two windows (cold and hot) by a camera outside of the test chamber (i.e., an optical dilatometer). A drawing of this setup is provided in Figure 5.2.

5.1.2.1 Materials

An enclosure to hold the samples was fabricated at NASA GSFC out of Aluminum 6061 (see Figure 5.5). This enclosure was sandblasted and painted black to maximize the contrast of the imaged samples. Cylindrical (200.0 mm long \times 6.4 mm) samples of materials to be measured were cut from long rods. Small (few mm^2), reflective dots were painted on these ends by hand to provide a high contrast, non-periodic pattern for determining offsets. In the second iteration of this experi-

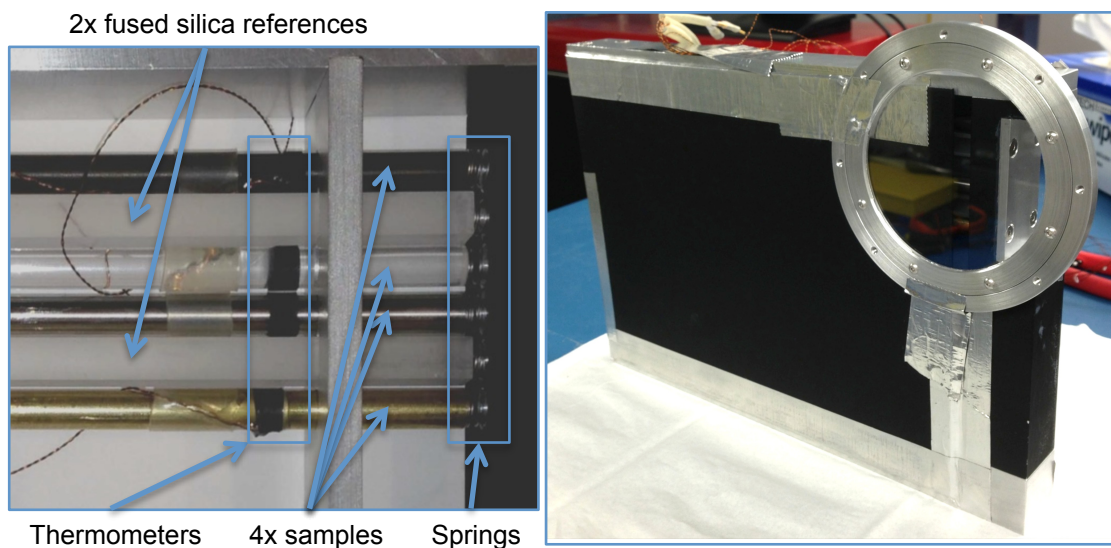


Figure 5.3: The sample mount for the optical dilatometer setup. On the left, the assembly is shown without the front plate and cold-window, both of which reduce the radiative thermal load on the test samples. Springs provide the force needed to keep all rods flush with a common reference surface (to the left outside of the image). The ends of the test samples and fused silica references are imaged at the location of the springs. In this way, the change in length of the test samples are measured relative to that of the fused silica rods. The temperature of each test sample is measured in two places along the length by diodes epoxied to the rods. The image on the right shows the fully assembled mount before being bolted to the cryostat's cold-plate.

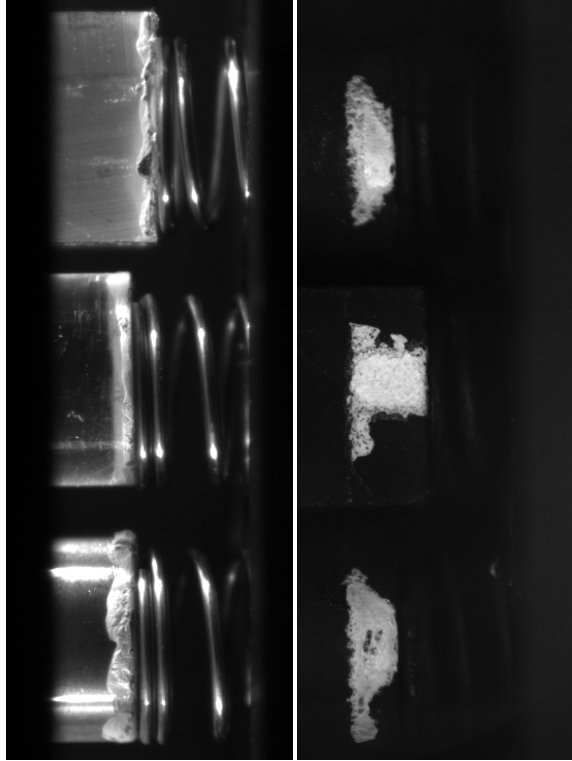


Figure 5.4: The ends of the test samples and fused silica references were sandblasted and painted black before applying high contrast marks. This was done to allow phase-only correlation (POC) methods to be used to determine sub-pixel displacements, as discussed in Section 5.1.3.1.

ment, the analysis was improved by sandblasting these ends and painting them black before applying the white marks, as shown in Figure 5.4. Thermometry diodes were attached to either end of each sample using epoxy and heat shrink tubing. By measuring multiple positions, it was possible to determine whether the samples were at a uniform temperature.

Fused silica rectangular prisms ($200.0 \text{ mm} \times 6.8 \text{ mm} \times 6.8 \text{ mm}$) were custom ordered to act as reference samples. This material is well known for having an extremely low coefficient of thermal expansion ($\sim 10^{-2} - 10^{-3} \times \frac{\Delta L}{L}$ of materials

being measured). Unfortunately, although the coefficient is negligible, it also lacks a constant value from one melt to the next (Jensen et al., 1980). The ends of these were also painted back and marked with white dots.

These materials were loaded into the enclosure and the front plate and a sapphire window were attached to reduce the radiative thermal load on the exposed ends of the samples. This assembly was then bolted to the cold-plate in the RIMAS cryostat, positioned so that the ends of the samples were visible through the chamber's window. A CCD with a zoom lens capable of focusing on the samples and achieving an image scale of $18 \mu\text{m}$ per pixel was mounted to the outside wall of the cryostat so as to image the ends of the samples. The images shown in Figure 5.4 were taken by this camera.

5.1.2.2 Procedure

The chamber was brought to a vacuum of $\sim 10^{-3}$ Torr by pumping the chamber before the cryocooler is turned on. The chamber then cooled and the pressure further reduced to $\sim 10^{-7}$ Torr as the remaining atmosphere condensed. Both imaging and temperature data were recoded during the cool-down; however the temperature gradient across the samples proved too great during this period, as shown in the bottom panel of Figure 5.5.

The system finally reached its minimum temperature after ~ 20 hours (Figure 5.5). Images and temperature data continued to be logged once per minute. Figure 5.6 shows how apparent the contraction of the 200 mm long samples is from room temperature to the minimum temperatures. With the system settled, the cryocooler

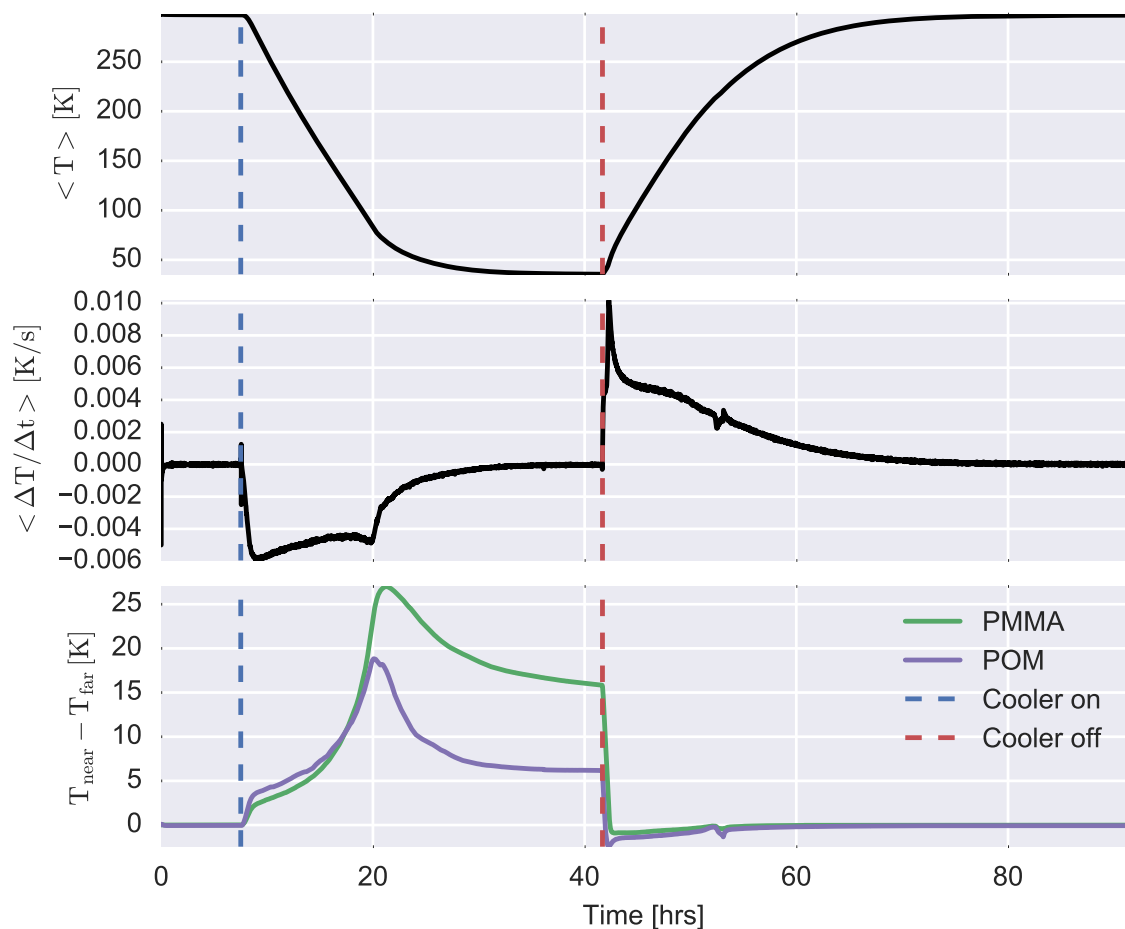
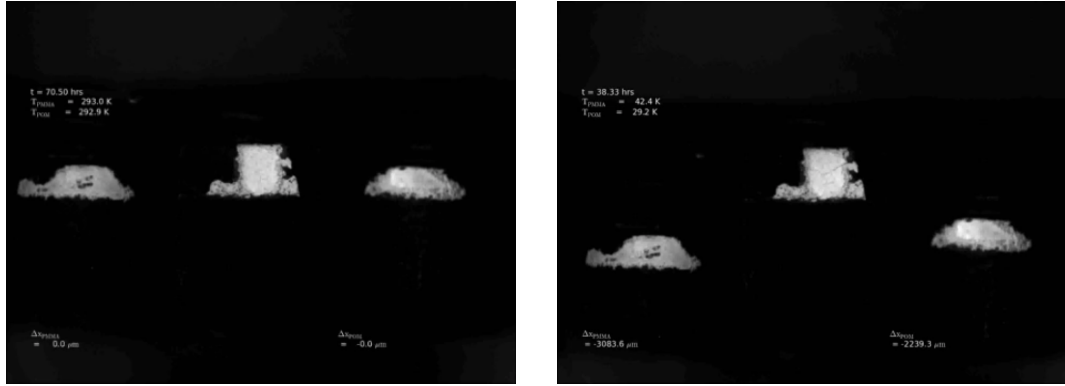


Figure 5.5: These curves show the temperature behavior of the samples during the course of an experiment. In this experiment Delrin (POM) and Plexiglas (PMMA) were measured. The top panel shows how the average temperature of the samples varies as a function of time while the second panel shows the instantaneous derivative of this. The bottom panel shows the difference in the temperatures recorded nearer the window (“near”) and that recorded further away (“far”) for two measured plastics. Only data acquired during the warm-up were used since the sample temperatures were made uniform by the increased atmosphere in the chamber during this time.



(a)

(b)

Figure 5.6: Two frames from the improved experiment. From left to right: PMMA, fused silica, POM. (a) An image taken at room temperature. (b) An image taken at the minimum temperatures. The PMMA sample is at 42.4 K and has contracted by 3.083 mm. The POM sample is at 29.2 K and has contracted by 2.239 mm.

was switched off and the chamber allowed to warm. The sudden drop in the temperature gradients across samples at this time, as seen in the bottom panel of Figure 5.5, is caused by the introduction of a slight atmosphere as formerly condensed molecules evaporate.

5.1.3 Analysis

The first image was loaded into a Python script to create pattern templates for each sample's unique mark. Image indices were determined which divided the image into slices with each containing the image of a single sample. To reduce noise in the calculated phase-only correlation (POC), the median image background was subtracted and points outside of the pattern were set to zero.

Temperature data were interpolated linearly versus recorded operating system time. The interpolation function was then used to determine the temperature at each sampled point in the system when each exposure was taken.

5.1.3.1 Phase-only Correlation

In the original analysis reflected light from the springs prevented a successful analysis by phase only correlation. Instead, least squares was used to determine translations of integer pixel values. This shortcoming led to the modification of the experiment shown in Figure 5.4.

Images from the second experiment were loaded into a Python environment and the POC calculated relative to the template images (i.e., the starting position). The POC methods presented in Takita et al. (2003, hereafter T03) were used. The normalized cross spectrum (\hat{R} , Equation 5.2) of two images, f and g , is calculated using the 2D discrete Fourier transforms (DFT) of the images, F and G .

$$\hat{R} = \frac{F\bar{G}}{|FG|} \quad (5.2)$$

The measured POC function (\hat{r}) is then the 2D inverse discrete Fourier transform (IDFT) of \hat{R} . T03 shows that Equation 5.3 can be used to determine translations between two images with sub-pixel precision by fitting this function to the measured POC function (Figure 5.7). In Equation 5.3 α is the function's amplitude (nominally = 1), N_1 and N_2 are the dimensions of the images in pixels, n_1 and n_2 are pixel indices and δ_1 and δ_2 are the fit translations in each image axis.

$$\hat{r}(n_1, n_2) \cong \frac{\alpha}{N_1 N_2} \frac{\sin[\pi(n_1 + \delta_1)]}{\sin[\frac{\pi}{N_1}(n_1 + \delta_1)]} \frac{\sin[\pi(n_2 + \delta_2)]}{\sin[\frac{\pi}{N_2}(n_2 + \delta_2)]} \quad (5.3)$$

T03 further shows how applying Hanning windows to each image reduces the effect of image edge discontinuities. Methods are also provided to weight the cross-phase spectrum. In each case, fit functions are provided. The predicted maximum error of these fits is ~ 0.01 pixel. When applied to image/pattern combinations from the thermal contraction experiment, the pixel offset was converted into microns using the measured pixel scale of $18.6\mu\text{m}/\text{pixel}$.

5.1.4 Results

As mentioned previously, this experiment was conducted to verify the applicability of past measurements and to measure the thermal contraction of new materials. Standardized metal alloys were also measured to test the accuracy of the experiment itself.

Of the materials with data available in the literature which were measured in the lab, stainless steel 303 has a defined composition (see [Arp et al., 1962](#)). This alloy was measured during the first experimental run, before the modification which improved the POC analysis. Additional efforts would produce sub-pixel results, however for the moment the results are presented at the 1 pixel level, as shown in [Figure 5.8](#).

Following the example of the Cryogenic Technology Group at the National Institute of Standards and Technology (NIST; <http://cryogenics.nist.gov/>), a 4^{th} order polynomial was used to fit these data. In this case, this fit was primarily

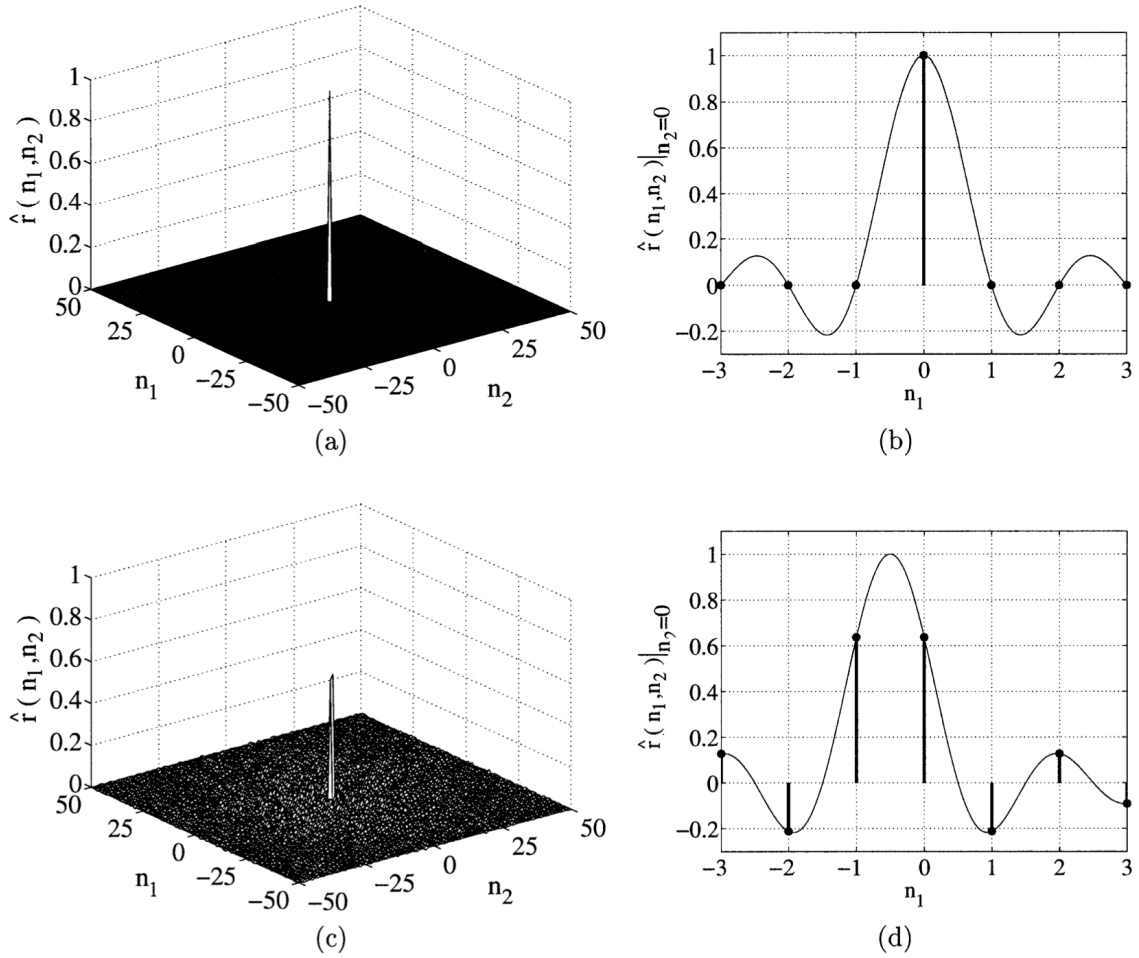


Figure 5.7: This plot from [Takita et al. \(2003\)](#) shows the phase-only correlation (POC) function ($\hat{r}(n_1, n_2)$) for (a and b) images translated by an integer number of pixels and (c and d) images translated by a half pixel. The POC function is the 2D inverse discrete Fourier transform (IDFT) of the cross spectrum of two images.

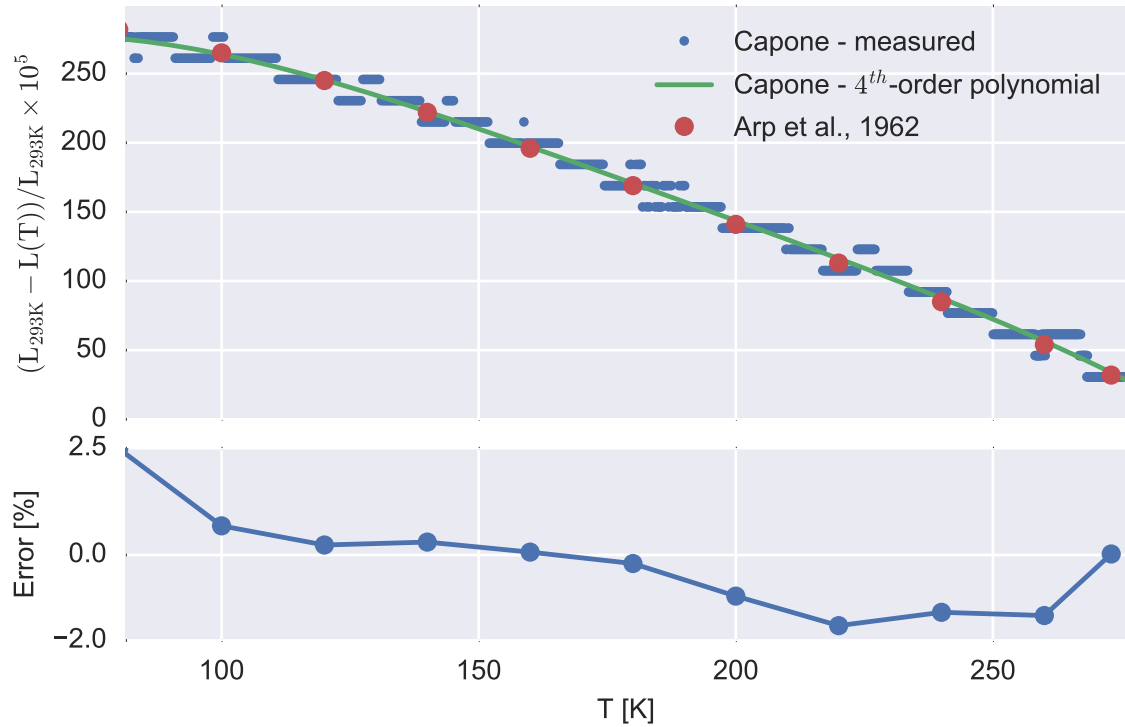


Figure 5.8: The pixel level results above are fit with a 4th order polynomial, as is common practice with this type of data. Measurements presented by [Arp et al. \(1962\)](#) are also plotted independently. Errors in the bottom panel are deviations between the polynomial fit and the historical measurements. The close agreement validates the experimental procedure at the few percent level. A sub-pixel analysis could be done for a higher precision comparison.

used to smooth the results for a sub-pixel comparison. The bottom panel of Figure 5.8 demonstrates agreement with measurements from the literature at the level of a few percent. Since errors of $\sim 10\%$ are acceptable, this optical dilatometer setup is sufficiently accurate. If greater accuracy is required, a sub-pixel analysis, such as POC, could be attempted or additional measurements of standardized alloys could be taken with the improved contrast setup.

Two plastics, POM and PMMA, were measured with the improved setup for potential use as compensators. Figure 5.9 presents the results of the sub-pixel POC analysis, which show a close agreement with previous measurements. The nearly constant values of the errors are likely due to a systematic error of the analysis such as the pixel-scale calibration or the value assumed for T_{hot} . For the purposes of designing thermal-compensators for RIMAS, this close agreement shows that values from the literature are valid at the few percent level for at least some plastics. Further investigation (i.e., careful calibration) of these data could be done to determine if the agreement is actually better.

5.1.5 Further Applications

Further estimates of the POC method's accuracy are possible outside of the experiment's goal of measuring the absolute thermal contraction of these materials. For most applications, thermal expansion is usually described by a linear equation with a constant coefficient of thermal expansion (CTE, usually $\alpha \triangleq \frac{1}{L} \frac{dL}{dT}$) over a range of 10's to 100's of degrees. Figure 5.10 shows a linear fit subtracted from measurements over a 20 K range near room temperature. The linear subtraction

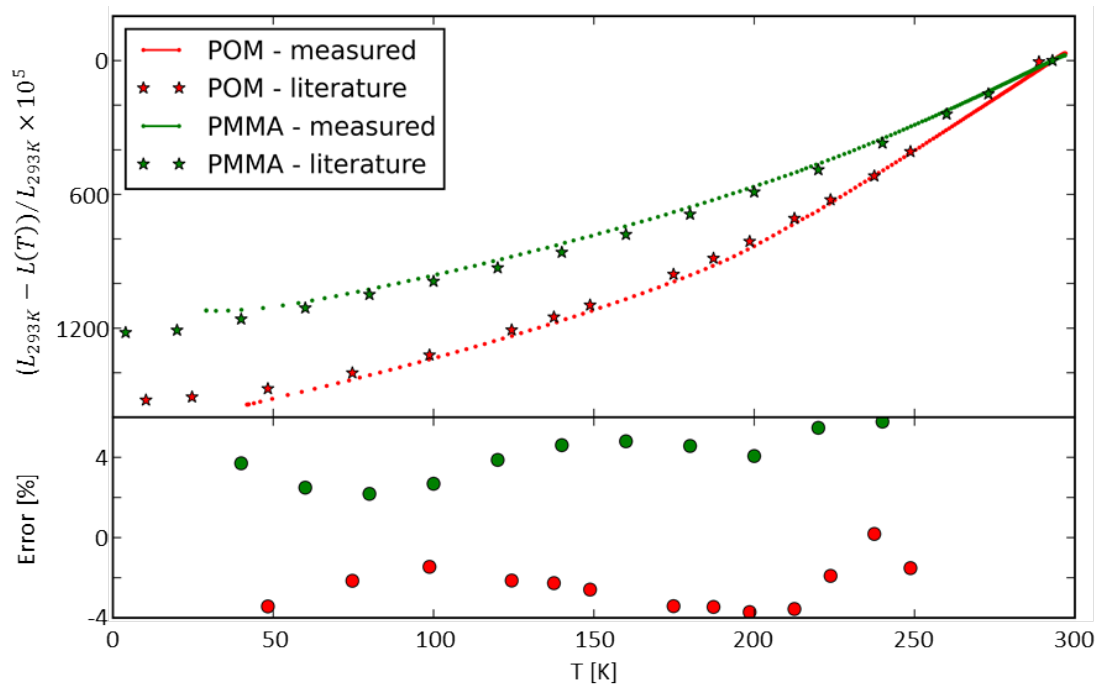


Figure 5.9: The relative thermal contraction of POM and PMMA. Literature values for POM are from [Schwarz \(1988\)](#). Values for PMMA were found in [Laquer and Head \(1952\)](#). Ignoring the constant offset, which is likely due to an offset in the zero point temperatures between the literature values and those presented here, the RMS error is $\sim 1\%$.

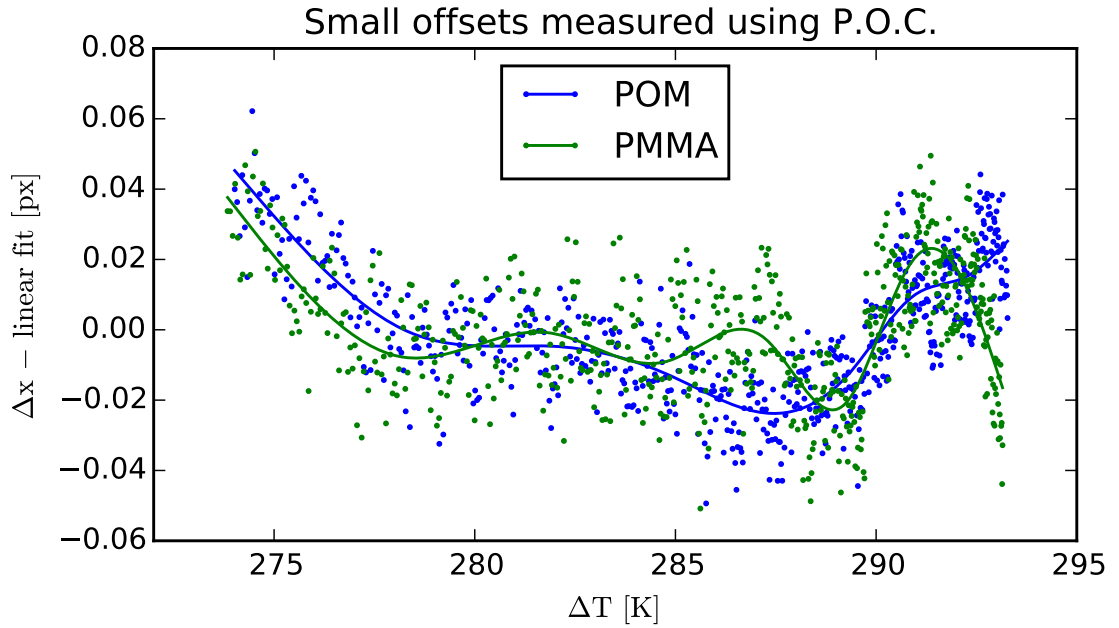


Figure 5.10: A linear fit was subtracted from each sample’s curve to demonstrate the relative measurement accuracy of the POC method in terms of pixels. The solid lines are 3rd order, natural smoothing splines fit using the methods discussed in Section 2.2.1.1. These fits were done to estimate systematic errors. Previous measurements of the thermal expansion of fused silica are consistent with the deviations from linearity shown in this plot.

alone suggests the relative precision of these POC measurements is on the order of 0.01 pixels, consistent with the findings of [Takita et al. \(2003\)](#) and others.

Going one step further, the gradual variations were fit with natural, 3rd order smoothing splines (see Section 2.2.1.1 for details). This is intended to represent systematic errors expected even in the relative measurements of this experiment. For example the experimental setup assumed that the fused silica references were unchanged by the system’s temperature, but previous measurements of similar samples find $\Lambda_{\text{FS}}(275\text{K}) \sim 0.7 \times 10^{-5}$. The rods used in the experiment were ~ 200 mm

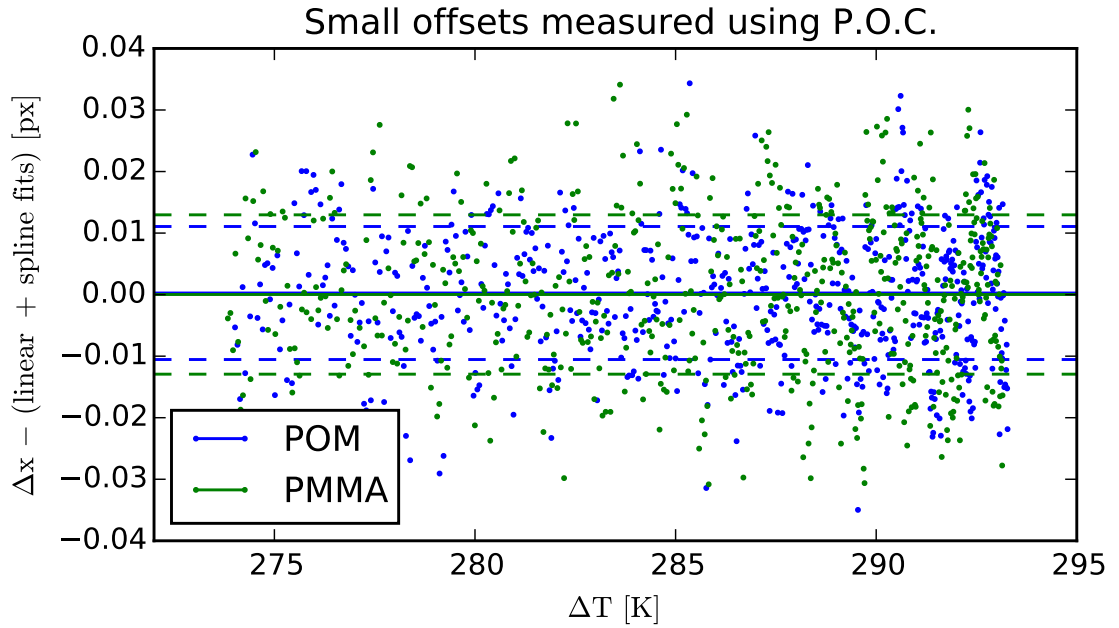


Figure 5.11: The spline fits from Figure 5.10 have also been subtracted. The dashed lines show the 1σ levels for each distribution.

long, so the expected change in length is $\gtrsim 1\ \mu\text{m}$, or ~ 0.08 pixels. As mentioned previously, the thermal expansion behavior of fused silica varies from sample to sample, but this estimate shows that this is one potential source of the systematic errors. Subtracting the spline fits produced $1\ \sigma$ errors of ~ 0.01 pixel (Figure 5.11).

Even the scatter shown in Figure 5.11 cannot be wholly attributed to the POC analysis. Figure 5.12 shows that the digitization of the temperature monitor can produce scatter for a given temperature as high as $1\ \mu\text{m}$ (0.05 pixels).

In summary, the optical dilatometer setup presented here, combined with POC analysis, provides an inexpensive and robust method for measuring the relative displacement of objects on the $\lesssim 1/100$ pixel level. The precision and accuracy of

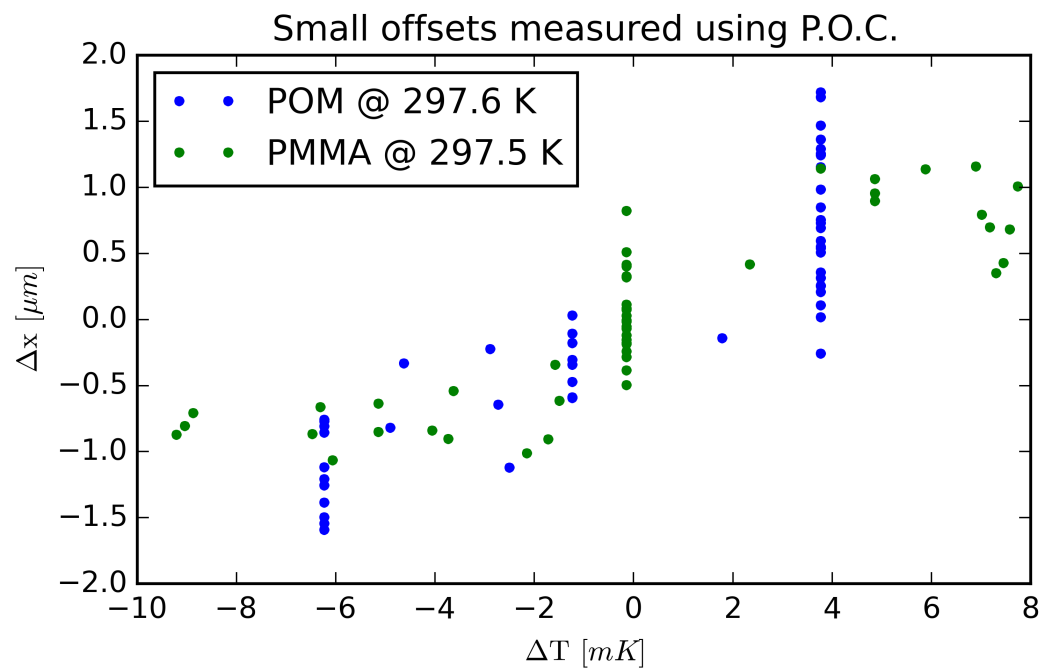


Figure 5.12: The impact of the thermometry monitor's resolution is apparent and is another source of systematic errors.

the method is limited by the imaging system's pixel scale and the systematic errors of the experimental setup. In this experiment many sources of systematic errors were subtracted by using fused silica as a reference. In another experiment, however, the ambient temperature outside of the cryostat would be a significant source of error since the mount holding the camera will contract and expand by amounts greater than level being measured.

Possible applications include verifying the performance of motorized stages, optomechanical assemblies and other scenarios where the object of study can be imaged simultaneously with a stable reference. These applications are particularly interesting for cryogenic work where alternative approaches tend to be complex and expensive.

5.2 Electrical Harness Modeling

5.2.1 Modeling Heat Transfer

The design of any cryogenic system requires careful consideration of thermal loads. Given that RIMAS's cryostat requires a vacuum, heat is only transferred via conduction and radiation. Significant electrical current ($I \sim 1$ Amp) is required to power stepper motors to rotate filter wheels which are located in the cryostat. The design of electrical harnesses used to transport this current into the cryostat must balance heat conduction from the outside with heat from Ohmic dissipation in the harness. In an effort to predict the contributions of these factors and optimize the design (wire material, wire gauge, number of leads, etc.) numerical calculations

have been performed for various possible designs.

5.2.1.1 1-D Relaxation Method

Much of the numerical models described in this section are based on the method implemented in Example 1.9-2 on pages 171 – 185 of [Nellis and Klein \(2009, hereafter NK09\)](#). The calculations described in this section were implemented in Python.

The system is taken to be one dimensional, which is reasonable for a wire where the temperature at any position along its length is uniform in the cross section. The length is broken up into N discrete nodes where heat flows through a node by conduction from the node above (\dot{q}_{top}) and the node below (\dot{q}_{bottom}) and by radiation (\dot{q}_{rad}). If the wire is carrying a current, heat is generated in each node by Ohmic dissipation (\dot{g}). The energy balance within a node is shown in [Figure 5.13](#). See NK09 for details on the numerical representation of this system.

The temperature at the external cryostat wall (the first node) is fixed at T_H while the cold-plate (the final node) is fixed at T_C . Internal nodes are initially set to linear values between T_H and T_C as a function of distance along the wire. An iterative approach is required since the thermal conductivity (κ) and electrical resistivity (ρ) of each node are dependent on the temperature of the node. The calculation proceeds until the sum of the differences between the temperatures calculated at the current step and the previous step is less than a specified allowable error.

Additionally, the option to specify the position of a cold-shield was added to the model presented in NK09. In this scenario, nodes on the cold side of the

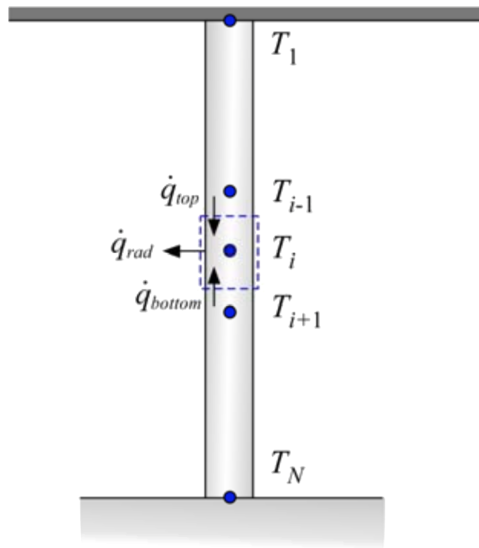


Figure 5.13: Figure 2 from page 174 of [Nellis and Klein \(2009\)](#) summarizes the one-dimensional steady-state calculations used to model electrical wires used in RIMAS. The first node, T_1 , is fixed at the temperature of the external wall ($T_H = 293$ K) while the final node, T_N , is fixed at the temperature of the cold-plate ($T_C = 60$ K).

specified cold-shield position are not exposed to radiative heat transfer from the cryostat exterior. Rather, they are in radiative contact with the cold temperature on both sides. Nodes on the hot side of the cold-shield are treated as before. Given the importance of radiation in cryogenic systems, this is a useful addition to the model.

Temperature dependent values of electrical resistivity (ρ) and thermal conductivity (κ) for copper, phosphor bronze (“phos. bronze”) and maganin were calculated by interpolating between the values provided in Tables 5.1 and 5.2.

Table 5.1: Electrical resistivity (ρ) values in Ω m for potential harness materials.

These values were calculated using data found at <http://www.lakeshore.com>.

Material	4.2 K	77 K	305 K
Copper	1.53×10^{-10}	2.03×10^{-9}	1.63×10^{-8}
Phos. Bronze	1.08×10^{-7}	1.12×10^{-7}	1.30×10^{-7}
Manganin	4.38×10^{-7}	4.63×10^{-7}	4.90×10^{-7}

5.2.1.2 Model Testing

The following tests of the code were taken from example 1.9-2 of NK09. Two scenarios with analytical solutions were used to test the performance of the numerical model. In both tests, the thermal conductivity and electrical resistivity of the wire material were held constant with temperature. Additionally, the emissivity (ϵ) of the wire was set to 0, which in turn made the position of the cold-shield irrelevant.

Table 5.2: Thermal conductivity (κ) values in W / (m K) for potential harness materials. These data are taken directly from <http://www.lakeshore.com>.

Material	10 K	20 K	80 K	150 K	300 K
Copper	700	1100	600	410	400
Phos. Bronze	4.6	10	25	34	48
Manganin	2	3.3	13	16	22

It was then possible to compare the numerical results with the analytical solution derived in Section 1.3.2 of NK09 (Equation 5.2.1.2). Figure 5.14 shows the agreement between the analytical and numerical solutions.

$$T = \frac{\dot{g}''' L^2}{2\kappa} \left[\frac{x}{L} - \left(\frac{x}{L} \right)^2 \right] - \frac{T_H - T_C}{L} x + T \quad (5.4)$$

where,

$$\dot{g}''' = \frac{16I^2\rho}{\pi^2 D^4}$$

Emissivity data were not available for potential wire types. To reasonably assume a value, it was necessary to test the impact of this parameter on the results. Calculations were done for 62.5 mA in 32 AWG phosphor bronze wire. This lower current represents the required 0.5 A divided by 8 parallel leads. Figure 5.15 shows the extreme importance of radiative transfer to the model. Since the true value of ϵ is unknown for these wire, $\epsilon = 0.5$ is adopted for the remainder of this discussion. The true value of ϵ is likely to be between 0.5 and 1 where the impact is less significant.

Figure 5.16 shows how the numerical approach requires a minimum number

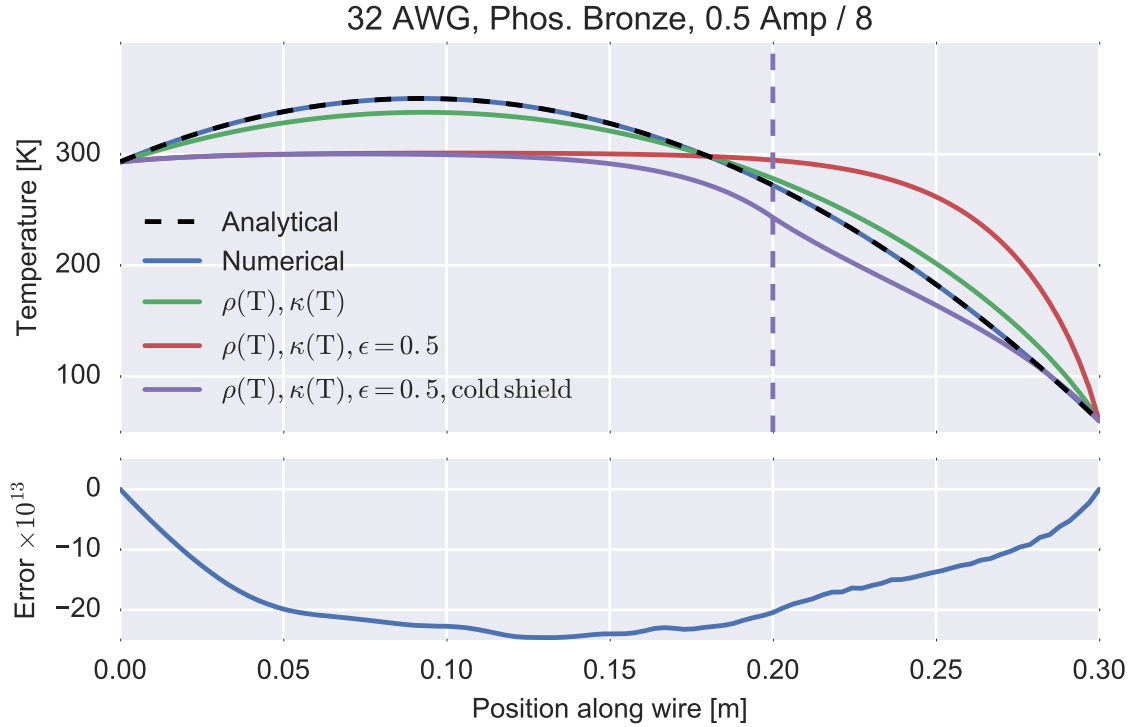


Figure 5.14: The blue curve shows the exact agreement between the analytical and numerical solutions. The numerical solution's errors are shown in the bottom panel. The remaining curves in the top panel show how the model changes as components are added. Adding the temperature-dependent values of ρ and κ have a minimal impact, however setting the emissivity (ϵ) to 0.5 rather than 0 has a dramatic effect. The final curve illustrates the importance of the introduction of the cold-shield to this model.

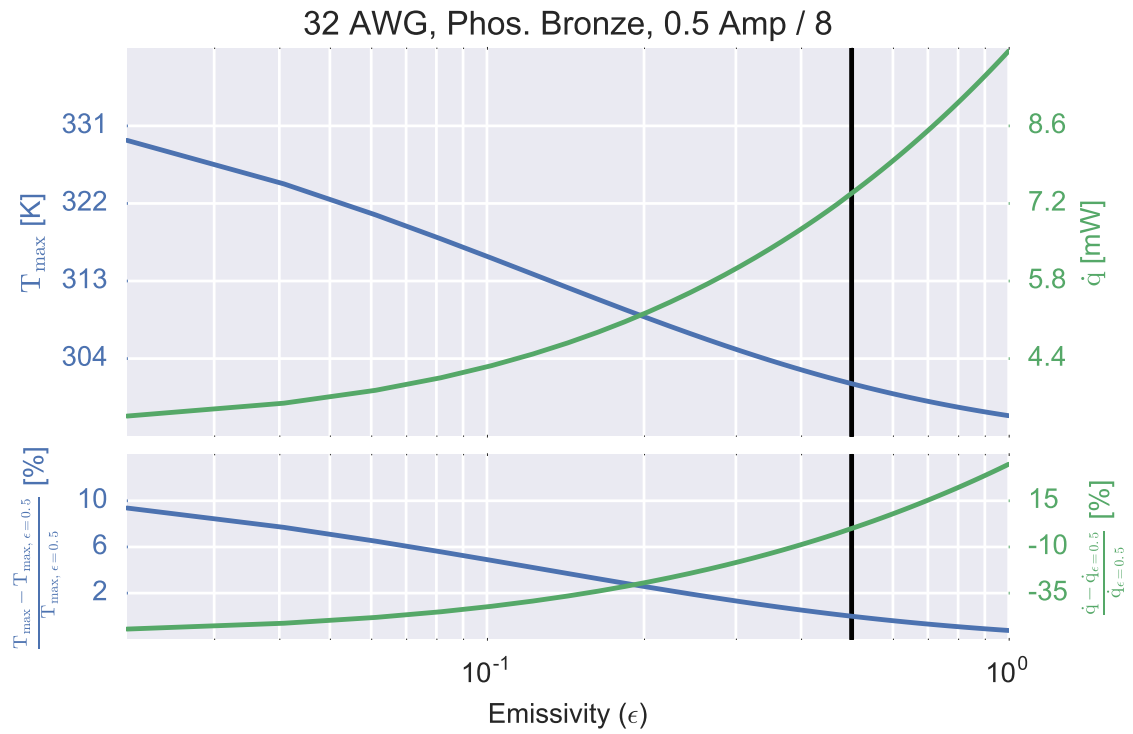


Figure 5.15: Maximum temperature (T_{\max}) and total heat transferred into the cryostat (\dot{q}) as a function of ϵ . The black line shows the assumed value of 0.5.

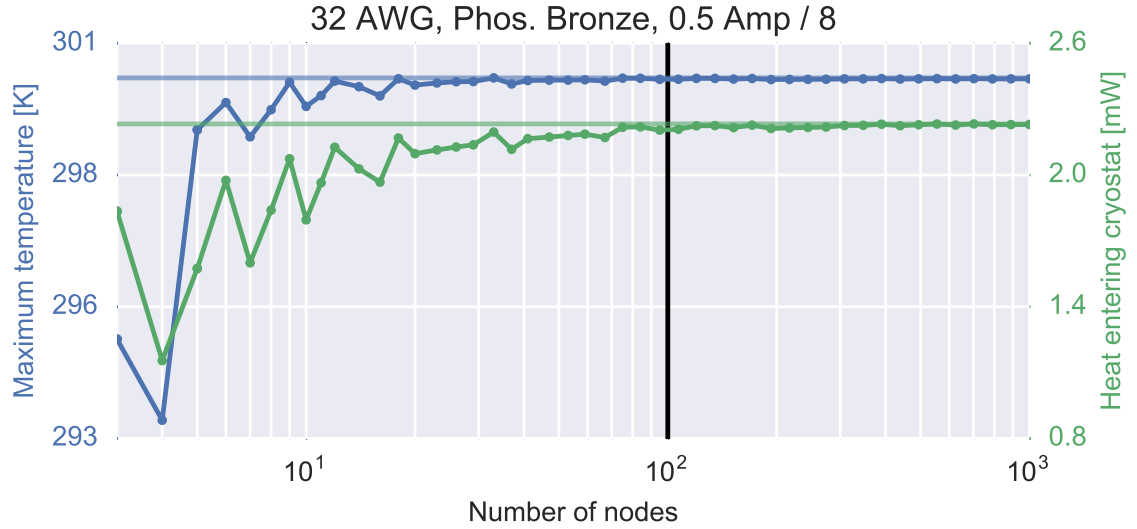


Figure 5.16: Maximum temperature (T_{\max}) and total heat transferred into the cryostat (\dot{q}) as a function of the number of nodes used in the 1D model. The light, horizontal lines show the value where the results converge. The black line shows the selected number of nodes.

of nodes to converge on a reliable result. For the remainder of this discussion, calculations were done using 100 nodes.

Figure 5.17 shows how the placement of the cold-shield impacts the temperature profile of a wire. Figure 5.18 shows the maximum temperature and heat transferred as a function of the cold-shield’s position. This second plot emphasizes the importance of adding the cold-shield to the model. For RIMAS, the true value is ~ 20 mm, and this value is adopted for the remainder of the discussion.

5.2.2 Design Optimization

There are several electrical harness design parameters which can be altered while still providing the electrical current required by a given device located within

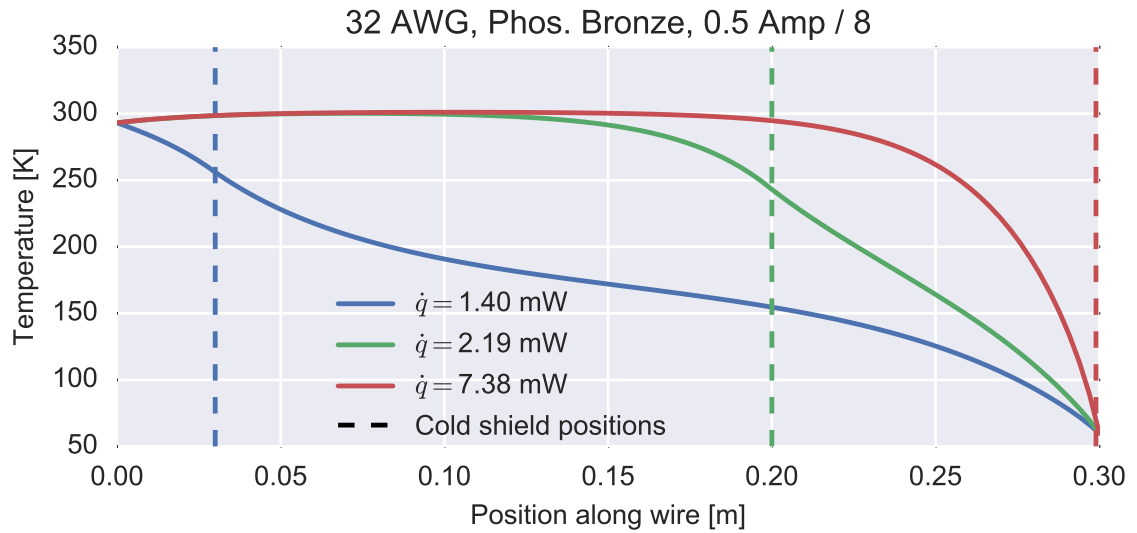


Figure 5.17: The curve where the cold-shield is placed at the end of the wire is equivalent to the original model described in NK09. The curve where the shield is at 20 mm is the estimated value for RIMAS.

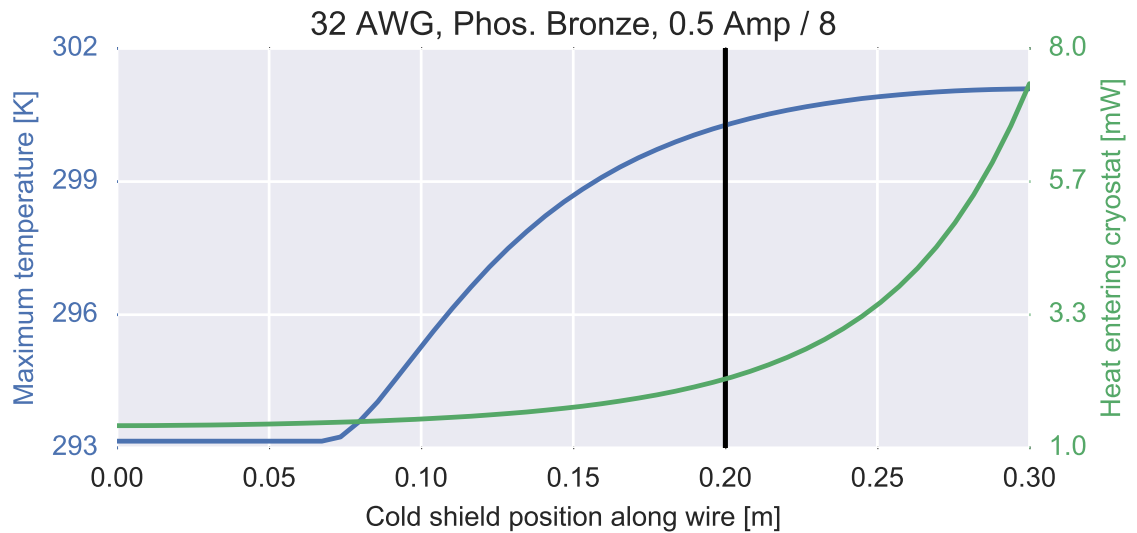


Figure 5.18: The total heat transported into the cryostat via the wire (\dot{q}) is a strong function of the cold-shield's position.

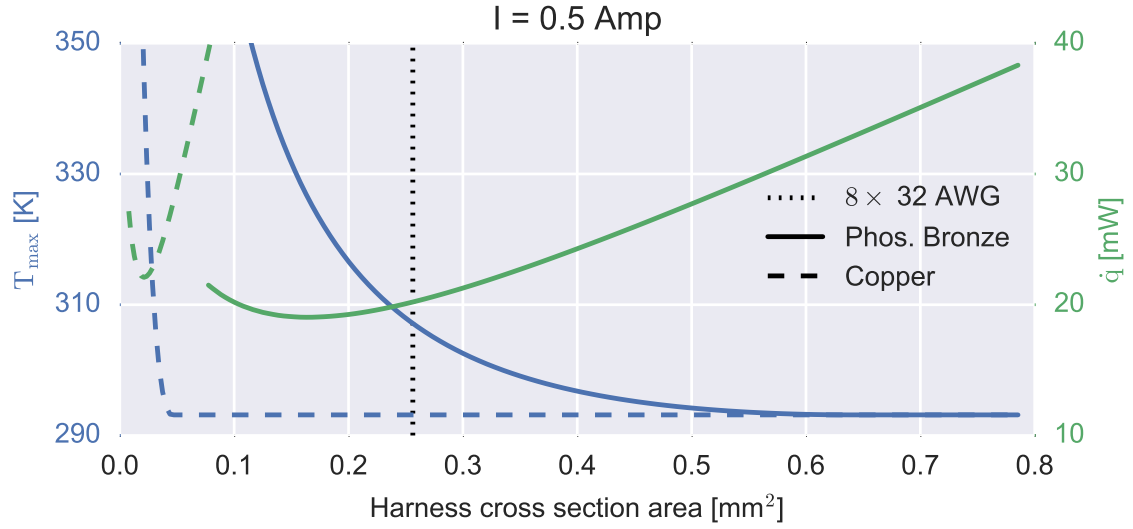


Figure 5.19: The final design for the motor harnesses has 8 leads of 32 AWG phosphor bronze. This design minimizes the heat transported into the cryostat and the maximum temperature of the wires.

the cryostat. The gauge can be increased (\rightarrow decreased diameter) to decrease heat flow via conduction from the exterior, but this will increase heat generation from Ohmic dissipation in the presence of an electrical current. The materials in Tables 5.1 and 5.2 were considered, providing a range of values for ρ and κ .

Figure 5.19 shows possible designs using copper and phosphor bronze. Given the uncertainty of ϵ and the more gradual curves for phosphor bronze, this material was selected as a safer option. The model assumes that the total current required by the motor is 0.5 Amps, however Figure 5.20 shows the advantage of running the motors at lower currents if possible.

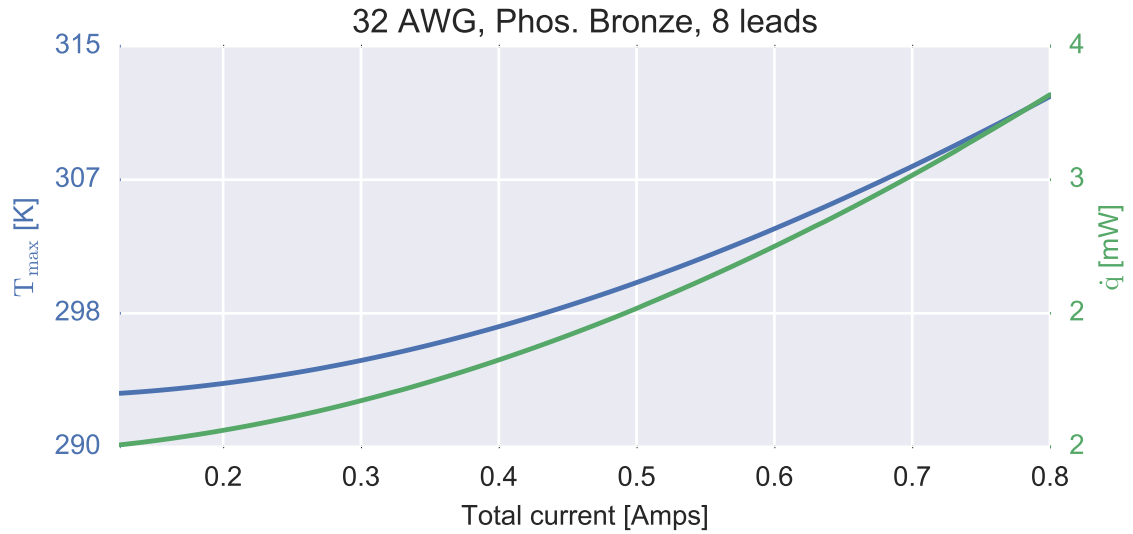


Figure 5.20: The total heat transferred into the cryostat can be reduced by reducing the current to the motor.

5.3 Cold-Plate Vibration Measurements

5.3.1 Motivation

The RIMAS cryostat achieves its cryogenic operating temperature using a Sumitomo Heavy Industries (SHI) HC-8E compressor connected to a SHI CH-208L cryocooler (for details, see <http://www.shicryogenics.com>). Vibrations from the compressor inevitably propagate into the cryocooler via the helium gas lines. The lines and cryocooler are both designed to minimize these vibrations, however they must be characterized to ensure the RMS displacements will not adversely impact RIMAS's optical performance.

5.3.2 Experimental Design

Accelerometers were considered to measure accelerations due to vibrations, however these have two important disadvantages. First, measuring acceleration does not provide a direct measurement of displacement. With a high enough sampling rate and a sufficiently sensitive device, this could be reconstructed, however a direct measurement is desirable. Second, readily available commercial accelerometers would likely function differently in the system's cryogenic, vacuum environment. If they function at all, they would require calibration.

A method used to characterize previous instruments was selected ([Kutyrev and Robinson, 2012](#)). A back-illuminated pinhole was bolted to various positions on the cold-plate to provide a point-source at the measurement position, as shown in [Figure 5.21](#). A CCD with a zoom-lens mounted to the cryostat's exterior was used to image the pinhole. By mounting the imaging system directly to the cryostat, only the motion of the cold-plate was measured, as opposed to the motion of the entire cryostat. Systematic errors introduced by the vibration of the lens-CCD were minimized by mounting the lens using six radial screws.

5.3.2.1 Procedure

The illuminated pinhole was bolted to the desired measurement position and the cryostat was sealed and brought to the operating pressure and temperature. The zoom-lens was focused on the final pinhole position. The pixel scale was determined using the known diameter of the pinhole mount and comparing this to the diameter

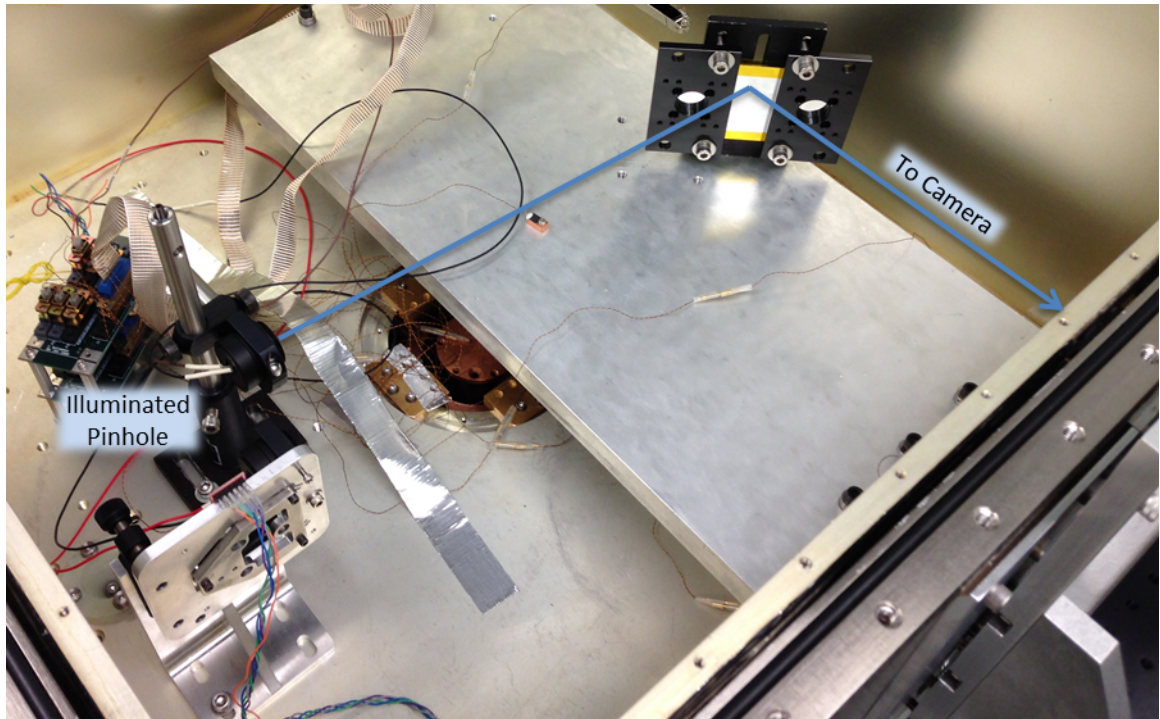


Figure 5.21: The test setup measuring vibrations at a detector position. This is very near the x-y translation mount and should represent the worst case scenario.

in pixels in the image. Images were then taken at a frame rate of ~ 40 Hz both with the compressor on and off.

5.3.3 Analysis

The acquired data were saved in the Flexible Image Transport System (FITS) format. Acquisition and exposure times were saved to the header. An analysis script written in Python identified the image of the pinhole by the maximum pixel value. The region around this pixel containing the image of the pinhole was then fit with a Gaussian function to achieve sub-pixel identification of the centroid. The precision of this method was estimate as $\sim 0.2 \mu\text{m}$ for a pixel scale of $32.2 \mu\text{m}/\text{pixel}$, as shown in Figure 5.22.

5.3.4 Results

Before the copper weave cold-straps used to connect the first cryocooler stage to the cold-plate were delivered, a ridged copper connection was used. The resulting vibrations were extreme, as shown in Figure 5.23 where 1σ in both x and y were $\sim 20 \mu\text{m}$. Given that an H2RG pixel is $18 \times 18 \mu\text{m}^2$, this would degrade the PSF unacceptably.

After the the delivery and installation of the copper weave cold-straps, the measured vibrations decreased significantly, as shown in Figure 5.24. While there are still detectable vibrations, they are \ll than an H2RG pixel. The 1σ displacement converts to 20 milli-arc-seconds on the sky.

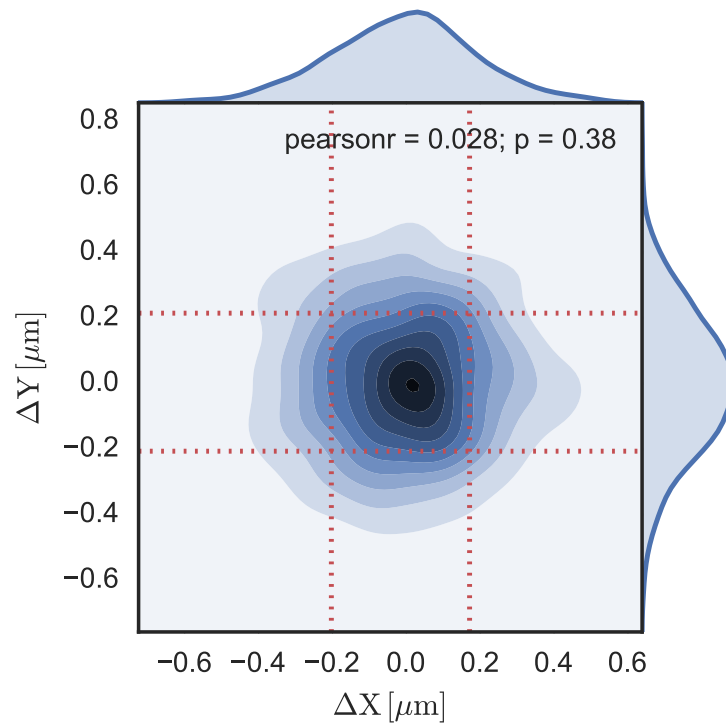


Figure 5.22: The kernel density estimate calculated from 2000 samples while the cryocooler was off. The pinhole was positioned as shown in Figure 5.21. The pixel scale of the images was $32.2 \mu\text{m}/\text{pixel}$. This plot provides a lower limit for the precision of this method.

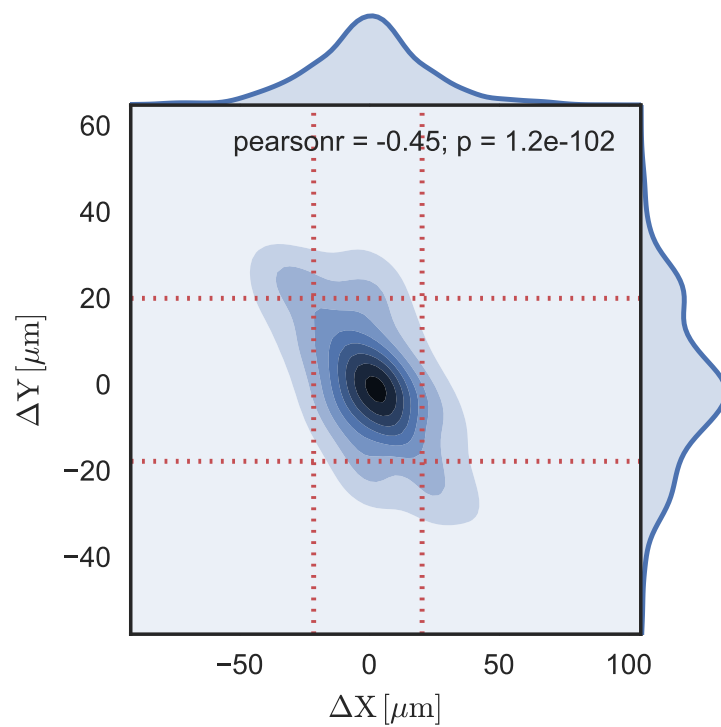


Figure 5.23: The same setup as in Figure 5.22, but with the cryocooler on. The cryocooler was ridgedly coupled to the cold-plate during these measurements.

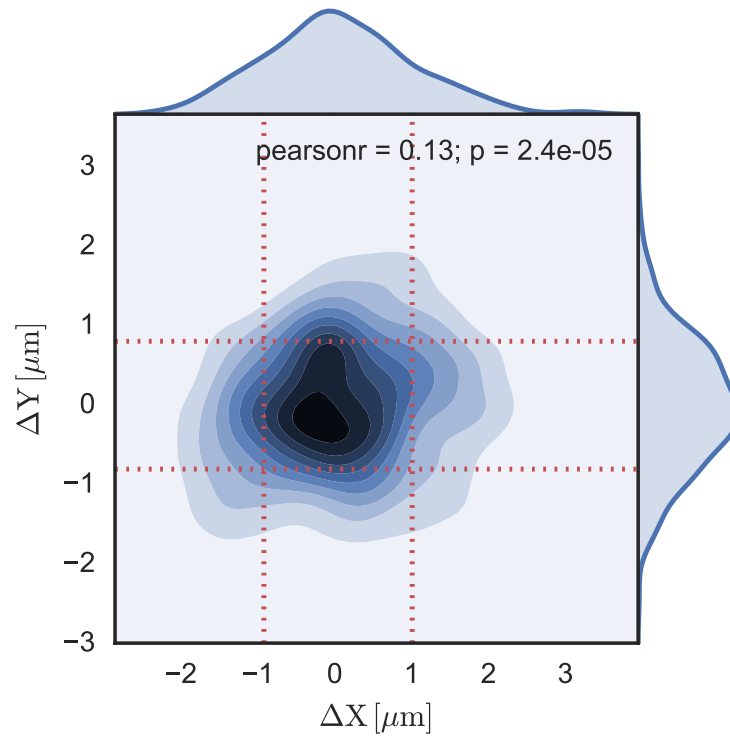


Figure 5.24: The same setup as in Figure 5.22, but with the cryocooler on. The cryocooler was connected to the cold-plate using copper weave straps during these measurements.

Chapter 6: Final Considerations

6.1 Summary

This thesis has summarized some of the ways in which LGRB afterglows can be used as probes of the very high redshift Universe. A generalized analysis framework was developed in Chapter 2 and applied to three afterglows, two with high extinction and one with little or none. The demonstrated ability of my software to detect evidence of photodestruction of dust in GRB 120119A suggests highly extinguished afterglows as a likely population for further investigation. However, the case of GRB 080607 provides a counter example, perhaps due to an intervening dusty region outside the immediate CBM. RIMAS's low spectral resolution modes ($R \sim 30$) will be well suited for this type of study as it will increase the number of NIR wavelengths sampled without requiring a burst to be exceptionally bright.

Once RIMAS is commissioned on the DCT, it will provide a valuable tool for investigating optically dark GRB afterglows, particularly those occurring at very high redshifts. Most of my contributions towards this end have focused on the optical systems which operate at cryogenic temperatures, as discussed in Chapter 4. I have used established methods to design a broadband NIR slit-imaging camera and have successfully aligned it to achieve seeing-limited performance. The preliminary

design for the remaining optics were provided by a collaborator at NASA-GSFC (see Table 1 on page iii). I completed these designs by performing tolerancing analyses and modeling the thermal properties of these systems. The result is the verified seeing limited performance of the collimator and YJ-band camera at cryogenic temperatures. Finally, I have used RCWA to ensure optimal designs of the moderate-R gratings.

In the course of my graduate research, I have developed and implemented a number of methods for designing and testing cryogenic systems, as detailed in Chapter 5. The successful optical dilatometer experiment verified thermal expansion values from the literature and provides a means of easily measuring additional materials, as required. The heat flow model of electrical harnesses in vacuum (built upon the work of [Nellis and Klein, 2009](#)) were used to optimize the material selection, as well as the total cross section. Finally, the cold-plate vibration measurements verified that the cryocooler was sufficiently decoupled so that the optical performance of the instrument is unaffected.

6.2 Lessons from RIMAS

The following list summarizes practical information for designing and building cryogenic optical systems like those in RIMAS:

- Tolerancing analyses are a required and standard part of any design process.

When performing such an analysis, it is essential to consider correlated errors.

For example, refractive indices of most optical materials increase between room

temperature and cryogenic temperatures.

- The significance of thermal considerations depends on the results of tolerancing analyses. For example, I determined that RIMAS's slit-imaging camera could achieve seeing-limited performance without the use of thermal-compensators, thereby simplifying the design.
- Comprehensive and reliable metrology is a requirement for sensitive optical systems. The quality and format of data packages provided by companies is not standardized, even when these data are explicitly a part of the purchase agreement. Solutions to this challenge include buying from a known manufacturer or planning to obtain these measurements in the laboratory. Although the latter allows a project to verify that the data are sufficient to constrain key design parameters, contact profilometers are the most readily available tools for this type of measurement. Their use on optical surfaces risks damage to critical components.
- Once optical elements are fabricated, metrology can be used to re-optimize the optomechanical designs. This iterative process improves the attainable final performance and loosens alignment tolerances.
- BBAR coatings sometimes fail to adhere to ZnSe. In general, have thin-film companies demonstrate their coating solution on a test sample before they coat the instrument's optics.
- RCWA is a great tool for designing and modeling optics which are periodic in

1 or 2 dimensions. Although commercially available software packages provide convenient interfaces, they are generally less transparent and flexible than free, open-source alternatives. I performed comparisons in Section 4.3.2.1 which demonstrate close agreement between these options. Calculations take much longer for gratings operating at high diffractive orders and/or having deep profiles.

- NIR LEDs are available to test the performance of NIR optical assemblies at known wavelengths. Filtered tungsten light sources provide a broadband option. Silicon detectors cut off past the band gap ($\lambda \gtrsim 1.1 \mu\text{m}$), requiring a less common detector for room temperature measurements of optical systems out to $2.4 \mu\text{m}$. Being able to test optical systems at room temperature is desirable since optics, particularly transmissive optics, must be cooled gradually to avoid damage. RIMAS takes $\gtrsim 1.5$ days to cool, although this is limited by the cryocooler, not the optics.
- POC analysis is a powerful tool for measuring relative translation, rotation, and changing magnification of an imaged object. Non-periodic, high contrast (relative to the background) objects are best.
- MCMC methods are particularly useful for understanding the covariance of parameter spaces and for marginalizing nuisance parameters. Applying these methods to laboratory data allows critical values to be easily extracted.

6.3 Future Applications

6.3.1 HARMONI Spectrograph

Starting in July of 2016, I will begin working as a post-doctoral researcher on the High Angular Resolution Monolithic Optical and Near-infrared Integral field spectrograph (HARMONI) in the Department of Physics at the University of Oxford. HARMONI will be one of the first-light instruments for the European Southern Observatory's (ESO) European Extremely Large Telescope (E-ELT, 39.3 meters) scheduled to come online in 2024. I will focus on the development of an engineering optomechanical model of the instrument's spectrograph units.

6.3.2 Planned Research in Transient Astronomy

During this three-year position, I plan to apply my analysis framework to a larger set of afterglows to look for further evidence of SED evolution other than what is expected from changing power-law break frequencies. I am also developing ideas for how transient follow-up efforts can be optimized. This problem is particularly challenging given the large position uncertainties for some types of event triggers, such as gravitational waves. I have begun investigating how open source machine learning codes can be used to identify transients in image data without previous observations of a given field. Google's TensorFlow is a promising software library which is used through either a Python or C++ application programming interface (API).

Appendix A: Lens Metrology Report

The following pages are taken from an internal report summarizing the analysis results of metrology performed at NASA-GSFC.

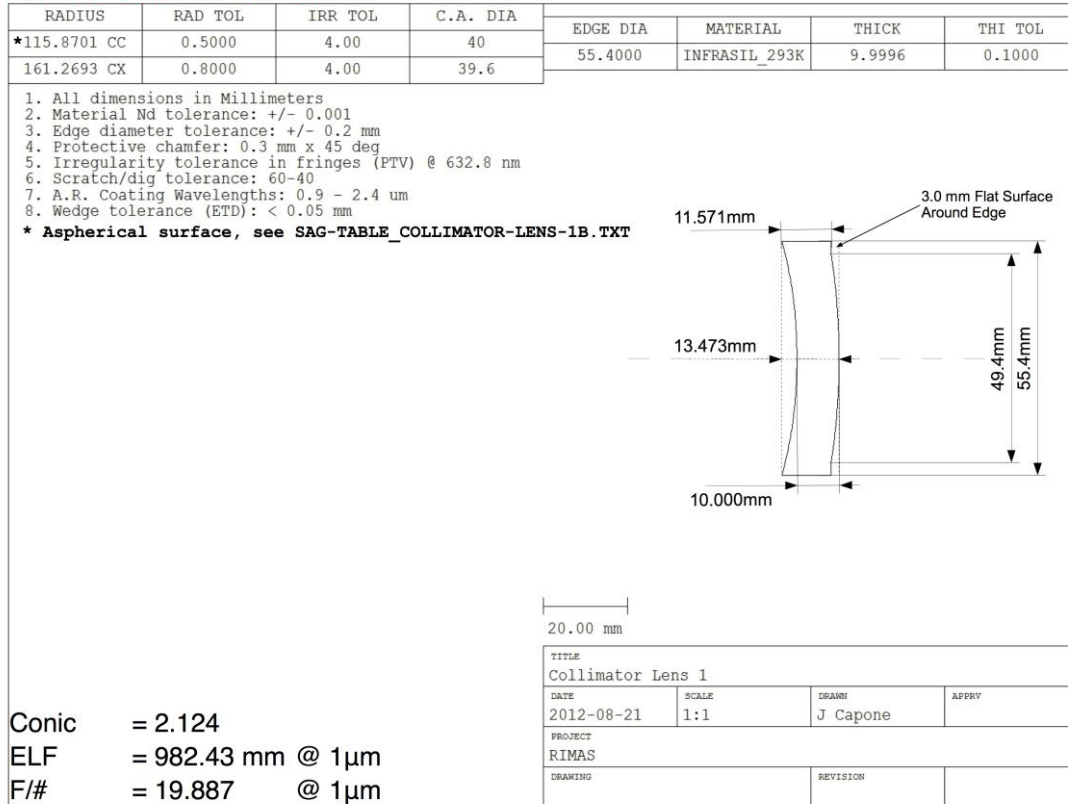
RIMAS - Science Optics

Lens metrology analysis by John I. Capone

Compliance color codes
Measured value is within tolerances
Measured value may be within tolerances
Measured value is not within tolerances
Note: tolerances were not specified for reference annuli widths, edge thicknesses or aspheric parameters.
Measured value is consistent with <1% of un-toleranced parameter
Measured value is consistent with 1-5% of un-toleranced parameter
Measured value is consistent with 5-10% of un-toleranced parameter
Measured value is not consistent with 10% of un-toleranced parameter

Collimator lens #1

KO Item Code: LMN5510-C



Metrology:

Property	Value	Specified	Source
Outer diameter	55.298 mm	55.4±0.2 mm	CMM - Kubalak
Flat to left	9.1453±0.0007 mm		CMM - Kubalak
Flat to right	1.8963±0.0007 mm		CMM - Kubalak
Center thickness	11.042±0.001 mm	10.0±0.1 mm	CMM - Kubalak
Edge thickness	11.9±0.2 mm	11.6 mm	Calipers - Capone
Centration - X	69±4 µm	See wedge	CMM - Kubalak
Centration - Y	78±4 µm	See wedge	CMM - Kubalak
Left radius of curvature	115.5±0.1 mm - CC	115.9±0.5 mm	CMM - Kubalak
Left conic	2.09±0.07	2.124	CMM - Kubalak
Right radius of curvature	161.7±0.1 mm - CX	161.3±0.8 mm	CMM - Kubalak
Reference annulus	1.94±0.05 mm	3.0 mm	Microscope - Capone
Chamfer	0.165±0.013 mm	0.2 mm	Microscope - Capone

Collimator lens #2

KO Item Code: LBV6142-C

RADIUS	RAD TOL	IRR TOL	C.A. DIA	EDGE DIA	MATERIAL	THICK	THI TOL
216.0962 CX	1.0000	4.00	48.4	61.4000	CAF2_293K	42.1278	0.1000
694.6597 CX	3.5000	4.00	43				

1. All dimensions in Millimeters
 2. Material Nd tolerance: +/- 0.001
 3. Edge diameter tolerance: +/- 0.2 mm
 4. Protective chamfer: 0.3 mm x 45 deg
 5. Irregularity tolerance in fringes (PTV) @ 632.8 nm
 6. Scratch/dig tolerance: 60-40
 7. A.R. Coating Wavelengths: 0.9 - 2.4 um
 8. Wedge tolerance (ETD): < 0.05 mm

3.9 mm Flat Surface Around Edge

39.419mm

42.128mm

53.6mm

61.4mm

20.00 mm

TITLE Collimator Lens 2			
DATE 2012-08-21	SCALE 1:1	DRAWN J Capone	APPRV
PROJECT RIMAS			
DRAWING		REVISION	

ELF = -389.93 mm @ 1μm
 F/# = -7.2747 @ 1μm

Metrology:

Property	Value	Specified	Source
Outer diameter	61.477 mm	61.4±0.2 mm	CMM - Kubalak
Flat to left	41.6878±0.0006 mm		CMM - Kubalak
Flat to right	0.612±0.001 mm		CMM - Kubalak
Center thickness	42.300±0.001 mm	42.1±0.1 mm	CMM - Kubalak
Edge thickness	39.2±0.2 mm	39.4 mm	Calipers - Capone
Centration - X	163±32 μm	See wedge	CMM - Kubalak
Centration - Y	273±32 μm	See wedge	CMM - Kubalak
Left radius of curvature	216.2±0.1 mm - CX	216±1 mm	CMM - Kubalak
Right radius of curvature	696±4 mm - CX	694.7±3.5 mm	CMM - Kubalak
Reference annulus	3.88±0.08 mm	3.9 mm	Microscope - Capone
Chamfer	0.258±0.037 mm	0.2 mm	Microscope - Capone

Collimator lens #3

KO Item Code: LCM6706-C

RADIUS	RAD TOL	IRR TOL	C.A. DIA	EDGE DIA	MATERIAL	THICK	THI TOL
1687.8845 CC	7.9396	4.00	49.6	67.4000	ZNSE_293K	5.5066	0.1000
682.1581 CX	3.0000	4.00	49.6				

1. All dimensions in Millimeters
 2. Material Nd tolerance: +/- 0.001
 3. Edge diameter tolerance: +/- 0.2 mm
 4. Protective chamfer: 0.3 mm x 45 deg
 5. Irregularity tolerance in fringes (PTV) @ 632.8 nm
 6. Scratch/dig tolerance: 60-40
 7. A.R. Coating Wavelengths: 0.9 - 2.4 um
 8. Wedge tolerance (ETD): < 0.05 mm

20.00 mm

TITLE			
Collimator Lens 3			
DATE	SCALE	DRAWN	APPRV
2012-08-21	1:1	J Capone	
PROJECT			
RIMAS			
DRAWING		REVISION	

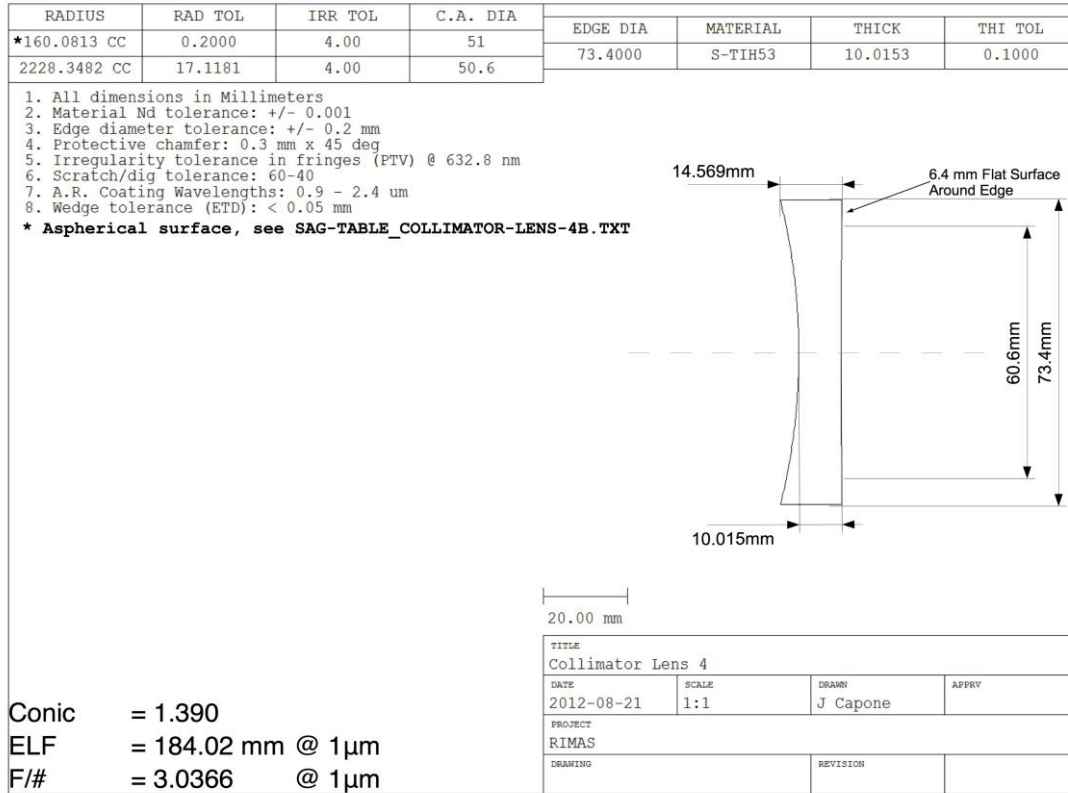
ELF = -771.26 mm @ 1µm
 F/# = -12.561 @ 1µm

Metrology:

Property	Value	Specified	Source
Outer diameter	67.396 mm	67.4±0.2 mm	CMM - Kubalak
Flat to left	4.7943±0.0002 mm		CMM - Kubalak
Flat to right	0.6886±0.0003 mm		CMM - Kubalak
Center thickness	5.4829±0.0004 mm	5.5±0.1 mm	CMM - Kubalak
Edge thickness	4.5±0.2 mm	5.2 mm	Calipers - Capone
Centration - X	115±11 µm	See wedge	CMM - Kubalak
Centration - Y	101±13 µm	See wedge	CMM - Kubalak
Left radius of curvature	1690±2 mm - CC	1687±8 mm	CMM - Kubalak
Right radius of curvature	685.0±0.6 mm - CX	682±3 mm	CMM - Kubalak
Reference annulus	2.728±0.014 mm	3.0 mm	Microscope - Capone
Chamfer	0.315±0.012 mm	0.2 mm	Microscope - Capone

Collimator lens #4

KO Item Code: LNQ7350-C



Metrology:

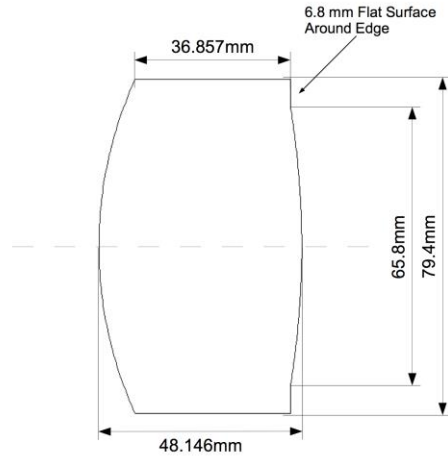
Property	Value	Specified	Source
Outer diameter	73.405 mm	73.4±0.2 mm	CMM - Kubalak
Flat to left	10.2102±0.0007 mm		CMM - Kubalak
Flat to right	0.2553±0.0002 mm		CMM - Kubalak
Center thickness	9.9550±0.0007 mm	10.0±0.1 mm	CMM - Kubalak
Edge thickness	14.0±0.2 mm	14.6 mm	Calipers - Capone
Centration - X	20±11 µm	See wedge	CMM - Kubalak
Centration - Y	179±10 µm	See wedge	CMM - Kubalak
Left radius of curvature	160.2±0.1 mm - CC	160.1±0.2 mm	CMM - Kubalak
Left conic	1.510±0.086	1.390	CMM - Kubalak
Right radius of curvature	2217±3 mm - CC	2228±17 mm	CMM - Kubalak
Reference annulus	2.90±0.05 mm	6.4 mm	Microscope - Capone
Chamfer	0.355±0.005 mm	0.2 mm	Microscope - Capone

Collimator lens #5

KO Item Code: LBV7948-C

RADIUS	RAD TOL	IRR TOL	C.A. DIA	EDGE DIA	MATERIAL	THICK	THI TOL
95.7403 CX	0.2500	4.00	61.4	79.4000	CAF2_293K	48.1460	0.1000
204.0279 CX	1.0000	4.00	55.8				

1. All dimensions in Millimeters
2. Material Nd tolerance: +/- 0.001
3. Edge diameter tolerance: +/- 0.2 mm
4. Protective chamfer: 0.3 mm x 45 deg
5. Irregularity tolerance in fringes (PTV) @ 632.8 nm
6. Scratch/dig tolerance: 60-40
7. A.R. Coating Wavelengths: 0.9 - 2.4 um
8. Wedge tolerance (ETD): < 0.05 mm



20.00 mm

TITLE Collimator Lens 5			
DATE 2012-08-21	SCALE 1:1	DRAWN J Capone	APPRV
PROJECT RIMAS			
DRAWING	REVISION		

ELF = -159.71 mm @ 1µm
F/# = -2.4273 @ 1µm

Metrology:

Property	Value	Specified	Source
Outer diameter	79.602 mm	79.4±0.2 mm	CMM - Kubalak
Flat to left	44.8338±0.0004 mm		CMM - Kubalak
Flat to right	3.5997±0.0007 mm		CMM - Kubalak
Center thickness	48.4335±0.0008 mm	48.1±0.1 mm	CMM - Kubalak
Edge thickness	35.5±0.2 mm	36.9 mm	Calipers - Capone
Centration - X	9±4 µm	See wedge	CMM - Kubalak
Centration - Y	361±4 µm	See wedge	CMM - Kubalak
Left radius of curvature	95.768±0.008 mm - CX	95.74±0.25 mm	CMM - Kubalak
Right radius of curvature	205.302±0.093 mm - CX	204±1 mm	CMM - Kubalak
Reference annulus	5.82±0.11 mm	6.8 mm	Microscope - Capone
Chamfer	0.402±0.016 mm	0.2 mm	Microscope - Capone

YJ camera lens #1

KO Item Code: LNQ8105-C

RADIUS	RAD TOL	IRR TOL	C.A. DIA	EDGE DIA	MATERIAL	THICK	THI TOL
490.8976 CC	2.5000	4.00	50.8	75.0000	INFRASIL_293K	4.9998	0.0500
120.9321 CC	0.6000	4.00	51.6				

1. All dimensions in Millimeters
 2. Material Nd tolerance: +/- 0.001
 3. Edge diameter tolerance: +/- 0.2 mm
 4. Protective chamfer: 0.3 mm x 45 deg
 5. Irregularity tolerance in fringes (PTV) @ 632.8 nm
 6. Scratch/dig tolerance: 60-40
 7. A.R. Coating Wavelengths: 0.9 - 1.4 um
 8. Wedge tolerance (ETD): < 0.02 mm

20.00 mm

TITLE			
YJ-band Camera Lens 1			
DATE	SCALE	DRAWN	APPRV
2012-08-21	1:1	J Capone	
PROJECT			
RIMAS			
DRAWING		REVISION	

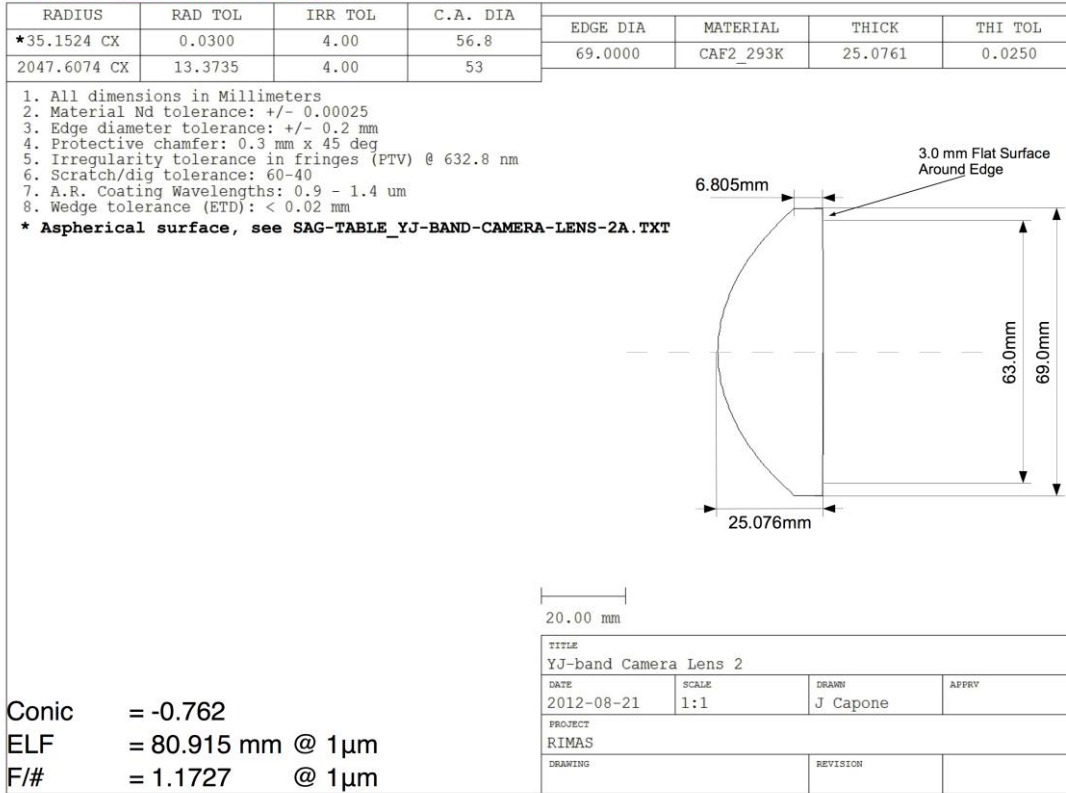
ELF = -215.23 mm @ 1µm
 F/# = -2.8697 @ 1µm

Metrology:

Property	Value	Specified	Source
Outer diameter	75.069 mm	75.0±0.2 mm	CMM - Kubalak
Flat to left	9.1290±0.0004 mm		CMM - Kubalak
Flat to right	4.086±0.001 mm		CMM - Kubalak
Center thickness	5.043±0.001 mm	5.00±0.05 mm	CMM - Kubalak
Edge thickness	10.0±0.2 mm	10.4 mm	Calipers - Capone
Centration - X	436±6 µm	See wedge	CMM - Kubalak
Centration - Y	90±5 µm	See wedge	CMM - Kubalak
Left radius of curvature	490.7±0.3 mm - CC	490.9±2.5 mm	CMM - Kubalak
Right radius of curvature	121.42±0.05 mm - CC	120.9±0.6 mm	CMM - Kubalak
Reference annulus	6.044±0.028 mm	6.7 mm	Microscope - Capone
Chamfer	0.311±0.021 mm	0.2 mm	Microscope - Capone

YJ camera lens #2

KO Item Code: LBV7525-C

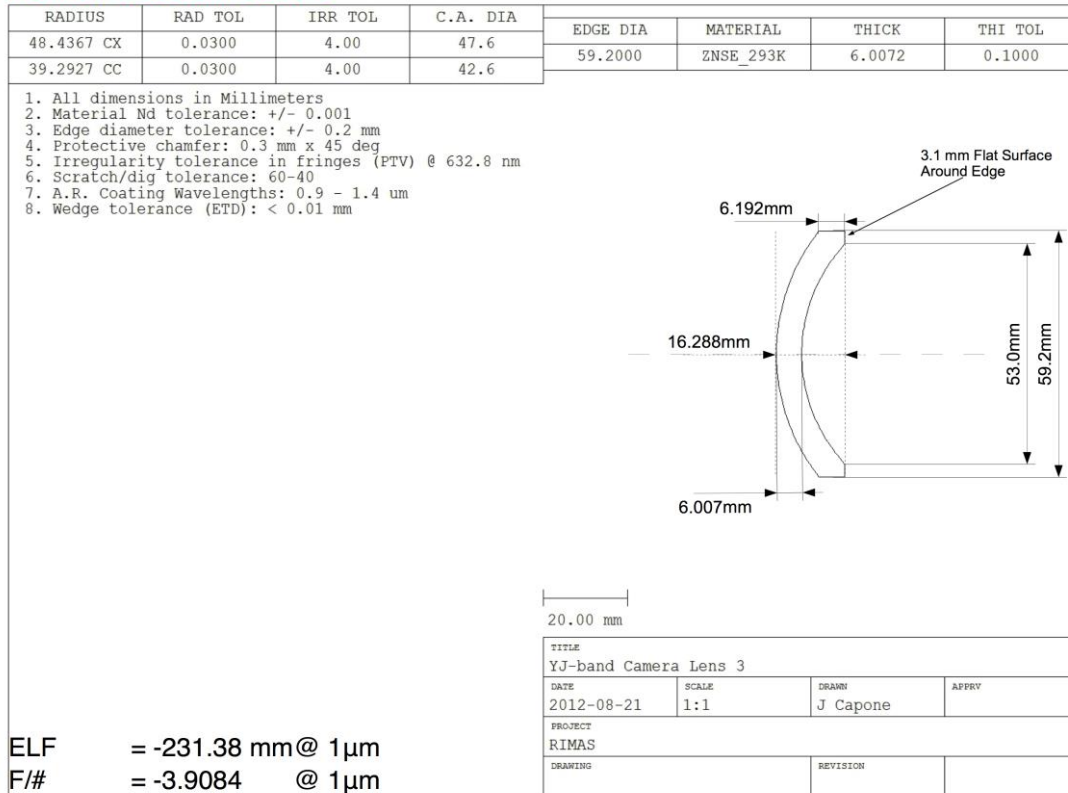


Metrology:

Property	Value	Specified	Source
Outer diameter	68.966 mm	69.0±0.2 mm	CMM - Kubalak
Flat to left	24.781±0.001 mm		CMM - Kubalak
Flat to right	0.2985±0.0002 mm		CMM - Kubalak
Center thickness	25.079±0.001 mm	25.000±0.025 mm	CMM - Kubalak
Edge thickness	5.9±0.2 mm	6.8 mm	Calipers - Capone
Centration - X	78±10 µm	See wedge	CMM - Kubalak
Centration - Y	133±12 µm	See wedge	CMM - Kubalak
Left radius of curvature	35.112±0.014 mm - CX	35.15±0.03 mm	CMM - Kubalak
Left conic	-0.771±0.002	-0.762	CMM - Kubalak
Right radius of curvature	2051±3 mm - CX	2048±13 mm	CMM - Kubalak
Reference annulus	2.99±0.15 mm	3.0 mm	Microscope - Capone
Chamfer	0.189±0.050 mm	0.2 mm	Microscope - Capone

YJ camera lens #3

KO Item Code: LMN6206-C



Metrology:

Property	Value	Specified	Source
Outer diameter	59.026 mm	59.2±0.2 mm	CMM - Kubalak
Flat to left	16.5838±0.0006 mm		CMM - Kubalak
Flat to right	10.5071±0.0007 mm		CMM - Kubalak
Center thickness	6.077±0.001 mm	6.0±0.1 mm	CMM - Kubalak
Edge thickness	5.9±0.2 mm	6.2 mm	Calipers - Capone
Centration - X	12±1 μm	See wedge	CMM - Kubalak
Centration - Y	8±1 μm	See wedge	CMM - Kubalak
Left radius of curvature	48.285±0.005 mm - CX	48.44±0.03 mm	CMM - Kubalak
Right radius of curvature	39.205±0.004 mm - CC	39.29±0.03 mm	CMM - Kubalak
Reference annulus	2.57±0.18 mm	3.1 mm	Microscope - Capone
Chamfer	0.378±0.048 mm	0.2 mm	Microscope - Capone

YJ camera lens #4

KO Item Code: LBV5323-C

RADIUS	RAD TOL	IRR TOL	C.A. DIA	EDGE DIA	MATERIAL	THICK	THI TOL
*40.4251 CX	0.2000	4.00	39.4	49.0000	BAF2_293K	23.0768	0.0500
168.7867 CX	0.5000	4.00	31.2				

1. All dimensions in Millimeters
 2. Material Nd tolerance: +/- 0.001
 3. Edge diameter tolerance: +/- 0.2 mm
 4. Protective chamfer: 0.3 mm x 45 deg
 5. Irregularity tolerance in fringes (PTV) @ 632.8 nm
 6. Scratch/dig tolerance: 60-40
 7. A.R. Coating Wavelengths: 0.9 - 1.4 um
 8. Wedge tolerance (ETD): < 0.02 mm
 * Aspherical surface, see SAG-TABLE_YJ-BAND-CAMERA-LENS-4A.TXT

5.1 mm Flat Surface Around Edge

14.268mm

23.077mm

38.8mm

49.0mm

20.00 mm

TITLE
YJ-band Camera Lens 4

DATE	SCALE	DRAWN	APPRV
2012-08-21	1:1	J Capone	

PROJECT
RIMAS

DRAWING	REVISION

Conic = -0.636
 ELF = 72.165 mm @ 1µm
 F/# = 1.4728 @ 1µm

Metrology:

Property	Value	Specified	Source
Outer diameter	48.972 mm	49.0±0.2 mm	CMM - Kubalak
Flat to left	21.9737±0.0007 mm		CMM - Kubalak
Flat to right	1.1108±0.0007 mm		CMM - Kubalak
Center thickness	23.085±0.001 mm	23.08±0.05 mm	CMM - Kubalak
Edge thickness	14.1±0.2 mm	14.3 mm	Calipers - Capone
Centration - X	7.9±0.8 µm	See wedge	CMM - Kubalak
Centration - Y	1.5±1.0 µm	See wedge	CMM - Kubalak
Left radius of curvature	40.398±0.019 mm - CX	40.4±0.2 mm	CMM - Kubalak
Left conic	-0.644±0.005	-0.636	CMM - Kubalak
Right radius of curvature	168.8±0.2 mm - CX	168.8±0.5 mm	CMM - Kubalak
Reference annulus	4.71±0.14 mm	5.1 mm	Microscope - Capone
Chamfer	0.313±0.013 mm	0.2 mm	Microscope - Capone

YJ camera lens #5

KO Item Code: LNQ2808-C

RADIUS	RAD TOL	IRR TOL	C.A. DIA	EDGE DIA	MATERIAL	THICK	THI TOL
26.9446 CC	0.0500	4.00	19.4	26.8000	CAF2_293K	8.0243	0.1000
126.9952 CC	0.4000	4.00	16.6				

1. All dimensions in Millimeters
 2. Material Nd tolerance: +/- 0.001
 3. Edge diameter tolerance: +/- 0.2 mm
 4. Protective chamfer: 0.3 mm x 45 deg
 5. Irregularity tolerance in fringes (PTV) @ 632.8 nm
 6. Scratch/dig tolerance: 60-40
 7. A.R. Coating Wavelengths: 0.9 - 1.4 um
 8. Wedge tolerance (ETD): < 0.02 mm

20.00 mm

TITLE YJ-band Camera Lens 5			
DATE 2012-08-21	SCALE 1:1	DRAWN J Capone	APPRV
PROJECT RIMAS			
DRAWING	REVISION		

ELF = -51.058 mm @ 1µm
 F/# = -1.9051 @ 1µm

Metrology:

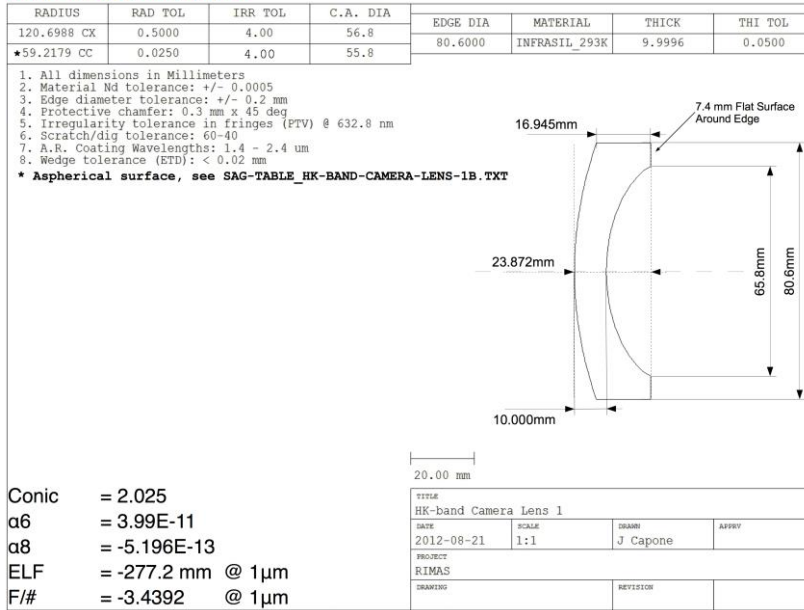
Property	Value	Specified	Source
Outer diameter	26.578 mm	26.8±0.2 mm	CMM - Kubalak
Flat to left	8.5566±0.0004 mm		CMM - Kubalak
Flat to right	0.3475±0.0004 mm		CMM - Kubalak
Center thickness	8.2091±0.0006 mm	8.0±0.1 mm	CMM - Kubalak
Edge thickness	11.4±0.2 mm	12.0 mm	Calipers - Capone
Centration - X	71±5 µm	See wedge	CMM - Kubalak
Centration - Y	3±5 µm	See wedge	CMM - Kubalak
Left radius of curvature	26.980±0.007 mm - CC	26.94±0.05 mm	CMM - Kubalak
Right radius of curvature	129.0±0.3 mm - CC	127.0±0.4 mm	CMM - Kubalak
Reference annulus	3.51±0.13 mm	3.0 mm	Microscope - Capone
Chamfer	0.381±0.047 mm	0.2 mm	Microscope - Capone

Damage:

No damage found by quick visual inspection.

HK camera lens #1

KO Item Code: LMN8010-C

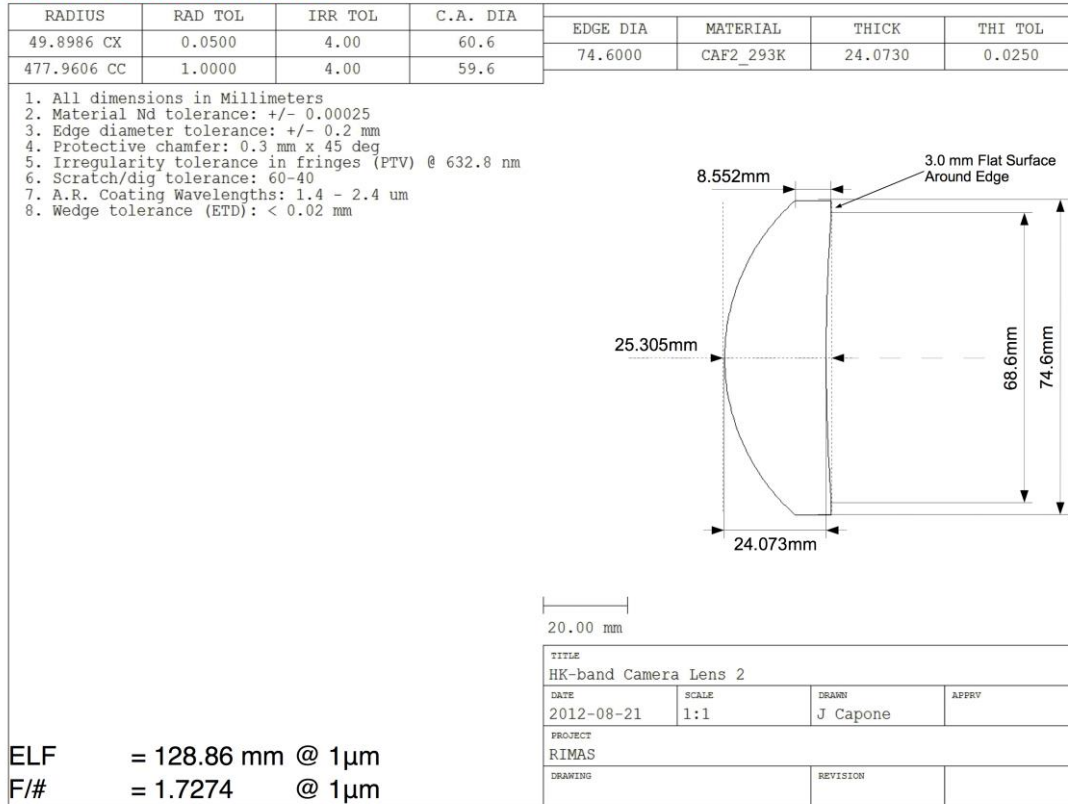


Metrology:

Property	Value	Specified	Source
Outer diameter	80.633 mm	80.0±0.2 mm	CMM - Kubalak
Flat to left	25.3359±0.0004 mm		CMM - Kubalak
Flat to right	15.252±0.003 mm		CMM - Kubalak
Center thickness	10.083±0.003 mm	10.00±0.05 mm	CMM - Kubalak
Edge thickness	18.1±0.2 mm	16.9 mm	Calipers - Capone
Centration - X	4±2 µm	See wedge	CMM - Kubalak
Centration - Y	19±2 µm	See wedge	CMM - Kubalak
Left radius of curvature	120.631±0.014 mm - CX	120.7±0.05 mm	CMM - Kubalak
Right radius of curvature	59.3±0.1 mm - CC	59.218±0.025 mm	CMM - Kubalak
Right conic	2.108±0.016	2.025	CMM - Kubalak
Right α ₆	3.9E-11±7.7E-11 mm	3.99E-11	CMM - Kubalak
Right α ₈	-7.15E-13±0.75E-13 mm	-5.196E-13	CMM - Kubalak
Reference annulus	6.454±0.014 mm	7.4 mm	Microscope - Capone
Chamfer	0.363±0.028 mm	0.2 mm	Microscope - Capone

HK camera lens #2

KO Item Code: LCM7524-C



Metrology:

Property	Value	Specified	Source
Outer diameter	74.467 mm	74.6±0.2 mm	CMM - Kubalak
Flat to left	24.9595±0.0007 mm		CMM - Kubalak
Flat to right	1.1725±0.0006 mm		CMM - Kubalak
Center thickness	23.7870±0.0009 mm	24.073±0.025 mm	CMM - Kubalak
Edge thickness	8.8±0.2 mm	8.6 mm	Calipers - Capone
Centration - X	848±7 μm	See wedge	CMM - Kubalak
Centration - Y	814±8 μm	See wedge	CMM - Kubalak
Left radius of curvature	50.052±0.003 mm - CX	49.90±0.05 mm	CMM - Kubalak
Right radius of curvature	485.7±0.4 mm - CX	478±1 mm	CMM - Kubalak
Reference annulus	2.968±0.013 mm	3.0 mm	Microscope - Capone
Chamfer	0.447±0.011 mm	0.2 mm	Microscope - Capone

HK camera lens #3

KO Item Code: LMN6906-C

RADIUS	RAD TOL	IRR TOL	C.A. DIA	EDGE DIA	MATERIAL	THICK	THI TOL
51.8908 CX	0.0300	2.00	59	68.6000	ZNSE_293K	6.0072	0.0500
42.5306 CC	0.0250	2.00	54				

1. All dimensions in Millimeters
 2. Material Nd tolerance: +/- 0.001
 3. Edge diameter tolerance: +/- 0.2 mm
 4. Protective chamfer: 0.3 mm x 45 deg
 5. Irregularity tolerance in fringes (PTV) @ 632.8 nm
 6. Scratch/dig tolerance: 60-40
 7. A.R. Coating Wavelengths: 1.4 - 2.4 um
 8. Wedge tolerance (ETD): < 0.01 mm

20.00 mm

TITLE			
HK-band Camera Lens 3			
DATE	SCALE	DRAWN	APPRV
2012-08-21	1:1	J Capone	
PROJECT			
RIMAS			
DRAWING		REVISION	

ELF = -262.18 mm @ 1µm
 F/# = -3.8219 @ 1µm

Metrology:

Property	Value	Specified	Source
Outer diameter	68.513 mm	68.6±0.2 mm	CMM - Kubalak
Flat to left	19.723±0.001 mm		CMM - Kubalak
Flat to right	13.758±0.001 mm		CMM - Kubalak
Center thickness	5.966±0.001 mm	6.01±0.05 mm	CMM - Kubalak
Edge thickness	6.4±0.2 mm	6.8 mm	Calipers - Capone
Centration - X	15±2 µm	See wedge	CMM - Kubalak
Centration - Y	2±2 µm	See wedge	CMM - Kubalak
Left radius of curvature	51.947±0.006 mm - CX	51.89±0.03 mm	CMM - Kubalak
Right radius of curvature	42.536±0.005 mm - CC	42.531±0.025 mm	CMM - Kubalak
Reference annulus	2.56±0.02 mm	3.0 mm	Microscope - Capone
Chamfer	0.357±0.026 mm	0.2 mm	Microscope - Capone

HK camera lens #4

KO Item Code: LBV6335-C

RADIUS	RAD TOL	IRR TOL	C.A. DIA	EDGE DIA	MATERIAL	THICK	THI TOL
50.4896 CX	0.1000	4.00	56.8	62.6000	BAF2_293K	35.1168	0.0500
*42.2620 CX	0.0800	4.00	52.4				

1. All dimensions in Millimeters
 2. Material Nd tolerance: +/- 0.00025
 3. Edge diameter tolerance: +/- 0.2 mm
 4. Protective chamfer: 0.3 mm x 45 deg
 5. Irregularity tolerance in fringes (PTV) @ 632.8 nm
 6. Scratch/dig tolerance: 60-40
 7. A.R. Coating Wavelengths: 1.4 - 2.4 um
 8. Wedge tolerance (ETD): < 0.01 mm
 * Aspherical surface, see SAG-TABLE_HK-BAND-CAMERA-LENS-4B.TXT

15.603mm
 3.0 mm Flat Surface Around Edge
 56.6mm
 62.6mm
 35.117mm
 20.00 mm

TITLE			
HK-band Camera Lens 4			
DATE	SCALE	DRAWN	APPRV
2012-08-21	1:1	J Capone	
PROJECT			
RIMAS			
DRAWING		REVISION	

Conic = -1.943
 ELF = 56.153 mm @ 1µm
 F/# = 0.89702 @ 1µm

Metrology:

Property	Value	Specified	Source
Outer diameter	62.562 mm	62.6±0.2 mm	CMM - Kubalak
Flat to left	26.5352±0.0005 mm		CMM - Kubalak
Flat to right	8.545±0.001 mm		CMM - Kubalak
Center thickness	35.080±0.001 mm	35.12±0.05 mm	CMM - Kubalak
Edge thickness	15.1±0.2 mm	15.6 mm	Calipers - Capone
Centration - X	3±1 µm	See wedge	CMM - Kubalak
Centration - Y	15±1 µm	See wedge	CMM - Kubalak
Left radius of curvature	50.570±0.004 mm - CX	50.5±0.1 mm	CMM - Kubalak
Right radius of curvature	42.196±0.038 mm - CX	42.26±0.08 mm	CMM - Kubalak
Right conic	-1.97±0.01	-1.943	CMM - Kubalak
Reference annulus	2.84±0.3 mm	3.0 mm	Microscope - Capone
Chamfer	0.198±0.023 mm	0.2 mm	Microscope - Capone

HK camera lens #5

KO Item Code: LNQ3105-C

RADIUS	RAD TOL	IRR TOL	C.A. DIA	EDGE DIA	MATERIAL	THICK	THI TOL
*28.2232 CC	0.0500	4.00	23	31.0000	CAF2_293K	5.0152	0.1000
71.2647 CC	0.7500	4.00	20				

1. All dimensions in Millimeters
 2. Material Nd tolerance: +/- 0.001
 3. Edge diameter tolerance: +/- 0.2 mm
 4. Protective chamfer: 0.3 mm x 45 deg
 5. Irregularity tolerance in fringes (PTV) @ 632.8 nm
 6. Scratch/dig tolerance: 60-40
 7. A.R. Coating Wavelengths: 1.4 - 2.4 um
 8. Wedge tolerance (ETD): < 0.02 mm

* Aspherical surface, see SAG-TABLE_HK-BAND-CAMERA-LENS-5A.TXT

Conic = -0.986
 ELF = -46.838 mm@ 1µm
 F/# = -1.5109 @ 1µm

TITLE			
HK-band Camera Lens 5			
DATE	SCALE	DRAWN	APPRV
2012-08-21	1:1	J Capone	
PROJECT			
RIMAS			
DRAWING		REVISION	

Metrology:

Property	Value	Specified	Source
Outer diameter	30.987 mm	31.0±0.2 mm	CMM - Kubalak
Flat to left	6.1743±0.0008 mm		CMM - Kubalak
Flat to right	1.1473±0.0009 mm		CMM - Kubalak
Center thickness	5.027±0.001 mm	5.0±0.1 mm	CMM - Kubalak
Edge thickness	10.0±0.2 mm	10.4 mm	Calipers - Capone
Centration - X	5±4 µm	See wedge	CMM - Kubalak
Centration - Y	17±5 µm	See wedge	CMM - Kubalak
Left radius of curvature	28.20±0.03 mm - CC	28.22±0.05 mm	CMM - Kubalak
Left conic	-0.99±0.02	-0.986	CMM - Kubalak
Right radius of curvature	71.2±0.1 mm - CX	71.26±0.75 mm	CMM - Kubalak
Reference annulus	2.45±0.02 mm	3.0 mm	Microscope - Capone
Chamfer	0.263±0.015 mm	0.2 mm	Microscope - Capone

Bibliography

- Abazajian, K. N. , Adelman-McCarthy, J. K. , Agüeros, M. A. , Allam, S. S. , Allende Prieto, C. , An, D. , Anderson, K. S. J. , Anderson, S. F. , Annis, J. , Bahcall, N. A. , and et al. *ApJS*, 182:543–558, June 2009.
- Allen, J. R. , O’Brien, K. , Lynn, J. D. , Thatte, N. A. , Bryson, I. , Clarke, F. , Schnetler, H. , and Tecza, M. . In *Ground-based and Airborne Instrumentation for Astronomy V*, volume 9147 of Proc. SPIE, page 91479M, July 2014.
- Arnaud, K. A. . In Jacoby, G. H. and Barnes, J. , editors, *Astronomical Data Analysis Software and Systems V*, volume 101 of *Astronomical Society of the Pacific Conference Series*, page 17, 1996.
- Arp, V. , Wilson, J. H. , Winrich, L. , and Sikora, P. . *Cryogenics*, 2(4):230–235, Jun 1962.
- Band, D. , Matteson, J. , Ford, L. , Schaefer, B. , Palmer, D. , Teegarden, B. , Cline, T. , Briggs, M. , Paciesas, W. , Pendleton, G. , Fishman, G. , Kouveliotou, C. , Meegan, C. , Wilson, R. , and Lestrade, P. . *ApJ*, 413:281–292, August 1993.
- Barnard, E. E. . *ApJ*, 25, April 1907.
- Barniol Duran, R. , Nakar, E. , and Piran, T. . *ApJ*, 772:78, July 2013.
- Barniol Duran, R. and Piran, T. . *ApJ*, 770:146, June 2013.
- Barthelmy, S. D. , Barbier, L. M. , Cummings, J. R. , Fenimore, E. E. , Gehrels, N. , Hullinger, D. , Krimm, H. A. , Markwardt, C. B. , Palmer, D. M. , Parsons, A. , Sato, G. , Suzuki, M. , Takahashi, T. , Tashiro, M. , and Tueller, J. . *Space Sci. Rev.*, 120:143–164, October 2005.
- Baumgartner, W. H. , Barthelmy, S. D. , Cummings, J. R. , Gehrels, N. , Krimm, H. A. , Lien, A. Y. , Markwardt, C. B. , Marshall, F. E. , Palmer, D. M. , Sakamoto, T. , Stamatikos, M. , Tueller, J. , and Ukwatta, T. N. . *GRB Coordinates Network*, 16127, 2014.

- Beardmore, A. P. , Barthelmy, S. D. , Chester, M. M. , Gehrels, N. , Kennea, J. A. , Krimm, H. A. , Kuin, N. P. M. , Littlejohns, O. M. , Marshall, F. E. , Page, K. L. , Siegel, M. H. , Swenson, C. A. , and Ukwatta, T. N. . *GRB Coordinates Network*, 12859, 2012.
- Bertin, E. . In Gabriel, C. , Arviset, C. , Ponz, D. , and Enrique, S. , editors, *Astronomical Data Analysis Software and Systems XV*, volume 351 of *Astronomical Society of the Pacific Conference Series*, page 112, July 2006.
- Bertin, E. and Arnouts, S. . *A&AS*, 117:393–404, June 1996.
- Bida, T. A. , Dunham, E. W. , Bright, L. P. , and Corson, C. . In J. M. Oschmann Jr., editor, *Society of Photo-Optical Instrumentation Engineers (SPIE) Conference Series*, volume 5489 of *Society of Photo-Optical Instrumentation Engineers (SPIE) Conference Series*, pages 196–206, October 2004.
- Bonnell, J. T. and Klebesadel, R. W. . In Kouveliotou, C. , Briggs, M. F. , and Fishman, G. J. , editors, *American Institute of Physics Conference Series*, volume 384 of *American Institute of Physics Conference Series*, pages 977–980, August 1996.
- Bouwens, R. J. , Bradley, L. , Zitrin, A. , Coe, D. , Franx, M. , Zheng, W. , Smit, R. , Host, O. , Postman, M. , Moustakas, L. , Labbé, I. , Carrasco, M. , Molino, A. , Donahue, M. , Kelson, D. D. , Meneghetti, M. , Benítez, N. , Lemze, D. , Umetsu, K. , Broadhurst, T. , Moustakas, J. , Rosati, P. , Jouvel, S. , Bartelmann, M. , Ford, H. , Graves, G. , Grillo, C. , Infante, L. , Jimenez-Teja, Y. , Lahav, O. , Maoz, D. , Medezinski, E. , Melchior, P. , Merten, J. , Nonino, M. , Ogaz, S. , and Seitz, S. . *ApJ*, 795:126, November 2014.
- Boyd, R. W. . *Journal of the Optical Society of America (1917-1983)*, 68:877–883, July 1978.
- Brainerd, J. J. and Lamb, D. Q. . *ApJ*, 313:231–262, February 1987.
- Browder, James Steve and Ballard, Stanley S. . *Appl. Opt.*, 8(4):793–798, Apr 1969. <http://ao.osa.org/abstract.cfm?URI=ao-8-4-793>.
- Burrows, D. N. , Hill, J. E. , Nousek, J. A. , Kennea, J. A. , Wells, A. , Osborne, J. P. , Abbey, A. F. , Beardmore, A. , Mukerjee, K. , Short, A. D. T. , Chincarini, G. , Campana, S. , Citterio, O. , Moretti, A. , Pagani, C. , Tagliaferri, G. , Giommi, P. , Capalbi, M. , Tamburelli, F. , Angelini, L. , Cusumano, G. , Bräuninger, H. W. , Burkert, W. , and Hartner, G. D. . *Space Sci. Rev.*, 120:165–195, October 2005.
- Butler, N. , Klein, C. , Fox, O. , Lotkin, G. , Bloom, J. , Prochaska, J. X. , Ramirez-Ruiz, E. , de Diego, J. A. , Georgiev, L. , González, J. , Lee, W. H. , Richer, M. G. , Román, C. , Watson, A. M. , Gehrels, N. , Kutyrev, A. , Bernstein, R. , Alvarez, L. C. , Ceseña, U. , Clark, D. , Colorado, E. , Córdova, A. , Farah, A. , García, B. , Guisa, G. , Herrera, J. , Lazo, F. , López, E. , Luna, E. , Martínez,

- B. , Murillo, F. , Murillo, J. M. , Núñez, J. M. , Pedrayes, M. H. , Quirós, F. , Ochoa, J. L. , Sierra, G. , Moseley, H. , Rapchun, D. , Robinson, F. D. , Samuel, M. V. , and Sparr, L. M. . In *Ground-based and Airborne Instrumentation for Astronomy IV*, volume 8446 of Proc. SPIE, page 844610, September 2012.
- Butler, N. , Watson, A. M. , Kuttyrev, A. , Lee, W. H. , Richer, M. G. , Klein, C. , Fox, O. , Prochaska, J. X. , Bloom, J. , Cucchiara, A. , Troja, E. , Littlejohns, O. , Ramirez-Ruiz, E. , de Diego, J. A. , Georgiev, L. , Gonzalez, J. , Roman-Zuniga, C. , Gehrels, N. , and Moseley, H. . *GRB Coordinates Network*, 16121, 2014.
- Capone, J. , Kuttyrev, A. , Veilleux, S. , Toy, V. , Robinson, F. D. , Lotkin, G. N. , Moseley, S. H. , Gehrels, N. , and Vogel, S. N. . In *American Astronomical Society Meeting Abstracts #223*, volume 223 of *American Astronomical Society Meeting Abstracts*, page 148.03, January 2014a.
- Capone, J. and RIMAS Collaboration, R. p. T. . In *American Astronomical Society Meeting Abstracts*, volume 227 of *American Astronomical Society Meeting Abstracts*, page 427.04, January 2016.
- Capone, J. I. , Content, D. A. , Fox, O. D. , Gehrels, N. A. , Kuttyrev, A. S. , Lotkin, G. N. , Moseley, S. H. , Robinson, F. D. , Toy, V. L. , Veilleux, S. , and Vogel, S. N. . In *Cryogenic Optical Systems and Instruments 2013*, volume 8863 of Proc. SPIE, page 88630D, September 2013.
- Capone, J. I. , Content, D. A. , Kuttyrev, A. S. , Robinson, F. D. , Lotkin, G. N. , Toy, V. L. , Veilleux, S. , Moseley, S. H. , Gehrels, N. A. , and Vogel, S. N. . In *Ground-based and Airborne Instrumentation for Astronomy V*, volume 9147 of Proc. SPIE, page 914736, July 2014b.
- Capone, J. I. , Content, D. A. , Kuttyrev, A. S. , Veilleux, S. , Moseley, S. H. , and Gehrels, N. A. . In *American Astronomical Society Meeting Abstracts*, volume 219 of *American Astronomical Society Meeting Abstracts*, page 446.14, January 2012. Poster session.
- Cenko, S. B. , Kelemen, J. , Harrison, F. A. , Fox, D. B. , Kulkarni, S. R. , Kasliwal, M. M. , Ofek, E. O. , Rau, A. , Gal-Yam, A. , Frail, D. A. , and Moon, D.-S. . *ApJ*, 693:1484–1493, March 2009.
- Cenko, S. B. , Toy, V. , Kuttyrev, A. , Capone, J. , Troja, E. , Cucchiara, A. , Veilleux, S. , and Gezari, S. . *GRB Coordinates Network*, 15838, 2014.
- Chornock, R. , Berger, E. , Fox, D. B. , Lunnan, R. , Drout, M. R. , Fong, W.-f. , Laskar, T. , and Roth, K. C. . *ApJ*, 774:26, September 2013.
- Clemens, D. P. , Sarcia, D. , Grabau, A. , Tollestrup, E. V. , Buie, M. W. , Dunham, E. , and Taylor, B. . *PASP*, 119:1385–1402, December 2007.
- Cline, T. L. , Desai, U. D. , Klebesadel, R. W. , and Strong, I. B. . *ApJ*, 185:L1, October 1973.

- Corruccini, R.J. and Gniewek, J.J. . *Thermal expansion of technical solids at low temperatures: a compilation from the literature*. National Bureau of Standards monograph. U.S. Dept. of Commerce, National Bureau of Standards, 1961. <https://books.google.com/books?id=kmt4Mnc6J5EC>.
- Costa, E. , Frontera, F. , Heise, J. , Feroci, M. , in't Zand, J. , Fiore, F. , Cinti, M. N. , Dal Fiume, D. , Nicastro, L. , Orlandini, M. , Palazzi, E. , Rapisarda#, M. , Zavattini, G. , Jager, R. , Parmar, A. , Owens, A. , Molendi, S. , Cusumano, G. , Maccarone, M. C. , Giarrusso, S. , Coletta, A. , Antonelli, L. A. , Giommi, P. , Muller, J. M. , Piro, L. , and Butler, R. C. . *Nature*, 387:783–785, June 1997.
- Craven, Peter and Wahba, Grace . *Numerische Mathematik*, 31(4):377–403, December 1978. ISSN 0945-3245. <http://dx.doi.org/10.1007/BF01404567>.
- Cucchiara, A. , Fumagalli, M. , Rafelski, M. , Kocevski, D. , Prochaska, J. X. , Cooke, R. J. , and Becker, G. D. . *ApJ*, 804:51, May 2015.
- Cucchiara, A. , Levan, A. J. , Fox, D. B. , Tanvir, N. R. , Ukwatta, T. N. , Berger, E. , Krühler, T. , Küpcü Yoldaş, A. , Wu, X. F. , Toma, K. , Greiner, J. , Olivares, F. E. , Rowlinson, A. , Amati, L. , Sakamoto, T. , Roth, K. , Stephens, A. , Fritz, A. , Fynbo, J. P. U. , Hjorth, J. , Malesani, D. , Jakobsson, P. , Wiersema, K. , O'Brien, P. T. , Soderberg, A. M. , Foley, R. J. , Fruchter, A. S. , Rhoads, J. , Rutledge, R. E. , Schmidt, B. P. , Dopita, M. A. , Podsiadlowski, P. , Willingale, R. , Wolf, C. , Kulkarni, S. R. , and D'Avanzo, P. . *ApJ*, 736:7, July 2011.
- Cucchiara, A. and Prochaska, J. X. . *GRB Coordinates Network*, 12865, 2012.
- Draine, B. T. . *Physics of the Interstellar and Intergalactic Medium*. 2011.
- Evans, P. A. , Beardmore, A. P. , Page, K. L. , Osborne, J. P. , O'Brien, P. T. , Willingale, R. , Starling, R. L. C. , Burrows, D. N. , Godet, O. , Vetere, L. , Racusin, J. , Goad, M. R. , Wiersema, K. , Angelini, L. , Capalbi, M. , Chincarini, G. , Gehrels, N. , Kennea, J. A. , Margutti, R. , Morris, D. C. , Mountford, C. J. , Pagani, C. , Perri, M. , Romano, P. , and Tanvir, N. . *MNRAS*, 397:1177–1201, August 2009.
- Evans, P. A. , Beardmore, A. P. , Page, K. L. , Tyler, L. G. , Osborne, J. P. , Goad, M. R. , O'Brien, P. T. , Vetere, L. , Racusin, J. , Morris, D. , Burrows, D. N. , Capalbi, M. , Perri, M. , Gehrels, N. , and Romano, P. . *A&A*, 469:379–385, July 2007.
- Fan, X. , Carilli, C. L. , and Keating, B. . *ARA&A*, 44:415–462, September 2006.
- Feldman, A. , Horowitz, D. , Waxler, R. M. , and Dodge, M. J. . Technical report, 1978.
- Fitzpatrick, E. L. . *PASP*, 111:63–75, January 1999.

- Foreman-Mackey, D. , Hogg, D. W. , Lang, D. , and Goodman, J. . *PASP*, 125: 306–312, March 2013.
- Foreman-Mackey, D. , Price-Whelan, A. , Ryan, G. , Emily, Smith, M. , Barbary, K. , Hogg, D. W. , and Brewer, B. J. . 2014. <http://dx.doi.org/10.5281/zenodo.11020>.
- Fox, D. B. and Roming, P. W. A. . *Philosophical Transactions of the Royal Society of London Series A*, 365:1293–1305, May 2007.
- Frail, D. A. , Waxman, E. , and Kulkarni, S. R. . *ApJ*, 537:191–204, July 2000.
- Frederiks, D. D. , Hurley, K. , Svinkin, D. S. , Pal’shin, V. D. , Mangano, V. , Oates, S. , Aptekar, R. L. , Golenetskii, S. V. , Mazets, E. P. , Oleynik, P. P. , Tsvetkova, A. E. , Ulanov, M. V. , Kokomov, A. A. , Cline, T. L. , Burrows, D. N. , Krimm, H. A. , Pagani, C. , Sbarufatti, B. , Siegel, M. H. , Mitrofanov, I. G. , Golovin, D. , Litvak, M. L. , Sanin, A. B. , Boynton, W. , Fellows, C. , Harshman, K. , Enos, H. , Starr, R. , von Kienlin, A. , Rau, A. , Zhang, X. , and Goldstein, J. . *ApJ*, 779:151, December 2013.
- Fukugita, M. , Ichikawa, T. , Gunn, J. E. , Doi, M. , Shimasaku, K. , and Schneider, D. P. . *AJ*, 111:1748, April 1996.
- Fynbo, J. P. U. , Jakobsson, P. , Prochaska, J. X. , Malesani, D. , Ledoux, C. , de Ugarte Postigo, A. , Nardini, M. , Vreeswijk, P. M. , Wiersema, K. , Hjorth, J. , Sollerman, J. , Chen, H.-W. , Thöne, C. C. , Björnsson, G. , Bloom, J. S. , Castro-Tirado, A. J. , Christensen, L. , De Cia, A. , Fruchter, A. S. , Gorosabel, J. , Graham, J. F. , Jaunsen, A. O. , Jensen, B. L. , Kann, D. A. , Kouveliotou, C. , Levan, A. J. , Maund, J. , Masetti, N. , Milvang-Jensen, B. , Palazzi, E. , Perley, D. A. , Pian, E. , Rol, E. , Schady, P. , Starling, R. L. C. , Tanvir, N. R. , Watson, D. J. , Xu, D. , Augusteijn, T. , Grundahl, F. , Telting, J. , and Quirion, P.-O. . *ApJS*, 185:526–573, December 2009.
- Galama, T. J. , Vreeswijk, P. M. , van Paradijs, J. , Kouveliotou, C. , Augusteijn, T. , Bönhardt, H. , Brewer, J. P. , Doublier, V. , Gonzalez, J.-F. , Leibundgut, B. , Lidman, C. , Hainaut, O. R. , Patat, F. , Heise, J. , in’t Zand, J. , Hurley, K. , Groot, P. J. , Strom, R. G. , Mazzali, P. A. , Iwamoto, K. , Nomoto, K. , Umeda, H. , Nakamura, T. , Young, T. R. , Suzuki, T. , Shigeyama, T. , Koshut, T. , Kippen, M. , Robinson, C. , de Wildt, P. , Wijers, R. A. M. J. , Tanvir, N. , Greiner, J. , Pian, E. , Palazzi, E. , Frontera, F. , Masetti, N. , Nicastro, L. , Feroci, M. , Costa, E. , Piro, L. , Peterson, B. A. , Tinney, C. , Boyle, B. , Cannon, R. , Stathakis, R. , Sadler, E. , Begam, M. C. , and Ianna, P. . *Nature*, 395:670–672, October 1998.
- Gehrels, N. , Chincarini, G. , Giommi, P. , et al. *ApJ*, 611:1005–1020, August 2004.
- Gehrels, N. , Piro, L. , and Leonard, P. J. T. . *Scientific American*, 287(6), 2002.

- Goodman, J. . ApJ, 308:L47–L50, September 1986.
- Gordon, K. D. , Clayton, G. C. , Misselt, K. A. , Landolt, A. U. , and Wolff, M. J. . ApJ, 594:279–293, September 2003.
- Granot, J. and Sari, R. . ApJ, 568:820–829, April 2002.
- Greiner, J. , Krühler, T. , Klose, S. , Afonso, P. , Clemens, C. , Filgas, R. , Hartmann, D. H. , Küpcü Yoldaş, A. , Nardini, M. , Olivares E., F. , Rau, A. , Rossi, A. , Schady, P. , and Updike, A. . A&A, 526:A30, February 2011.
- Hewett, P. C. , Warren, S. J. , Leggett, S. K. , and Hodgkin, S. T. . *MNRAS*, 367: 454–468, April 2006.
- Hjorth, J. , Sollerman, J. , Møller, P. , Fynbo, J. P. U. , Woosley, S. E. , Kouveliotou, C. , Tanvir, N. R. , Greiner, J. , Andersen, M. I. , Castro-Tirado, A. J. , Castro Cerón, J. M. , Fruchter, A. S. , Gorosabel, J. , Jakobsson, P. , Kaper, L. , Klose, S. , Masetti, N. , Pedersen, H. , Pedersen, K. , Pian, E. , Palazzi, E. , Rhoads, J. E. , Rol, E. , van den Heuvel, E. P. J. , Vreeswijk, P. M. , Watson, D. , and Wijers, R. A. M. J. . *Nature*, 423:847–850, June 2003.
- Hook, I. M. , Jørgensen, I. , Allington-Smith, J. R. , Davies, R. L. , Metcalfe, N. , Murowinski, R. G. , and Crampton, D. . *PASP*, 116:425–440, May 2004.
- Jakobsson, P. , Hjorth, J. , Fynbo, J. P. U. , Watson, D. , Pedersen, K. , Björnsson, G. , and Gorosabel, J. . ApJ, 617:L21–L24, December 2004.
- Jensen, J. E. , Tuttle, W. A. , Stewart, R.B. , Brechna, H. , and Prodel, A. G. . 1, August 1980.
- Jorgenson, R. A. , Murphy, M. T. , and Thompson, R. . *MNRAS*, 435:482–501, October 2013.
- Kim, Y. , Im, M. , Jeon, Y. , Kim, M. , Choi, C. , Hong, J. , Hyun, M. , Jun, H. D. , Karouzos, M. , Kim, D. , Kim, D. , Kim, J.-W. , Kim, J. H. , Lee, S.-K. , Pak, S. , Park, W.-K. , Taak, Y. C. , and Yoon, Y. . ApJ, 813:L35, November 2015.
- Kirby, Richard K. . *Journal of Research of the National Bureau of Standards*, 57(2): 91–94, 1956.
- Klebesadel, R. W. , Strong, I. B. , and Olson, R. A. . ApJ, 182:L85, June 1973.
- Kobayashi, S. and Sari, R. . ApJ, 542:819–828, October 2000.
- Kouveliotou, C. , Meegan, C. A. , Fishman, G. J. , Bhat, N. P. , Briggs, M. S. , Koshut, T. M. , Paciesas, W. S. , and Pendleton, G. N. . ApJ, 413:L101–L104, August 1993.
- Krolik, J. H. and Pier, E. A. . ApJ, 373:277–284, May 1991.

- Krühler, T. , Küpcü Yoldaş, A. , Greiner, J. , Clemens, C. , McBreen, S. , Primak, N. , Savaglio, S. , Yoldaş, A. , Szokoly, G. P. , and Klose, S. . *ApJ*, 685:376–383, September 2008.
- Kuin, N. P. M. and Marshall, F. E. . *GRB Coordinates Network*, 16130, 2014.
- Kutyrev, A. S. , Lotkin, G. , and Capone, J. I. . 2012. Occurred at GSFC.
- Kutyrev, A. S. and Robinson, D. . 2012. Tests done at GSFC.
- Kuzmenko, P. J. , Little, S. L. , Little, L. M. , Wilson, J. C. , Skrutskie, M. F. , Hinz, P. M. , Leisenring, J. M. , and Durney, O. . In *Modern Technologies in Space- and Ground-based Telescopes and Instrumentation II*, volume 8450 of Proc. SPIE, page 84503P, September 2012.
- Kvamme, E. T. , Trevias, D. , Simonson, R. , and Sokolsky, L. . In Hatheway, A. E. , editor, *Optomechanics 2005*, volume 5877 of Proc. SPIE, pages 276–286, August 2005.
- Lamb, D. Q. and Reichart, D. E. . *ApJ*, 536:1–18, June 2000.
- Laquer, H.L. and Head, E.L. . *LOW TEMPERATURE THERMAL EXPANSION OF PLASTICS*. Oct 1952.
- Leviton, D. B. , Frey, B. J. , and Kvamme, T. . In J. B. Heaney & L. G. Burriesci, editor, *Society of Photo-Optical Instrumentation Engineers (SPIE) Conference Series*, volume 5904 of *Society of Photo-Optical Instrumentation Engineers (SPIE) Conference Series*, pages 222–233, August 2005.
- Leviton, D. B. , Frey, B. J. , and Madison, T. J. . In *Society of Photo-Optical Instrumentation Engineers (SPIE) Conference Series*, volume 6273 of *Society of Photo-Optical Instrumentation Engineers (SPIE) Conference Series*, July 2006.
- Leviton, D. B. , Frey, B. J. , and Madison, T. J. . In *Society of Photo-Optical Instrumentation Engineers (SPIE) Conference Series*, volume 6692 of *Society of Photo-Optical Instrumentation Engineers (SPIE) Conference Series*, October 2007a.
- Leviton, D. B. , Frey, B. J. , Madison, T. J. , Gong, Q. , and Tecza, M. . In *Society of Photo-Optical Instrumentation Engineers (SPIE) Conference Series*, volume 6692 of *Society of Photo-Optical Instrumentation Engineers (SPIE) Conference Series*, October 2007b.
- Li, A. . In Ho, L. C. and Wang, J.-W. , editors, *The Central Engine of Active Galactic Nuclei*, volume 373 of *Astronomical Society of the Pacific Conference Series*, page 561, October 2007.
- Littlejohns, O. M. , Butler, N. R. , Cucchiara, A. , Watson, A. M. , Fox, O. D. , Lee, W. H. , Kutyrev, A. S. , Richer, M. G. , Klein, C. R. , Prochaska, J. X. , Bloom, J. S. , Troja, E. , Ramirez-Ruiz, E. , de Diego, J. A. , Georgiev, L. , González, J. ,

- Román-Zúñiga, C. G. , Gehrels, N. , and Moseley, H. . MNRAS, 449:2919–2936, May 2015.
- Loewen, EG and Popov, E . *Diffraction Gratings and Applications*. CRC Press, 1 edition, 1997.
- MacFarlane, M. J. and Dunham, E. W. . In J. M. Oschmann Jr., editor, *Society of Photo-Optical Instrumentation Engineers (SPIE) Conference Series*, volume 5489 of *Society of Photo-Optical Instrumentation Engineers (SPIE) Conference Series*, pages 796–804, October 2004.
- Maiolino, R. , Marconi, A. , Salvati, M. , Risaliti, G. , Severgnini, P. , Oliva, E. , La Franca, F. , and Vanzi, L. . A&A, 365:28–36, January 2001.
- Malesani, D. , Tagliaferri, G. , Chincarini, G. , Covino, S. , Della Valle, M. , Fugazza, D. , Mazzali, P. A. , Zerbi, F. M. , D’Avanzo, P. , Kalogerakos, S. , Simoncelli, A. , Antonelli, L. A. , Burderi, L. , Campana, S. , Cucchiara, A. , Fiore, F. , Ghirlanda, G. , Goldoni, P. , Götz, D. , Mereghetti, S. , Mirabel, I. F. , Romano, P. , Stella, L. , Minezaki, T. , Yoshii, Y. , and Nomoto, K. . ApJ, 609:L5–L8, July 2004.
- Mangano, V. , Cummings, J. R. , Cusumano, G. , Gehrels, N. , La Parola, V. , Markwardt, C. B. , Osborne, J. P. , Sbarufatti, B. , and vanden Berk, D. E. . *GRB Coordinates Network*, 7847, 2008.
- Marshall, F. E. , Cummings, J. R. , Gronwall, C. , Kennea, J. A. , Maselli, A. , Sakamoto, T. , Siegel, M. H. , and Ukwatta, T. N. . *GRB Coordinates Network*, 16118, 2014.
- Matz, S. M. , Forrest, D. J. , Vestrand, W. T. , Chupp, E. L. , Share, G. H. , and Rieger, E. . ApJ, 288:L37–L40, January 1985.
- Meegan, C. A. , Fishman, G. J. , Wilson, R. B. , Horack, J. M. , Brock, M. N. , Paciasas, W. S. , Pendleton, G. N. , and Kouveliotou, C. . Nature, 355:143–145, January 1992.
- Mészáros, P. . *Reports on Progress in Physics*, 69:2259–2321, August 2006.
- Metzger, M. R. , Djorgovski, S. G. , Kulkarni, S. R. , Steidel, C. C. , Adelberger, K. L. , Frail, D. A. , Costa, E. , and Frontera, F. . Nature, 387:878–880, June 1997.
- Misselt, K. A. , Clayton, G. C. , and Gordon, K. D. . ApJ, 515:128–139, April 1999.
- Morgan, A. N. , Perley, D. A. , Cenko, S. B. , Bloom, J. S. , Cucchiara, A. , Richards, J. W. , Filippenko, A. V. , Haislip, J. B. , LaCluyze, A. , Corsi, A. , Melandri, A. , Cobb, B. E. , Gomboc, A. , Horesh, A. , James, B. , Li, W. , Mundell, C. G. , Reichart, D. E. , and Steele, I. . MNRAS, 440:1810–1823, May 2014.

- Nellis, G. and Klein, S. . *Heat Transfer*. Cambridge University Press, 2009. ISBN 9780521881074. <https://books.google.com/books?id=D4FFiD6hZ94C>.
EXAMPLE1.9-2: Cryogenic Current Leads.
- Nelson, JD , Youngworth, RN , and Aikens, DM . *SPIE Proceedings*, 7433, 2009.
- Nevière, M . *Appl. Opt*, 31:427–428, 1992.
- NOAO. <http://www.noao.edu/ets/gnirs/SDN0013-02.htm>.
- Optimax Systems, Inc., 2012. www.optimaxsi.com. Tolerancing Chart.
- Paciesas, W. S. , Meegan, C. A. , Pendleton, G. N. , Briggs, M. S. , Kouveliotou, C. , Koshut, T. M. , Lestrade, J. P. , McCollough, M. L. , Brainerd, J. J. , Hakkila, J. , Henze, W. , Preece, R. D. , Connaughton, V. , Kippen, R. M. , Malozzi, R. S. , Fishman, G. J. , Richardson, G. A. , and Sahi, M. . *ApJS*, 122:465–495, June 1999.
- Paczynski, B. . *ApJ*, 308:L43–L46, September 1986.
- Paczynski, B. and Rhoads, J. E. . *ApJ*, 418:L5, November 1993.
- Palmer, Christopher A , Loewen, Erwin G , and Thermo, RGL . *Diffraction grating handbook*. Newport Corporation Springfield, Ohio, USA, 2005.
- Perley, D. A. , Cenko, S. B. , Corsi, A. , Tanvir, N. R. , Levan, A. J. , Kann, D. A. , Sonbas, E. , Wiersema, K. , Zheng, W. , Zhao, X.-H. , Bai, J.-M. , Bremer, M. , Castro-Tirado, A. J. , Chang, L. , Clubb, K. I. , Frail, D. , Fruchter, A. , Göğüş, E. , Greiner, J. , Güver, T. , Horesh, A. , Filippenko, A. V. , Klose, S. , Mao, J. , Morgan, A. N. , Pozanenko, A. S. , Schmidl, S. , Stecklum, B. , Tanga, M. , Volnova, A. A. , Volvach, A. E. , Wang, J.-G. , Winters, J.-M. , and Xin, Y.-X. . *ApJ*, 781:37, January 2014.
- Perley, D. A. , Morgan, A. N. , Updike, A. , Yuan, F. , Akerlof, C. W. , Miller, A. A. , Bloom, J. S. , Cenko, S. B. , Li, W. , Filippenko, A. V. , Prochaska, J. X. , Kann, D. A. , Tanvir, N. R. , Levan, A. J. , Butler, N. R. , Christian, P. , Hartmann, D. H. , Milne, P. , Rykoff, E. S. , Rujopakarn, W. , Wheeler, J. C. , and Williams, G. G. . *AJ*, 141:36, February 2011.
- Piran, T. . *Phys. Rep.*, 314:575–667, June 1999.
- Piran, T. . *Nature*, 422:268–269, March 2003.
- Piran, T. . *Reviews of Modern Physics*, 76:1143–1210, October 2004.
- Piro, L. , Costa, E. , Feroci, M. , Frontera, F. , Amati, L. , Dal Fiume, D. , Antonelli, L. A. , Heise, J. , Zand, J. i. , Owens, A. , Parmar, A. N. , Cusumano, G. , Vietri, M. , and Perola, G. C. . *ApJ*, 514:L73–L77, April 1999.

- Prochaska, J. X. , Chen, H.-W. , Dessauges-Zavadsky, M. , and Bloom, J. S. . ApJ, 666:267–280, September 2007.
- Prochaska, J. X. , Shiode, J. , Bloom, J. S. , Perley, D. A. , Miller, A. A. , Starr, D. , Kennedy, R. , and Brewer, J. . *GRB Coordinates Network*, 7849, 2008.
- Rauch, M. . *ARAA*, 36:267–316, 1998.
- Ren, D and Allington-Smith, JR . *Opt. Eng.*, 38(3), 1999.
- Richards, J. W. , Homrighausen, D. , Freeman, P. E. , Schafer, C. M. , and Poznanski, D. . MNRAS, 419:1121–1135, January 2012.
- Roming, P. W. A. , Kennedy, T. E. , Mason, K. O. , Nousek, J. A. , Ahr, L. , Bingham, R. E. , Broos, P. S. , Carter, M. J. , Hancock, B. K. , Huckle, H. E. , Hunsberger, S. D. , Kawakami, H. , Killough, R. , Koch, T. S. , McLelland, M. K. , Smith, K. , Smith, P. J. , Soto, J. C. , Boyd, P. T. , Breeveld, A. A. , Holland, S. T. , Ivanushkina, M. , Pryzby, M. S. , Still, M. D. , and Stock, J. . *Space Sci. Rev.*, 120:95–142, October 2005.
- Ruderman, M. . In Bergman, P. G. , Fenyves, E. J. , and Motz, L. , editors, *Seventh Texas Symposium on Relativistic Astrophysics*, volume 262 of *Annals of the New York Academy of Sciences*, pages 164–180, October 1975.
- Sari, R. and Piran, T. . ApJ, 455:L143, December 1995.
- Sari, R. and Piran, T. . ApJ, 517:L109–L112, June 1999.
- Sari, R. , Piran, T. , and Narayan, R. . ApJ, 497:L17–L20, April 1998.
- Schady, P. and Mangano, V. . *GRB Coordinates Network*, 7858, 2008.
- Schlaflly, E. F. and Finkbeiner, D. P. . ApJ, 737:103, August 2011.
- Schlegel, D. J. , Finkbeiner, D. P. , and Davis, M. . ApJ, 500:525–553, June 1998.
- Schmidt, W. K. H. . *Nature*, 271:525–527, February 1978.
- Schwarz, G. . *Cryogenics*, 28:248–254, 1988.
- Singer, S. . *Proceedings of the IEEE*, 53(12):1935–1948, Dec 1965. ISSN 0018-9219.
- Spitzer, L. . *Physical processes in the interstellar medium*. 1978.
- Stamatikos, M. , Barthelmy, S. D. , Baumgartner, W. , Cummings, J. , Fenimore, E. , Gehrels, N. , Krimm, H. , Mangano, V. , Markwardt, C. , McLean, K. , Palmer, D. , Sakamoto, T. , Sato, G. , Tueller, J. , and Ukwatta, T. . *GRB Coordinates Network*, 7852, 2008.

- Stamatikos, M. , Barthelmy, S. D. , Baumgartner, W. H. , Beardmore, A. P. , Cummings, J. R. , Fenimore, E. E. , Gehrels, N. , Krimm, H. A. , Markwardt, C. B. , Palmer, D. M. , Sakamoto, T. , Tueller, J. , and Ukwatta, T. N. . *GRB Coordinates Network*, 12884, 2012.
- Stoll, R. , Martini, P. , Derwent, M. A. , Gonzalez, R. , O'Brien, T. P. , Pappalardo, D. P. , Pogge, R. W. , Wong, M.-H. , and Zhelem, R. . In *Ground-based and Airborne Instrumentation for Astronomy III*, volume 7735 of Proc. SPIE, page 77354L, July 2010.
- Swift, G. W. and Packard, R. E. . *Cryogenics*, 19:362–363, 1979.
- Takita, K. , Aoki, T. , Sasaki, Y. , Higuchi, T. , and Kobayashi, K. . *IEICE*, E86-A (8):1925–1934, August 2003.
- Tanvir, N. R. , Fox, D. B. , Levan, A. J. , et al. *Nature*, 461:1254–1257, October 2009.
- Tanvir, N. R. , Levan, A. J. , Cucchiara, A. , Perley, D. , and Cenko, S. B. . *GRB Coordinates Network*, 16125, 2014.
- Toy, V. , Cenko, S. B. , Kutyrev, A. , Capone, J. , Troja, E. , Cucchiara, A. , Veilleux, S. , and Gezari, S. . *GRB Coordinates Network*, 15850, 2014.
- Toy, V. L. and Kutyrev, A. S. . 2016. Tests done at GSFC.
- Trissel, R. and Piccirillo, B. . January 2012.
- van Dokkum, P. G. . *PASP*, 113:1420–1427, November 2001.
- van Paradijs, J. , Groot, P. J. , Galama, T. , Kouveliotou, C. , Strom, R. G. , Telting, J. , Rutten, R. G. M. , Fishman, G. J. , Meegan, C. A. , Pettini, M. , Tanvir, N. , Bloom, J. , Pedersen, H. , Nørdgaard-Nielsen, H. U. , Linden-Vørnle, M. , Melnick, J. , van der Steene, G. , Bremer, M. , Naber, R. , Heise, J. , in't Zand, J. , Costa, E. , Feroci, M. , Piro, L. , Frontera, F. , Zavattini, G. , Nicastro, L. , Palazzi, E. , Bennett, K. , Hanlon, L. , and Parmar, A. . *Nature*, 386:686–689, April 1997.
- Ventura, G. , Bianchini, G. , Gottardi, E. , Peroni, I. , and Peruzzi, A. . *Cryogenics*, 39(5):481–484, 1999.
- Waxman, E. and Draine, B. T. . *ApJ*, 537:796–802, July 2000.
- Willingale, R. , Starling, R. L. C. , Beardmore, A. P. , Tanvir, N. R. , and O'Brien, P. T. . *MNRAS*, 431:394–404, May 2013.
- Zafar, T. , Watson, D. , Elíasdóttir, Á. , Fynbo, J. P. U. , Krühler, T. , Schady, P. , Leloudas, G. , Jakobsson, P. , Thöne, C. C. , Perley, D. A. , Morgan, A. N. , Bloom, J. , and Greiner, J. . *ApJ*, 753:82, July 2012.

Zaroubi, S. . In Wiklind, T. , Mobasher, B. , and Bromm, V. , editors, *The First Galaxies*, volume 396 of *Astrophysics and Space Science Library*, page 45, 2013.